Acta Universitatis Sapientiae

Electrical and Mechanical Engineering

Volume 16, 2024

Contents

S. Zengah, A. Baltach, A. Djebli, A. Benhamena Compilation of Stress Concentration Factors in the Vicinity of a Geometric Discontinuity in Structures
A. Belhanafi, O. Ladjedel, L. Adjllout Effect of Blade Number of an Anchor Agitator on the Laminar Flow in a Cylindrical Vessel
M. C. Malti, Z. Sari Hassoun, K. Aliane, Y. Rekiouk, B. di Pierro, M. A. Kherrafi Numerical Analysis of Efficiency Improvement in Flat Plate Solar Collectors using Offset Strip Fins
A. Aboura, A. Abdou, T. Bouchala, M. Chebout, B. Abdelhadi, M. Khabel Reconstruction of Defect Paths Using Eddy Current Testing Array 3D Imaging
T. Javanbakht, S. Laurent, D. Stanicki, E. David Comparative Study of Dielectric Properties and Other Physical Properties of Superparamagnetic Iron Oxide Nanoparticles and Polyethylene Nanocomposites
J. Zbojovský, R. Cimbala Effect of Thermal Ageing on the Electrical Insulation Properties of the Oil-Paper Insulation
S. Bucko, R. Cimbala Thermal Dependence of Ferrofluids Dielectric Response
M. Pavlík, M. Kolcun, D. Mazur Analysis of Hot Spots on Photovoltaic Panels
F. Margita, L. Beňa The use of WAM Systems for Determining the Ampacity of Overhead Power Lines
M. M. Ahmed Adaptive Digital Notch Filter for Enhanced Stability in Grid-Connected Inverter Systems

J. Király, D. Medved Operation of V2G Chargers in Smart Grids	124
D. Medved, M. Kolcun, J. Király, D. Mazur Power Management and Charging Strategies for Electric Vehicles	135
Á. Czimbalmos, Á. Fehér, L. Márton Model Predictive Control of Aerodynamic Levitation Systems	149
K. Ferencz, E. Rigó, J. Domokos, L. Kovács Implementation of Network Data Analysis Using the Neo4j Graph Database	162



DOI: 10.47745/auseme-2024-0001

Compilation of Stress Concentration Factors in the Vicinity of a Geometric Discontinuity in Structures

Sahnoun ZENGAH¹, Abdelghani BALTACH^{1,2}, Abdelkader DJEBLI¹, Ali BENHAMENA¹

¹ Mechanics of Materials, Energy and Environment Laboratory (L2M2E), University of Mascara, 29000 Mascara, Algeria, e-mail: s.zengah@univ-mascara.dz
²Department of Mechanical Engineering, University of Tiaret, 14000, Tiaret, Algeria

Manuscript received September 19, 2024; revised November 06, 2024

Abstract: The analytical method estimates the stress concentration factor (K_l) using theoretical equations, while the numerical approach overcomes the limitations of analytical solutions in dealing with complex geometries. Simulations were conducted to evaluate how variations in hole diameter affect the stress concentration factor, revealing that larger diameters significantly increase the stress concentration factor. The presence of holes induces localized over-stress, compromising structural integrity. The research focuses on circular and elliptical holes under tensile loading, integrating both analytical and numerical techniques. Results validated against analytical solutions pinpoint areas of maximum stress concentration, which are crucial for the design and optimization of perforated structures. This study provides valuable insights for engineers, enhancing understanding of perforated plates' behavior under load, ultimately improving their reliability and safety in various industrial applications. The primary aim is to quantify the SCF, highlighting the risks posed by geometric discontinuities and their potential to lead to plastic deformation or structural failure.

Keywords: Stress concentration factors, Numerical analysis, FEM.

1. Introduction

Stress concentration is a prevalent issue in the mechanical design of components and parts. This phenomenon occurs as a localized increase in stress in regions where the geometry of the component is altered, typically at discontinuities or notches, often resulting from machining processes. The areas of stress concentration are usually where fatigue cracks initiate, and they can also lead to sudden failure in brittle materials. The phenomenon was first elucidated by G. Kirchhoff in 1898 [1], who analyzed the stresses around a hole.

Subsequently, numerous authors have developed analytical solutions for structures with progressively more intricate geometries [1, 2].

Some of the earliest rupture tests were conducted well before the Industrial Revolution, demonstrating that the tensile strength of iron wires varied inversely with their length. These findings suggested that material defects influenced strength [3]. These findings suggested that material defects influenced strength [4, 5]. This qualitative interpretation was later refined by Griffith in 1920, who established the theoretical foundation for fracture mechanics [1].

The utilization of ductile materials under tensile loads has, at times, resulted in failures occurring at stress levels well below the elastic limit. Initially, efforts to prevent these failures involved over-dimensioning structures; however, the need to lighten structures and reduce costs led to the emergence of fracture mechanics [4, 6].

Technically, evaluating and managing stress concentrations is essential to prevent premature structural failures. Finite element method (FEM) is commonly employed to model and predict stress levels in these critical zones. Such simulations help engineers identify high-stress areas and optimize designs to minimize stress gradients. To mitigate the adverse effects of stress concentrations, various approaches are considered. These include designing smooth transitions in geometries, implementing localized reinforcement with additional materials or inserts, and applying surface treatment techniques to smooth out critical zones. These measures aim to reduce stress levels and enhance material fatigue resistance.

Fracture mechanics was developed to investigate the propagation of macroscopic cracks. This approach is closely tied to the presence of discontinuities within materials, which alter stress, strain, and displacement states [3, 7]. Depending on the material and loading conditions, linear elastic fracture mechanics (LEFM) is utilized when plasticity is either absent or highly localized at the crack tip [8, 9].

1.1 Stress Intensity Factors

Introduced by Irwin in 1957 [2], stress intensity factors correspond to specific kinematic movements of cracks. In the context of LEFM, stresses and strains near a crack exhibit an asymptotic expansion with a singular term expressed as:

$$\begin{cases}
\sigma_{ij} = K_{\alpha} \frac{1}{\sqrt{2\pi r}} f_{ij}^{\alpha} (\theta) \\
\varepsilon_{ij} = K_{\alpha} \frac{1}{\sqrt{2\pi r}} g_{ij}^{\alpha} (\theta)
\end{cases} (\alpha = I, II, III) . \tag{1}$$

The equation represents the singularity at r = 0 or asymptotic solution as tends to zero.

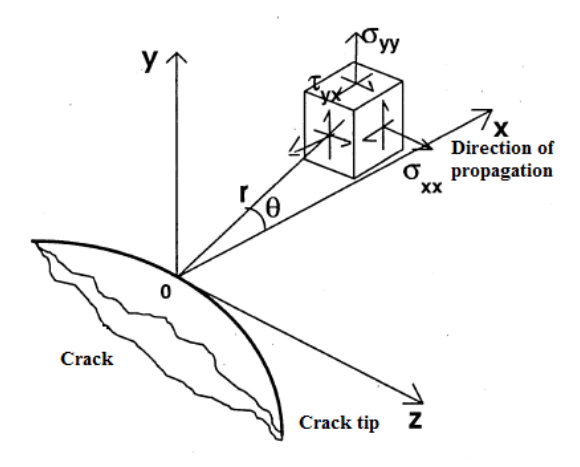


Figure 1: Crack in a polar coordinate system [10]

 K_{α} is the magnitude of the singularity, it is called the Stress Intensity Factor (SIF) [10]. The stress intensity factor is given for the failure mode α , with α being I, II, or III. The figure below (*Fig.* 2) represents the three failure modes.

The functions f and g provide the angular distribution, with their expressions being applicable to plane stress and strain conditions [11, 12].

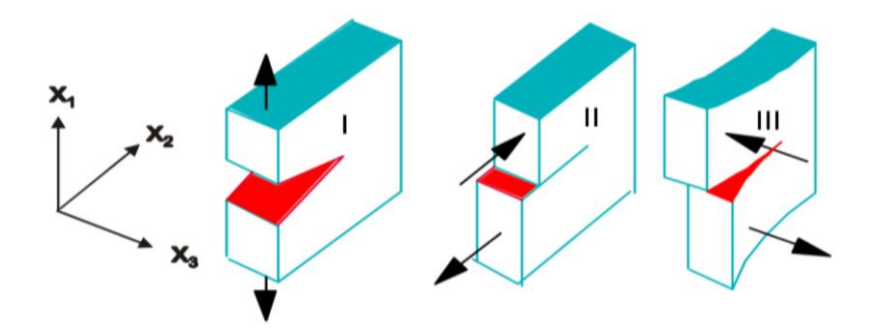


Figure 2: Modes of loading. (a) Cleavage mode: mode I. (b) In-plane shear mode: mode II. (c) Antiplane shear mode: mode III. [11]

The system considered here us represented in Fig. 3. This later is an "infinite" panel containing a crack of length (2a) along the x axis and subjected to uniform tension along y axis.

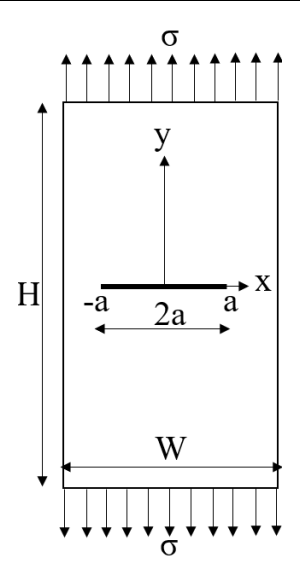


Figure 3: The center cracked plate in tension – CC(T) specimen [13]

In practice, such a model can be reasonably used when the dimensions of the crack are 10 to 20 times smaller than those of the plate [13, 14].

1.2 Stress concentration phenomena

Stress concentration phenomena are critically important in mechanics. Often unexpected and not always intuitive, they can lead to over-stress and, consequently, fatigue failures. Consider an elongated plate with width W and thickness t subjected to a tensile force F [8, 15, 16, 17]. This plate experiences a stress defined by:

$$\sigma = F/W \cdot t \tag{2}$$

This represents the simplest case of uniaxial stress, serving as the primary definition of stress. Now, examining the same plate perpendicular to the tensile force, directly above the center of a hole, the thickness at that point is (W-d)t, where d is the diameter of the hole:

$$\sigma = F/(W-d) \cdot t \tag{3}$$

This represents the force-to-section ratio, similar to the previous case. However, this is not accurate; at the edge of the hole, the stress is actually higher than this calculated value. Since static equilibrium dictates that the sum of stresses

over the considered section must equal F, it follows that at other points, the stress must be lower than what is predicted by equation (3) [18].

1.3 Theoretical Stress Concentration Factor (K_t)

Let us consider a thin plate having a elliptical hole of length 2a and subjected to uniaxial tension (see Fig. 4). The influence of a stress riser can be evaluated quantitatively through mathematical methods, including the stress concentration factor. This factor, denoted as K_t , is defined as the ratio of the maximum stress within the component to the reference stress, represented by the following equation:

$$K_{t} = 1 + 2 \cdot \frac{a}{b} = 1 + 2 \cdot \sqrt{\frac{a}{\rho}}$$
 (4)

where a is the half-length of the notch and ρ is the radius of curvature of the notch (with $a = \rho$). Consequently, K_t can be approximated as $K_t = 3$:



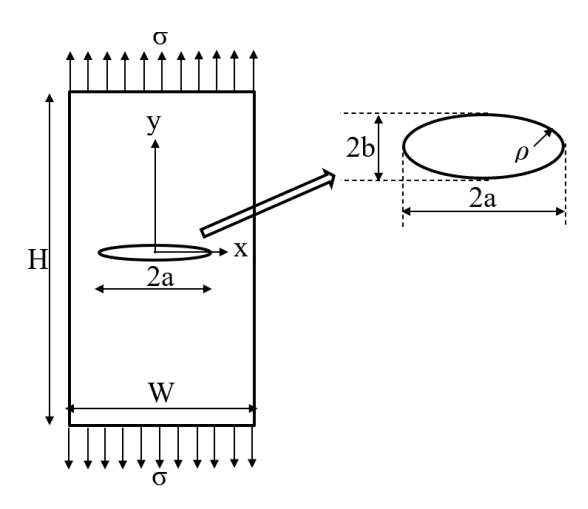


Figure 4: Infinite plate with elliptic hole under tension [19]

Furthermore, the stress concentration factor K_t can be calculated from the following formula [20]:

$$K_t = \frac{\sigma_{\text{max}}}{\sigma}$$
, (6)

where $K_t = \frac{\sigma_{\text{max}}}{\sigma}$; σ_{max} is the maximum stress and σ is the applied or global stress. The theoretical stress concentration factor K_t depends solely on the geometry of the component and the type of loading.

2. Problem of a 3D Perforated Plate Under Tensile Stress Field

Consider a finite rectangular plate with dimensions h=100 mm, W=50 mm, and a thickness t=1 mm, containing a central circular hole of diameter d=12 mm. The plate is subjected to a uniform tensile load F=5 kN. The geometric configuration of the plate is illustrated in *Fig.* 5. The objective is to evaluate the stress concentration around the hole, both analytically using strength of materials principles and numerically through simulations conducted in ABAQUS.

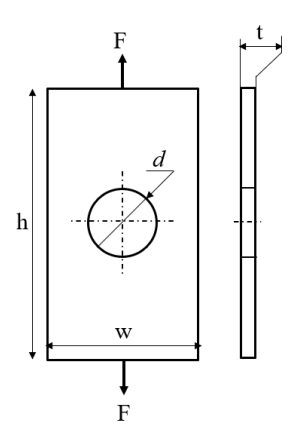


Figure 5: Perforated plate subjected to tensile stress

2.1. Analytical Study

The purpose of this analysis is to evaluate the stress applied σ_{app} in the section of the plate S_1 , away from the hole:

$$S_1 = W \cdot t \quad , \tag{7}$$

$$\sigma_{app} = \frac{F}{S_1} \ . \tag{8}$$

Calculating this gives $\sigma_{app} = 100 \text{ MPa}$.

Next, it is necessary to calculate the nominal stress in the section passing through the center of the hole (refer to Fig. 6).

$$S_2 = (W - d) \cdot t \quad , \tag{9}$$

$$\sigma_{nom} = \frac{F}{S_2} \ . \tag{10}$$

This yield $\sigma_{nom} = 131.57 \text{ MPa}$.

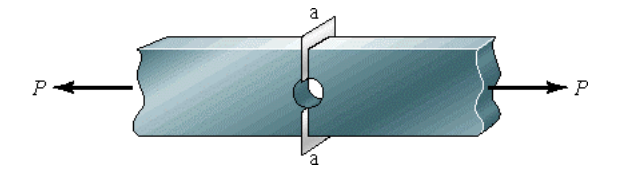


Figure 6: Section passing through the center of the hole

The maximum stress σ_{max} at the section intersecting the center of the hole (see *Fig. 7*) is determined using the following equation.

$$\sigma_{\max} = K_t \cdot \sigma_{nom} , \qquad (11)$$

where: σ_{max} represents the maximum stress at the center of the hole, K_t is the stress concentration factor, and σ_{nom} denotes the stress at the center of the hole.



Figure 7: Maximum stress in the section passing through the center of the hole

The value of the stress concentration factor K_t is obtained from graphical charts [21, 22]. In this study case:

$$\sigma_{\max} = K_t \cdot \sigma_{nom} , \qquad (12)$$

 $\frac{d}{W} = \frac{12}{50} = 0.24$; based on the charts, it can be concluded that $K_t = 2.4$; this leads to: $\sigma_{\text{max}} = 315.76 \text{ MPa}$.

2.2. Numerical Simulation of Stress Concentration Phenomenon

The analytical resolution of mechanical problems is limited to specific cases. In contrast, numerical methods based on the discretization of these problems offer a very effective alternative and are commonly used in mechanics to solve

complex situations. The finite element method (FEM) is the most widely used because it can handle problems with complex geometries and spans various fields of physics. Thanks to advancements in computing (processing power, visualization, and simulation tools), its implementation has become more accessible.

2.2.1. Geometric and Mechanical Characteristics

The material used exhibits elastic behavior in accordance with Hooke's law.

Table 1: Mechanical and Geometric Characteristics of the Plate

Young modulus E (MPa)	Poisson's Ratio <i>v</i>	Length (mm)	Width (mm)	Thickness mm	Material	Loading $\sigma_{app}(ext{MPa})$
270000	0.3	100	50	1	Steel	100

Representations of the geometry, the selected mesh, the boundary conditions, and the loading are provided in *Fig. 8*, *Fig. 9*, and *Fig. 10*.

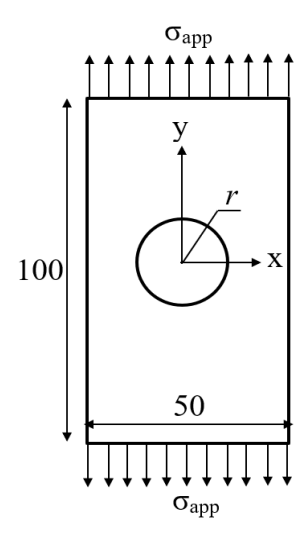


Figure 8: Geometry of the plate with circular hole

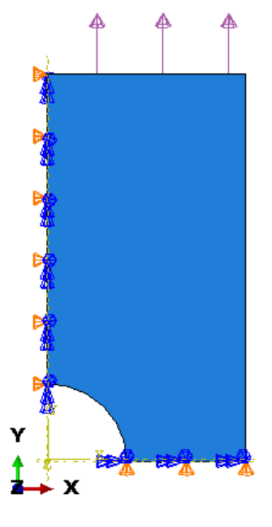


Figure 9: Boundary conditions and plate loading

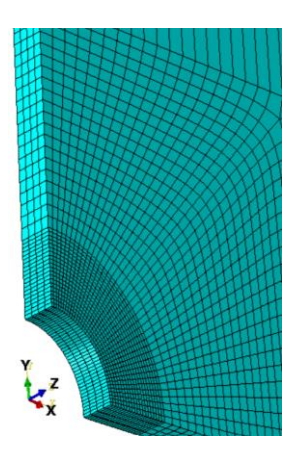


Figure 10: Mesh of the plate with circular hole

3. Results and Discussions

This section focuses on numerical simulations conducted using computational software (ABAQUS) to study and determine stress concentration in a plate subjected to a uniform tensile field. Particular attention is given to the influence of the hole diameter on the stress concentration factor K_t . Commonly used parameters are employed to analyze the behavior of perforated plates made from specific materials. The approach incorporates both analytical and numerical calculations of stress concentration, examining regions both at the edge and away from circular and elliptical holes under tensile loading. The presence of holes in structural components, commonly found in applications such as bolt holes or access ports, induces stress concentration, characterized by a localized increase in stress around the hole. The stress concentration factor (SCF) quantifies this increase and is influenced by the size of the hole. Larger holes generally lead to a higher SCF, as they disrupt the stress flow through the material more significantly, resulting in greater localized stresses. The SCF can be estimated using either analytical or numerical methods.

3.1. Plate with a central hole

Fig. 11 illustrates the distribution of the stress concentration factor, obtained from the results of the numerical simulation.

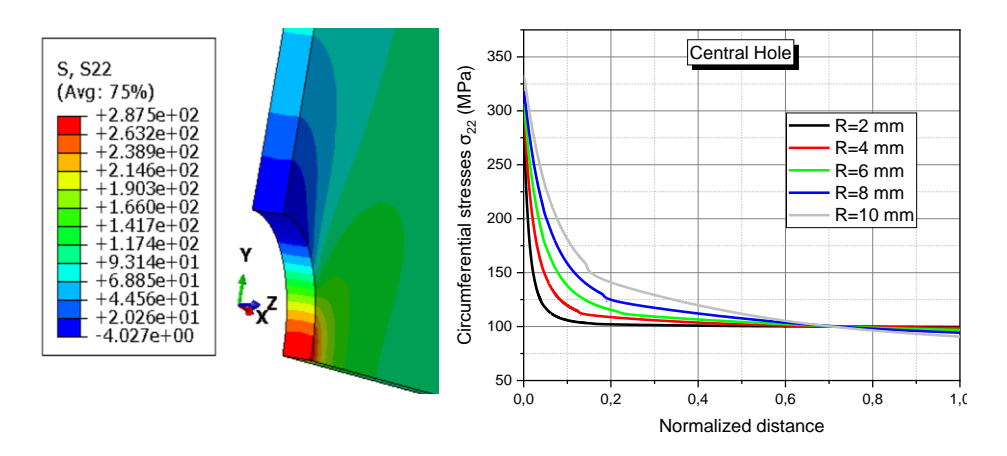


Figure 11: Circumferential stresses distribution at the edge of the circular hole (*r* =10 mm case)

Figure 12: Variation of circumferential stresses as a function of normalized distance

Fig. 11 and Fig. 12 illustrate the variation of circumferential stresses under tensile loading as a function of normalized radius for various values of r evaluated at specific intervals (r = 2, r = 4, r = 6, r = 8, r = 10 mm).

Fig. 13 illustrates how the Stress Concentration Factor (SCF) varies under tensile loading relative to the ratio $2 \cdot r/W$. This ratio allows for a comparative analysis of how the distance from the hole affects the stress concentration factor in relation to the plate width. Understanding these relationships is crucial for predicting failure locations and optimizing the design of perforated structures subjected to tensile stress.

The graph illustrates the variation in normal stress σ as the radius r increases from a reference point. Normal stress in tension represents the force per unit area, reflecting the material's response to stretching forces. The values of r (2, 4, 6, 8, 10) likely indicate radial measurements from a specific point within the material or system under analysis. An increase in stress with radius may suggest a non-uniform stress distribution, whereas a decrease implies that the tensile effect diminishes with increasing distance from the point of applied force.

The SCF quantifies stress increase at a specific location compared to the average stress in the material, crucial for evaluating material performance and durability under load.

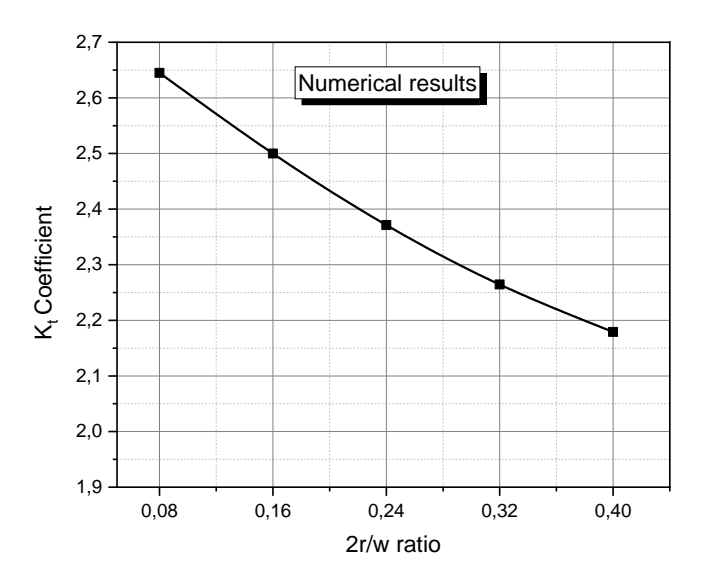


Figure 13: Variation of the K_t of traction stress as a function of the $2 \cdot r/W$ ratio

3.1.1. Correlation and Validation

Fig. 14 presents a comparison between the analytical results derived from relation and the numerical results. This comparison aims to validate the accuracy of the models used.

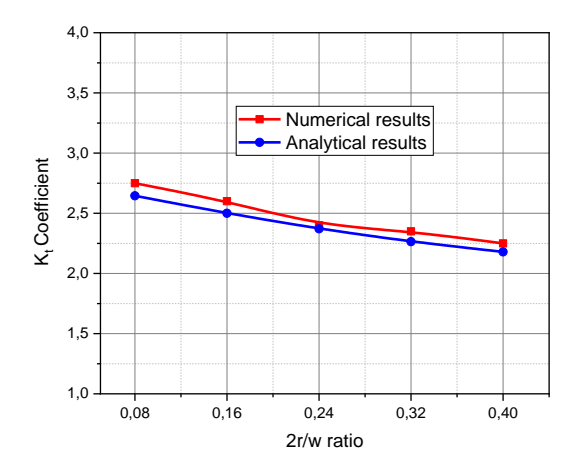


Figure 14: Comparison of the variation of the Stress Concentration Factor (SCF) under tensile loading between analytical and numerical results as a function of hole size $2 \cdot r/W$

3.2. Plate with a Half-Lateral Hole

Similar to case no. 1, the stress concentration in a plate with a half-lateral hole is analyzed. *Fig. 15* presents the distribution of the stress concentration factor, derived from the numerical simulation results.

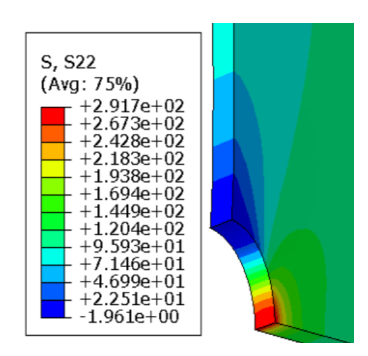


Figure 15: Circumferential stresses distribution at the edge of the circular hole

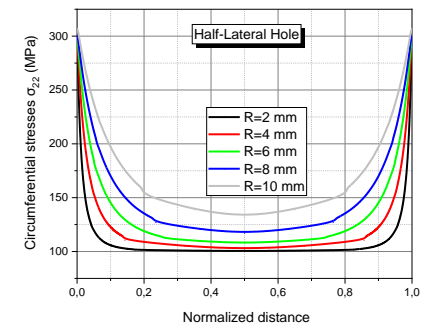


Figure 16: Variation of circumferential stresses as a function of normalized distance

Fig 15 and Fig. 16 illustrate the variation of normal stress under tensile loading as a function of distance. Fig. 17 depicts the variations of the Stress Concentration Factor (SCF) under tensile loading relative to the ratio $2 \cdot r/W$. These figures provide critical insights into how the distance from the hole affects both the normal stress distribution and the SCF, which are essential for assessing the structural integrity of perforated components under tensile forces.

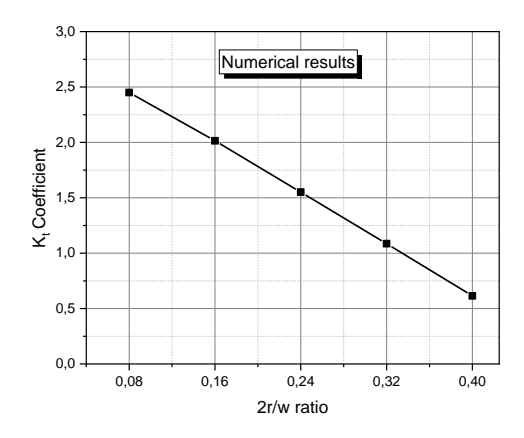


Figure 17: Variation of the SCF of traction stress as a function of the 2r/W ratio

3.2.1. Correlation and Validation

For a clearer explanation, we present in *Fig. 18* the values of the stress concentration factor, calculated both analytically and numerically, as a function of the 2r/W ratio.

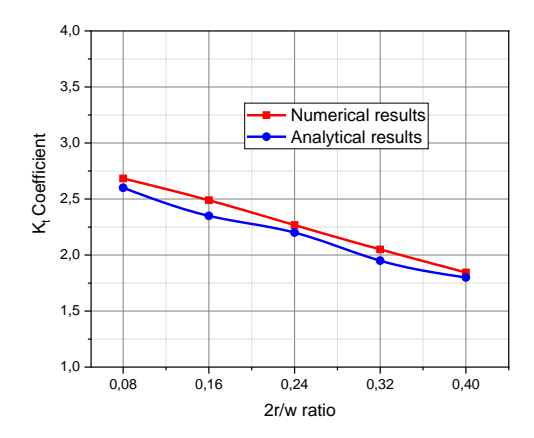


Figure 18: Comparison of the variation of the Stress Concentration Factor (SCF) under tensile loading between analytical and numerical results as a function of $2 \cdot r/W$

This figure illustrates the variation of the K_t coefficient as a function of the $2 \cdot r/w$ ratio, where two sets of results are compared: numerical results and analytical results. The K_t coefficient decreases monotonically as the $2 \cdot r/w$ ratio increases, indicating an inverse relationship between K_t and $2 \cdot r/w$. The numerical and analytical results are very close throughout the curve, suggesting a strong agreement between the two methods.

3.3. Discussions

Notably, the numerical simulation results for the first and second plates indicate that the Stress Concentration Factor *SCF* at the edge of the holes varies with changes in diameter. Specifically, the *SCF* value increases as the diameter enlarges. This trend highlights the importance of considering diameter variations in the design process to mitigate potential structural vulnerabilities. The analysis of the stress concentration factor in plates with holes indicates that this critical value increases proportionally with the hole diameter. This finding necessitates a careful approach to design and analysis to ensure optimal performance and adequate structural safety.

Particularly the Finite Element Method (FEM), is employed to model the mechanical behavior of structures with holes. These simulations allow for the prediction of stress and deformation patterns under various loading conditions and environmental factors. The FEM effectively captures complex geometries and boundary conditions that are often challenging to analyze analytically.

The Stress Concentration Factor *SCF* quantifies the localized amplification of stress around holes or other geometric discontinuities. This parameter is essential for evaluating the potential for structural failure, as high *SCF* values indicate areas where stresses may exceed material limits, leading to plastic deformation or fracture. Stresses are significantly higher near the edges of a hole due to the abrupt change in geometry, which concentrates stress in those regions.

A larger diameter results in a wider zone impacted by concentrated stresses, leading to higher *SCF* values as the diameter increases.

7. Conclusions

This study highlights the importance of considering geometric discontinuities, such as holes, in structural design. To address this, it investigates stress concentration in plates containing circular or elliptical holes under uniform stress fields, employing both analytical and numerical methods:

Analytical methods based on elasticity theory provide equations to estimate Stress Concentration Factors *SCF*, which are effective for simpler geometries. Finite Element Analysis (FEA) using ABAQUS software was also employed to

simulate stress distributions around holes, offering advantages for complex geometries and loading conditions where analytical solutions are impractical. The software accurately models mechanical behavior under applied loads, predicting stresses and deformations.

The *SCF* increases with hole diameter, indicating higher stress levels at hole edges. The shape of the hole influences stress concentration differently; elliptical holes exhibit varying *SCF*s depending on orientation relative to the load. For instance, an ellipse with its major axis perpendicular to the load direction may have a higher *SCF* than one with its major axis parallel.

The ratio of hole diameter to plate width d/W significantly impacts SCF. Proper hole sizing and placement are crucial to minimize stress concentrations and ensure structural integrity. Design optimization strategies may include adding local reinforcements or adjusting geometric shapes to distribute stress more evenly.

This study underscores the importance of considering geometric discontinuities like holes in structural design. Findings emphasize that *SCF* increases with hole diameter, necessitating careful design to avoid high stress concentrations.

For robust and reliable design solutions, engineers should integrate numerical simulations with experimental validation, ensuring structural performance and safety across various industrial applications.

References

- [1] Griffith, A., "The Phenomena of Rupture and Flow in Solids", *Philosophical transactions of the royal society of London. Series A, containing papers of a mathematical or physical character*, vol. 221, no. 582–593, pp. 163–198, 1920.
- [2] Irwin, G.R., "Analysis of Stresses and Strains Near the End of a Crack Traversing a Plate", J. Appl. Mech., vol. 24, pp. 361–364, 1957.
- [3] Thomas, N., Weijermars, R., "Comprehensive atlas of stress trajectory patterns and stress magnitudes around cylindrical holes in rock bodies for geoscientific and geotechnical applications", *Earth-Science Reviews.*, vol. 179. pp. 303–371, 2018.
- [4] Xue-feng, L., Kun, D., Jian, Z., Zhi-qiang, Y., "Failure behaviors of square-tunnel-structured rock specimens under various inclined boundary stress conditions", *Engineering Failure Analysis*, vol. 157, pp. 107888, 2024.
- [5] Gibson, L.J., Ashby, M.F, "Cellular Solids: Structure and Properties", 2nd ed., Cambridge University Press, 1997.
- [6] Erdogan, F., "Fracture Mechanics", Int. J. Solids and Structures., vol. 37, pp. 171–183, 2000.
- [7] Ozkan, M.T., Erdemir, F., "Determination of stress concentration factors for shafts under tension", *Mater Test.*, Vol. 62, no. 4, pp. 413–421, 2020.
- [8] Andia, P.C., Costanzo, F., Gray, G.L., "A Classical Mechanics Approach to the Determination of the Stress and Strain Response of Particle Systems. Model", *Simul. Mater. Sci. Eng.*, vol. 14, pp. 741–757, 2006.

- [9] Marcal, P.V., & King, I.P., "Elastic-plastic analysis of two-dimensional stress systems by the finite element method", *International Journal of Mechanical Sciences*, vol. 9, no. 3, pp. 143–155, 1967.
- [10] Miannay, D., "Mécanique de la rupture", Les Éditions de la Physique, pp. 104-150, 1995.
- [11] Raphaël, E., Gennes, P.G., "The adhesion between elastomers", in Soft Order in Physical Systems. Boston, MA: Springer US, pp. 57–71, 1994.
- [12] Miao, X., Yu, Q., Zhou, C., Li, J., Wang, Y., & He, X., "Experimental and numerical investigation on fracture behavior of CTS specimen under I-II mixed mode loading", *European Journal of Mechanics - A/Solids*, vol. 72, pp. 235–244. 2018.
- [13] Graba, M., "Catalogue of maximum crack opening stress for CC (T) specimen assuming large strain condition", *Open Engineering*, Vol. 3, no. 2, PP. 174–190, 2013.
- [14] Mayr, C.M., Rother, K., "Improved stress concentration factors for circular shafts for uniaxial and combined loading", *Mater Test.*, Vol. 61, no. 3, pp. 193–203, 2019.
- [15] Petersen, R.E., "Stress concentration factor", ESDU Engineering data. Structures. London, pp. 146–235.1974.
- [16] Santos, A., Guzman, R., Ramirez, Z., Cardenas, C., "Simulation of stress concentration factors in combined discontinuities on flat plates". *Journal of Physics: conference series IOP Publishing*, vol. 743, no 1, pp. 012014. 2016.
- [17] Taylor, D., Kelly, A., Toso, M., Susmel, L., "The variable-radius notch: Two new methods for reducing stress concentration", *Eng. Fail. Anal.*, vol. 18, pp. 1009–1017. 2011.
- [18] Delyová, I., Hroncová, D., Sivák, P., "Use of FEM in identification of stress in place of concentration factor", Am. J. Mech. Eng., vol. 4, pp. 454–459. 2016.
- [19] Tari, V., "Analytical verification of FFT-based micromechanical simulations near an elliptical crack tip by using composite voxels", *Mechanics of Advanced Materials and Structures* pp.1–10. 2023.
- [20] Makhutov, N.A., Reznikov, D.O., "Generalization of Neuber's rule for the assessment of local stresses and strains in stress concentration zones for a wide range of applied strains", in *Proc. Procedia Struct. Integr*, 2019, pp. 199–206.
- [21] Milella, P.P. "Fatigue and corrosion in metals", Springer Science & Business Media, 552. 16. 2012.
- [22] Pilkey, W.D., Pilkey, D.F., Zhuming, B.I., "Peterson's stress concentration factors", Hoboken, John Wiley & Sons, 4th Edition E-Book January 2020.



DOI: 10.47745/auseme-2024-0002

Effect of Blade Number of an Anchor Agitator on the Laminar Flow in a Cylindrical Vessel

Abdelghani BELHANAFI¹, Omar LADJEDEL¹, Lahouari ADJLLOUT¹

¹ Department of Mechanical Engineering, Faculty of Mechanics, University of Sciences and Technology of Oran Mohamed Boudiaf (USTO-MB), El Mnaouer, PO Box 1505, Bir El Djir 31000, Oran, Algeria, e-mail: abdelghani.belhanafi@univ-usto.dz, ladjedelomar@yahoo.com, adjlout@yahoo.fr

Manuscript received May 21, 2024; revised November 03, 2024

Abstract: The mixing of non-Newtonian fluids is a common phenomenon in industrial processes, where efficiency depends on the hydrodynamics of the stirring tank. A numerical study was conducted in a cylindrical vessel equipped with an agitator operating at a low Reynolds number. The liquid height was kept equal to the tank diameter. ANSYS CFD CFX was used to solve the numerical equations employing the MRF (Multiple Reference Frame) approach. The profiles and velocity distribution in vertical and horizontal planes were analyzed and discussed. The results show a reasonably good agreement with experimental data. To achieve a perfect circular flow in the vertical direction, the number of blades in the classical anchor was increased.

Keywords: Mixing, anchor agitator, blade number, laminar flow, CFD.

1. Introduction

Laminar mixing is commonly encountered in processes involving physical and chemical changes in many industries. The study of agitation systems has been initiated in several works. For example, Karray et al. [1] focused on the hydromechanical study of a cylindrical tank equipped with a classical anchor in a stationary regime. They examined the displacement effect of the anchor arm under turbulent flow conditions. Using CFD methods, Iranshahi et al. [2] compared the viscous mixing characteristics of the Ekato Paravisc mixer with those of an anchor and a double-helical ribbon. They found that the characteristics of the Paravisc mixer were between those of the other impellers at low Reynolds numbers. Zied et al. [3] proposed combining a classical anchor with the superposition of two turbine stages operating in a down-pumping direction to improve hydrodynamic flow. Ameur et al. [4] used a combination of Scaba 6SRGT and anchor agitators to enhance stirring efficiency for shear-thinning

liquids. Recently, Ameur et al. [5] tested newly designed impellers with a classical anchor in laminar regimes, resulting in improved fluid circulation and wider well-stirred regions for vessels equipped with circular horizontal blades.

Using CFD, Poonam and Farhad [6] focused on mixing xanthan gum, a pseudoplastic fluid with yield stress, using two-blade and four-blade anchor impellers. Their optimization study identified 0.102 and 0.079 as the optimal stirrer width-to-vessel diameter and stirrer clearance-to-vessel diameter ratios. respectively. They found that the anchor with four blades performed better than the two-blade version. Chhabra and Richardson [7] reported that anchors could be used for agitating both Newtonian and non-Newtonian fluids, primarily generating tangential flows with secondary axial and radial flows at high rotational speeds. Niedzielska et al. [8] experimentally investigated power consumption and heat transfer coefficients for ribbon impellers in laminar regimes. Nurul et al. [9] compared the torque produced by anchor and helical blade impellers for mixing highly viscous fluids (grease), finding that the helical blade produced 0.25 N·m, while the anchor blade produced 0.28 N·m. Anne-Archard et al. [10] used CFD to analyze hydrodynamics and power consumption in laminar flows, establishing Metzner-Otto correlations for power-law fluids and discussing shear rate distributions for helical and anchor agitators. Sinthuran et al. [11] studied gas dispersion in viscous Newtonian fluids using a coaxial mixer with a central impeller (PBT) and an anchor agitator, demonstrating its effectiveness in dispersing gas against buoyancy forces. Murthy et al. [12] developed a new correlation for calculating power consumption in anchor mixing systems using CFD simulations based on the Metzner-Otto concept. Abhishek et al. [13] proposed a novel method for measuring solid suspension in anchoragitated vessels by observing density variations with different D/T ratios. Finally, Hae et al. [14] conducted experimental and numerical studies to examine unmixed regions in a tank equipped with an anchor impeller for Newtonian fluids.

The objective of this work is to study the mechanical agitation of a highly viscous fluid using an agitator in three configurations, based on increasing the number of blades in a tank equipped with an anchor impeller. This investigation aims to obtain the optimal impeller design for mixing viscoplastic fluids in a cylindrical tank, analyzed through CFD modeling.

2. Agitated systems

As presented in *Fig. 1*, three geometrically scaled vessels were chosen, each with a different number of blades on a classical anchor: an agitator with two blades (case 1), three blades (case 2), and four blades (case 3). The first system configuration is similar to the one described by Murthy et al. [12] (*Fig. 1*). Each system consists of a flat-bottom cylindrical vessel with a diameter of

D=H=0.3 m. The anchor impeller has two arms with a diameter of $d=0.9 \cdot D$ and a height of $h=0.75 \cdot D$, attached to the shaft of the stirred vessel. The angle between the blades is $\theta=180^{\circ}$ for case 1, $\theta=120^{\circ}$ for case 2, and $\theta=90^{\circ}$ for case 3.

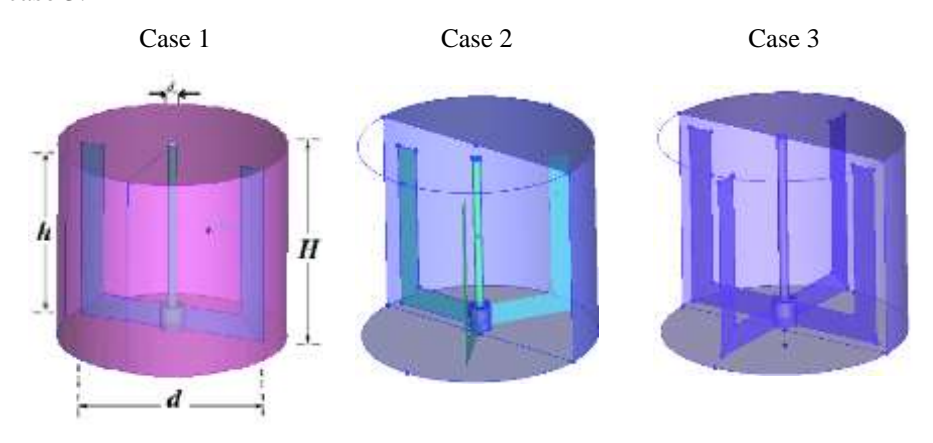


Figure 1: Mixing vessel dimensions

3. Method

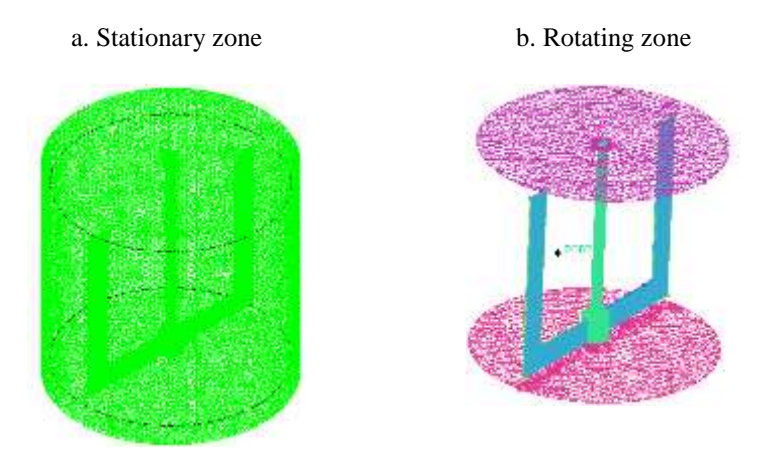


Figure 2: Tetrahedral mesh generation

Three-dimensional computational fluid dynamics (CFD) simulations were carried out using the CFD software ANSYS CFX to investigate the flow field in an agitated vessel stirred by a two-blade, three-blade, and four-blade anchor

agitator. The computational domain was meshed using tetrahedral cells in ANSYS ICEM CFD (*Fig.* 2). The domain was divided into two distinct zones for each of the three geometries. The tank walls constitute the stationary zone (*Fig.* 2a), discretized with 88,066 nodes. The rotating zone (*Fig.* 2b) describes the rotational motion of the fluid around the impeller and was discretized with 201,372 nodes for case 1, 276,234 nodes for case 2, and 341,948 nodes for case 3. Boundary conditions were defined in ANSYS CFX-Pre using the multiple reference frame (MRF) approach. In this approach, the interface between the two regions is treated by the frozen rotor method, which connects the flow fields at the interior surfaces (interface) separating the two domains. The computations were performed on a system with an Intel Core i7 CPU (2.20 GHz) and 8 GB of RAM.

4. Governing Equations

The Herschel-Bulkley model combines the effects of Bingham and power-law behavior in a fluid giving the shear stress as:

$$\tau = \tau_{y} + K \cdot \dot{\gamma}^{n} \,. \tag{1}$$

In (1), τ_y is the yield stress, K the consistency index, $\dot{\gamma}$ the shear rate and n is the flow behavior index. The average shear rate can be related to the impeller speed (N) by:

$$\dot{\gamma} = K_s \cdot N \ . \tag{2}$$

In (2), K_s is the Metzner-Otto's constant. The apparent viscosity results:

$$\eta = \frac{\tau}{K_s \cdot N} = \frac{\tau_y + K \cdot (K_s \cdot N)^n}{K_s \cdot N} \,. \tag{3}$$

The Reynolds number (Re) and the power number (N_p) are, respectively, calculated as:

$$Re = \frac{K_s \cdot N^2 \cdot d^2 \cdot \rho}{\tau_y + K \cdot (K_s \cdot N)^n},$$
(4)

where d is the impeller diameter, and

$$N_P = \frac{P}{\rho \cdot N^3 \cdot d^5} \,. \tag{5}$$

In (5), ρ is the density of the fluid and P is the power consumption.

5. Results and discussion

5.1 Comparison with Experimental Results

Fig. 3 shows the radial profile of the dimensionless angular velocity component, defined for $\theta = 90^{\circ}$. The comparison between the numerical results and the experimental results reported by Murthy et al. (2003) shows good agreement, demonstrating the validity of the adopted numerical method.

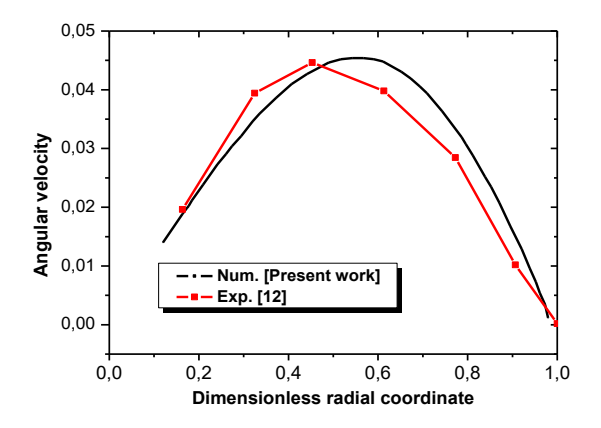


Figure 3: Radial profiles of the angular velocity at θ =90°

5.2 Effect of Blade number

5.2.1 Mean Velocity in r- θ Plane

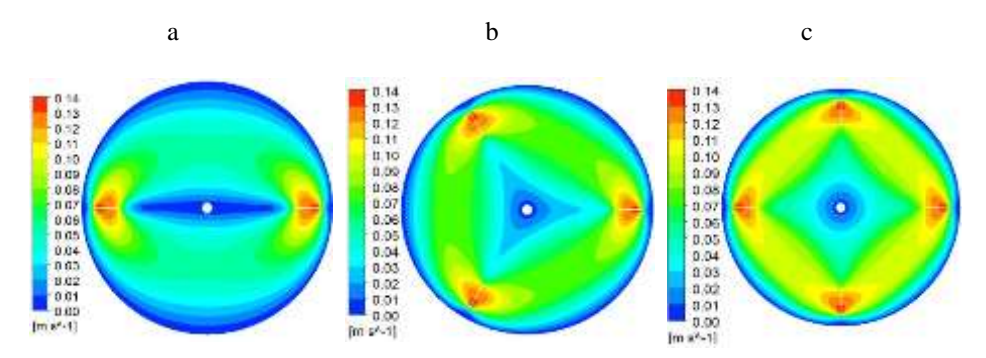


Figure 4: Mean velocity distribution in the horizontal plane: z = 0.15 m, N = 10 rpm, n = 0.8

The results of the velocity contours at the mid-height of the tanks are illustrated in Fig.~4. Globally, it is noted that the maximum values of the wake are developed in the area swept by the blades in all three cases. In case 3, the recirculation loop is more extended throughout the entire volume of the tank, reducing the stagnant fluid zone (Fig.~4c). For the classical anchor agitator (Fig.~4a), the maximum values are concentrated around the two vertical arms. As clearly illustrated, increasing the number of blades enlarges the well-stirred region and ensures mixing throughout the entire vessel volume.

5.2.2 Velocity in r-z Plane

Fig. 5 represents the mean velocity distribution in three different vertical planes for the tank. In this figure, the blue regions indicate stagnant (unmixed) zones, while the red regions indicate areas of high mixing caused by the impeller. Comparing these configurations, it is noted that the velocity is very low in the classical anchor configuration, case 1 (Fig. 5a). In the two other configurations, case 2 and case 3 (Fig. 5b and Fig. 5c), the maximum values of the mean velocity appear near the mechanical source and begin to decay continuously until becoming negligible near the shaft. In contrast, no recirculation motion is observed at the center of the stirred vessel in case 1 (Fig. 5a). Indeed, the anchor with three blades creates larger circulation loops of mean velocity between the blades in case 2 (Fig. 5b).

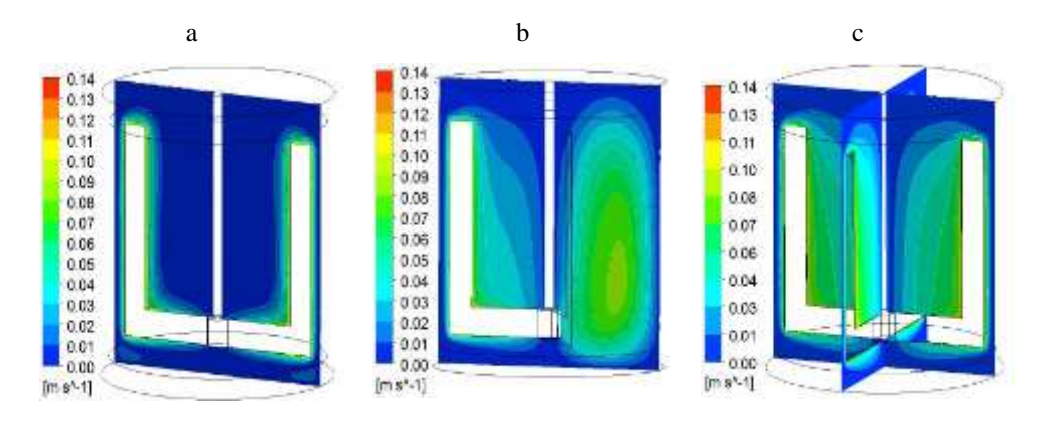


Figure 5: Mean velocity distribution in the vertical plane: N = 10 rpm, n = 0.8

On the horizontal plane, the mean velocity distribution is shown at the top parts of the vessels. In each case, a low-velocity region was observed behind the vertical arm, likely due to the contact surface between the blades and the fluid. In the first system, large non-agitated zones are observed (*Fig. 6a*). These dead zones can be reduced or eliminated by increasing the number of blades.

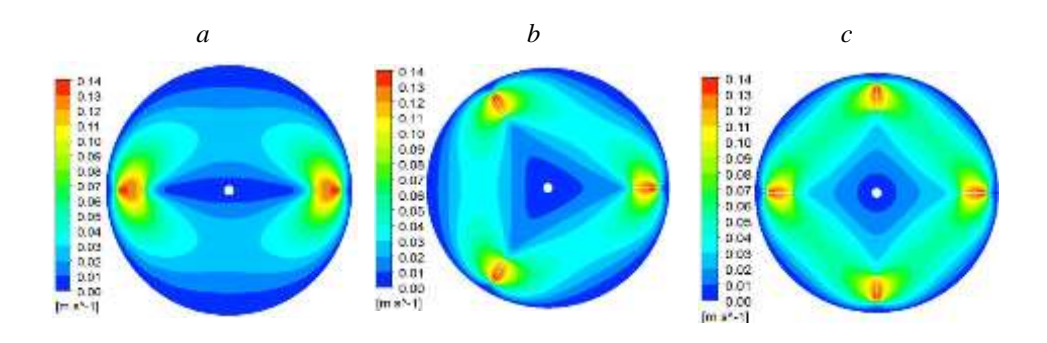


Figure 6: Mean velocity distribution in the horizontal plane, on the top, N = 10 rpm, n = 0.8

5.2.3 Streamlines

A 3D configuration of streamlines is shown in Fig. 7. This figure illustrates a highly turbulent mixing flow, particularly at the central parts of the vessels for the 2^{nd} and 3^{rd} configurations (Fig. 7b and Fig. 7c). Unlike the two-blade anchor in case 1, a small single loop of streamlines is observed at the mid-height of the tank (Fig. 7a). The primary circulation loop of streamlines is observed at the vessel base for the four-blade anchor agitator (Fig. 7c). This suggests that this type of impeller distributes the fluid more evenly throughout the volume. The three-blade anchor agitator directs the fluid toward the free surface of the liquid (Fig. 7b). This phenomenon was not observed in the classical anchor configuration, case 1 (Fig. 7a).

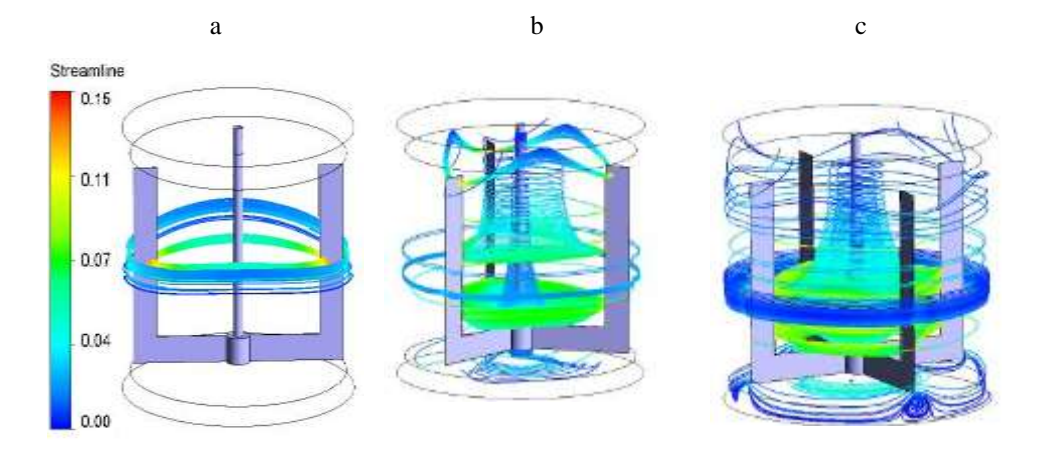


Figure 7: Streamlines for three cases: N = 10 rpm, n = 0.8

5.2.4 Dimensionless velocity profiles

5.2.4.1 Radial velocity component

The profiles shown in Fig.~8 represent the distribution of dimensionless radial velocity for the three cases. From the velocity components, it can be seen that the fluid is well distributed in the radial direction. At R = 0.075 m, the distribution of radial velocity increases with the increasing number of blades. This is due to the effect of the number of arm contact surfaces on the fluid dynamics. The radial component is more significant for the two configurations: case 2 and case 3. However, in the tank equipped with the classical anchor (case 1), the velocity is very low. Arguably, the radial velocity component is affected by the number of blades.

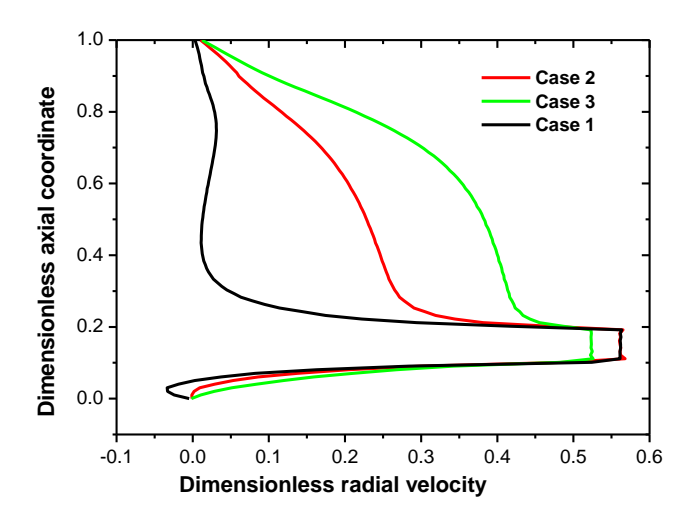


Figure 8: Radial velocity at radial position R = 0.075 m, N = 10 rpm, n = 0.8, $\theta = 30^{\circ}$

5.2.4.2 Tangential Velocity component

The tangential velocity along the tank radius is plotted in Fig.~9 for a rotational speed of N=10 rpm. As observed in configuration case 3, the tangential velocity increases gradually until reaching the highest values at the blade tip, then decreases rapidly at the vessel wall. This dynamic phenomenon is due to the acceleration of the fluid resulting from the increased number of blades on the agitator. However, in the first case, the velocity is very low compared to the other configurations, due to the large space between the two vertical arms of the classical anchor. The optimum values are obtained for tanks equipped with three and four blades, with $V^*=0.33$ at $R^*=0.98$.

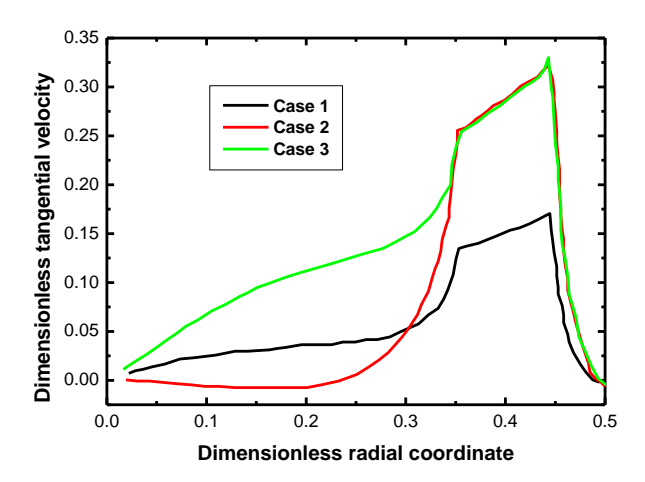


Figure 9: Tangential velocity at axial position z = 0.150 m, N = 10 rpm, n = 0.8, $\theta = 45^{\circ}$

6. Conclusion

The objective of this work was to determine the effect of different impeller types of anchor agitators in a cylindrical tank. From the presented results, the following conclusions can be drawn.

The anchor with three blades (case 2) creates larger amplitude circulation loops of mean velocity between the vertical arms. A high turbulence behavior of the streamlines is observed in the central part of the tanks for case 2 and case 3. In contrast to the classical anchor (case 1), a small single loop of streamlines is observed at mid-height of the tank. This is due to the large space between the two vertical arms of the classical anchor. It has been clearly observed that the dimensionless velocities in the radial direction are directly affected by the number of blades.

It can be concluded that when the number of arms is increased from 2 to 4, the flow is directly affected by the new active mixing region throughout the entire volume of the tank.

References

- [1] Karray, S., Driss, Z., Kchaou, H., Abid, M. S., "Numerical simulation of fluid-structure interaction in a stirred vessel equipped with an anchor impeller", *Journal of Mechanical Science and Technology*, vol. 25 (7), pp. 1749–1760, 2011.
- [2] Iranshahi, A., Heniche, M., Bertrand, F., and Tanguy, P. A., "Numerical investigation of the mixing efficiency of the Ekato Paravisc impeller", *Chem. Eng. Sci*, vol. 61, pp. 2609–2617, 2006.

- [3] Archard, A., Marouche, M., and Boisson, H. C., "Hydrodynamics and Metzner-Otto correlation in stirred vessels for yield stress fluids", *Chem. Eng. J*, vol. 125, pp. 15–24, 2006.
- [4] Ameur, H., and Ghenaim, A., "Mixing of Complex Fluids in a Cylindrical Tank by a Modified Anchor Impeller", *Energy Technology & Environmental Science*, vol. 3, pp. 7472–7477, 2018.
- [5] Ameur, H., and Youcefi, S., "Newly suggested shapes of impellers for stirring highly viscous fluids in vessels", *Science paper*, vol. 35, pp, 1–20, 2021.
- [6] Prajapati, P., and Mozaffari, F.E., "CFD Investigation of the Mixing of Yield-Pseudoplastic Fluids with Anchor Impellers", *Chem. Eng. Technol.*, vol. 32 (8), pp. 1211–1218, 2009.
- [7] Chhabra, R.P., and Richardson, J.F., "Non-Newtonian flow in the process industries", Fundamentals and engineering applications, Butterworth-Heinemann, 1999.
- [8] Niedzielska, A., and Kuncewicz, C., "Heat transfer and power consumption for ribbon impellers", Mixing efficiency Chemical Engineering Science, vol. 60, pp. 2439–2448, 2005.
- [9] Nurul, F. M. Y., Edmund, U. E., Ismail, F. I., and Akmal, N. M., "Mixing Performance of Anchor and Helical Stirrer Blades for Viscous Fluid Applications", *CFD Letters*, vol. 13.1, pp. 58–71, 2021.
- [10] Driss, Z., Salah, A. D., Driss, B., Necib, H., Kchaou, B., and Abid, M.S., "CFD investigation of the hydrodynamic structure around a modified anchor system", in *CFD Techniques and Energy Applications*, pp. 129–150, 2018.
- [11] Sinthuran, J. Argang, K. A., and Farhad, E.-M., "Enhanced aeration efficiency in non-Newtonian fluids using coaxial mixers: High-solidity ratio central impeller with an anchor", Chemical engineering Journal, 378, pp. 122081, 2019.
- [12] Murthy, S., and Jayanti, K., "Mixing of Power-Law Fluids Using Anchors: Metzner-Otto Concept Revisited", *AIChE Journal, January*, vol. 49, pp, 30–40, 2003.
- [13] Abhishek, M. S., Choudhari, S., and Muller. F., "Observations of solid–liquid systems in anchor agitated vessels", *Chemical engineering research and design*, vol. 90, pp. 750–756, 2012.
- [14] Hae, J. J., Hye, K. J., Young, J. K., and Wook, H. R., "Analysis of dynamical systems structures and mixing patterns in an anchor agitator", *Journal of chemical engineering of Japan*, vol. 51, no. 2, pp, 136–142, 2018.
- [15] Belhanafi, A., Driss, Z., and Abid, M. S., "Pumping Effects of a Square Tank Equipped with Single-Stage and Bi-Stage Impellers", *Acta Universitatis Sapientiae Electrical and Mechanical Engineering*, vol. 14, pp. 1–12, 2022.
- [16] Belhanafi, A., and Touhami, B., "Numerical study of bottom shape effect on the mixing for stirred tank", *Acta Universitatis Sapientiae Electrical and Mechanical Engineering*, vol. 15, pp. 86–97, 2023.



DOI: 10.47745/auseme-2024-0003

Numerical Analysis of Efficiency Improvement in Flat Plate Solar Collectors using Offset Strip Fins

Mohamed Chakib MALTI¹, Zakaria SARI HASSOUN¹, Khaled ALIANE¹, Younes REKIOUK³, Bastien DI PIERRO², Mohammed Abdelbassit KHERRAFI³

 MECACOMP Laboratory, Mechanical Engineering Department, Faculty of Technology, Abou Bekr Belkaid University, Tlemcen, Algeria
 Fluid Mechanics and Acoustics Laboratory, Claude Bernard University, Lyon 1, UMR 5509, Lyon; France
 ETAP Laboratory, Mechanical Engineering Department, Faculty of Technology, Abou Bekr Belkaid University, Tlemcen, Algeria

Manuscript received October 15, 2024; revised November 06, 2024

Abstract: This study aims to enhance the efficiency of flat plate solar collectors by integrating offset strip fins and utilizing Ansys Fluent for numerical analysis, validating results from a SolidWorks-designed solar air dryer. It outlines system components and objectives based on a standard model, supporting both theoretical and experimental analyses for applications in air conditioning and agro-food drying. Key boundary conditions, such as inlet temperature, air velocity, and absorber emissivity, were defined while maintaining experimental dimensions. Mesh tests ensured simulation accuracy for essential thermodynamic parameters, including outlet temperature and pressure, using the realizable k-epsilon turbulence model. The advanced model features obstacles that increase the heat transfer area by 53.6 % and create secondary turbulent flow. Staggered offset strip fins improved temperature by 12.6 % at an air velocity of 0.92 m/s (Re = 6000), significantly enhancing the overall effectiveness of the solar collector.

Keywords: Flat plate solar collectors, offset strip fins, temperature, velocity.

1. Introduction

The swift advancement of industrialization and rising energy demands strain limited fossil fuel resources and the environment. Therefore, it is essential to investigate all avenues for renewable energy generation. Among renewable sources, solar energy presents significant potential for fulfilling energy requirements sustainably. Consequently, various technologies have been developed and are being enhanced to utilize this potential effectively [1]. The

sun provides the most plentiful and accessible energy on Earth through direct solar irradiance and indirect forms like wind and hydro. Hence, solar energy stands as a viable, eco-friendly alternative that is readily available and can satisfy both present and future global energy needs without adverse effects [2]. Solar collectors are crucial for efficiently capturing Earth's abundant solar energy [3], with flat plate air collectors frequently employed for low to medium temperature applications due to their simplicity and ease of maintenance. Nonetheless, their relatively low efficiency poses challenges in justifying the initial costs over extended periods [4]. This paper emphasizes recent research efforts aimed at enhancing the efficiency of flat plate air collectors through design optimization, addressing the dual challenge of maximizing solar energy absorption at minimal cost while ensuring energy availability at night [5].

2. Technics of increasing the performance of a flat air solar collector

A flat plate air collector captures solar radiation for fluid heating using a dark absorber sheet that converts solar energy into heat, which is then transferred to circulating fluid. The absorber sheets, made from metals like copper or aluminum, are coated for better absorption, while integrated pipes carry the fluid. Glazing, typically glass or plastic, allows solar radiation in while minimizing heat loss, with insulation materials used to further reduce losses [6-9]. Experimental investigation by A. E. Kabeel et al [10] about thermal performance of flat and V-corrugated plate solar air heaters with and without Phase Change Materials as thermal energy storage, the authors integrated paraffin to the solar collectors for optimizing the global yield, they finally concluded that The V-corrugated solar air heater with PCM maintains outlet temperatures 1.5–7.2 °C higher than ambient for 3.5 hours after sunset at a flow rate of 0.062 kg/s, compared to 1–5.5 °C for the flat plate heater over 2.5 hours. At a lower flow rate of 0.009 kg/s, the V-corrugated heater stays 2–13 °C above ambient for 7.5 hours, while the flat plate heater remains 1.5–10 °C higher for 6 hours. M. A. Kherrafi et al [11] studied an indirect solar dryer, concluding it enhanced economic efficiency and reduced greenhouse gas emissions [12]. Furthermore H. Alsammarraie et al [13] explored nanofluid characteristics and their effects on heat transfer, identifying key factors like particle size and concentration. M. Nejlaoui et al [14] optimized flat plate solar collector performance in Qassim, achieving higher efficiency with a smaller collector area. Vednath P. Kalbande et al [15] reviewed nanofluid-based solar collectors integrated with thermal energy storage, noting that nanofluid properties significantly enhance system performance. P. Visconti et al [16] found that Al2O3-based nanofluids improved traditional solar thermal collector efficiency. Finally, Kamel Haine and Dagnija Blumberga [17] evaluated solar energy

efficiency across continents, emphasizing the importance of technical and social factors in enhancing solar energy efficiency.

3. Materials and methods

3.1 Solar panel

The convective heat exchange in a covered solar collector, involving the glass pane, absorber surface, and external environment, is illustrated in *Fig. 1a*. Additionally, *Fig. 1b* depicts the heat fluxes and thermal losses associated with a flat-plate solar collector [18].

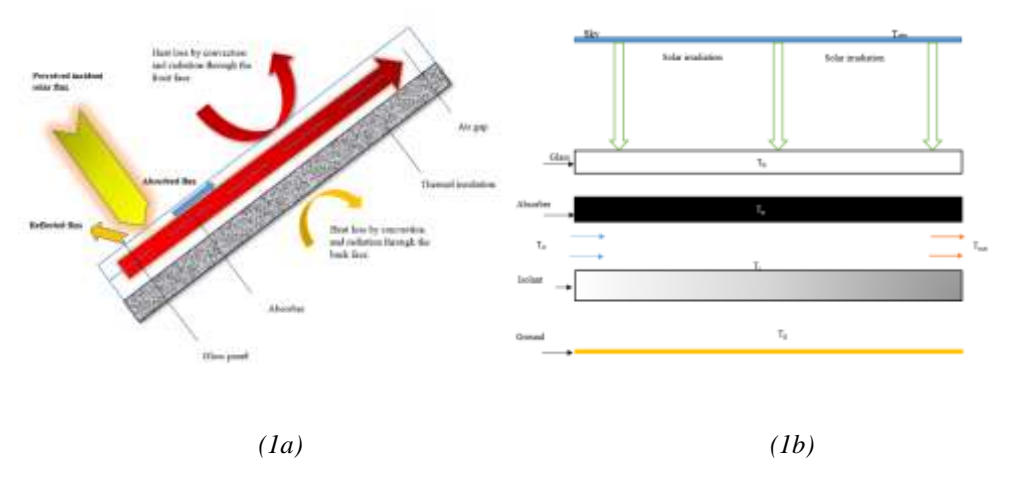


Figure 1: Different heat exchanges and most important components in a flat plate solar collector

3.2 Modeling equations of fluid flow

The system model is governed by averaged equations (1), (2) and (3) [19-21]:

$$\frac{\partial U_i}{\partial x_i} = 0 , \qquad (1)$$

$$\frac{\partial U_i}{\partial t} + U_j \cdot \frac{\partial U_i}{\partial x_j} = -\frac{1}{\rho} \cdot \frac{\partial P}{\partial x_i} + \frac{\mu}{\rho} \cdot \frac{\partial^2 U_i}{\partial x_i^2}, \qquad (2)$$

$$\frac{\partial T}{\partial t} + U_j \cdot \frac{\partial T}{\partial X_J} = \frac{\partial}{\partial X_j} \left[\left(\frac{\mu}{Pr} + \frac{\mu_t}{Pr_t} \right) \cdot \frac{\partial T}{\partial X_j} \right] + \frac{1}{\rho \cdot C_p} \cdot \varphi , \qquad (3)$$

where the unknown U_i is the velocity field (m·s⁻¹), P is the pressure (Pa), and T is the temperature (K). The physical parameters are ρ which is the density

(kg·m⁻³), μ represents the dynamic viscosity (Pa·s⁻¹), and C_p the specific heat capacity (J·kg⁻¹·K⁻¹).

The equation (1) represents the conservation of mass for an incompressible fluid, the equation (2) describes conservation of momentum, and equation (3) illustrates energy conservation.

4. Validation and results discussion

4.1 Physical model

The boundary conditions that have been defined are as follows: Inlet temperature $T_{in} = 300 \text{ K}$, inlet velocity $V_{in} = V_i$, i = 1...5, thermal flux $Q = 800 \text{ W/m}^2$, dark aluminum absorber emissivity is 0,9. Simulation parameters are gathered in the *Table 1*.

Table 1: Air properties

Air properties	ρ (Kg.m ⁻³)	μ (kg·m ⁻¹ ·s ⁻¹)	$\lambda (W \cdot m^{-1} \cdot K^{-1})$	Pr
Value	1,225	0,00001789	0,0242	0,744

On one hand the Nusselt number can be calculated by Petukhov formula [22]:

$$Nu_p = \frac{(f/8)\cdot (Re-1000)\cdot Pr}{1+12.7\cdot (f/8)^{\frac{1}{2}}\cdot (Pr^{\frac{2}{3}}-1)},$$
(4)

$$f = (0.79 \cdot \ln(Re) - 1.64)^{-2},$$
 (5)

$$Re = \frac{V \cdot D_h}{V} \,. \tag{6}$$

The equation (4) is valid when: 0.5 < Pr < 2000 and $3000 < Re < 5 \times 10^6$ [22]. Equation (5) and (6) illustrate the friction factor and the Reynolds number respectively.

From another part, the theoretical equation of Nusselt number is defined by:

$$Nu_D = \frac{h \cdot D_h}{\nu} \,. \tag{7}$$

h is known to be the heat transfer coefficient (W·m⁻²·K⁻¹), D_h is the hydraulic diameter (m), k is the thermal conductivity (W·m⁻¹·K⁻¹), V is the air velocity (m·s⁻¹) and V is the kinematic viscosity (m·s⁻²), and Pr is the Prandtl number (dimensionless). Fig. 2 and Fig. 3 describe the isometric and top views of the collector's section, while Table 2 provides the length, width and thickness of

this one. The hydraulic diameter for a rectangular duct is defined by a specific formula that is shown in equation (8) [23,24]:

$$D_h = \frac{4 \cdot l \cdot h}{2 \cdot (l + h)},\tag{8}$$

where l is the width (m), and h is the thickness (m).

Table 2: Solar collector dimensions

Dimensions	L	l	h	D_h
Value (mm)	2000	1000	50	95

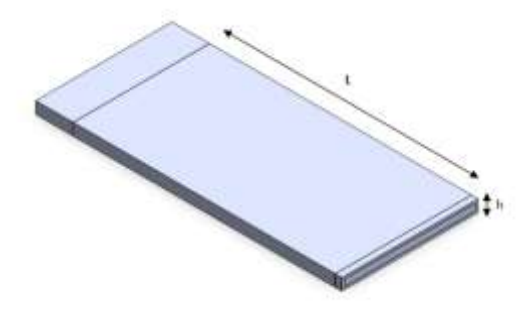


Figure 2: Top view of the solar collector

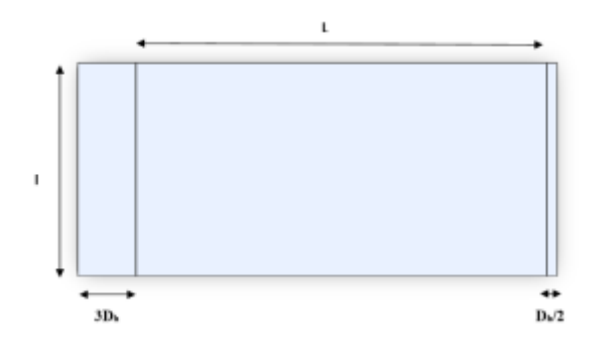


Figure 3: Isometric view of the solar collector

In order to stabilize the fluid flow and obtain a compatible pressure value in the interesting area, also to be able to calculate the performance coefficient (PEC), a calming section of up to three times the length of the hydraulic diameter (D_h) has been made at the entrance of the solar collector. Whereas a length almost equal to half of the hydraulic diameter has been established at the

outlet of the collector to make sure that the fluid interacts only with the obstacles as well as the wall of the flat plate solar collector.

4.2 Mesh

The mesh was selected based on the number of elements, skewness, and orthogonal quality to ensure accurate numerical results. *Fig. 4* illustrates the mesh structure applied to the collector's geometry.

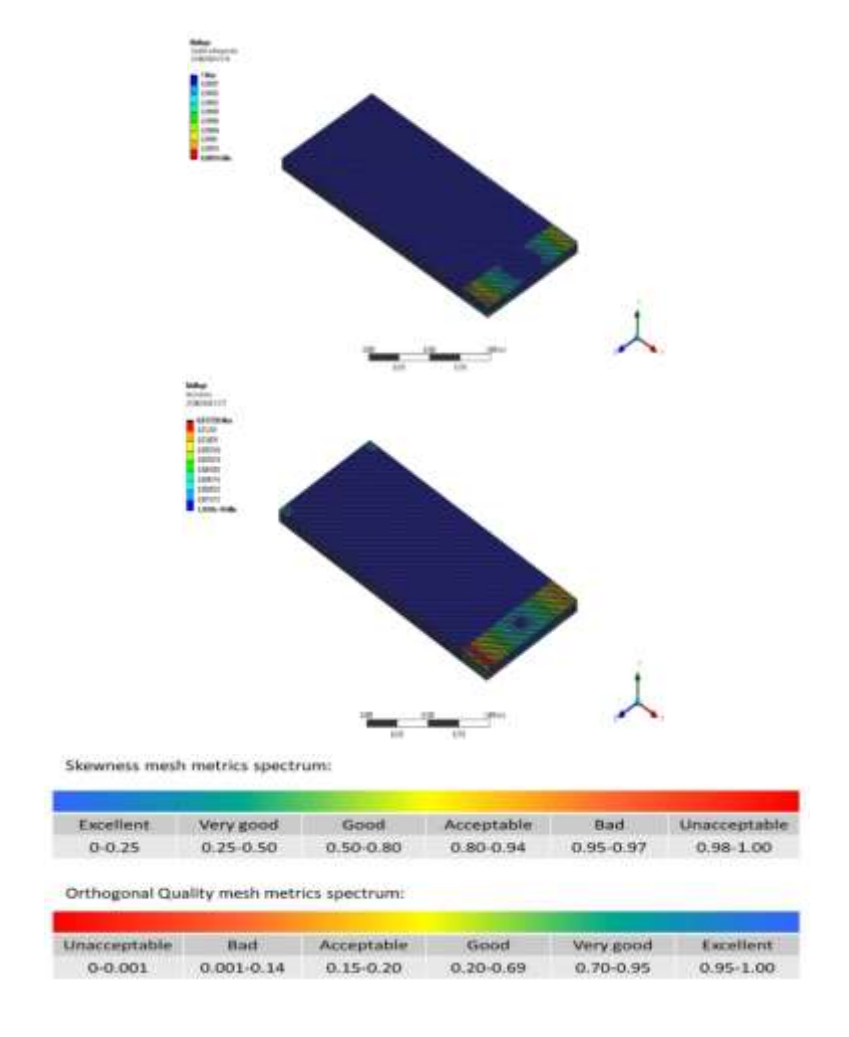


Figure 4: Orthogonal and skewness mesh quality scale

To demonstrate that the results are independent of the mesh used, various meshes were created and presented in Table 3 and Fig. 4. The parameters

monitored included the air temperature at the solar collector's outlet and the pressure in the (zx) plane, with the air velocity maintained at 0.61 m/s (Re = 4000).

Meshes	1	2	3	4
Size of the elements	0.01	0.006	0.005	0.004
Number of elements	223088	1035358	1767860	3570060
T _{out} (K)	307.2428	307.0313	306.9700	306.8016
Temperature relative error (%)		0.0688	0.01996	0.0548
Pressure (Pa)	0.1131	0.1068	0.1051	0.1006
Pressure relative		5.5702	1.5917	4.2816

Table 3: Outlet temperature and pressure variation as function of number of elements

The graph indicates that the temperature and pressure remain nearly constant across different element counts. The relative errors listed in Table 3 are negligible, leading to the selection of the smallest number of elements for the numerical study due to its quick calculation and accurate results.

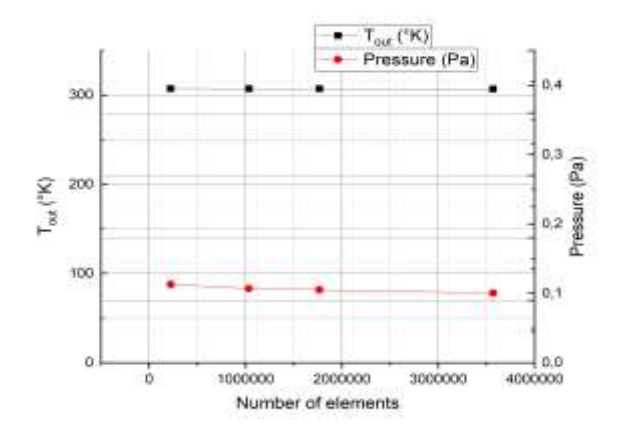


Figure 5: Outlet temperature variation as function of the size of elements used

Numerical validation involves varying air inlet velocity, calculating the Nusselt number using the Petukhov correlation (4) [25], and comparing it with simulation results for model validation (6), as shown in *Table 4* and *Figure 5*.

V _{in} (m/s)	0.92	1.23	1.54	1.85	2.15
Reynolds number	6000	8000	10000	12000	14000
h (W/m².K)	5.61	6.65	7.54	8.44	9.11
<i>Nu</i> _D (6)	22.02	26.10	29.60	33.73	35.76
<i>Nu_P</i> (4)	20.06	25.60	30.72	35.52	40.28
Relative error (%)	9.77	1.95	3.65	6.72	11.22

Table 4: Variation of Nu_D and Nu_P as function of Reynolds number

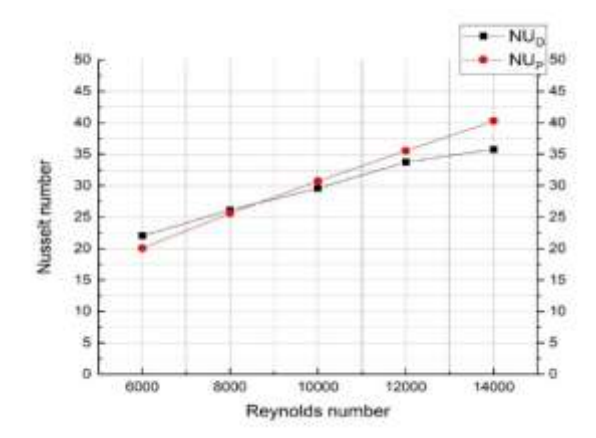


Figure 6: Variation of the Nusselt numbers as function of Reynolds number

The graph shows that the Nusselt number (Nu_D) varies proportionally with the Reynolds number (Nu_P) between 6000 and 14000. The model is validated for Reynolds numbers 7000 to 12000, with low relative errors (1.95% to 6.72%). However, it is unreliable outside this range, showing errors over 9% at Re = 6000 and over 11% at Re = 14000.

5. Personal contribution and efficiency enhancement

To enhance solar air collector efficiency, 10 rows of 12 staggered metallic offset strip fins were added, increasing the heat transfer area by 53.6%. *Fig.* 7 illustrates the dimensions of these aluminum obstacles.

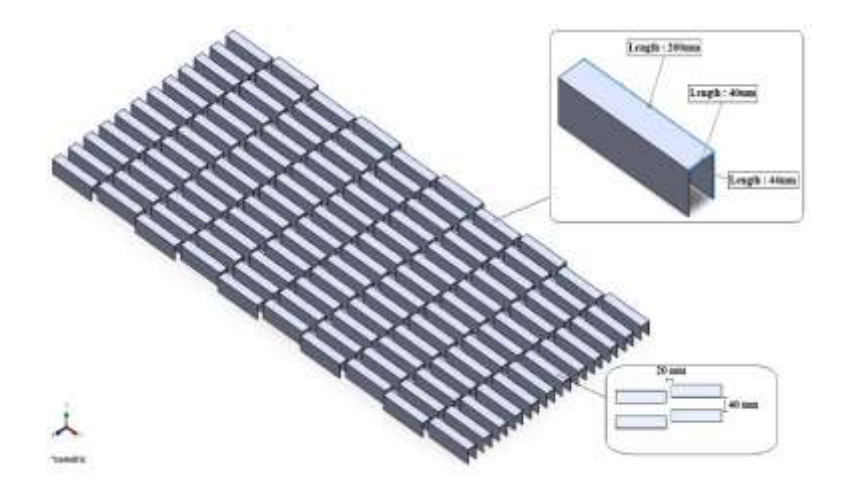


Figure 7: Isometric view of the offset strip fins

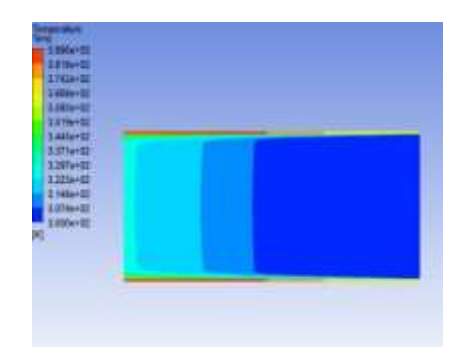


Figure 8: Temperature's contour in offset strip fins solar collector

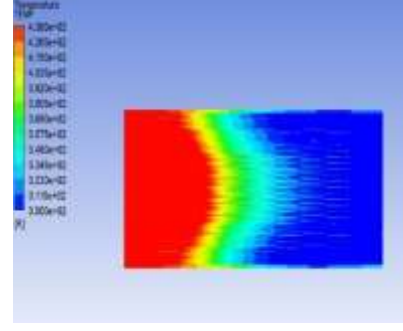


Figure 9: Temperature's contour in smooth solar collector

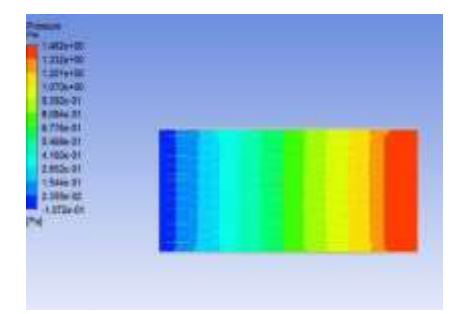


Figure 10: Pressure's contour in offset strip fins solar collector

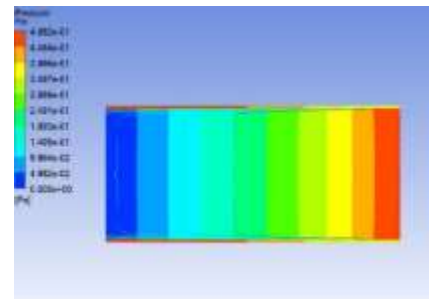


Figure 11: Pressure's contour in smooth solar collector

Fig. 8 and Fig. 9 show temperature contours for offset strip fins (OSF) and smooth solar collectors respectively, at $T_{in} = 300 \text{ K}$, $Q = 900 \text{ W/m}^2$, and $V_{in} = 0.92 \text{ m/s}$ (Re = 6000). The fluid flow goes from left to right. The maximum temperature of the smooth collector reaches 389 K, while the maximum temperature of the OSF model reaches 438 K, improving thermal efficiency by 12.6 %. Fig. 10 and Fig. 11 indicate that adding strip fins causes significant pressure drops – 0.496 Pa to 0 Pa for the smooth collector and 1.462 Pa to -0.107 Pa for the OSF – due to increased friction force. This analysis helps calculate the performance coefficient (PEC), confirming the OSF model's thermal and geometric validity.

The performance coefficient formula is represented by [26]:

$$PEC = \frac{Nu/Nu_s}{(f/f_s)^{\frac{1}{3}}},\tag{7}$$

where the index s refers to the smooth surface, Nu and f are Nusselt and friction factor, respectively [27].

$$f = \frac{\Delta P}{\frac{L}{D_h} \cdot \frac{\rho V^2}{2}}.$$
 (8)

Table 5. below gathered inlet and outlet air pressures to evaluate the *PEC* number at an inlet velocity of $0.92 \text{ m} \cdot \text{s}^{-1}$ (Re = 6000).

Collector type	Required parameters	P _{in} (Pa)	P _{out} (Pa)	Friction factor	Nusselt Number
OSF solar collector		1.93	0.85	0.035	51.88
Smooth solar collector		0.56	0.029	0.017	29.32
PEC			1.39		

Table 5: Inlet and outlet pressures in both OSF and simple solar collectors

General conclusion

This research involved a 3D numerical comparative analysis of a smooth solar air collector and one with offset strip fins (OSF). It began with an introduction to global energy demand and an overview of solar collectors, discussing their components, recent studies, and mathematical models. The analysis highlighted the advantages and disadvantages of thermal solar collectors, we then highlighted the simple model validation, and suggested a brand-new model by adding offset strip fins increasing heat transfer area by 53.6%, which systematically led to enhance the collector's efficiency. The findings concluded that integrating obstacles into a simple solar air collector

enhances its yield, reaching a performance coefficient of 1.39 for a Reynolds number of 6000, and a maximum temperature increase of approximately 12.6%, demonstrating the superiority of the improved model, suitable for various applications, both industrial and domestic.

Acknowledgments

The support from Abou Bekr Belkaid University, Tlemcen, is fully acknowledged for giving me the original versions of the software used for this study.

References

- [1] Suman S., Khan M. K., and Pathak M., "Performance enhancement of solar collectors-A review", Renewable and Sustainable Energy Reviews. vol. 49 pp. 192–210, Sept. 2015.
- [2] Chen Z., Furbo S., Perers B., Fan J., and Andersen E., "Efficiencies of flat plate solar collectors at different flow rates", Energy Procedía, vol. 30, pp. 65–72, 2012.
- [3] Chopra K., Tyagi V. V., Pandey A. K., and Sari A., "Global advancement on experimental and thermal analysis of evacuated tube collector with and without heat pipe systems and possible applications", Applied Energy, vol. 228, pp. 351–389, 2018.
- [4] Sabiha M. A., Saidur R., Mekhilef S., and Mahian O., "Progress and latest developments of evacuated tube solar collectors", Renewable and Sustainable Energy Reviews, vol. 51, pp. 1038–1054, 2015.
- [5] Tang R., Sun Z., Li Z., Yu Y., Zhong H., and Xia C., "Experimental investigation on thermal performance of flat plate collectors at night", Energy Conversion and Management, vol. 49, pp. 2642–2646, 2008.
- [6] Pandey K. M., and Chaurasiya R., "Review on analysis and development of solar flat plate collector", Renewable and Sustainable Energy Reviews, vol. 67, pp. 641–650, 2017.
- [7] Nguyen M. H., Ouldboukhitine S. E., Durif S., Saulnier V., and Bouchair A., "Passive fire protection of steel profiles using wood", Engineering Structures, vol. 275, pp. 2023, Mar. 2022, https://doi.org/10.1016/j.engstruct.2022.115274.
- [8] Abuşka M., Kayapunar A., "Experimental and numerical investigation of thermal performance in solar air heater with conical surface", Heat and Mass Transfer, vol. 57, pp. 1791–1806, Apr. 2021.
- [9] Khoukhi M., Maruyama S., "Theoretical approach of a flat plate solar collector with clear and low-iron glass covers taking into account the spectral absorption and emission within glass covers layer", Renewable Energy, vol. 30, pp. 1177–1194, 2005.
- [10] Kabeel A. E. et al., "Experimental investigation of thermal performance of flat and v-corrugated plate solar air heaters with and without PCM as thermal energy storage", Energy Conversion and Management, 2016.
- [11] Hamed M. et al., "Numerical analysis of an integrated storage solar heater", International Journal of Hydrogen Energy, 2017.
- [12] Kherrafi M. A. et al., "Performance enhancement of indirect solar dryer with offset strip fins: Experimental investigation and comparative analysis", Solar Energy, 2023.

- [13] Alsammarraie H. et al., "Numerical and experimental studies of the nanofluid characteristics that affect heat transfer enhancement: Review and comparison", Journal of Advanced Research in Fluid Mechanics and Thermal Sciences, Aug. 2023.
- [14] Nejlaoui M., Alghafis A., Sadig H., "Design optimization and experimental validation of low-cost flat plate collector under central Qassim climate", Journal of Applied and Computational Mechanics, vol. 7, no. 2, 2021.
- [15] Kalbande V. P., "Advancements in thermal energy storage systems by applications of nanofluid-based solar collectors: A review", Environmental and Climate Technologies, vol. 24, no. 1, pp. 310–340, 2020, https://doi.org/10.2478/rtuect-2020-0018.
- [16] Visconti P. et al., "Measurement and control system for thermosolar plant and performance comparison between traditional and nanofluid solar thermal collectors", International Journal on Smart Sensing and Intelligent Systems, vol. 9, no. 3, Sept. 2016.
- [17] Haine K., Blumberga D., "Evaluation of solar energy efficiency by composite index over four continents", Environmental and Climate Technologies, vol. 25, no. 1, pp. 774–785, 2021, https://doi.org/10.2478/rtuect-2021-0058.
- [18] Houhou H., "Theoretical and experimental study of solar drying of certain agro-food products", Memoir of Magister in Mechanical Engineering, University of Biskra, pp. 9–35, 39.
- [19] Taler D., "Numerical modelling and experimental testing of heat exchangers", Springer International Publishing, Cham, 21 May 2018.
- [20] Alfatih A. et al., "On the formulation of mass, momentum, and energy conservation in the KdV equation", Acta Applicandae Mathematicae, vol. 133, pp. 113–131, 2014.
- [21] Bekkouche S., "Modeling the thermal behavior of some solar devices", Doctoral thesis, Abou-bakr-Belkaid University Tlemcen, 2008.
- [22] Taler D. et al., "Simple heat transfer correlations for turbulent tube flow", E3S Web of Conferences, vol. 13, p. 0200, 2017.
- [23] Karma R., "Thermo-hydraulic performance of solar air heater with finned absorber plate forming multiple rectangular air flow passages in parallel under laminar flow conditions", Applied Thermal Engineering, vol. 221, pp. 119673, Feb. 2023.
- [24] Curd E. F. et al., "Air-handling processes", Industrial Ventilation Design Guidebook, pp. 677–806, 2001.
- [25] Sleicher C. A., Rouse M. W., "A convenient correlation for heat transfer to constant and variable property fluids in turbulent pipe flow", International Journal of Heat and Mass Transfer, vol. 18, no. 5, pp. 677–683, May 1975.
- [26] Li X. L. et al., "A performance recovery coefficient for thermal-hydraulic evaluation of recuperator in supercritical carbon dioxide Brayton cycle", Energy Conversion and Management, vol. 256, p. 115393, Mar. 2022.
- [27] Ramadhan A. I. et al., "Experimental and numerical study of heat transfer and friction factor of plain tube with hybrid nanofluids", Case Studies in Thermal Engineering, vol. 22, p. 100782, Dec. 2020.



DOI: 10.47745/auseme-2024-0004

Reconstruction of Defect Paths Using Eddy Current Testing Array 3D Imaging

Abderrahmane ABOURA¹, Abdelhak ABDOU², Tarik BOUCHALA³, Mohamed CHEBOUT⁴, Bachir ABDELHADI⁵, Marwen KHABEL⁶

Department of Electrical Engineering, Faculty of Science and Technology,
 University of Msila, e-mail: abderrahmane.aboura@univ-msila.dz (Corresponding Author)
 Electrical Engineering Department, Faculty of Science and Technology,
 University of Batna2,

e-mail: abdelhak.abdou@univ-Batna2.dz

³Department of Electrical Engineering, Faculty of Science and Technology, University of Msila, e-mail: tarek.bouchala@univ-msila.dz

⁴Department of Electrical Engineering, Faculty of Science and Technology, University of Djelfa, e-mail: m.chebout@univ-djelfa.dz

⁵Department of Electrical Engineering, Faculty of Science and Technology, University of Msila, e-mail: b.abdelhadi@univ-Batna2.dz

⁶Department of Electrical Engineering, Faculty of Science and Technology, University of Msila, e-mail: marwen.khabel@univ-msila.dz

Abstract: In a world where the reliability and lifespan of industrial equipment are critical, our research aims to go beyond the traditional limits of non-destructive testing. We seek to achieve accurate detection and comprehensive imaging of defects in their various forms by harnessing the capabilities of eddy current testing with multiplexing technology on multi-element sensors. This approach allows us to save time and ensure the quality of results. This paper presents a method for detecting and imaging different defect paths on an aluminium plate. Our methodology involves the strategic deployment of multi-sensor techniques specifically designed for eddy current testing. To address the inherent challenge of mutual magnetic induction between these sensors, we employ the alternating feed method, which is an advanced technology that ensures data integrity and significantly accelerates scanning times. By combining this technology with multi-sensor techniques, we capture signals that provide valuable insights into the presence of defects. Additionally, we produce 3D imaging that enables us to trace their paths, regardless of size. These preliminary results lay the foundation for future research aimed at accurately characterizing and visualizing the shapes and dimensions of these defects, thereby contributing to a more comprehensive understanding of defect behaviour.

Keywords: Eddy current testing, multiplexing, eddy current array, imaging defect.

1. Introduction

In the field of non-destructive evaluation (NDE) for conductive materials, eddy current testing (ECT) stands as a leading electromagnetic technique. Grounded in the principles of electromagnetic induction, ECT leverages this phenomenon to deliver its impressive capabilities [1], [2]. When a time-varying magnetic field interacts with a material under examination, it induces eddy currents within the material. Disturbances in these eddy current paths allow for the detection of cracks or other irregularities within the object being inspected. ECT offers a broad range of applications, including material thickness measurements, proximity assessments, corrosion evaluations, and the sorting of materials based on their electromagnetic properties [3].

One of the primary historical applications of ECT was the identification of discontinuities and the subsequent diagnosis of potential issues. In the domains of steam generators and aircraft wing panels for instance [4], [5],[6], stress corrosion cracks (SCC) and fatigue cracks (FC) constitute common forms of structural degradation. However, certain types of defects, such as cavitation and internal corrosion, often elude detection during routine inspections due to their concealed and imperceptible nature [7].

Detection of defects is not always limited to superficial ones, but also to internal and uncovered ones of various sizes [8],[9]. On the other hand, while using a large and representative database, machine learning techniques can evaluate and classify defects according to theirs shape, size and path [10].

In this research endeavor, our focus is centered on employing three-dimensional simulations within the Comsol Multiphysics program [11] to an aluminum plate. The simulations involved the intentional introduction of defects of varying sizes and orientations—namely, straight, zigzag, and circular defects. Subsequently, we analyze the impedance measured by each element of the eddy current sensor array (ECA).

Utilizing this ECA in multiplexed mode enabled the acquisition of 3D imaging, yielding novel and refined results. This approach enhances clarity and precision and paves the way for advanced research opportunities.

By distinctly visualizing and characterizing these defects, we contribute qualitatively to this domain, promoting increased security and safety at a physical level. This is particularly critical in averting potential catastrophic consequences, such as accidents linked to reactors.

Beyond its implications for reactor safety, this research holds significance on a humanitarian level. Emphasizing the importance of reinforcing inspection procedures, our work underscores the crucial role these advancements play in ensuring the safety of both employees and the wider public.

2. Mathematical modeling of the electromagnetic phenomenon

Eddy Current Non-Destructive Testing (ECNDT) is grounded in the principles of electromagnetic fields. The examination and mathematical representation for computing induced currents within the inspected material are based on the laws of electromagnetism, incorporating quasistatic approximations of Maxwell's equations. Various strategies exist for modelling the interaction between the probe and the tested structure, particularly in complex geometries where numerical methods are commonly employed.

The modelling and simulation of eddy current testing provide a robust foundation for an early assessment of part inspection. Numerous numerical formulations, particularly those utilizing the finite element method (FEM), have been proposed to address the challenges associated with this open boundary problem—both in its differential and integral aspects [12]. Noteworthy among the differential formulations are the H- Φ formulation introduced by Bossavit and Verite [13], the T- Ω formulation detailed by Carpenter [14], and later expanded by Brown [15] and Albanese and Rubinacci [16], and the A-V formulation proposed by Biro [17]. The primary advantage of the differential formulation lies in the sparsity of the matrices in the solving system, which is essential for reducing computational costs.

In this manuscript, we employ a three-dimensional Finite Element (FE) methodology to compute signals from eddy current probes in the presence of cracks, with the goal of characterizing material properties. The system of equations governing the dynamics of these multiphysics systems, where variables evolve over time and space, can be derived from Maxwell's equations, as outlined below:

$$\nabla \times (\mu^{-1}\nabla \times \mathbf{A}) + j\omega\sigma\mathbf{A} + \sigma\nabla V = 0 \tag{1}$$

$$\nabla \cdot \sigma(j\omega \mathbf{A} + \nabla V) = 0 \tag{2}$$

$$\nabla \times (\mu^{-1}\nabla \times \mathbf{A}) = \mathbf{I} \tag{3}$$

$$\mathbf{J} = -j\omega\sigma\mathbf{A} - \sigma\nabla V \tag{4}$$

Using Galerkin techniques, the imposition of Dirichlet boundary conditions requires fixing nodal potentials at known values [18], [19]. Neumann boundary conditions, on the other hand, are naturally incorporated into the formulation. In our specific scenario, where both the magnetic vector potential and electric scalar potential are utilized, we adopt the Galerkin weak form represented by the following expressions:

$$\int_{\Gamma} \boldsymbol{\Psi} \cdot \nabla \times (\mu^{-1} \nabla \times \boldsymbol{A}) d\Gamma + \int_{\Gamma} \sigma \boldsymbol{\Psi} \cdot (j\omega \boldsymbol{A} + \nabla V) d\Gamma = \int_{\Gamma} \boldsymbol{\Psi} \cdot \boldsymbol{J}_{s} d\Gamma \quad (5)$$

$$\int_{\Gamma} \boldsymbol{\Psi} \cdot \nabla \cdot \sigma(j\omega \, \boldsymbol{A} + \nabla V) d\Gamma = 0 \tag{6}$$

$$Z = R + j\omega L = \frac{1}{I^2} (P + j2\omega W) \tag{7}$$

 Γ : The boundary of the domain, often the surface of the material being analyzed, the integrals are computed over this boundary surface.

 Ψ : The test (or weight) function used in the weak formulation of the problem; it's used to multiply the terms in the equation to form the weak form of the problem.

The elements of impedance are defined as follows:

$$R = P/I^2$$
, and $L = 2W/I^2$ (8)

In this instance, the unspecified parameters P and W can be articulated as:

$$P = \int_{\Gamma} \mathbf{J} \cdot \mathbf{E}^* d\Gamma \text{ and } W = \int_{\Gamma} \mathbf{H} \cdot \mathbf{B}^* d\Gamma$$
 (9)

P and W are defined by the specific properties of the material (aluminum) being tested, as their values depend on how the material interacts with electric and magnetic fields. For aluminum, these interactions are influenced by its electrical conductivity and magnetic permeability.

3. Executing and Showcasing the Proposed Models

Having witnessed the impressive effectiveness of COMSOL® Multiphysics simulation software in non-destructive testing using eddy currents in previous work [8], [9], and its consistent delivery of very satisfactory results in line with laboratory-scale experimental results [20], we chose to harness its capabilities in modeling our system, using the AC/DC module.

To streamline the detection of defects and capture their images through meticulous scanning and inspection for path identification, our model employs multiple sensors activated sequentially and alternately, employing a technique known as multiplexing, as illustrated in *Fig. 1*. This method is carefully designed to alleviate potential issues of mutual induction that might arise between adjacent sensors.

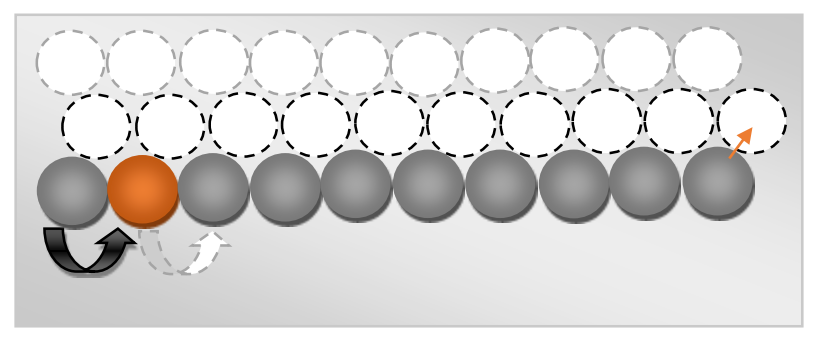


Figure 1: Illustration of the multiplexing method based on eddy current array

Fig. 1 illustrates the sequential activation of individual eddy current coils. The process begins with the orange element being activated, followed by the next element, and so on, until all the sensor elements, depicted in gray, are activated. The sensor then advances in small 1 mm increments, occupying the area shown by the transparent elements (transparent circles) in the figure. This process is repeated until the array of elements covers the entire area to be examined.

This technique, known as multiplexing, essentially combines multiple analog message signals into a unified digital signal on a shared medium. When applied to eddy current array data, multiplexing ensures that no two adjacent elements or coils are activated simultaneously, thereby minimizing the unwanted effects of mutual inductance—magnetic coupling between closely positioned coils. To precisely control each coil when sending its eddy current signal, an internal multiplexing system is employed, which effectively mitigates mutual inductance. The impedances measured by each element of the eddy current array when the probe is moved in the scaning direction, are saved as a matrix in order to be converted to a 3D images under Matlab software.

Beyond enhancing imaging capabilities, multiplexing also allows for post-scan analysis of individual data channels. This approach improves channel resolution, increases sensitivity by reducing mutual inductance, and lowers noise levels, collectively resulting in an improved signal-to-noise ratio.

Each sensor coil has 100 turns of wire with 0.03×10^{-6} m² cross-sectional area and 6×10^{7} S/m conductivity.

The scanning procedure is performed with the probe positioned parallel to the y-axis. The lift-off, which is the distance between the coil and the plate, is set to 0.5 mm.

During the scanning process, each sensor element is advanced step-by-step along the aluminum plate (Fig. 1), which has a conductivity of $3.774.10^7$ S/m.

The study examines three different defect shapes: C-shape, I-shape, and V-shape. There have been simulated different flaws: straight, inclined, and circular

paths, corresponding to C-shape, I-shape, and V-shape defects as illustrated in the table below and Fig. 2, Fig. 3 and Fig. 4.

- **I-Shaped Defect:** This defect consists of two straight segments oriented perpendicularly to each other. Each segment has a length of 20 mm, a width of 1.5 mm, and a depth of 1 mm.
- V-Shaped Defect: The V-shaped defect is composed of two equal sides, each measuring 15 mm in length, forming a symmetrical configuration. The vertex of the V-shape includes a convex arc with an outer radius of 2 mm and an inner radius of 1 mm. Both the width and depth of this defect measure 1 mm.
- **C-Shaped Defect:** The C-shaped defect is a semicircle with an outer radius of 17 mm and an inner radius of 15 mm. The width, calculated as the difference between the outer and inner radii, is 2 mm. The depth of the defect is also 2 mm

Plate parameter value [mm]	Plate width 100	Plate length 100	Plate thickness 8
Defect_I-shape parameter value[mm]	Crack width	Crack length 20	Crack depth
Defect_V-shape parameter value[mm]	Crack width 1	Crack length 30	Crack depth 1
Defect_C-shape parameter value [mm]	Crack width 2	Crack length 47.1-53.4	Crack depth 2
Sensor parameter value [mm]	Coil inner 0.5	Coil outer 2	Coil height
Physical parameter value	Relative Permeability 1	Frequency 10000 Hz	Lift-off 0.5 mm

Table 1: Parameter values

The type of element used significantly impacts the number of degrees of freedom required for the numerical resolution of the problem. In our study, we opted for tetrahedral elements in our mesh, as this choice facilitates automatic meshing of various geometries.

The selection of element size greatly influences the accuracy of the numerical solution obtained. To accurately capture the variations in the quantities of interest, it's crucial to tailor the mesh size to the specific problem at hand. Balancing mesh sizes across different domains is illustrated in (*Fig. 2*).

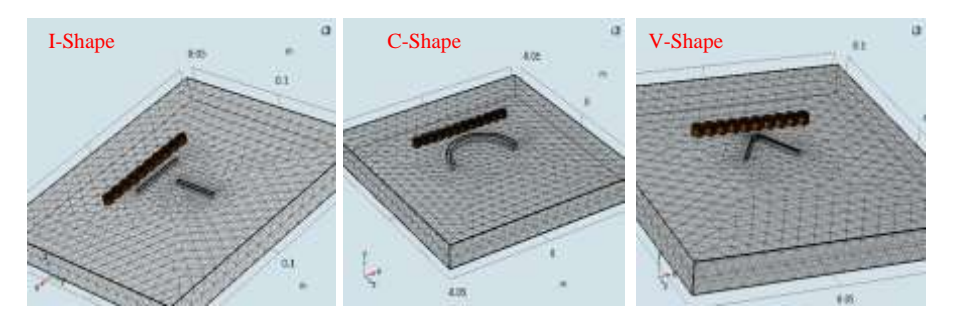


Figure 2: Geometry and meshing for different defect shapes

4. Reconstruction of defect shape from the impedance amplitude impedance

Fistly, we move the eddy cuurent array (ECA) sensor according to the appropriate axis and we record the obtained impedance and position of each element. Then, we reconstruct the carthography of the impedance on the scanned surface for different defect shapes (I, C and V shapes). In fact, the obtained results are shown in *Fig. 3*.

Upon analyzing the results obtained in all three cases, it is evident that the defect has been successfully reconstructed with its true shape and trajectory. As a result, the diagnosis of the defect has become not only faster but also more accurate and reliable. However, for a more comprehensive assessment of the defect, it is crucial to determine its unknown depth. This aspect can be addressed in future work by utilizing techniques such as neural networks or other probabilistic and deterministic methods to extract and track the defect depth through the impedance measurements in the affected area.

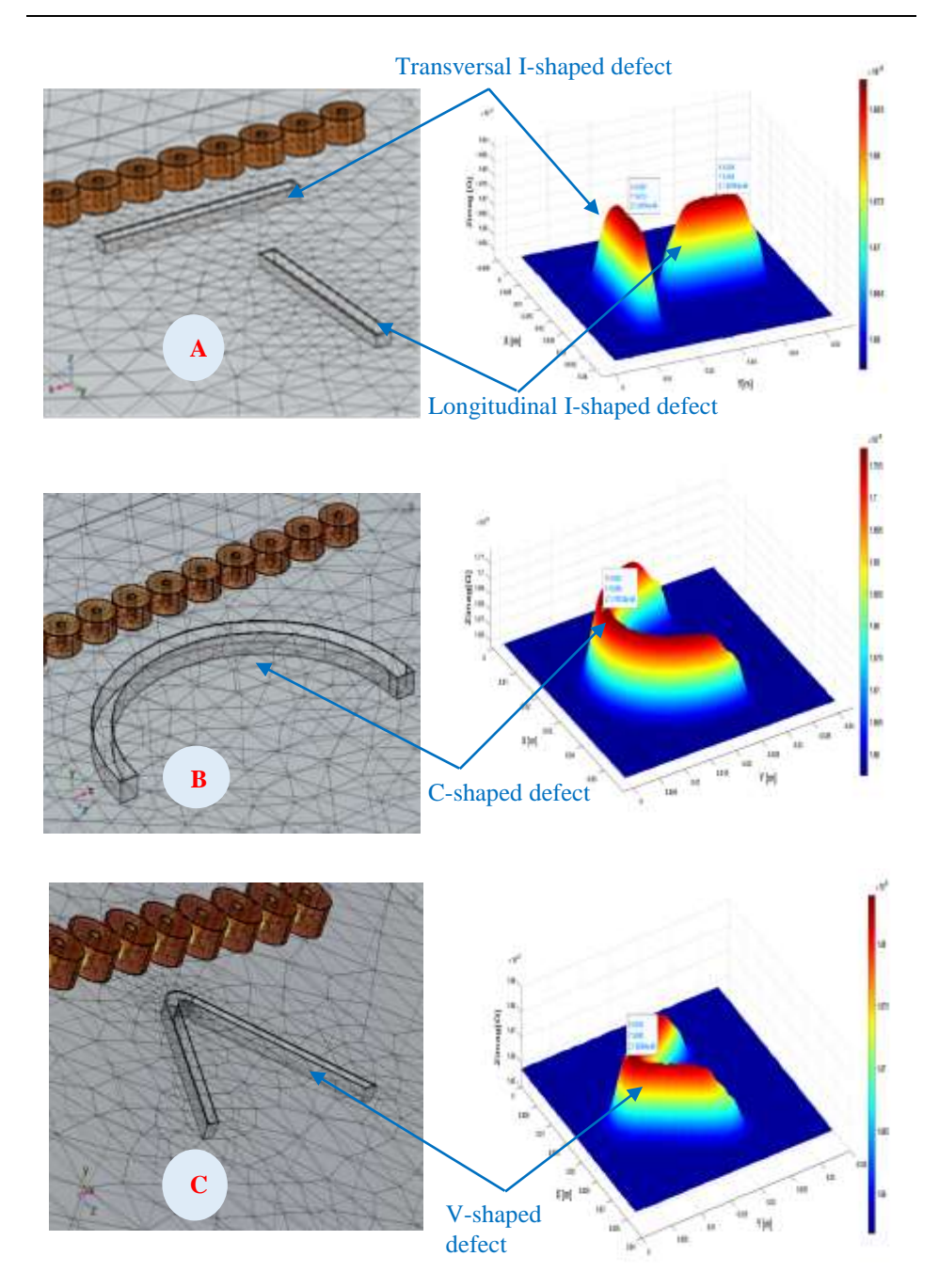


Figure 3: Defect shape reconstruction from impedance amplitude imaging for three cases. A, B and C represent I, C and V defect shapes, respectively

5. Conclusion

In this study, we introduced a model designed to detect defects of varying sizes along diverse paths and orientations, including straight, inclined, and circular trajectories. Our approach employed multiplexing technology operating at a fixed frequency in harmonic mode.

Utilizing ECA probe, impedance data were gathered at each position, leveraging the multiplexing method to mitigate mutual induction between sensing elements and simplifying the exciting electric circuit. This enabled efficient detection of surface defects and subsequent determination of their paths through 3D imaging, achieved by organizing impedance data in alignment with the sensors' scanning path.

The obtained results underscore the significance of this technique, streamlining the detection process and providing comprehensive defect images. Further research is anticipated to enhance our understanding and provide a more comprehensive depiction of defect dimensions.

For future work, this study can be expanded by incorporating additional important parameters. One key aspect to explore is defect depth estimation, as it is a critical factor in nondestructive testing applications due to the potential severity of deep defects. Additionally, since defect depth often varies in practice, investigating defects with irregular depth would provide valuable insights. The advancement of artificial intelligence (AI) could also be leveraged to identify, classify, and characterize complex defects, particularly when utilizing a comprehensive and well-structured database.

References

- [1] Ruzlaini, G., Mahmood, D., Aizat, S., & Mamat, I. F., "Defect Characterization Based on Eddy Current Technique: Technical Review," *Advances in Mechanical Engineering*, 6, 1–11, 2014. https://doi.org/10.1155/2014/182496.
- [2] Kot, P., Muradov, M., Gkantou, M., Kamaris, G. S., Hashim, K., & Yeboah, D., "Recent advancements in non-destructive testing techniques for structural health monitoring," Applied Sciences, 11(6), 2750, 2021. https://doi.org/10.3390/app11062750.
- [3] Wen, D., Fan, M., Cao, B., & Ye, B., "Adjusting LOI for Enhancement of Pulsed Eddy Current Thickness Measurement," *IEEE Transactions on Instrumentation and Measurement*, 69(2), 521–527, 2020. https://doi.org/10.1109/TIM.2019.2904331.
- [4] Stolyarova, A. A., Lunina, V. P., Zhdanova, A. G., & Shchukisa, E. G., "Revealing and Assessing the Deposit Amount on Heat-Exchanger Tubes of NPP Steam Generators According to the Operational Data of Routine Eddy Current Monitoring," *Thermal Engineering*, 67(2), 129–137, 2020. https://doi.org/10.1134/S0040601519120103.
- [5] Yang, G., Dib, G., Udpa, L., Tamburrino, A., & Udpa, S. S., "Rotating field EC-GMR sensor for crack detection at fastener site in layered structures," *IEEE Sensors Journal*, 15(1), 463–470, 2015. https://doi.org/10.1109/JSEN.2014.2341653.

- [6] Valentyn, V., "Enhanced eddy current techniques for detection of surface-breaking cracks in aircraft structures," *Transport and Aerospace Research*, 2021(1), 1–14, 2021. https://doi.org/10.2478/tar-2021-0001.
- [7] Wang, L., & Chen, Z., "Sizing of crack using multi-output support vector regression method from multi-frequency eddy current testing signals," *International Journal of Applied Electromagnetics and Mechanics*, 64(1–4), 721–728, 2020. https://doi.org/10.3233/JAE-209383.
- [8] Abderrahmane, A., Abdelhak, A., Bouchaala, B., Abdeslam, A., & Merwane, K., "Scanning by multi-sensors to detect surface and internal defects," *Proceedings of the 2022 International Conference of Advanced Technology in Electronic and Electrical Engineering (ICATEEE)*, 2022. https://doi.org/10.1109/ICATEEE57445.2022.10093732.
- [9] Aboura, A., Abdou, A., Bouchala, T., Khebal, M., Abdelhadi, B., & Guettafi, A., "Inspection of aluminum sheets using a multi-element eddy current sensor: 2D and 3D imaging of surface defects of various sizes and internal defects at various depths," *Studies in Engineering and Exact Sciences*, 5(2), e5786, 2024. https://doi.org/10.54021/seesv5n2-024.
- [10] Bangda, C., Zhijie, Z., Yuliang, W., Dong, W., & Zexue, Z., "A metal classification system based on eddy current testing and deep learning," *IEEE Sensors Journal*, 24(3), 3266–3276, 2024. https://doi.org/10.1109/JSEN.2023.3340717.
- [11] Chun, Y. L., Ren, Y. H., Megan, T., & Yi, C. W., "Pulsed eddy current sensor for cascade electrical conductivity and thickness estimation in nonferrous metal plates," *IEEE Sensors Journal*, 23(8), 8323–8334, 2023. https://doi.org/10.1109/JSEN.2023.3257316.
- [12] Ahmed, N., Moneer, A., Fahmi, S., Damhuji, R., Kharudin, A., & Al-Douri, Y., "Challenges in improving the performance of eddy current testing: Review," *Measurement and Control*, 52(1–2), 46–64, 2019. https://doi.org/10.1177/0020294018801382.
- [13] Sear, J., "A novel variant of the H-U field formulation for magnetostatic and eddy current problems," COMPEL - The International Journal for Computation and Mathematics in Electrical and Electronic Engineering, 38(5), 1545–1561, 2019. https://doi.org/10.1108/ COMPEL-12-2018-0536.
- [14] Calvano, F., "Electromagnetic Non-Destructive Evaluation and Inverse Problems," Ph.D. dissertation, Dept. Elect. Eng., Univ. of Naples Federico II, Naples, Italy, 2010. https://doi.org/10.6092/UNINA/FEDOA/8375.
- [15] Brown, M. L., "Calculation of 3-dimensional eddy currents at power frequencies," Engineering Physics, 129(1), 46–53, 1982. https://doi.org/10.1049/ip-a-1.1982.0007.
- [16] Albanese, R., "Solution of three-dimensional eddy current problems by integral and differential methods," *IEEE Transactions on Magnetics*, 24(1), 98–101, 1988. https://doi.org/10.1109/20.43865.
- [17] Biro, O., & Kurt, P., "On the Use of the Magnetic Vector Potential in the Finite Element Analysis of Three-Dimensional Eddy Currents," *IEEE Transactions on Magnetics*, 25(4), 3145–3159, 1989. https://doi.org/10.1109/20.34388.
- [18] Zuo, M. H. M., & Teixeira, F. L., "Finite element analysis of electromagnetic boundary value problems with Galerkin formulation," *IEEE Transactions on Magnetics*, 31(6), 3483–3486, 1995. https://doi.org/10.1109/20.477828.
- [19] Kovar, L. S., O'Rourke, R. W., & Morrow, M. J. S., "Galerkin finite element methods in the analysis of electromagnetic fields: Application to boundary condition modelling," *IEEE Transactions on Microwave Theory and Techniques*, 50(3), 739–748, 2002. https://doi.org/10.1109/22.987701.
- [20] Abdelhak, A., Abderrahmane, A., Tarik, B., Bachir, A., & Amor, G., "Numerical simulation and experimental studies of rotational eddy current detection of cracks around rivet holes," *Studies in Engineering and Exact Sciences*, 5(2), e5964, 2024. https://doi.org/10.54021/seesv5n2-047.



DOI: 10.47745/auseme-2024-0005

Comparative Study of Dielectric Properties and Other Physical Properties of Superparamagnetic Iron Oxide Nanoparticles and Polyethylene Nanocomposites

Taraneh JAVANBAKHT¹, Sophie LAURENT^{2,3}, Dimitri STANICKI², Eric DAVID¹

Department of Mechanical Engineering, École de Technologie Supérieure, Montreal, Quebec, Canada H3C 1K3, Canada, e-mail: t.javanbakht@gmail.com
 Laboratory of NMR and Molecular Imaging, University of Mons, Avenue Maistriau 19, B-7000 Mons, Belgium
 Center for Microscopy and Molecular Imaging, 6041 Gosselies, Belgium

Manuscript received, July 04, 2024; revised October 17, 2024

Abstract: The present paper proposes a new investigation of the dielectric properties of superparamagnetic iron oxide nanoparticles (SPIONs)/PE nanocomposites in comparison with the neat polymer at different temperatures. The SPIONs used were without or with positively or negatively surface charge. Different frequency-domain dielectric responses were observed for the different samples. The usual decrease of the values of the real part of the permittivity of all the three SPIONs nanocomposites in the range was observed with the increase of temperature. Moreover, the values of the real part of the permittivity of PE-bare SPIONs increased slightly at lower frequencies, whereas those of PE-positively charged SPIONs and PE-negatively charged SPIONs were constant at higher frequencies and showed an increase at medium frequencies and a plateau at lower frequencies. The imaginary part of their permittivity also showed dielectric responses for the samples.

Keywords: SPIONs, surface charge, physical properties, dielectric properties, functionalization.

1. Introduction

The dielectric properties of non-conductive materials are important physical properties describing their interaction with an external electrical field at frequencies below microwave frequencies [1], [2]. These properties determine the response of materials subjected to an AC electrical field and are relevant in

number of applications such Joule heating, drying or electrostatic energy storage [3], [4].

Polymer nanocomposites are important materials with diverse applications in science and engineering such as for energy storage, sensors and actuators [5], [6], [7]. Efficient, reliable, and affordable production technologies are required for mass production of these materials with stable characteristics [8]. The insertion of metallic or ceramic materials into a matrix, which is usually a polymer, can provide desirable properties for electrical applications [9]. Fabrics [10], buildings [11], and construction materials [11], as well as metallic [12] or polymer [13] matrices can be used for the manufacture of nanomaterials [14]. The dielectric properties of biological materials can be investigated in the interaction of tissues with electromagnetic energy [15], [16]. Physiological changes of the water content, protein content, types and cell structure of biological materials have impact on their dielectric properties. In fact, the dielectric properties of these materials are not identical [17], [18].

During several years, superparamagnetic iron oxide nanoparticles (SPIONs) have found diverse applications in engineering. These nanoparticles are promising because of their magnetic properties, high biocompatibility, and easy functionalization of their surfaces with target molecules [19]. They have diverse physicochemical and mechanical properties that make them usable alone or as nanocomposites, which are often prepared in mixtures with polymers [20], [21], [21]. SPIONs can be classified into three categories: first category with micrometer-sized (300–3.5 μ m), second category with standard-sized (10–150 nm), and third category that is ultra-small (<10 nm). Their magnetic properties allow their application for direct delivery of matter into the pathogen zone that does not influence the whole organism [22], [23]. The functionalization of these nanoparticles with organic and inorganic materials is required for their diverse applications in science and engineering. The core part of nanoparticles can be coated with an organic or inorganic layer [20], [21] or/and encapsulated in a polymer-based matrix [21].

The objective of the current work was to investigate the dielectric properties and other physical properties of SPIONs with low density polyethylene (LDPE) nanocomposites. Our hypothesis was that the dielectric properties of SPIONs depended on their surface charge. This study was required for performing a further step in an upcoming comparative investigation on the change of the dielectric properties of SPIONs with other polymeric matrices.

To the authors' knowledge, this comparative investigation on these nanocomposites having no surface charge, positive or negative surface charge on their nanoparticles has not been carried out, yet. The results of this study can be applied for the design and development of new electrical insulation and mechanical support systems.

2. Materials and Methods

A. Samples preparation

SPIONs were premixed with the PE powder in a 2:100 weight ratio. PE/SPIONs composites were then prepared by melt compounding, the premixed LDPE/SPIONs being extruded in a twin-screw extruder and pelletized. Then, the samples were molded using with heating press at 160 °C. Disk-shaped molded samples were used for broadband dielectric spectroscopy (BDS) characterization.

B. Transmission electron microscopy (TEM)

A Microscope Fei Tecnai 10 operating at an accelerating voltage of 100 kV (Oregon, OR, USA) was used for TEM imaging. The samples were prepared on carbon-coated copper-grids (Formvar/carbon 300 mesh; Cu TED PELLA) by placing a 4 μ L drop of 0.5 mM suspension (IONPs in water), allowing the liquid to dry at room temperature. The iTEM (Münster, Germany) was used for the statistical treatment of the TEM images. The particles' diameters were measured for the calculation of the mean diameter, the standard deviation and the polydispersity index (PDI). Between 500 and 700 nanoparticles were counted.

C. Thermogravimetric analysis (TGA)

A Pyris Diamond thermogravimetric analyzer (TG/DTA), PerkinElmer technology, Shelton, CT, USA) was used to determine the thermal degradation of the materials and quantify the weight percentage of the inorganic content. Samples were heated from 50°C to 600°C at a rate of 10 °C/min under a nitrogen flow of 100 ml/min.

D. Scanning electron microscopy (SEM)

Cross-sections of the samples were used for SEM imaging and ton dispersive spectroscopy (EDS) measurements, that were carried out with a HITACHI SU8230 SEM. Coating of samples with Pt was performed before SEM imaging to avoid charging effects.

E. Broadband Dielectric Spectroscopy (BDS) measurements

A dielectric frequency-domain spectrometer was used for the measurement of the dielectric response of the samples [20]. Isothermal measurements were conducted in a frequency range from 0.1 to 10⁶ Hz at temperature varying from 20 °C to 100 °C. The dielectric properties of the nanocomposites of PE-SPIONs and PE were measured in triplicate. The energy of activation of the interfacial relaxation mechanism was obtained using the linear least squares analysis from the plots of [ln(frequency)] versus [1000/T]. The frequency values for which the

imaginary permittivity values was maximum were considered for the plots [24], [25].

3. Results and Discussion

Fig. 1 shows the TEM images of SPIONs. The average sizes of bare SPIONs, positively charged SPIONs, and negatively charged SPIONs were 7.84 ± 2.61 nm, 8.38 ± 2.33 nm, and 8.53 ± 2.25 nm, respectively.

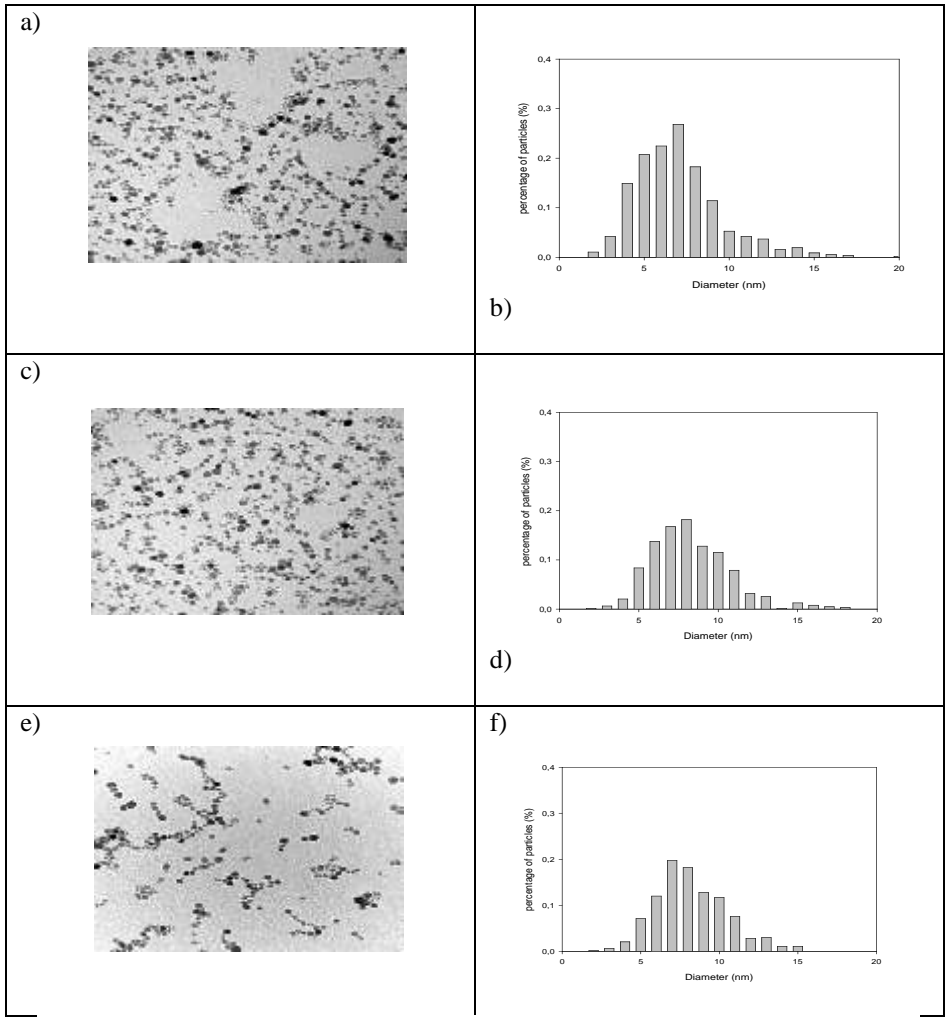


Figure 1: TEM images of a, b) bare SPIONs, c, d) positively charged SPIONs, and e, f) negatively charged SPIONs

Fig. 2 shows the TGA curves of samples. The curves of PE-bare SPIONs, PE-positively charged SPIONs, PE-negatively charged SPIONs, and PE are represented with red line, green line, blue line, and black line, respectively.

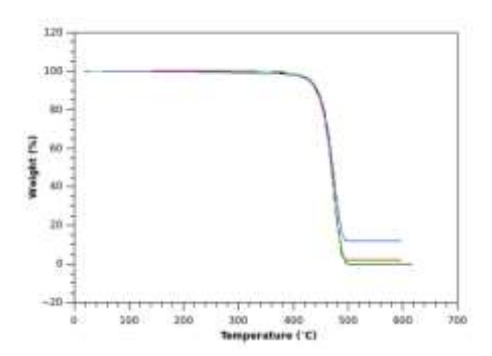


Figure 2: TGA curves of PE-bare SPIONs, PE-positively charged SPIONs, PE-negatively charged SPIONs, and PE in red, green, blue, and black line, respectively. The weight loss percentage indicated in the y-axis was from 100% to 0% for all samples

As shown in Fig. 2, all samples burnt in the 400-500°C range. Comparing the weight loss curves, all samples decomposed in a single step. The peak temperature of decomposition for PE-bare SPIONs, PE-positively charged SPIONs, PE-negatively charged SPIONs, and PE were at 470 °C, 470 °C, 470 °C, and 472.6 °C, respectively. Taking into account the heating rate, which was $10 \, ^{\circ}$ C/min, the presence of SPIONs in the nanocomposites of PE-SPIONs did not have a significant influence on the temperature of decomposition of these nanocomposites in comparison with that of the polymer.

Table 1 shows the residual weight percentage of samples. As expected, the residual weight percentages of the nanocomposites of SPIONs-PE were more than that of PE alone. Moreover, the PE-bare SPIONs and the PE-negatively charged SPIONs had almost the same residual weight percentages, that were more than that of the PE-positively charged SPIONs.

Fig. 3 and Fig. 4 show the SEM images and EDS spectra of PE-bare SPIONs, PE-positively charged SPIONs, PE-negatively charged SPIONs and PE. The pics of Pt in the EDS spectra correspond to the coating of samples. The images of samples, C, O, Si and Fe are in grey, red, green, blue, and orange, respectively. Some traces of Na were also found on the surface of the last sample.

The amount of iron was more on the surface of PE-bare SPIONs in comparison with other nanocomposites. Its amount was the least for the PE-negatively charged SPIONs. The amount of O was the most for this last nanocomposite and the least for PE-positively charged SPIONs.

	•	
Sample	Residual weight (%)	
PE-bare SPIONs	2.109	
PE-positively charged SPIONs	1.190	
PE-negatively charged SPIONs	2.000	
PE	0.027	

Table 1: The residual weight percentage of samples

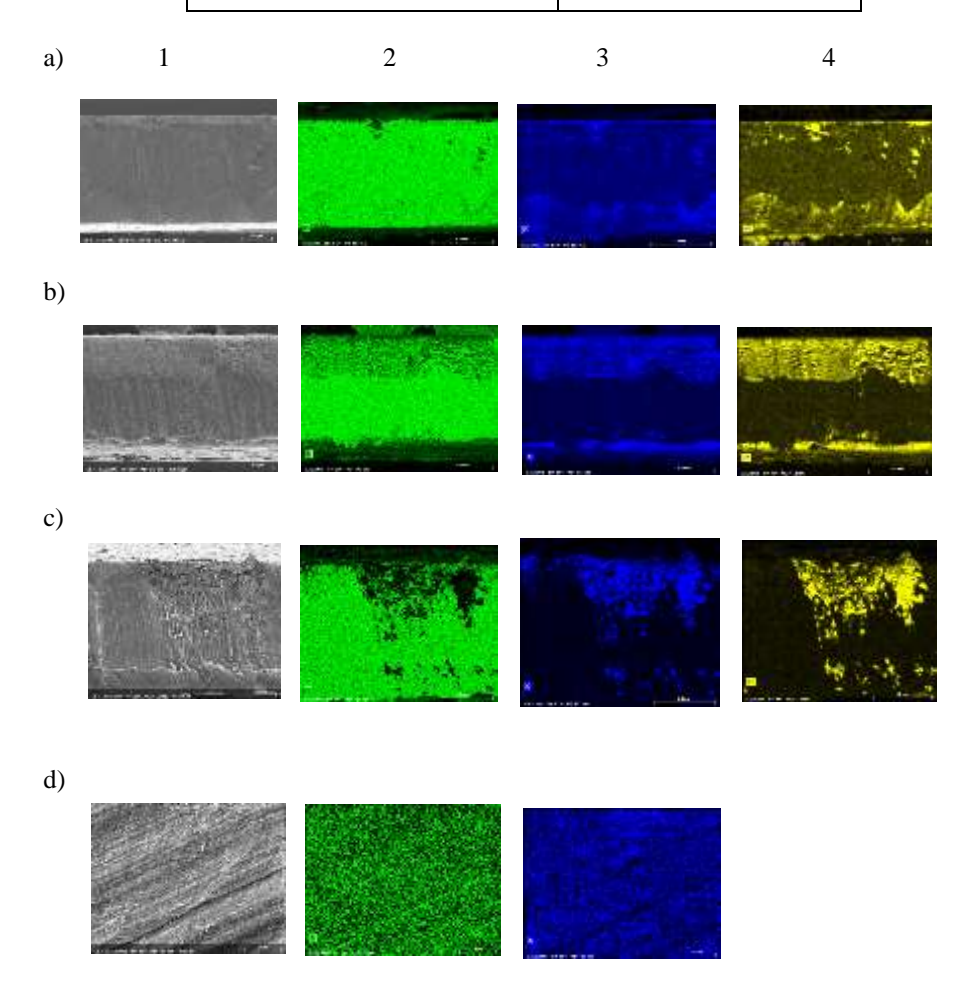


Figure 3: The SEM images of (a) PE-bare SPIONs, (b) PE-positively charged SPIONs, (c) PE-negatively charged SPIONs, and (d) PE. Carbon, oxygen and iron on the surface of samples are observed in green, blue and yellow in the images of the columns 2, 3 and 4, respectively

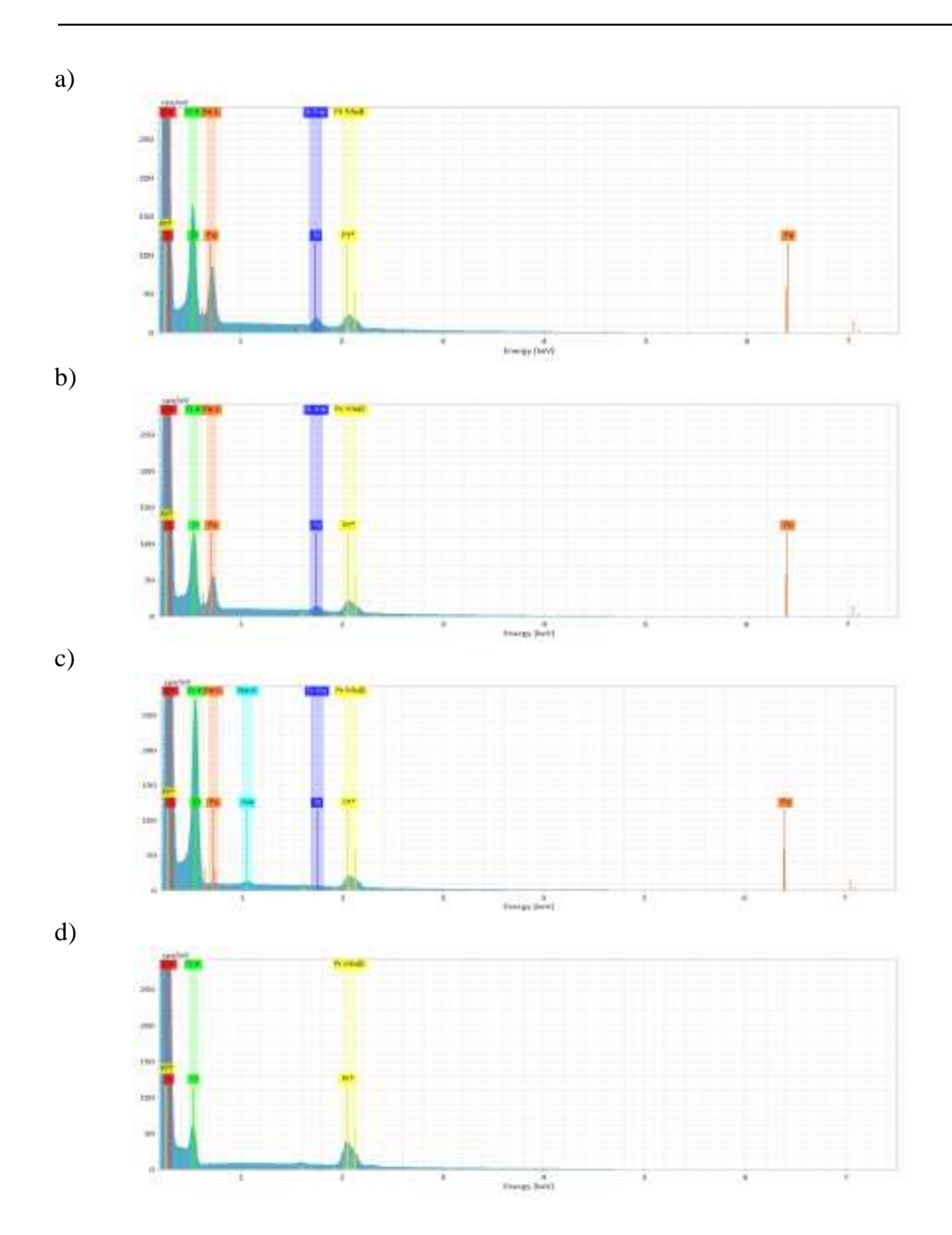


Figure 4: The EDS spectra of (a) PE-bare SPIONs, (b) PE-positively charged SPIONs, (c) PE-negatively charged SPIONs, and (d) PE

Fig. 5 shows the real and imaginary parts of the relative permittivity of PEbare SPIONs, PE-positively charged SPIONs, PE-negatively charged SPIONs and PE at different temperatures.

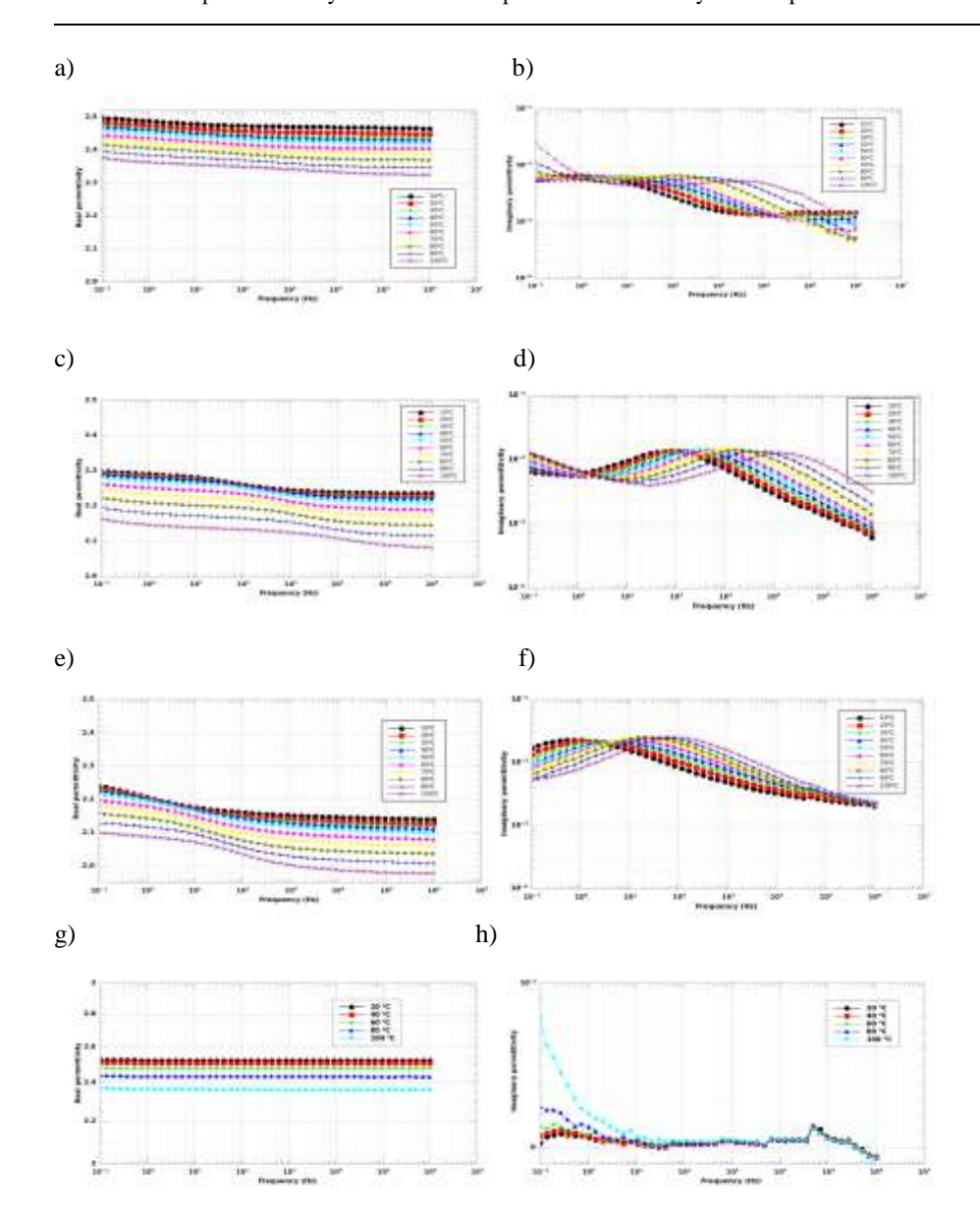


Figure 5: The real part and imaginary part of the relative permittivity of the nanocomposites of (a) and (b) PE-bare SPIONs, (c) and (d) PE-positively charged SPIONs, (e) and (f) PE-negatively charged SPIONs and (g) and (h) PE at different temperatures

As shown in *Fig. 5*, the values of the real part of the permittivity of all the three nanocomposites of SPIONs-PE and of neat PE were found to decrease with the increase of temperature, as expected and in agreement with the Clausius-Mossotti equation. The dielectric response of neat PE showed its usual low-loss dielectric response presenting a rather frequency-independent behavior (known as flat loss behavior [26]) excepted at the highest temperature where charge fluctuations lead to an increase of the dielectric losses towards low frequencies. For all SPIONs composites, containing either bare, positively and negatively charged SPION, a relaxation mechanism, in the form of a temperature dependant loss peak, was observed due to the interfacial polarization between the nonconductive matrix and the more conductive particles. The frequency position of this peak is essentially inversely proportional to the effective conductivity of the filler. Indeed, solving the Laplace equation for a dilute dispersion of ellipsoids (the so-called Maxwell approximation) leads to the following expression for the effective complex permittivity of the composition [27]:

$$\sum_{j=1}^{2} q_{j} \cdot \left(\hat{\mathcal{E}}_{c} - \hat{\mathcal{E}}_{j} \right) \cdot \left[1 + A \cdot \frac{\hat{\mathcal{E}}_{j} - \hat{\mathcal{E}}_{1}}{\hat{\mathcal{E}}_{1}} \right]^{-1} = 0 , \qquad (1)$$

where *j* denotes the phase, *q* the volume fraction of each phase, the relative complex permittivity and *A* is a geometrical factor known as the depolarization factor (A = 1/3 for a sphere). Assuming the both filler and matrix complex permittivity can be simply expressed by a real permittivity and a conductivity $\varepsilon = \varepsilon - j \frac{\sigma}{\omega \varepsilon_c}$ then the above equation reduces to a Debye-type process:

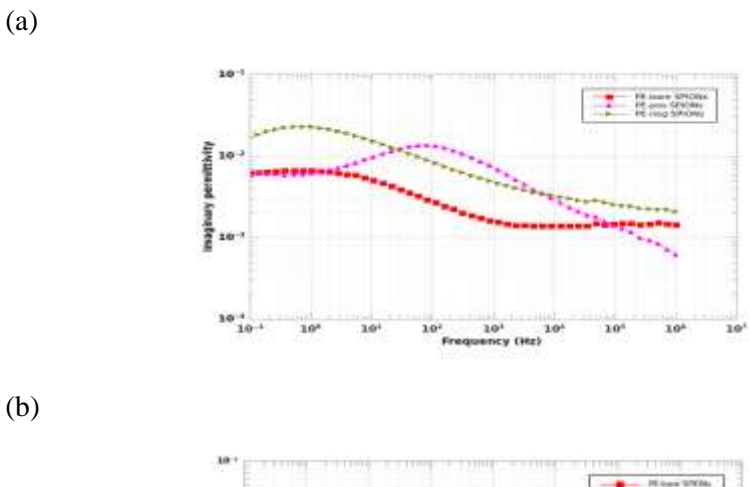
$$\varepsilon_c = \varepsilon_{\infty} + \frac{\Delta \varepsilon}{1 + j\omega \tau}.$$
 (2)

With the retardation (or relaxation) time inversely proportional to the filler's conductivity:

$$T \propto \frac{\varepsilon_0}{\sigma_f}.$$
 (3)

The above approach can be extended to consider the presence of an interfacial layer between the filler particles and the matrix material [28]. In that case, the retardation time will be rather related to the conductivity of the interfacial layer [28]. A common case where this situation occurs is when a water layer is present on the surface of a hydrophilic filler [29]. In all cases, the retardation time of the loss peak was found to decrease with the increase of temperature, indicating an increase of either filler of interfacial layer conductivity.

Fig. 6 shows the imaginary part of the relative permittivity of the nanocomposites of PE-SPIONs at 10 °C and 100 °C.



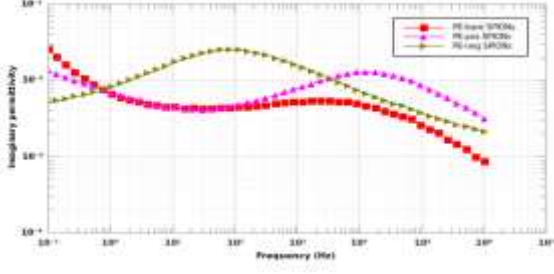


Figure 6: The imaginary part of the relative permittivity of the nanocomposites of PE-SPIONs at 10 °C and 100 °C

The local maximum shift was observed for the imaginary part of the relative permittivity of the nanocomposites of PE-SPIONs for each temperature in *Fig.* 6.

Fig. 7 shows the relaxation rate of the interfacial processes as function of the inverse temperature for the three composites. In all cases the activation plot is in good agreement with an Arrhenius-type thermal activation.

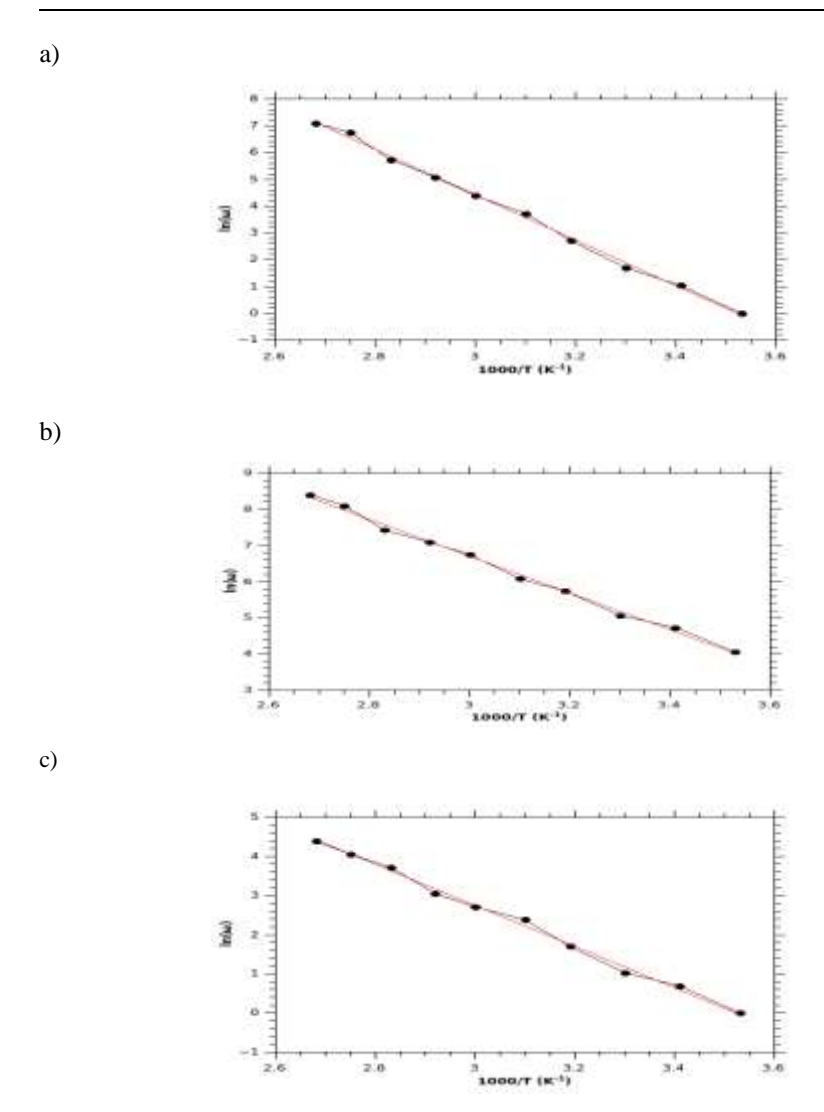


Figure 7: The Arrhenius plots of a) PE-bare SPIONs, b) PE-positively charged SPIONs and c) PE-negatively charged SPIONs.

The slopes were used to determine the energy of activation for the relaxation process of samples. Activation energies determined from the slope of the plots were 69.6 kJ/mol, 45.5 kJ/mol and 40.8 kJ/mol for PE-bare SPIONs, PE-positively charged SPIONs and PE-negatively charged SPIONs, respectively. This showed that the values of the energy of activation of the relaxation process for the nanocomposites of SPIONs were not identical, with the activation energy of PE-bare SPIONs significantly higher than for the two other composites.

The decrease of relative permittivity in nanocomposites has been attributed to the interaction between the polymer matrix and the nanoparticles [29].

The low-density region and the less stoichiometric region form the interaction zone, which has an increased free volume and some traps. The study with a multicore model consisting of a bonded region, a transition region and a normal region showed that the nanoparticles can be considered as isolated particles as they provide slight filler loading [30], [31], 32]. When the movement of orientable dipoles are restricted along the direction of the electric field, the relative permittivity is decreased. When more concentrations of nanoparticles load the matrix, the distance between neighboring nanoparticles decreases that can result in the overlap of the transition regions of neighboring nanoparticles. This phenomenon has impact on the dielectric properties of nanocomposites. The relative permittivity of nanoparticles is higher than that of the polymer, which results in the higher relative permittivity of nanocomposite [29], [33], [34]. The obtained data will be computed with modeling in a further work.

Several other materials alone or with polymers have been investigated for their physicochemical [35], [36], biological [37], [38], [39] and mechanical properties [40], [41], [42]. The analysis of their dielectric properties would be required for a better development of their preparation. The consideration of the physical properties of these materials as those of PE-SPIONs without and with surface charge as described above leads to promise for their applications.

4. Conclusion

This study was focused on the analysis of the dielectric and other physical properties of the PE-SPIONs nanocomposites. The dielectric properties of the composite samples were dominated by the presence of an interfacial polarization process exhibiting an Arrhenius-type thermal activation. Significant differences were found between the bare, positively, and negatively charged SPIONs due to the different surface chemistry. The current work also revealed that the values of the real part of the permittivity of PE-bare SPIONs increased slightly at lower frequencies, whereas those of PE-positively charged SPIONs and PE-negatively charged SPIONs were constant at higher frequencies and showed an increase at medium frequencies and a plateau at lower frequencies. More investigation will lead to the development of these materials for their applications in science and engineering.

Acknowledgements

We acknowledge the financial support from NSERC (Alliance International grant) for the support of this work.

References

- [1] Nelson, S.O. "Dielectric properties of materials and measurement techniques", *Drying Technology*, vol. 8, pp. 1123–1142, 1990.
- [2] Nelson, S.O., Trabelsi, S. "Factors influencing the dielectric properties of agricultural and food products", *Journal of Microwave Power and Electromagnetic Energy*, vol. 46, pp. 93–107, 2012.
- [3] Musa, N. et al. "Frequency and temperature dependence of ethanol using the cole-cole relaxation model", *American Journal of Condensed Matter Physics*, vol. 10, pp. 44–49, 2020.
- [4] Kannan, S. et al. "The effect of radiofrequency heating on the dielectric and physical properties of eggs", *Progress In Electromagnetics Research B*, vol. 51, pp. 201–220, 2013.
- [5] Shivashankar, H. et al. "Investigation on dielectric properties of PDMS based nanocomposites", *Physica B: Condensed Matter*, vol. 602, 412357, 2021.
- [6] Sadasivuni, K.K. et al. "A review on porous polymer composite materials for multifunctional electronic applications", *Polymer-Plastics Technology and Materials*, vol. 58, pp. 1253–1294, 2019.
- [7] Elhi, F. et al. "Cellulose-multiwall carbon nanotube fiber actuator behavior in aqueous and organic electrolyte", *Materials*, vol. 13, 3213, 2020.
- [8] Getmanov, A.G., Thang, T.Q. "Dielectric properties of nanocomposites based on epoxy resins and titanium dioxide", *International Journal of Circuits, Systems and Signal Processing*, vol. 15, pp. 1400–1406, 2021.
- [9] Ciobanu, R.C. et al. "Simulation of dielectric properties of nanocomposites with non-uniform filler distribution", *Polymers*, vol. 15, 1636, 2023.
- [10] Wang, Y., Gordon, S., Baum, T., Xu, Z. "Multifunctional stretchable conductive woven fabric containing metal wire with durable structural stability and electromagnetic shielding in the x-band". *Polymers*, vol. 12, 399, 2020.
- [11] Akyıldız, A., Durmaz, O. "Investigating electromagnetic shielding properties of building materials doped with carbon nanomaterials", *Buildings*, vol. 12, 361, 2022.
- [12] Carneiro, Í., Simões, S. "Effect of morphology and structure of MWCNTs on metal matrix nanocomposites", *Materials*, vol. 13, 5557, 2020.
- [13] Moskalyuk, O.A., Belashov, A.V., Beltukov, Y.M., Ivan'kova, E.M., Popova, E.N., Semenova, I.V., Yelokhovsky, V.Y., Yudin, V.E. "Polystyrene-based nanocomposites with different fillers: Fabrication and mechanical properties", *Polymers*, vol. 12, 2457, 2020.
- [14] Ali, A., Mitra, A., Aïssa, B. "Metamaterials and metasurfaces: A review from the perspectives of materials, mechanisms and advanced metadevices", *Nanomaterials*, vol. 12, 1027, 2022.
- [15] Pethig, R. "Dielectric properties of biological materials: Biophysical and medical applications", *IEEE Transactions on Electrical Insulation*, vol. 1-19, pp. 453–474, 1984.
- [16] Wang, X., et al. "High-resolution probe design for measuring the dielectric properties of human tissues", *Biomedical Engineering*, vol. 20, 86, 2021.
- [17] Wang, Z. "Research and application of microwave method for measuring electrical parameters of biological tissue (in Chinese)", Nanjing: Nanjing University of Science and Technology, 2009.
- [18] Yilmaz, T, Kılıç, MA, Erdoğan, M, et al. "Machine learning aided diagnosis of hepatic malignancies through in vivo dielectric measurements with microwaves", *Phys. Med. Biol.*, vol. 61, pp. 5089–102, 2016.
- [19] Xie, W., Guo, Z., Gao, F., Gao, Q., Wang, D., Liaw, B., Cai, Q., Sun, X., Wang, X., Zhao, L. "Síntesis controlada por forma, tamaño y estructura y biocompatibilidad de nanopartículas de óxido de hierro para teranóstica magnética", *Theranostics*, vol. 8, pp. 3284–3307, 2018.

- [20] Javanbakht, T., Laurent, S., Stanicki, D., David, E. "Related physicochemical, rheological, and dielectric properties of nanocomposites of superparamagnetic iron oxide nanoparticles with polyethyleneglycol", *Journal of Applied Polymer Science*, vol. 136, pp. 48280–48290, 2019.
- [21] Javanbakht, T., Laurent, S., Stanicki, D., Frenette, M. "Correlation between physicochemical properties of superparamagnetic iron oxide nanoparticles and their reactivity with hydrogen peroxide", *Canadian Journal of Chemistry*, vol. 98, pp. 601–608, 2020.
- [22] Seabra, A., Pelegrino, M., Haddad, P. "Antimicrobial applications of superparamagnetic iron oxide nanoparticles: Perspectives and challenges", In Nanostructures for Antimicrobial Therapy, 1st ed.; Ficai, A., Grumezescu., A.M., Eds., Elsevier Inc.: Cham, Switzerland, pp. 531–550, 2017.
- [23] Bustamante-Torres, M. et al. "Polymeric composite of magnetite iron oxide nanoparticles and their application in biomedicine: A review", *Polymers*, vol. 14, 752, 2022.
- [24] Fanari, F. et al. "Broadband dielectric spectroscopy (BDS) investigation of molecular relaxations in durum wheat dough at low temperatures and their relationship with rheological properties", *Food Science and Technology*, vol. 16, 113345, 2022.
- [25] Boned, C., Lagourette, B., Clausse, M. "Dielectric behaviour of ice microcrystals: A study versus temperature", *Journal of Glaciology*, vol. 22, pp. 145–154, 1979.
- [26] Jonscher, A.K. "Universal Relaxation Law", Chelsea Dielectric Press, London, 1996.
- [27] Torquato, S. "Random Heterogeneous Materials", Springer, 2002.
- [28] Steeman, P.A.H., Maurer, F.H.J. "An interlayer model for the complex dielectric constant of composites", *Colloid and Polymer Science*, vol. 268, pp. 315–325, 1990.
- [29] Couderc, H., David, E., Fréchette, M. "Study of Water Diffusion in PE-SiO2 Nanocomposites by Dielectric Spectroscopy", *Trans. on Electrical and Electronic Materials*, vol. 15, pp. 291– 296, 2014
- [30] Tanaka, T., Montanari, G.C., Malhaupt, R. "Process, understanding and challenges in the field of nanodielectrics", *IEEE Trans. Dielectr. Electr. Insul.*, vol. 11, pp. 763–784, 2004.
- [31] Tanaka, T., Kozako, M., Fuse, N., Ohki, Y. "Proposal of a multi-core model for polymer nanocomposite dielectrics", *IEEE Trans. Dielectr. Electr. Insul.*, vol. 12, pp. 669–681, 2005.
- [32] Zhao, W., Fan, Y., Chen, H. "Dielectric properties and corona resistance of Si-B/epoxy nanocomposites", *J. Mater. Sci. Mater. Electron.*, vol. 30, pp. 16298–16307, 2019.
- [33] Hardoň, S. et al. "Influence of nanoparticles on the dielectric response of a single component resin based on polyetherimide", *Polymers*, vol. 14, 2202, 2022.
- [34] Zhou, C. et al. "Improving the dielectric properties of polymers by incorporating nanoparticles", 10th International Conference on Electrical Insulation (INSUCON), Birmingham, 2006.
- [35] Djavanbakht, T., Carrier, V., André, J. M., Barchewitz, R., Troussel, P. "Effets d'un chauffage thermique sur les performances de miroirs multicouches Mo/Si, Mo/C et Ni/C pour le rayonnement X mou" Journal de Physique IV, France, vol. 10, pp. 281–287, 2000.
- [36] Javanbakht, T., Hadian, H., Wilkinson, K. J. "Comparative study of physicochemical properties and antibiofilm activity of graphene oxide nanoribbons", *Journal of Engineering Sciences*, vol. 7(1), pp. C1–C8, 2020.
- [37] Wetteland, C.L., Liu, H. "Optical and biological properties of polymer-based nanocomposites with improved dispersion of ceramic nanoparticles", *Journal of Biomedical Materials Research*, vol. 106, pp. 2692–2707, 2018.
- [38] Javanbakht, T., Sokolowski, W. "Thiol-ene/acrylate systems for biomedical shape-memory polymers", *Shape Memory Polymers for Biomedical Applications*, pp. 157–166, 2015.
- [39] Javanbakht, T., Ghane-Motlagh, B., Sawan, M. "Comparative study of antibiofilm activity and physicochemical properties of microelectrode arrays", *Microelectronic Engineering*, vol. 229, 111305, 2020.

- [40] Modal, D., Willett, T.L. "Mechanical properties of nanocomposite biomaterials improved by extrusion during direct ink writing", *Journal of Mechanical Behavior of Biomedical Materials*, vol. 104, 103653, 2020.
- [41] Javanbakht, T., David, E. "Rheological and physical properties of a nanocomposite of graphene oxide nanoribbons with polyvinyl alcohol", *Journal of Thermoplastic Composite Materials*, 0892705720912767, 2020.
- [42] Kostas, V. et al. Synthesis, "Characterization and mechanical properties of nanocomposites based on novel carbon nanowires and polystyrene", Applied Sciences, vol. 10, 5737, 2020.



DOI: 10.47745/auseme-2024-0006

Effect of Thermal Ageing on the Electrical Insulation Properties of the Oil-Paper Insulation

Ján ZBOJOVSKÝ¹, Roman CIMBALA²

1.2 Department of Electric Power Engineering, Faculty of Electrical engineering and Informatics, Technical University of Košice, Košice, e-mail: jan.zbojovsky@tuke.sk, roman.cimbala@tuke.sk Manuscript received March 15, 2009; revised April 15, 2009

Abstract: The article focuses on the electrical insulation properties of oil-paper insulation and its application in practice at AC voltage. It also discusses the effect of moisture and thermal ageing on the breakdown strength and breakdown voltage of oil-paper combinations. Measurements are made of the breakdown voltage and breakdown strength of liquid insulators and paper type KREMPEL-DPP, impregnated with two types of oils, SHELL Diala S4 ZX-I and Mogul Trafo CZ-A. The moisture content in the liquid insulants before and after thermal ageing is also measured.

Keywords: Insulation, transformer oil, impregnation paper, electrical breakdown strength.

1. Introduction

Nowadays, the oil-paper insulation system is one of the most widely used insulations in the power electrical engineering. This insulation is made up of solid and liquid components. The solid consists of insulating paper and the liquid consists of oil, which serves as an impregnant. Oil also serves as a cooling medium in transformers.

Oil-paper insulation is used in a number of electrical devices even with high power at voltage levels of HV and VHV. Impregnated paper has excellent insulating properties and an important place in the electric power industry. At high voltages, on the order of hundreds of kV, oil-paper insulation is the only insulator used [1].

The combination of oil and paper insulants is used in transformer to strip the windings. Together, these insulants have sufficient electrical properties. While paper has good mechanical strength, oil has the function of impregnant and

coolant of the transformer. Both insulants have their negative properties but when they are combined, some of the bad properties are compensated, i.e., the properties of one insulator improve the properties of the other and vice versa [2]. Another use of this insulation is in power cables for voltages from 110 kV where the thickness of the impregnated paper is important. The thinner the insulating paper, the higher the electrical strength of the cable insulation [3]. Oil impregnated paper is also used in power capacitors. It is used in DC-link capacitors, in capacitors designed for power factor improvement in capacitors designed to improve power factor at a frequency of 50 Hz, etc. Mineral oil is used to impregnate the paper for this purpose.

2. Factors influencing the electrical insulation properties of the oilpaper insulation

A. Thermal stress of oil-paper insulation

In electrical equipment, during operation, insulators are often exposed to temperatures that differ significantly from room temperature (20 °C). The properties of insulants are substantially affected by such temperatures. High or low temperatures are caused by the ambient environment or by the electrical equipment itself due to electrical energy losses. For this reason, it is necessary to know what are the lowest and highest temperature a given insulation can withstand in relation to its application. According to these parameters, the insulation is selected to be suitable over the entire temperature range that the equipment can reach [3].

The highest temperature that can be considered for an insulation without any disturbance of its properties, taking into account transient thermal process in the equipment, is called the short-term thermal endurance. This, compared to the permanent thermal e (resistance to thermal ageing), is determined by the dimensional stability of the material. When selecting insulating materials for electrical equipment, it is necessary to include both of these values.

The consequences of increasing temperature are decreasing mechanical strength and decreasing modulus of elasticity of insulants. For the properties of liquid insulants, e.g., oil, its viscosity decreases and evaporation from the oil increases. As for the variation of electrical properties with increasing temperature, they deteriorate, the electrical resistance of the oil decreases and the tg δ increases. The electrical breakdown strength decreases along with the breakdown voltage. At temperatures lower than the rated operating temperature, these processes are reversed. The viscosity of the liquid insulants increases and the oil becomes thicker. The changes that occur with temperature variations are

not permanent and the properties revert back to the optimum when the temperature is restored to the rated operating value [4], [5].

B. Electrical stress of oil-paper insulation

The electric field has indirect effects on the insulation. The only direct effect is the effect of DC voltage, and only on solid insulators of lower quality. However, we have observed from long-term practice that the indirect effect of electrical voltage is more important. Studying the reasons for thermal breakdowns resulted in measures, thanks to which we can prevent the temperature from permanently damaging the insulation. However, breakdown problems continued to occur, even though the risk of thermal breakdown was eliminated at operating voltage. During the insulation tests, a higher voltage than the subsequent operating voltage was used, but there was no breakdown. The breakthrough occurred after various lengths of time without any known causes. Later investigation revealed that the breakdown occurred as a discharge in the insulation cavities [6].

Solid insulations in most cases have small air cavities. Air cavities can be created during the production of the insulation itself, or they arose during the operating conditions inside the insulation, or between insulation and live parts. Under the action of the electric field, the air or other gas is stressed much more than the rest of the insulation. Air has a much lower electrical strength than solid or liquid insulation. This causes a breakdown in the air cavity of the insulation, even at low voltage. This voltage is much lower than the breakdown voltage of the entire insulation. We call this breakdown partial discharges because they did not travel the entire distance between the two electrodes [7].

The discharges have both direct and indirect effects on the cavities of the insulation, especially at locations that are adjacent to the cavities. These effects cause physical and chemical changes in the properties of the insulants. This process is also known as insulation ageing because the discharges often cause irreversible damage and deterioration of the electrical insulation properties of the insulator. These surges result in the breakdown of the entire insulation, even at voltage gradients lower than the electrical strength. For this reason, discharge in insulation has received attention [8].

C. Effect of moisture on the electrical breakdown strength of oil and paper insulation

The most serious cause of deterioration of insulation is water. It adversely affects all insulation systems and their dielectric characteristics. The worst effect on the insulation of electrical equipment is caused by the water content in the paper insulation of the equipment. Paper gets much wetter than oil and thus the

water content of the paper is greater. To clarify, oil can contain 10 to 20 mg/kg of water, and at this content, up to 2 % of water by weight can be found in paper.

Oil contains water in three states: dissolved, emulsified and free.

The water content of the oil has a negative effect on the electrical strength of the oil. The higher the moisture content, the electrical breakdown strength decreases and hence the breakdown voltage assumes lower values [9].

Paper insulation can contain water in the following states: water in the form of vapor, water absorbed in monolayers, water absorbed in polymolecular layers, water condensed in capillaries, and free water.

In all states, except the first and fifth, water can be taken as absorbed into fibrous dielectrics. These three states depend on the relative humidity of the liquid and are conditioned by the law of absorption.

Thermal ageing of the paper and the presence of electrical stresses cause the formation of water and carbon oxides in the equipment. The fact that electrical equipment contains insulating paper or other solid insulating material increases the moisture and contaminants that pollute the electrical equipment and acts as an absorbent for polar contaminants and water [10].

At humidity below 4 %, the electrical breakdown strength of the paper appears to be nearly constant. As soon as the humidity starts to rise a significant decrease in the electrical breakdown strength is observed.

3. Measurement of the electrical breakdown strength of oil-impregnated paper insulation

A. Measuring the electrical breakdown voltage of oils

Two oils were considered for this measurement:

- Shell Diala S4 ZX-I
- Mogul Trafo CZ-A

The result of the measurement was a comparison of the breakdown voltage of the two oils. The measurements were performed on the measuring device Oil Dielectric Test Set DTS-60D. The measurement was repeated 10 times, always with a one-minute interval. After the measurement of one of the oils was completed, the vessel with electrodes was cleaned and the measurement on the second oil sample was carried out. The measurement was repeated before the oils were aged and after 1900 hours of ageing. In *Fig. 1* it is shown the electrode placement and shape.



Figure 1: Electrode placement and shape in the DTS-60D

B. Preparation of samples for measurement

Krempel insulating paper with a thickness of 0.075 mm and dimensions of 4.5x4.5 cm was used as a sample. Before the measurements were taken, it was placed in a dryer for 22 hours at 70 °C. The samples were then placed in cleaned, degreased and dried containers and impregnated with Shell Diala S4 ZX-I and Mogul Trafo CZ-A oils. The impregnated samples were aged for 1900 hours at 110 °C.

C. Procedure for measuring the breakdown voltage

The voltage increase was 2 kV/s until breakdown. The first measurement was on 1 layer of insulating paper, measurement was repeated 4 times. Gradually one layer of insulating paper was added at a time and 4 experiments were performed on each. The maximum number of layers was 6. The procedure was identical for the second type of oil. The ageing of both oils was carried out at 110 °C. Another measurement was taken after approximately 240 hours of ageing. The presence of moisture was detected with a Megger KF-LAB MKII.

4. Results of the experiments

The graphical dependence of the average values of the breakdown voltage is shown in Fig. 2. For each measurement, 10 tests were performed and the average value was calculated. From the results it is possible to observe the deterioration of the properties of both oils. When measured before ageing, it can be observed that Shell Diala S4 ZX-I oil has a higher value of the breakdown voltage than Mogul Trafo CZ-A. After 1900 hours, the deterioration is approximately the same for both oils. From Fig. 2, it can be seen that Shell Diala S4 ZX-I oil has higher electrical breakdown strength than Mogul Trafo CZ-A both before and after ageing. Voltage has been applied to the electrodes of the DTS-60D apparatus, and it has been observed, that the average value of the breakdown voltage in case of Mogul Trafo CZ-A was 8.77 kV and Shell Diala S4 ZX-I was 8.79 kV. Here it can be clearly seen that the deterioration is almost the same. From this point of view, it can be concluded that both oils handle thermal ageing in the same way.

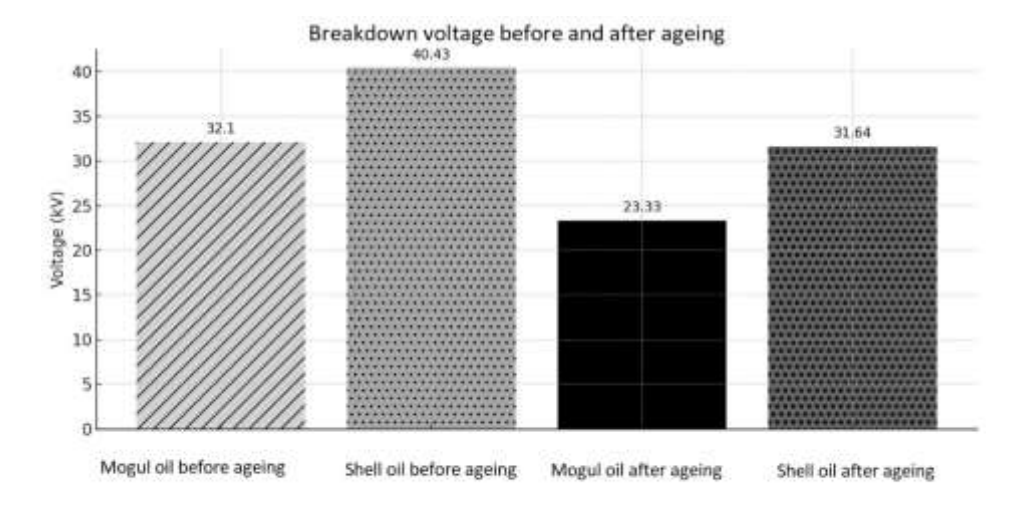


Figure 2: The graphical dependence of the electrical strength of the average values of the breakdown voltage

First, measurements were made on samples that were undried and dried. Both samples were impregnated with each of the oils. For the un-aged oil-paper insulation, it can be observed in *Fig. 3* and *Fig. 4* that the paper specimens impregnated with Shell Diala S4 ZX-I oil have higher values of impact strength than Mogul Trafo CZ-A, both for the not-dried and dried paper.

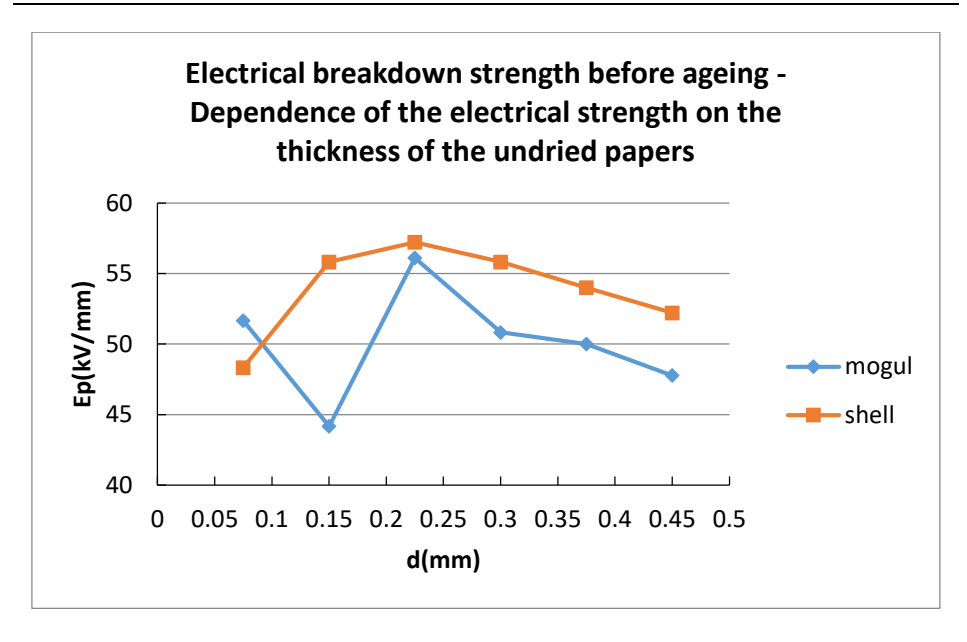


Figure 3: Graphical dependence of the electrical breakdown strength on the thickness of undried papers

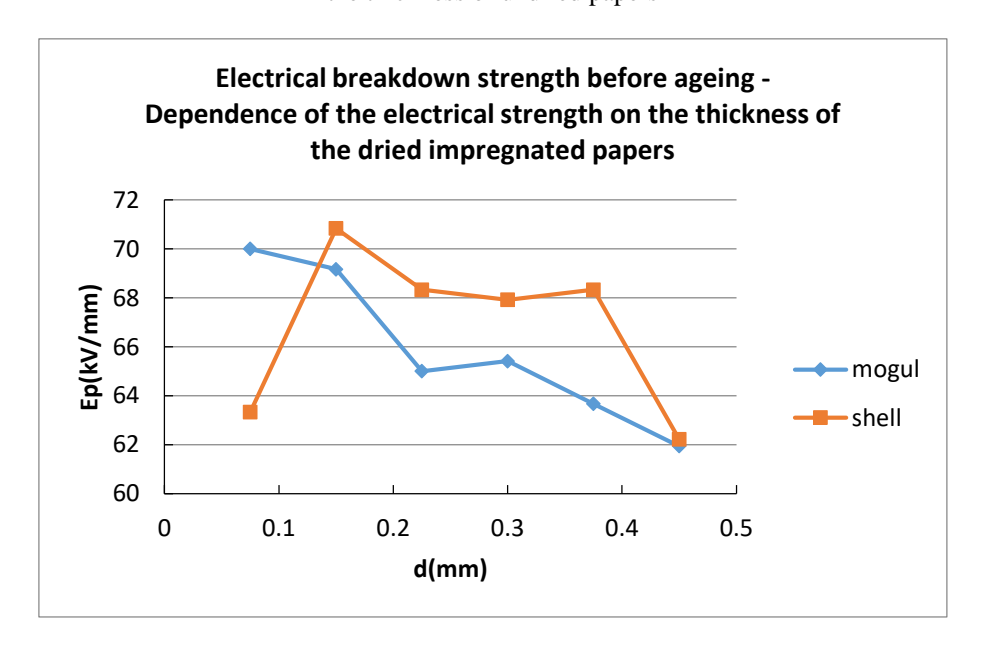


Figure 4: Graphical Dependence of electrical breakdown strength on the thickness of dried papers without ageing

Based on the results of the measurements, it was decided that only dried papers would be used in the next measurement as the magnitude of the breakdown stresses was much higher for dried than for undried samples. This statement is also evident from *Fig. 3* and *Fig. 4* where it can be clearly seen that the impact strength is higher for the dried papers with respect to the number of layers. After ageing, the Shell Diala S4 ZX-I sample has worse parameters. As can be seen in *Fig. 5* the values are not very different but Mogul Trafo CZ-A has slightly better impact strength.

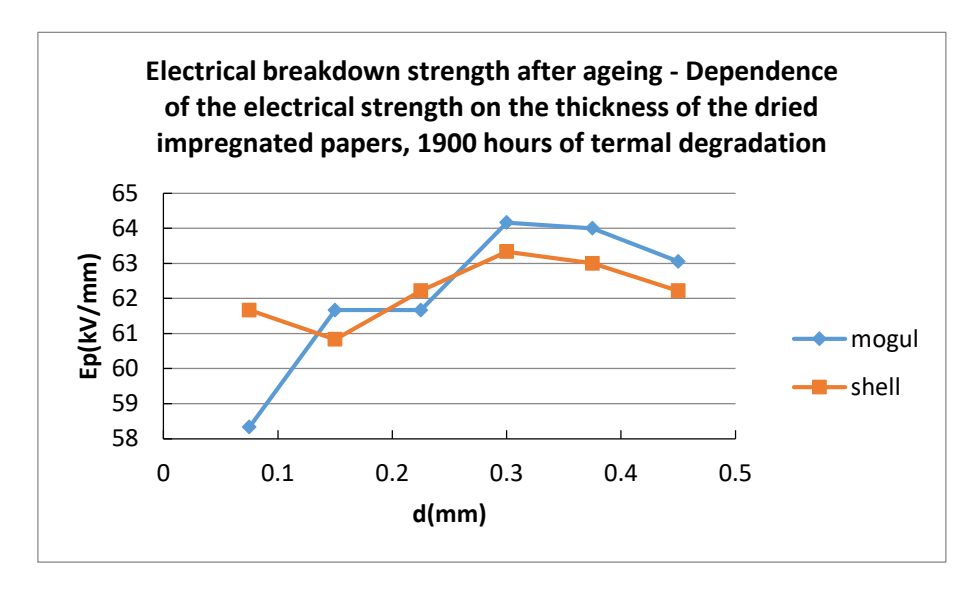


Figure 5: Graphical dependence of the electrical breakdown strength on the thickness of the dried papers after 1900 hours of ageing

It can be concluded that Shell Diala S4 ZX-I has better anti-ageing properties with increasing thickness of paper insulation and with dried papers. After 1900 hours of ageing, Shell Diala S4 ZX-I has a poorer electrical strength than Mogul Trafo CZ-A, with the exception of one and three layers of paper insulation. In the following graphs we have plotted the electrical breakdown strength versus ageing time for both types of oils. It is possible to notice a deterioration in properties with respect to ageing time.

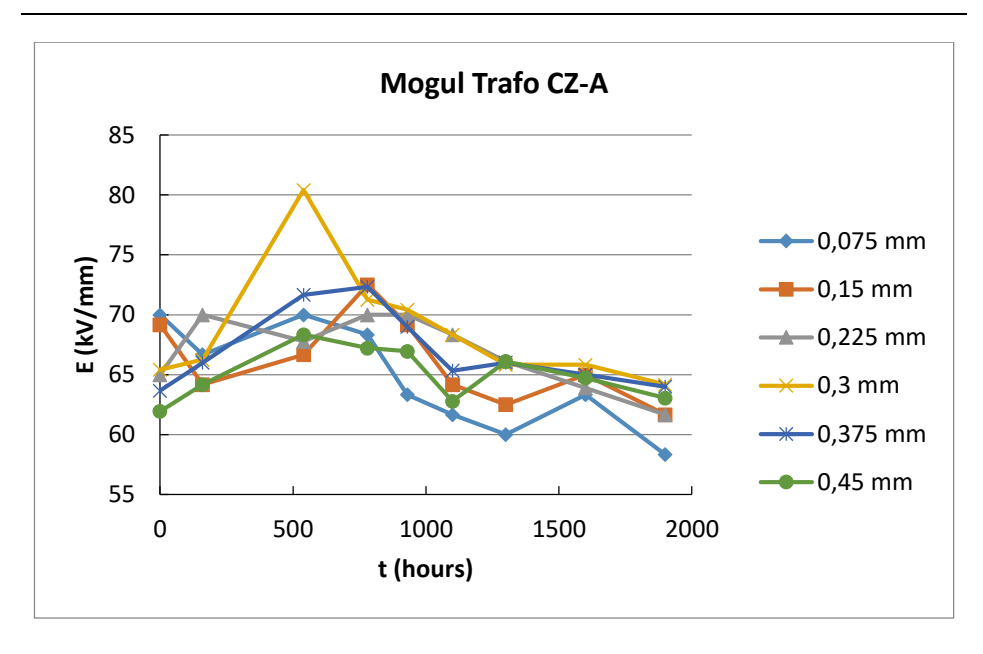


Figure 6: Graphical dependence of electrical breakdown strength on ageing time for Mogul Trafo CZ-A oil

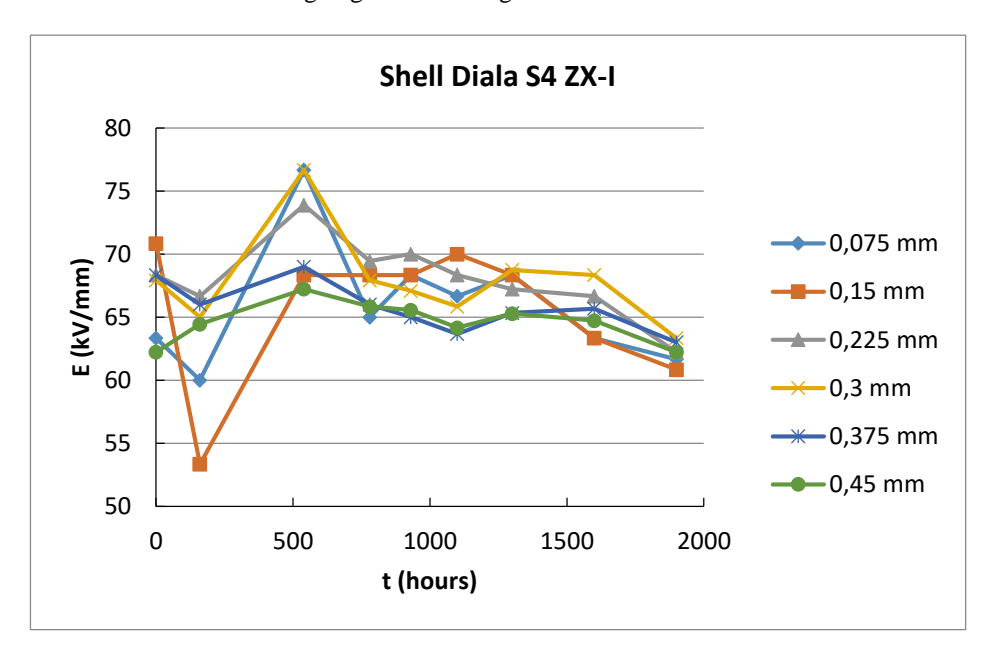


Figure 7: Graphical dependence of electrical breakdown strength on ageing time for Shell Diala S4 ZX-I oil

For further comparison of the oils, a thickness of 4 layers of insulating paper was chosen.

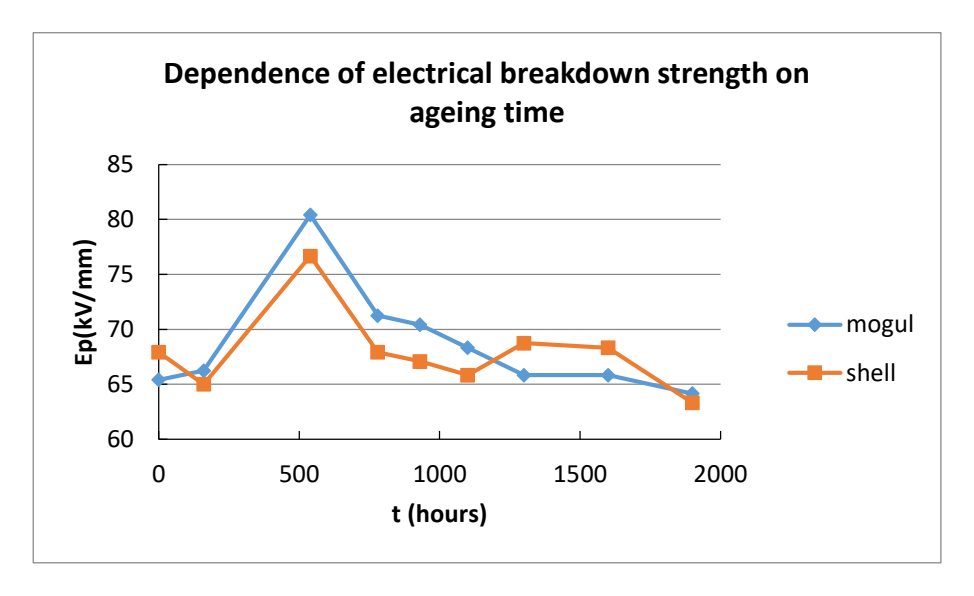


Figure 8: Graphical dependence of the electrical breakdown strength on the ageing time in case of 4 paper samples

In *Fig.* 8 it can be seen how the breakdown strength of the two oils changes. Before ageing, it is confirmed, as mentioned above, that Shell Diala S4 ZX-I has a better value. However, this changes after about 150 hours and Mogul Trafo CZ-A has better properties. Both oils have an upward trend in terms of breakthrough strength up to about 500 hours of ageing. This improvement in values may be due to drying of the oil-paper insulation during thermal ageing. The values of the impact strength are not very different. After about 1200 hours of ageing, the breakpoint occurs again and the values of the impact stress are higher Shell Diala S4 ZX-I. At 1900 hours of ageing, these values are almost the same.A discoloration of the oils was observed during ageing, which was also due to the dissolution of the resin from the insulating paper. At about 1600 hours of ageing, higher oil density was observed, especially for Mogul Trafo CZ-A oil. After ageing, the density increased further due to processes caused by thermal stress.

On the following table are shown results from the measuring of the moisture. The presence of moisture was detected with a device Megger KF-LAB MKII. Moisture detection works on the principle of Karl Fischer titration, which is the standard method for determining the water content of various samples.

Ageing time	No ageing	1600 hrs.	1900 hrs.	1900 hrs. at 80 °C
Mogul Trafo CZ-A	13.95 ppm	13.63 ppm	10.59 ppm	13.68 ppm
Shell Diala S4 ZX-I	12.78 ppm	12.38 ppm	11.62 ppm	13.87 ppm

Table 1: Moisture content in the oils

5. Conclusion

In this paper, the electrical breakdown voltage was measured and the breakdown electrical strength of liquid insulators and paper impregnated with liquid insulator at AC voltage was calculated. Krempel paper with a thickness of 0.075 mm and two insulating mineral oils Mogul Trafo CZ-A and Shell Diala S4ZX-I were used for impregnating the paper. The breakdown voltage was measured for both dried and undried impregnated paper, then further measurements were performed on the dried paper sample due to the higher breakdown voltage value of 1.375 kV for one layer of paper. Subsequently, the samples were aged for 1900 hours and 9 measurements were performed. In the first measurement, the electrical strength of the selected oils without paper insulation was measured at AC voltage. The electrode distance was 2.5 mm. It can be seen from the measurements that after ageing, the properties of both oils deteriorated and the average value of the breakdown voltage decreased almost equally by about 8.8 kV. It can also be observed that Shell Diala S4 ZX-I oil has better value of the Mogul Trafo CZ-A both before and after ageing. From this it can be concluded that Shell Diala S4 ZX-I oil has better breakdown strength and hence better electrical insulation properties. When the impregnated paper is measured with both the oils, deterioration in properties is observed in case of Shell Diala S4 ZX-I oil. Before ageing, the paper impregnated with Shell Diala S4 ZX-I oil had a higher value of electrical breakdown strength than the paper impregnated with Mogul Trafo CZ-A oil. By approximately 500 hours of ageing, the values visibly increase. This may be due to the insulation system drying out. From this value onwards the breakdown voltage drops significantly for both oils. At 1200 hours of ageing, the breakdown values of Shell Diala S4 ZX-I are again higher than those of Mogul Trafo CZ-A. The differences between the values of the breakdown voltages of the two oils are not large, in the order of 1 to 2 kV. After ageing, when the oils are heated to 80°C, the values of moisture are higher due to the release of moisture from the oils. When we look at the individual oils, it is noticeable that Mogul Trafo CZ-A is better in terms of drying, because when comparing the values before and after ageing, the difference is 3.36 ppm. Shell Diala S4 ZX-I is quite a bit worse as the difference is only 1.16 ppm. When comparing the pre-ageing values of the oils, Shell Diala S4 ZX-I has a lower value of moisture.

Acknowledgements

This research was funded by the Ministry of Education, Youth and Sports within the project VEGA 1/0380/24 and the Slovak Agency for Research and Development based on contracts no. APVV-22-0115.

References

- [1] Abdi, S., Haddad, A. M., Harid, N., and Boubakeur, A., "Modelling the Effect of Thermal Aging on Transformer Oil Electrical Characteristics Using a Regression Approach", *Energies*, vol. 16, no. 1, Art. no. 1, Jan. 2023, doi: 10.3390/en16010381.
- [2] Safiddine, L., Zafour, H. Z., Rao, U. M., and Fofana I., "Regeneration of Transformer Insulating Fluids Using Membrane Separation Technology", *Energies*, vol. 12, no. 3, Art. no. 3, Jan. 2019, doi: 10.3390/en12030368.
- [3] Munajad, A., Subroto, C., and Suwarno, "Study on the Effects of Thermal Aging on Insulating Paper for High Voltage Transformer Composite with Natural Ester from Palm Oil Using Fourier Transform Infrared Spectroscopy (FTIR) and Energy Dispersive X-ray Spectroscopy (EDS)", Energies, vol. 10, no. 11, Art. no. 11, Nov. 2017, doi: 10.3390/en10111857.
- [4] Lyutikova, M. N., Korobeinikov, S. M., and Buzaev, V.V., "Determination of Water Content in Liquid Insulation of High-Voltage Equipment by Different Methods", *Power Technol. Eng.*, vol. 53, no. 5, pp. 623–630, Jan. 2020, doi: 10.1007/s10749-020-01127-9.
- [5] Feng, D., Hao, J., Yang, L., Liao, R., Chen, X., and Li, J., "Comparison of AC breakdown characteristics on insulation paper (pressboard) immersed by three-element mixed insulation oil and mineral oil", *High Volt.*, vol. 5, no. 3, pp. 298–305, Jun. 2020, doi: 10.1049/hve.2019.0103.
- [6] Zhou, L. J., Wu, G. N., and Liu, J., "Modeling of transient moisture equilibrium in oil-paper insulation", *IEEE Trans. Dielectr. Electr. Insul.*, vol. 15, no. 3, pp. 872–878, Jun. 2008, doi: 10.1109/TDEI.2008.4543125.
- [7] Feng, D., Yang, L., Liao, R., Zhou, L., and Lin, Y., "Effect of Moisture Content on the Production and Partitioning of Furfural in Oil-Paper Insulation", *IEEE Trans. Dielectr. Electr. Insul.*, vol. 25, no. 6, pp. 2389–2397, Dec. 2018, doi: 10.1109/TDEI.2018.007238.
- [8] Lisoň, L., Zbojovský, J., Kolcunová, I., and Kmec, M., "Research of electrophysical properties of oil-paper insulation", presented at the *Proceedings of the 2014 15th International Scientific Conference on Electric Power Engineering*, EPE 2014, 2014, pp. 403–406. doi: 10.1109/EPE.2014.6839506.
- [9] Zhou, Y., Chen, W., Yang, D., and Zhang, R., "Raman Spectrum Characteristics and Aging Diagnosis of Oil-paper Insulation with Different Oil-paper Ratios", *IEEE Trans. Dielectr. Electr. Insul.*, vol. 27, no. 5, pp. 1587–1594, Oct. 2020, doi: 10.1109/TDEI.2020.008938.
- [10] Przybylek, P., "Investigations of the temperature of bubble effect initiation oil-paper insulation", *Prz. Elektrotechniczny*, vol. 86, no. 11B, pp. 166–169, 2010.



DOI: 10.47745/auseme-2024-0007

Thermal Dependence of Ferrofluids Dielectric Response

Samuel BUCKO¹, Roman CIMBALA¹

¹ Department of Electrical Power Engineering, Faculty of Electrical Engineering and Informatics, Technical University of Košice, Letná 9, 04200, Košice, Slovakia, e-mail: samuel.bucko@tuke.sk

Manuscript received April 10, 2024; revised November 09, 2024

Abstract: This paper deals with dielectric spectroscopy in the frequency domain, where polarization events in ferrofluid samples with concentrations of 0.25% and 0.5% vol. were monitored. The samples were compared with a carrier fluid, in this case transformer mineral oil ITO 100. Polarization phenomena were observed in different frequency ranges, which are related to the presence of Fe₃O₄ nanoparticles in the ferrofluid. For a better interpretation of the results, temperature dependence was used to help in defining the polarization events and their mechanisms in composite materials such as ferrofluids.

Keywords: Ferrofluid, nanoparticles, dielectric spectroscopy, transformer, thermal dependence.

1. Introduction

The power transformer is one of the most important parts of the power system. For this reason, high demands are placed on its safety, durability and, last but not least, on its environmental impact [1]. In the case of distribution and transmission transformers, the most commonly used transformer is the one with an oil-paper insulation system. Oil represents two roles in the case of transformers, namely: electrical insulation in combination with paper and as cooling medium that dissipates the heat generated by losses [2].

In recent decades, the use of nanofluids based on transformer oil has been considered. In this case, a certain volume of nano-sized solid particles is dispersed in the liquid and due to Brownian motion, it is ensured that these nanoparticles do not sediment [3]. Insulating liquids treated in this way exhibit better insulating properties and better heat dissipation. In the case of nanoparticle materials, a ferromagnetic material that is affected by the magnetic field around the transformer core may be a suitable solution [4].

In the case of insulating liquids, various nanoparticle materials such as ZnO or iron-based nanoparticles are used. The iron oxide-based nanoparticles are influenced by the external magnetic field of the transformer. Such an effect can cause the cooler liquid around the walls of the transformer vessel to have a higher magnetization and thus be drawn into the center. Due to losses in the magnetic and electrical circuit, heat is generated which heats the nanofluid and through such a process a natural circulation of the fluid in the transformer vessel is created [5].

From the point of view of safe operation, it is necessary to carry out regular sampling on the transformers, and the samples are subjected to various diagnostic methods. Based on these diagnostic tools, we can monitor the ageing process of the insulation system, detect deteriorating insulation conditions in time and adjust the operating conditions, make repairs or replace the equipment in question [6]. Such regular checks can prevent the insulation and thus the whole plant from failing, which can cause power outages, destruction of the plant itself, or an accident that can have high economic and environmental impacts [7].

Long-term research focusing on nanofluids containing Fe_3O_4 nanoparticles dispersed in transformer oils shows that such composite materials can improve some of the properties of carrier fluids [8], [9]. For example, the breakdown voltage be increased due to the contribution of nanoparticles in the fluid [10] [11]. Since solid materials are better thermal conductors, even a small amount of Fe_3O_4 particles can improve the thermal conductivity of the insulating fluid [5], [12].

In the case of nanofluids that are based on transformer oil and nanoparticles that are formed from iron oxides, such nanofluids can also be called ferrofluids. The most important parameter when using such ferrofluids as a substitute for conventional transformer oils is the stability of the whole system [13]. Degradation agents cause disruption of the surfactant that coats the nanoparticles. This surfactant has the task of limiting the clumping of the nanoparticles. Any clusters formed have a negative effect on the dielectric properties [14]. In the case of a formed cluster, the Brownian forces no longer act and the ferrofluid starts to disintegrate and sediment [15]. The temperature of the liquid has a significant effect on the formation of clusters. In the case of hot-spot locations (e.g., interthread short circuits), there is a local increase in temperature, which can also cause the ferrofluid to break down at such a location [16], [17].

Several methods can be used for the diagnosis of dielectric materials, but in this publication the focus is on frequency dielectric spectroscopy. Frequency dielectric spectroscopy (FDS) is a method that uses a sinusoidal voltage waveform that is applied to the object under study by electrodes. At the same time, the response of the sample to this voltage is monitored by the current flowing between the electrodes and the sample. Using the amplitude of the current and its phase shift, it is possible to calculate the impedance of the sample and from its other quantities such as capacitance or loss factor.

In the case of common insulating liquids, a change in conductivity can be observed at low frequencies (DC to 10 Hz), which may be caused by a higher moisture content in the sample. Polarization phenomena appear in higher frequency regions, from hundreds of kHz to MHz. [18]. Based on the values obtained, it is possible to determine the relaxation time that applies to a given type of polarization. Once the polarization has been characterized, it is then possible to define the mechanism of polarization. For frequency bands up to 2MHz, it is possible to record, for example, the process of electron tunnelling between water molecules, which produces dipoles with a characteristic relaxation phenomenon [19].

In the case of the use of FDS for nanofluids, more specifically ferrofluids, it is necessary to know what may be causing the polarization phenomenon. In some frequency regions it is difficult to capture and pinpoint polarization phenomena, so it is necessary to supply higher energy to the system under investigation. This increase in energy can be achieved by supplying thermal energy to the system. Since polarization and conduction phenomena are strongly temperature dependent in the FDS problem, many studies also deal with the temperature dependence of the observed phenomena [20], [21], [22].

To investigate the effect of temperature on the properties of the ferrofluid, the FDS with temperature dependence was employed, given that the ferrofluid is a composite material. The nanoparticles, the carrier fluid, and the surfactant have different values of permittivity and respond differently to temperature change. This information was used at the selection of the appropriate measurement method.

2. Sample characterization and experimental setup

For the formation of ferrofluid, the ITO 100 transformer oil was used, which is mostly used in distribution transformers. In this transformer oil, which is a carrier fluid, nanoparticles of Fe₃O₄ magnetite were dispersed using the following process. The nanoparticles were coated with a surfactant - oleic acid. The fabrication process involved the synthesis of Fe³⁺ and Fe²⁺ ions at 80°C, which were dissolved in an aqueous solution with a concentration of 25% NH₄OH. Subsequently, oleic acid was applied at 80°C. Magnetic decantation and multiple rinsing with acetone were used to achieve higher purity and stability of the nanoparticles. Subsequently, the nanoparticles thus prepared were added to the carrier liquid at 120°C. A more detailed description of the process is given in [23]. Ferrofluid samples were produced in the laboratory of the Institute of Experimental Physics, Slovak Academy of Science.

The measurement set-up is presented in *Fig.1*. It is consisted of an electrode system for liquid samples by Tettex, type 2903. This electrode system was

supplemented by a heating system which was controllable. The capacitance of the empty electrode system is 60pF. The capacitance and loss factor values were measured using LCR meter E4980A by Agilent. The loss factor and capacitance values were determined through measurements conducted with a constant voltage amplitude of 2V, while the frequency values were varied within the range of 20 Hz to 2 MHz. For each frequency value, 50 samples were measured from which an arithmetic average was calculated.

The values of the components of the complex permittivity were calculated from the measured data:

$$\varepsilon' = \frac{c_{sample}}{c_{empty}},\tag{1}$$

where ε ' is the real part of the complex permittivity, C_{sample} represents the measured capacitance of the sample at the selected equivalent parallel capacitance setting and C_{empty} is the capacity of the empty electrode system (60pF).

The imaginary part of complex permittivity was calculated:

$$\varepsilon'' = \varepsilon' \cdot \tan\delta \,, \tag{2}$$

where $tan \delta$ is the dissipation factor.

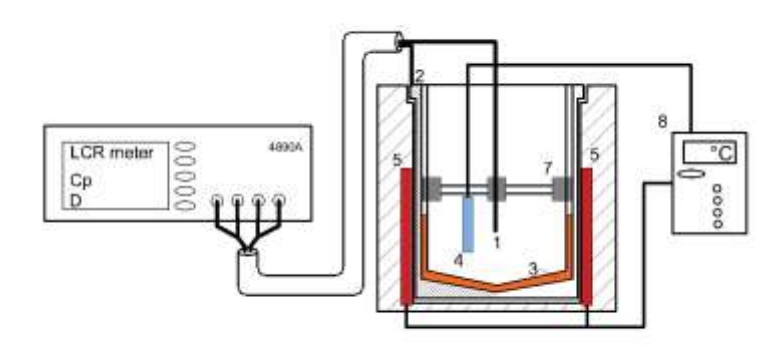


Figure 1: Experimental setup. 1 - High electrode, 2 – Low electrode, 3 – Sample, 4 – Thermocouple, 5 – Heater, 6 – Thermal regulation, 7 – Insulators

3. Results and discussion

Fig. 1 shows the values of the individual components of the complex permittivity for pure mineral oil and for a ferrofluid with a nanoparticle content of 0.25% vol. In both cases, there is a notable deviation in the values within the frequency range of 20 Hz to 100 Hz. In this region, signal interference may occur in the readings of the LCR meter as a result of the influence of the public 50 Hz grid and its subharmonics. Therefore, this frequency band will be excluded from further evaluation. In the case of the real component of the complex permittivity, it can be seen that across the entire measured spectrum the value for pure oil is constant, around 2.8. In the case of ferrofluid, the shape of waveform is constant up to a frequency of 50kHz and then there is a drop down to a level of 0.62. A higher value of the real part of the complex permittivity of the carrier liquid than that observed in ferrofluid can be attributed to the hydrophobic nature of the Fe₃O₄ nanoparticles, which impart an enhanced affinity for air humidity to the ferrofluid [24]. Such a decrease can be attributed to relaxation phenomenon, which is confirmed by the waveform of the imaginary component, where the dielectric relaxation mechanism is in the range 20 kHz to 2 MHz with a peak around 300 kHz.

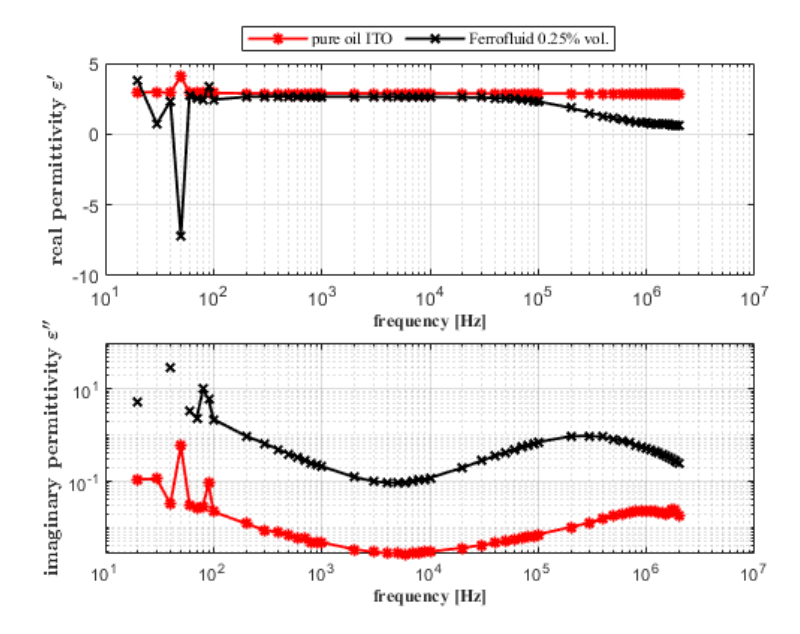


Figure 2: Real and imaginary part of complex permittivity for pure mineral oil and ferrofluid with 0.25% vol. of nanoparticles Fe₃O₄ measured at temperature 40°C

In the case of pure ITO 100 oil, a dielectric relaxation mechanism can be seen in the 1 MHz region, but it is not clearly visible in the waveform of the real component.

The higher value for the imaginary component of the complex permittivity in *Fig. 1* is due to the higher loss factor of the other components contained in the ferrofluid, oleic acid and magnetite nanoparticles.

In the case of pure oil, it can be considered that at higher temperatures, the sample reaches higher energy, and a polarization action occurs in a higher frequency band, which can be caused, for example, by water nanoparticles in the sample. Electrons may migrate between these nanoparticles to form dipoles.

As can be seen from Fig. 2, such an effect could be confirmed at higher frequencies, above 2 MHz, which is already beyond the limits of the measurement setup. In the real part, when the curve begins to decrease at both lower and higher temperatures, the incipient relaxation mechanism can also be observed. In the case of the real part of the complex permittivity at pure transformer oil, a decrease around 0.2 can be seen for the waveforms measured at higher temperatures. This difference may be due to moisture contribution. This moisture has entered the sample from the atmosphere, since the samples of the oil and the samples of the ferrofluids were neither subjected to a drying process prior to the experiment.

In the case of the imaginary component in the temperature dependence of the pure oil, a shift of the minimum towards higher frequencies can be seen, and in the region of lower frequencies the value is significantly higher. This phenomenon is caused by the conductivity contribution from nanoparticles as well as surfactant (oleic acid).

Fig. 3 shows the FDS in the case of ferrofluid, which has a nanoparticle content of 0.25% vol. and which was heated to temperatures of 40, 60 and 80°C. From the diagrams of the real component of the complex permittivity, it can be assumed that the relaxation mechanism shifts to regions of higher frequency. This assumption is confirmed by the waveform of the imaginary part. The difference between the real permittivity waveforms can be attributed to moisture removal during heating of the sample and stabilization of its temperature.

In the case of imaginary permittivity, much higher values are seen than in the case of pure oil. Again, this increase can be attributed to the components that the ferrofluid contains. The polarization phenomenon in the region of 20 kHz to 1 MHz with peaks in the region of 300-400 kHz may be related to nanoparticles interacting with each other, e.g., by the participation of dipoles between two differently charged nanoparticles, or the binding of water molecules in the ferrofluid to the surface of the nanoparticle as reported by Primo et al. in [25].

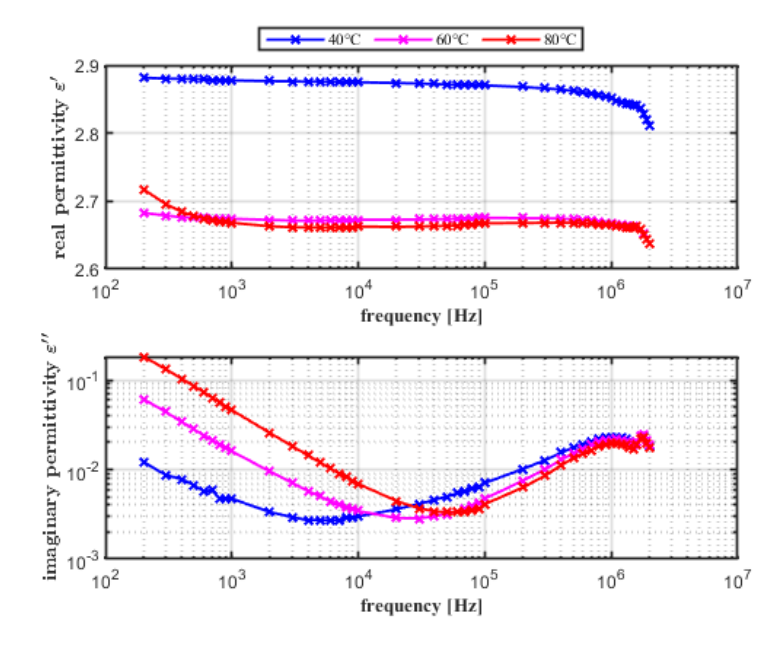


Figure 3: Thermal influence on FDS of transformer oil ITO 100

In the case of a higher concentration of nanoparticles in the ferrofluid, the contribution to the conductivity is expected to be due to a higher concentration of oleic acid on the surface of the nanoparticles. The conductivity phenomena dominate in the lower frequency regions, as can be seen in *Fig. 4* for 0.5 vol% nanoparticle concentration. The epsilon values for 0.25 vol% in *Fig. 3* range from 0.96 to 3.02 for a frequency of 200 Hz. At this frequency and twice the volume of nanoparticles in the ferrofluid, *Fig. 4* shows an increase in the imaginary part of the dielectric constant, which ranges from 1.45 to 4.48 in the temperature spectrum.

Another possible explanation for the higher values for the sample with 0.5% nanoparticle volume is the increase in the ratio of the individual components in the sample, in particular the formation of chains between nanoparticles with a disturbed surfactant layer. At higher nanoparticle concentrations, the "chain" phenomenon is more likely to occur than at the 0.25% concentration.

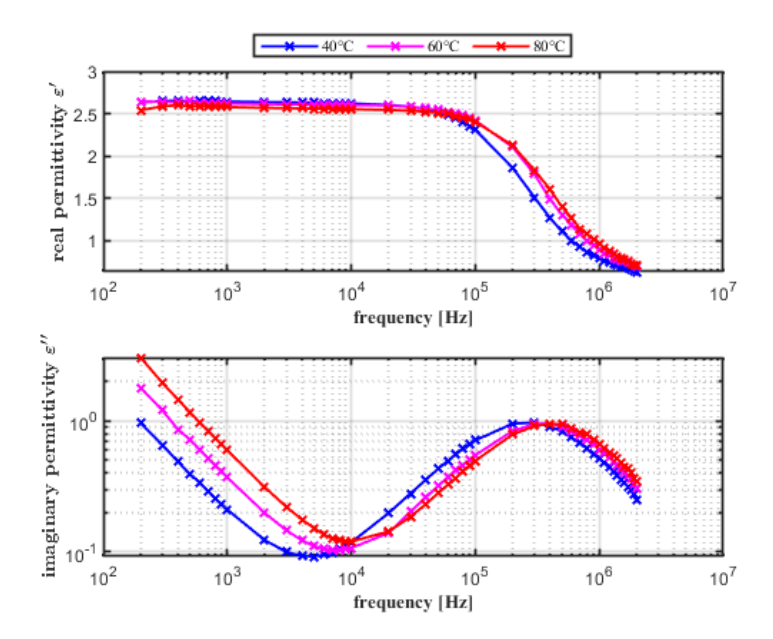


Figure 4: Thermal influence of dielectric polarization of ferrofluid with nanoparticle contribution 0.25% vol

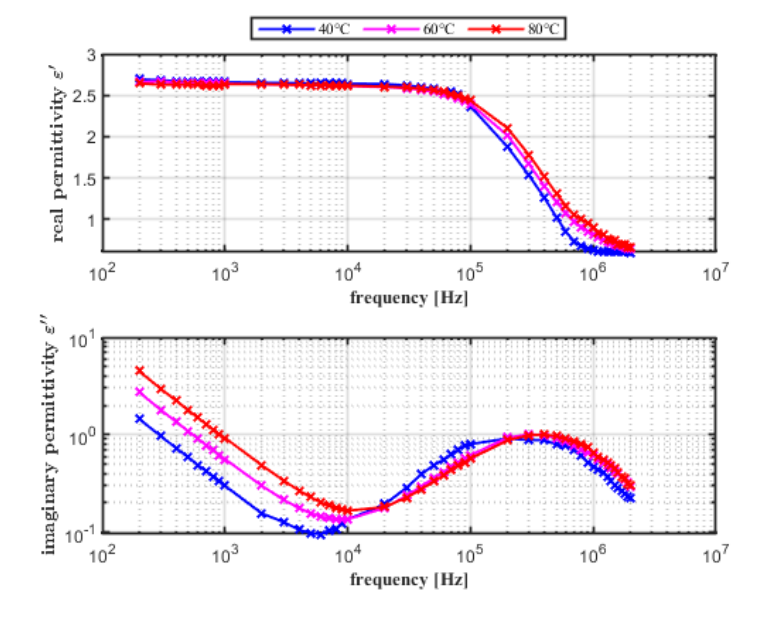


Figure 5: Thermal influence of dielectric polarization of ferrofluid with nanoparticle contribution 0.5% vol

For both concentrations of Fe_3O_4 nanoparticles, there is a characteristic relaxation mechanism in the same region with similar values at the maximum point for 0.25%-0.95 and for 0.5%-1.01. The cause of this relaxation mechanism may be due to the tunnelling of electrons from one electrically neutral particle to the next, causing the formation of dipoles. A similar phenomenon can occur in pure oil, but there the dipole moment will be caused by the formation of dipoles between nanodroplets of water [19].

4. Conclusion

In this work, polarization processes were investigated thanks to frequency-dependent spectroscopy, which, as one of the diagnostic methods, is characterized by its speed, low equipment requirements and, consequently, lower costs. In the case of new nanoparticle-based materials, the applicability of diagnostic tools used for conventional insulating materials is important. In addition, the widest possible range of measurement methods is needed for a consistent understanding of the processes that take place, e.g., during the application of an electric field to a ferrofluid.

In future work, it would be useful to focus on the area of relaxation processes at higher frequency regions and to determine the activation energy from the value of the relaxation time. In the lower frequency range, it is necessary to obtain a detailed view of this area, which will demonstrate the mechanism in this domain due to the temperature dependence.

Acknowledgements

This research was funded by the Ministry of Education, Youth and Sports within the project VEGA 1/0380/24 and the Slovak Agency for Research and Development based on contracts no. APVV-22-0115.

References

- [1] Fofana, I., and Hadjadj, Y., "Power Transformer Diagnostics, Monitoring and Design Features", *Energies 2018, Vol. 11, Page 3248*, vol. 11, no. 12, p. 3248, Nov. 2018, doi: 10.3390/EN11123248.
- [2] Abdi, S., Harid, N., Safiddine, L., Boubakeur, A., and Haddad, A., "The Correlation of Transformer Oil Electrical Properties with Water Content Using a Regression Approach", *Energies 2021, Vol. 14, Page 2089*, vol. 14, no. 8, p. 2089, Apr. 2021, doi: 10.3390/EN14082089.
- [3] Said, Z., et al., "Recent advances on the fundamental physical phenomena behind stability, dynamic motion, thermophysical properties, heat transport, applications,

- and challenges of nanofluids", *Phys Rep*, vol. 946, pp. 1–94, Feb. 2022, doi: 10.1016/J.PHYSREP.2021.07.002.
- [4] Sun, B., Guo, Y., Yang, D., and Li, H., "The effect of constant magnetic field on convective heat transfer of Fe3O4/water magnetic nanofluid in horizontal circular tubes", *Appl Therm Eng*, vol. 171, p. 114920, May 2020, doi: 10.1016/J.APPLTHERMALENG.2020.114920.
- [5] El Dine, S. N., Mininger, X., and Nore, C., "Heat Transfer in a Ferrofluid-Based Transformer: Multiphysics Modeling using the Finite Element Method", *IEEE J Multiscale Multiphys Comput Tech*, 2022, doi: 10.1109/JMMCT.2022.3200019.
- [6] Lin, M. J., Chen, L. B., and Yu, C. T., "A Methodology for Diagnosing Faults in Oil-Immersed Power Transformers Based on Minimizing the Maintenance Cost", *IEEE Access*, vol. 8, pp. 209570–209578, 2020, doi: 10.1109/ACCESS. 2020.3038827.
- [7] Abbasi, A. R., "Fault detection and diagnosis in power transformers: a comprehensive review and classification of publications and methods", *Electric Power Systems Research*, vol. 209, p. 107990, Aug. 2022, doi: 10.1016/J.EPSR. 2022.107990.
- [8] Mariappan, Y., and Rengaraj, M., "A comprehensive review on nanotechnology for enhancement in performance of transformer liquid insulation", *Mater Today Proc*, vol. 47, pp. 229–234, Jan. 2021, doi: 10.1016/J.MATPR.2021.04.128.
- [9] Paulovičová, K., *et al.*, "Rheological and thermal transport characteristics of a transformer oil based ferrofluid", *Acta Phys Pol A*, vol. 133, no. 3, pp. 564–566, Mar. 2018, doi: 10.12693/APHYSPOLA.133.564.
- [10] Bhatt, M., and Bhatt, P., "Breakdown Probability, Reliability and Streamer Dynamics in Transformer Oil based Hybrid Nanofluid", *Advances in Electrical and Computer Engineering*, vol. 23, no. 2, pp. 67–74, 2023, doi: 10.4316/AECE. 2023.02008.
- [11] Koutras, K. N., Tegopoulos, S. N., Charalampakos, V. P., Kyritsis, A., Gonos, I. F., and Pyrgioti, E. C., "Breakdown Performance and Partial Discharge Development in Transformer Oil-Based Metal Carbide Nanofluids", *Nanomaterials*, vol. 12, no. 2, Jan. 2022, doi: 10.3390/nano12020269.
- [12] Yu, D., Zhengyong, H., Bin, D., Gang, C., Tianqin, L., and Jian, L., "Analysis of Thermal Conductivity Calculation Model of Nano Insulating Oil", 7th IEEE International Conference on High Voltage Engineering and Application, ICHVE 2020 - Proceedings, Sep. 2020, doi: 10.1109/ICHVE49031.2020.9279467.
- [13] Cong, H., Shao, H., Du, Y., Hu, X., Zhao, W., and Li, Q., "Influence of Nanoparticles on Long-Term Thermal Stability of Vegetable Insulating Oil", *IEEE Transactions on Dielectrics and Electrical Insulation*, vol. 29, no. 5, pp. 1642–1650, Oct. 2022, doi: 10.1109/TDEI.2022.3190805.
- [14] Suhaimi, S. N., Rahman, A. R. A., Din, M. F. M., Hassan, M. Z., Ishak, M. T., and Bin Jusoh, M. T., "A Review on Oil-Based Nanofluid as Next-Generation Insulation for Transformer Application", *J Nanomater*, vol. 2020, 2020, doi: 10.1155/2020/2061343.
- [15] Lee, W.-K. and Ilavsky, J., "Particle size distribution in ferrofluid macro-clusters", 2012, doi: 10.1016/j.jmmm.2012.10.018.

- [16] Borzuei, M., and Baniamerian, Z., "Role of nanoparticles on critical heat flux in convective boiling of nanofluids: Nanoparticle sedimentation and Brownian motion", *Int J Heat Mass Transf*, vol. 150, p. 119299, Apr. 2020, doi: 10.1016/J.IJHEATMASSTRANSFER.2019.119299.
- [17] Ng, W. M. et al., "Sedimentation Kinetics of Magnetic Nanoparticle Clusters: Iron Oxide Nanospheres vs Nanorods", Langmuir, vol. 36, no. 19, pp. 5085–5095, May 2020, doi: 10.1021/ACS.LANGMUIR.0C00135/ASSET/IMAGES/MEDIUM/ LA0C00135 0008.GIF.
- [18] Zukowski, P., *et al.*, "Research on Changes in the Phase Shift Angle and Admittance of the Cellulose–Bio-Oil Composite under the Influence of Increasing Moisture during the Long-Term Operation of Power Transformers", *Energies 2023, Vol. 16*, *Page 7880*, vol. 16, no. 23, p. 7880, Dec. 2023, doi: 10.3390/EN16237880.
- [19] Zukowski, P., Rogalski, P., Kierczynski, K., and Koltunowicz, T. N., "Precise Measurements of the Temperature Influence on the Complex Permittivity of Power Transformers Moistened Paper-Oil Insulation", *Energies 2021, Vol. 14, Page 5802*, vol. 14, no. 18, p. 5802, Sep. 2021, doi: 10.3390/EN14185802.
- [20] Gao, Yang, J., L., Wang, Y., Liu, X., Du, Y., and Yao, R., "Effect of moisture and thermal degradation on the activation energy of oil-paper insulation in frequency domain spectroscopy measurement", *IET Generation, Transmission and Distribution*, vol. 10, no. 9, pp. 2042–2049, Jun. 2016, doi: 10.1049/IET-GTD.2015.0946.
- [21] Chowdhury, S., Haque, N., Chatterjee, S., Pradhan, A. K., and Chakravorti, S., "Estimation of Activation Energy of Transformer Insulation from Frequency Domain Spectroscopy Measurement Performed at a Particular Temperature", 2021 Electrical Insulation Conference, EIC 2021, pp. 132–136, 2021, doi: 10.1109/EIC49891.2021.9612317.
- [22] Garg, A., Banerjee, C. M., Baral, A., and Chakravorti, S., "Influence of Temperature Transient on Frequency Domain Dielectric Response of Oil-Paper Sample", *Proceedings of 2021 5th International Conference on Condition Assessment Techniques in Electrical Systems, CATCON 2021*, pp. 62–65, 2021, doi: 10.1109/CATCON52335.2021.9670487.
- [23] Molcan, M., Skumiel, A., Tothova, J., Paulovicova, K., Kopcansky, P., and Timko, M., "The Influence of Viscosity on Heat Dissipation under Conditions of the High-Frequency Oscillating Magnetic Field", *Magnetochemistry* 2024, Vol. 10, Page 2, vol. 10, no. 1, p. 2, Dec. 2023, doi: 10.3390/MAGNETOCHEMISTRY10010002.
- [24] Gao, X., et al., "Dual bioinspired superhydrophobicity and magnetically-induced self-healing ferrofluid-based SLIPS to inhibit corrosion of copper", Colloids Surf A Physicochem Eng Asp, vol. 703, p. 135378, Nov. 2024, doi: 10.1016/j.colsurfa.2024.135378.
- [25] Primo, V. A., Perez, D., Garcia, B., and Burgos, J. C., "Analysing the impact of Moisture on the AC Breakdown Voltage of Fe3O4 Based Nanodielectric Fluids", pp. 1–4, Nov. 2018, doi: 10.1109/ICD.2018.8514740.



DOI: 10.47745/auseme-2024-0008

Analysis of Hot Spots on Photovoltaic Panels

Marek PAVLÍK¹, Michal KOLCUN¹, Damian MAZUR²

¹ Department of Electric Power Engineering, Technical University of Košice, 04001 Košice, Slovakia, e-mail: marek.pavlik@tuke.sk, Michal.Kolcun@tuke.sk
² Department of Electrical and Computer Engineering Fundamentals, Rzeszow University of Technology, Powstancow Warszawy 12, Rzeszow, Poland, e-mail: mazur@prz.edu.pl

Manuscript received April 07, 2024; revised September 01, 2024

Abstract: The increase in photovoltaic systems necessitates addressing hot spot issues. Analysis reveals that shading, dust, and manufacturing defects can lead to hot spot formation. A proposed voltage measurement method, based on the Hot Spot Index (HSI), enables hot spot identification and localization. Experiments confirm its effectiveness in detection. Additionally, nearby surrounding areas are also affected, indicating their potential thermal impact. This proactive approach allows minimizing the adverse effects of hot spots on the performance and lifespan of PV systems.

Keywords: Photovoltaic panels, hot spots, comparative voltage measurement, Hot Spot Index, PV system performance.

1. Introduction

The necessity to reduce greenhouse gas emissions and the increasing demand for electrical energy has led to a higher proportion of electricity production from renewable sources. In Slovakia, besides hydroelectric power plants, conditions also favor the direct conversion of solar energy into electrical energy. The increase in installed photovoltaic power plants has been significant in recent years, influenced by several factors. Firstly, state support provides subsidies for the establishment of photovoltaic sources, and secondly, there are concerns among households and industries regarding the rising prices of electricity recorded in the recent period [1], [2].

The increased number of photovoltaic sources brings with it an increased risk to their stable operation for distribution companies as well as for the operator of the photovoltaic source. During the operation of the photovoltaic source, numerous problems arise, which will be discussed in this paper. These problems

result in a reduction in the amount of electricity generated, thereby prolonging the return on investment [1], [3].

Photovoltaic energy sources are unidirectional sources, hence the need for transformation of DC energy to AC energy. Losses occur during this transformation, depending on various factors. The operation of the photovoltaic source itself is accompanied by many changing conditions - varying temperature conditions and changing solar radiation. These significant changes influence the generated output from the photovoltaic source (PVS). Many parameters, such as the temperature of the photovoltaic panel, its degradation, defects, and others, cause significant differences in the amount of electricity generated. On the other hand, photovoltaic power plants pose significant challenges during their operation [4], [5].

2. Hot spots

Hot spots are a common occurrence and are difficult to predict. Temperatures in these areas can reach up to 150°C, leading to permanent and irreversible damage to the photovoltaic panel, such as glass breakage due to high temperature, degradation of cells, and therefore, of the panel, etc. When PV cells are connected in series and one of the cells is shaded, the overall current in the series connection of these cells decreases, causing the good cells to produce higher voltage, which often can adversely affect the bad cell [1], [6].

The operating current of this entire series section approaches the short-circuit current of the shaded cell. The energy generated in the good cells will concentrate in the shaded PV cell, increasing the overall temperature of the faulty PV cell because a large amount of energy is concentrated on a small area. This energy is "consumed" in this faulty PV cell and converted into heat, which can reach up to the aforementioned 150°C. The huge consumption of energy in a small area leads to local overheating in the PV panel. This causes a reduction in the efficiency of the PV panel and a decrease in the amount of electrical energy produced in this panel as well as in the entire photovoltaic system. In severe cases, hot spots can cause permanent damage to the PV panel, reduce its lifespan, and thereby increase the payback period of the photovoltaic power plant [1], [5], [7].

The main cause of hot spots on PV panels is shading. When a part of a PV panel is shaded, the PV cells connected in series generate a large reverse voltage on the shaded PV cell. This causes heat to accumulate in the shaded area, leading to an increase in temperature in the affected area and the formation of hot spots. Additionally, shading can reduce the overall efficiency of the PV panel because the PV cells in the shaded area are not able to produce electricity at the same rate as the rest of the PV panel. Another factor contributing to the formation of hot spots is the accumulation of dust and dirt on the PV panel. Dirt and dust on the

surface of the PV panel can reduce the amount of sunlight reaching the PV cells, decreasing their efficiency. This leads to reduced performance and increased temperature of the photovoltaic panel. Moreover, impurities can affect the airflow over and around the panel, which is crucial for heat dissipation and maintaining a consistent temperature of the PV panel. As has been mentioned multiple times, temperature significantly affects the operation of the photovoltaic panel, resulting in reduced power generation from this photovoltaic panel as well as the entire system. The design and construction of the PV panel can also play a role in the occurrence of hot spots. Insufficient insulation or inadequate ventilation can lead to overheating and the formation of hot spots, as heat cannot be efficiently dispersed. In some cases, the cells themselves may be poorly designed or manufactured, leading to reduced performance and an increase in the amount of generated heat [8], [9].

To prevent the formation of hot spots, it's necessary to consider the causes of their formation. Regular cleaning of PV panels is essential to prevent hot spots, although it can be inefficient during normal operation. Occasional rain can help in cleaning PV panels. Proper insulation and cooling of PV panels can also help in dispersing heat and preventing overheating, though this affects the cost of the PV system design. In case of shading, the use of bypass diodes is also a possibility. Bypass diodes have become a common component of PV panels, so in such cases, the performance of the PV system is less affected by shading or the failure of a single PV panel. Currently, most panels use three diodes for 60 or 72 PV cells, or one diode for every 20 or 24 PV cells. Bypass diodes are typically calculated for a specific current and voltage. Therefore, they are selected based on the specifications of the specific PV panel in which they are used. They are usually placed on the back of the panel and are designed to be as compact as possible [1], [7].

Hot spots arise due to the heterogeneity of PV modules due to uneven illumination. These undesirable locations can occur due to shadows, dirt, and damage to PV modules, or manufacturing defects. Consequently, temperature increases, leading to decreased efficiency and panel lifespan. Hot spot detection is critical because traditional methods such as thermography are time-consuming and require direct sunlight to create significant temperature differences for accurate detection. Temperature also affects the shape of the V-A characteristics, causing the voltage of the PV module to decrease with increasing temperature. Therefore, if a hot spot occurs during PV system operation, it will primarily manifest as a voltage drop, as shown in *Fig. 1*, where the shaded cell generates lower current, causing a bypass diode to activate and leading to a reduction in the overall output voltage of the string.

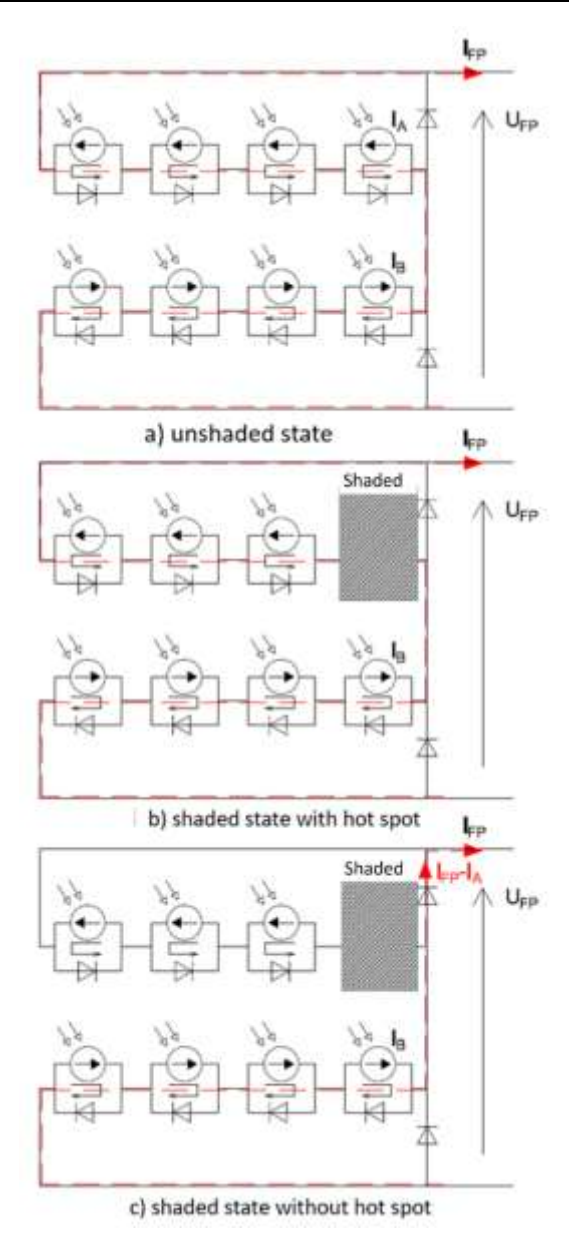


Figure 1: Three scenarios for explaining the hot spots creating

Fig. 1 illustrates and compares three scenarios:

- a) Unshaded state;
- b) Shaded state (one module shaded) with a hot spot;
- c) Shaded state (one module shaded) without a hot spot.

In the unshaded state (a), the PV module operates smoothly, and currents I_A and I_B are equal, both equal to I_{FP} . However, in scenario b), where one module on the PV array is shaded and afflicted with a hot spot, the situation differs. Comparing scenarios b) and c), there is a discrepancy in the value of the generated current I_{FP} . In scenario c), if the PV array did not contain a hot spot, the bypass diode would be activated, allowing current I_B to flow only in the lower part of the circuit. However, in the region affected by the hot spot, the value of the parallel resistor decreases, diverting current to the upper part of the PV array without activating the bypass diode. On the other hand, if one section of the PV array is completely shaded (with a high value of the parallel resistor), the bypass diode reacts, preventing current flow through the upper part. Additionally, if the PV array did not include bypass diodes, the generated current in the entire series section (upper + lower part) would be zero.

3. Evaluation of hot spots areas

Fig. 2 depicts a simulation model consisting of three PV cells connected in series. The second PV cell is shaded (voltage on the voltage-controlled current source is set to 0), and a hot spot is created on this PV cell - the value of the second parallel resistor RP2 is set to 0.01 Ω . As mentioned earlier, the hot spot causes a decrease in the value of the parallel resistance in the branch where the hot spot is located.

The resulting V-A characteristic of the PV array with and without a hot spot is depicted in *Fig. 3*, where the following observations can be made:

- a) The hot spot caused a change in the shape of the V-A characteristic, as evident in *Fig. 3*. This change in shape also manifested in an alteration of the knee shape of the V-A characteristic.
- b) The short-circuit current (I_{SC}) was not reduced by the presence of the hot spot; it remained the same at 10A, similar to the shaded PV array. It means that the short-circuit current remains approximately the same, but the shape of the knee changes, which also causes a shift in the MPP point.
- c) The open-circuit voltage (U_{OC}) decreased from 68.5 V to 67 V, representing a decrease of 2.2% due to the hot spot. In contrast, for the shaded PV array, the U_{OC} decreased from 68.5 V to 45.3 V, a decrease of 34%. These results indicate that in the case of a shaded PV array without a hot spot, the U_{OC} decreases substantially more than in the case of a shaded PV array with a hot spot. If the part where the hot spot appeared were not 100 percent shaded, it is assumed that the open-circuit voltage would decrease less. However, the statement in the first sentence would still hold true.

- d) A load line, depicted in black, intersects the V-A characteristics in all three cases in *Fig. 3*. A voltage drop from 65.4 V (blue curve normal) to 43.6 V (green curve shaded) or to 63 V (red curve hot spot) can be observed.
- e) In the absence of bypass diodes, the current value would be 0A for the shaded PV array (green curve).

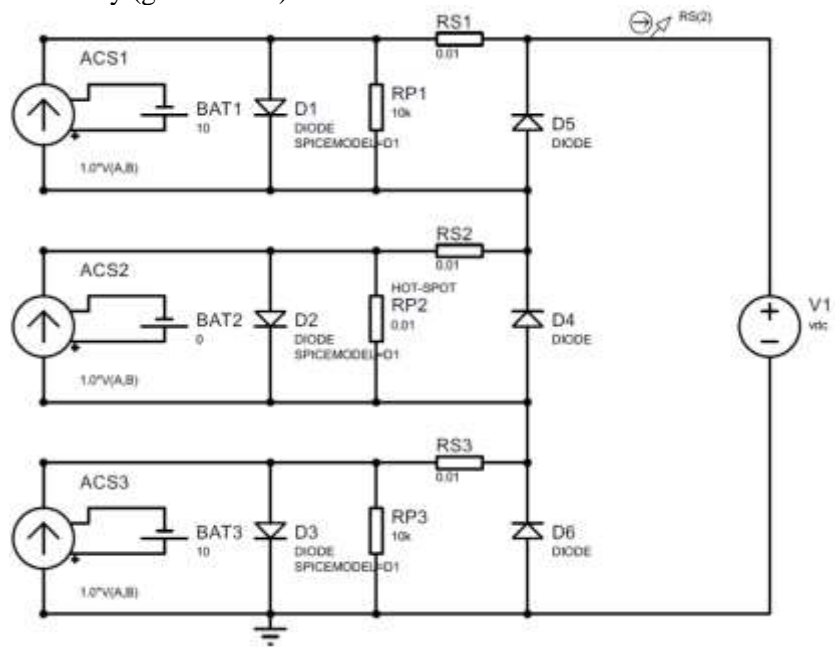


Figure 2: Simulation model for understanding hot spots

From the results shown in Fig. 3, it is observable that there is a greater voltage drop in the shaded PV array compared to the case with a hot spot. Therefore, if a hot spot occurs during the operation of the PV system, it will result in a less significant voltage drop than when that part is shaded. In the case of shading, the shaded part acts as an open circuit, leading to a voltage drop, and the current bypasses this part through the bypass diode.

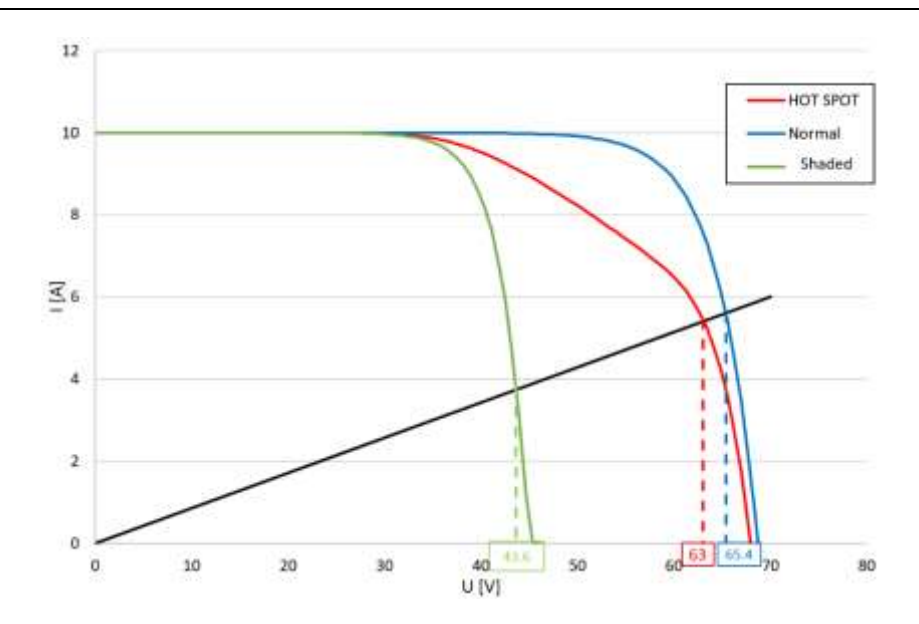


Figure 3: Comparison of V-A characteristics of PV panels – HOT SPOT (red), Normal (blue), and Shaded (green)

Based on the aforementioned, it is possible to measure the voltage on the PV array while gradually shading a certain portion of it. By comparing the voltages, the Hot Spot Index (*HSI*) can be calculated using the formula:

$$HSI = \frac{U_0 - U_1}{U_0} \cdot 100\%, \tag{1}$$

where HSI is the hot spot index, U_0 is the voltage of the PV array without hot spots or other defects, and U_1 is the voltage of the PV array during subsequent measurements. If this procedure is repeated for each part of the PV array, it is possible to identify whether a hot spot has formed on the PV array and also where exactly this hot spot is located on the PV array. In the first step, the first part of the PV array was shaded, which was then connected to the load, and subsequently, the voltage U_1 was measured. Each part of the PV array was gradually shaded, and the voltage U_1 was again measured on the next part of the PV array. The reference value U_0 was the voltage value under the same load, but for the PV array without defects. In this way, measurements were taken for 2 photovoltaic panels, assuming the existence of a hot spot. The photovoltaic panel was divided into 60 parts, each gradually shaded, and the HSI index was calculated step by step.

During this measurement, the intensity of sunlight impacting the PV array during the measurement is not crucial since this measurement falls into the

category of comparative measurements. However, it is important for this value to change as little as possible. To ensure the highest precision of the measurement, the measurements were conducted during the night in a laboratory setting. The photovoltaic panels were illuminated by a projector, which provided a constant illumination value. Additionally, the projector allowed for setting boundaries for the illumination incident on the PV array. After illuminating the photovoltaic panel with the projector, a portion of the PV array was shaded for 10 seconds. After this period, measurements were taken 5 times, and subsequently, the average voltage value U_I and then the HSI index value were calculated.

In Fig. 4 and Fig. 5, the values of the HSI index for each shaded part of the PV array and for both photovoltaic panels are displayed. In the graphs, red columns are marked where the existence of a hot spot is presumed. These red columns exhibited significantly lower values compared to the remaining columns.

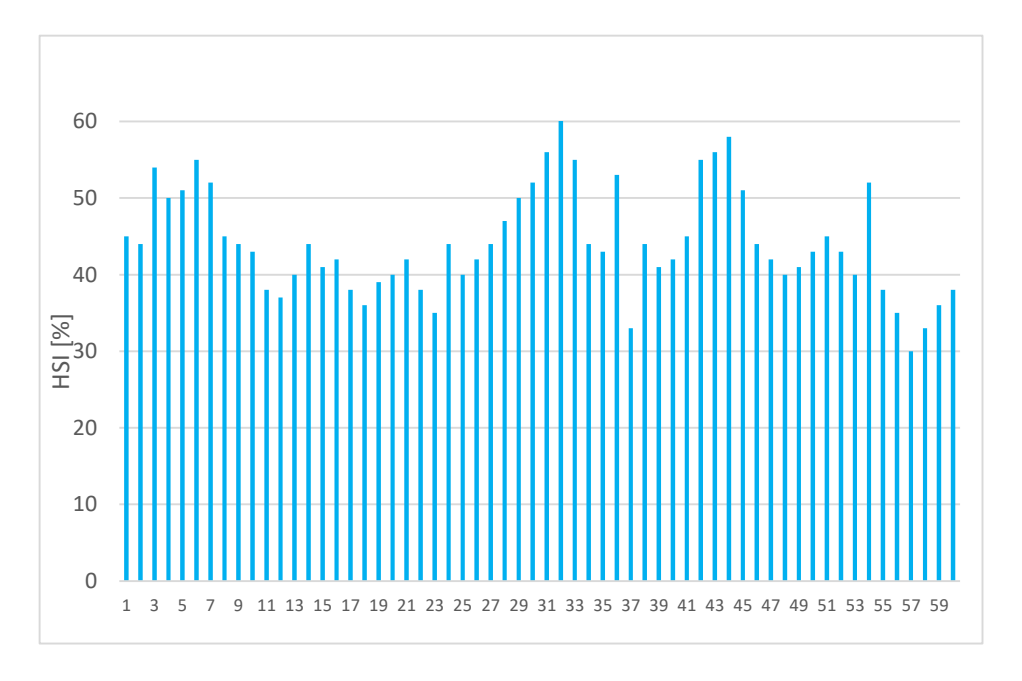


Figure 4: Photovoltaic panel without hot spot

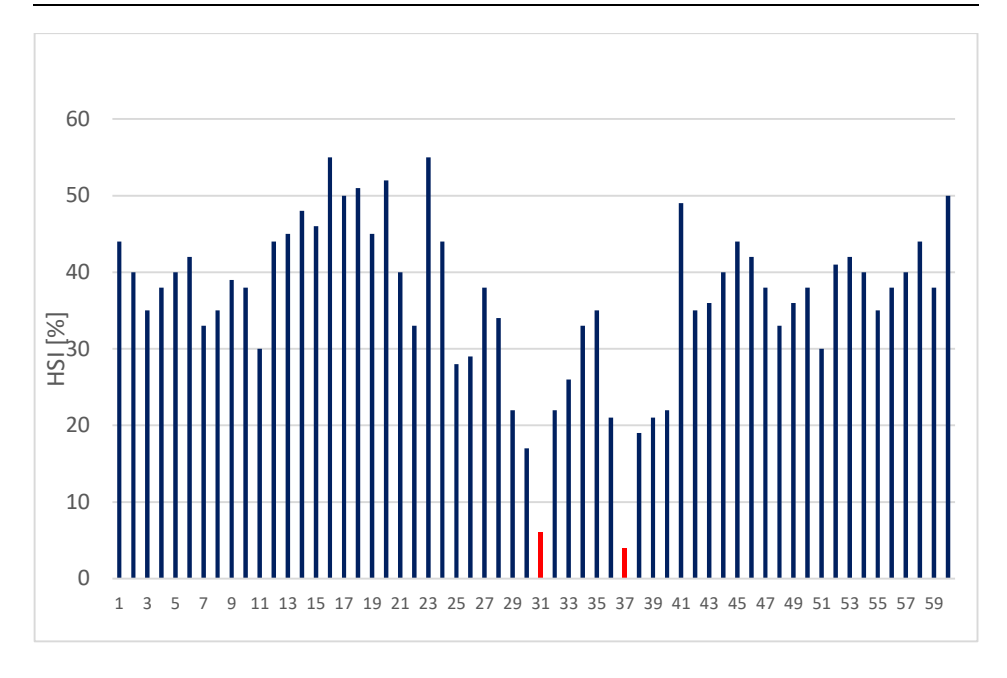


Figure 5: Photovoltaic panel with two hot spot area

In *Fig. 4*, the *HSI* index for the 1st PV panel is depicted, where it can be observed that none of the shaded areas reached markedly lower values than the remaining shaded areas. Therefore, it can be assumed that no hot spot is present on this PV panel. Furthermore, in the case shown in *Fig. 5*, it can be observed that the parts of the PV panel surrounding the area with the hot spot achieve low *HSI* index values. It can be assumed that these surrounding parts are also affected. Therefore, it can be inferred that the occurrence of one "faulty" spot with a hot spot may influence nearby areas with its elevated temperature.

4. Conclusion and discussion

The study examines issues associated with the formation of hot spots on photovoltaic panels. It identifies shading, dust, and manufacturing defects as causes of hot spot formation. A proposed voltage measurement method based on the Hot Spot Index (HSI) enables hot spot identification and localization. Experiments confirm its effectiveness in detection. Additionally, it is revealed that nearby areas are also affected, indicating their potential thermal impact. This proactive approach allows minimizing the adverse effects of hot spots on the performance and lifespan of PV systems. This manuscript emphasizes the importance of identifying and monitoring hot spots on photovoltaic panels. The

proposed *HSI* measurement method has proven to be an effective tool for detecting and locating these issues. The insights gained enable a better understanding of the mechanisms behind hot spot formation and support the implementation of preventive measures to minimize their negative impacts. This analysis contributes to optimizing the performance and longevity of photovoltaic systems.

Acknowledgements

This work was supported by the Slovak Research and Development Agency under contract No. APVV-19-0576 and APVV-21-0312.

References

- [1] Pavlík, M., "Obnoviteľné zdroje energie vo všeobecnosti", 1.vyd. Technická univerzita v Košiciach, 2019. 75 s. ISBN 978-80-553-3317-5.
- [2] Refaat, A., Elgamal, M., and Korovkin, N. V., "A Novel Photovoltaic Current Collector Optimizer to Extract Maximum Power during Partial Shading or Mismatch Conditions", 2019 IEEE Conference of Russian Young Researchers in Electrical and Electronic Engineering (EIConRus), Saint Petersburg and Moscow, Russia, 2019, pp. 407–412, doi: 10.1109/EIConRus.2019.8657173.
- [3] Qian, J., Thomson, A., Blakers, A., and Ernst, M., "Comparison of Half-Cell and Full-Cell Module Hotspot-Induced Temperature by Simulation", in *IEEE Journal of Photovoltaics*, vol. 8, no. 3, pp. 834-839, May 2018, doi: 10.1109/JPHOTOV.2018.2817692.
- [4] Imtiaz, A. M., Khan, F. H., and Kamath, H., "All-in-One Photovoltaic Power System: Features and Challenges Involved in Cell-Level Power Conversion in ac Solar Cells", in *IEEE Industry Applications Magazine*, vol. 19, no. 4, pp. 12–23, July-Aug. 2013, doi: 10.1109/MIAS.2012.2215658.
- [5] Dhimish, M., Holmes, V., Mehrdadi, B., Dales, M., and Mather, P., "Output-Power Enhancement for Hot Spotted Polycrystalline Photovoltaic Solar Cells", in *IEEE Transactions on Device and Materials Reliability*, vol. 18, no. 1, pp. 37–45, March 2018, doi: 10.1109/TDMR.2017.2780224.
- [6] Dhimish, M., Mather, P., and Holmes, V., "Evaluating Power Loss and Performance Ratio of Hot-Spotted Photovoltaic Modules", in *IEEE Transactions on Electron Devices*, vol. 65, no. 12, pp. 5419–5427, Dec. 2018, doi: 10.1109/TED.2018.2877806.
- [7] Winston, D. P., "Efficient Output Power Enhancement and Protection Technique for Hot Spotted Solar Photovoltaic Modules", in *IEEE Transactions on Device and Materials Reliability*, vol. 19, no. 4, pp. 664–670, Dec. 2019, doi: 10.1109/TDMR.2019.2945194.
- [8] Chiriac, G., Nituca, C., Cuciureanu, D. and Murgescu, I., "Analysis of hot-spots effects on the performances of a photovoltaic system used in Romania", 2017 International Conference on Electromechanical and Power Systems (SIELMEN), Iasi, Romania, 2017, pp. 239–244, doi: 10.1109/SIELMEN.2017.8123325.
- [9] Alajmi, M., Awedat, K., Aldeen, M. S., and Alwagdani, S., "IR Thermal Image Analysis: An Efficient Algorithm for Accurate Hot-Spot Fault Detection and Localization in Solar Photovoltaic Systems", 2019 IEEE International Conference on Electro Information Technology (EIT), Brookings, SD, USA, 2019, pp. 162–168, doi: 10.1109/EIT.2019.8833855.



DOI: 10.47745/auseme-2024-0009

The use of WAM Systems for Determining the Ampacity of Overhead Power Lines

František MARGITA¹, Ľubomír BEŇA²

¹ Department of Electric Power Engineering, Faculty of Electrical Engineering and Informatics, Technical University of Košice, e-mail: frantisek.margita@tuke.sk
² Department of Electric Power Engineering, Faculty of Electrical Engineering and Informatics, Technical University of Košice, e-mail: lubomir.bena@tuke.sk

Manuscript received April 19, 2024; revised October 24, 2024

Abstract: This study expands upon previous research by focusing on determining the dynamic thermal rating (DLR) of a specific overhead transmission line. It utilizes real-time data from WAMS (Wide Area Measurement Systems), specifically using PMUs (Phasor Measurement Units). The paper presents a comprehensive overview of thermal evaluations, which are categorized into dynamic (including direct, indirect, transient, and steady state) and static (conventional) rating. Furthermore, the article examines standards that outline principles, technologies, and algorithms for estimating conductor temperature.

Keywords: ACSR, CIGRE 601, PMU, thermal rating, WAMS.

1. Introduction

The ampacity of overhead transmission lines refers to the maximum electrical current they can sustain without compromising their electrical and mechanical integrity. ACSR (Aluminium-conductor steel-reinforced cable) conductors, with aluminum as the main material, are widely used in these lines. Manufacturers specify a maximum operating temperature typically between 90 and110°C. Exceeding this can make the material brittle, reducing its lifespan. Overloading electrical conductors is a common concern in many studies, impacting transmission capacity due to current overload issues [1], [2], [3].

It's crucial to avoid exceeding maximum extension or sag of overhead transmission lines to maintain safe distances from the ground, nearby objects, or other conductors below. Nominal values assigned during design phase set limits on energy transmission to ensure material strength remains intact. Standards specify minimum safe conductor heights for different conditions, prioritizing reliability even under critical circumstances. Factors influencing line ampacity are illustrated in *Fig. 1* [4].

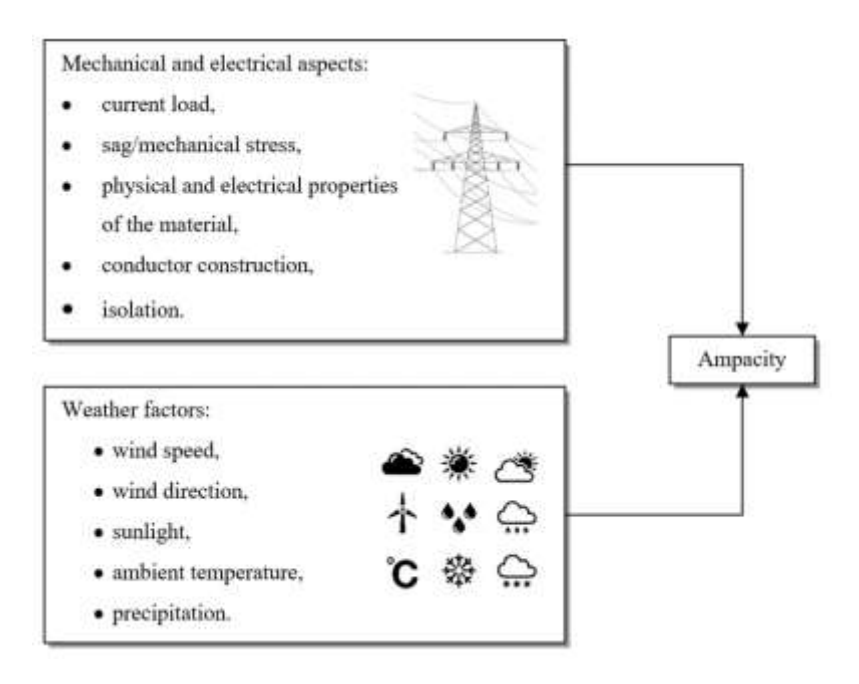


Figure 1: Factors affecting the ampacity of a conductor

2. Evaluation of thermal performance in overhead electrical lines

Ampacity determination involves two main approaches: static and dynamic. Static ampacity, or SLR, uses a probabilistic method, whereas dynamic ampacity, or DLR, is deterministic. DLR methods can be direct or indirect. Long line ampacity often relies on stability limits or voltage constraints, whereas short lines are limited by temperature [5].

A. Static line rating

In SLR, electrical grids assume constant conductor ampacity, regardless of season, with a conservative estimate focusing on theoretical rather than actual values [6]. SLR is computed utilizing a thermal model that relies on the thermal equilibrium of the bare conductor, assuming low perpendicular wind speeds (e.g., 0.5 m/s), seasonal air temperatures nearing peak values (e.g., 35 C or higher in

summer), and full solar heating (e.g., 1000 W/m^2), as outlined in CIGRE Technical Brochure 299 [7].

Meteorological conditions for SLR assessment can vary depending on the region's environment and energy companies' risk tolerance. Each transmission line may have different standard thermal ratings, including normal (continuous), long-term emergency, and short-term emergency ratings [8].

B. Dynamic line rating

DLR adjusts ampacity in real-time to match environmental changes, aiming to maximize current loading. Thermal ampacity of overhead lines fluctuates due to heating and cooling processes. Cooling effects like wind or lower temperatures can increase thermal ampacity, allowing for greater power transmission [4].

C. Indirect dynamic line rating

In DLR, transmission line ampacity dynamically adjusts based on environmental factors like ambient temperature, wind speed, solar radiation, etc. Indirect methods, known as weather-dependent line rating, use meteorological data collected along the line for evaluation. This includes inputs from weather sensors positioned along the line to assess the conductor's thermal balance equation, forming the basis for computations in DLR systems. [5].

D. Direct dynamic line rating

The direct method of DLR involves measuring electrical line properties like conductor temperature, mechanical stress, and sag. Additional data from a weather monitoring system is typically included in line evaluation. Various approaches have been proposed for estimating DLR of overhead transmission lines [5].

E. Steady-state dynamic line rating

The temperature of the conductor will stabilize at different values depending on the current. Therefore, the steady-state dynamic ampacity refers to the current level at which the conductor temperature reaches a stable equilibrium. This calculation deals with the stable temperature of the conductor before or after a transient event caused by parameter changes. The steady-state solution aims to find the stable conductor temperature with a known current and constant climate conditions [9].

F. Transient dynamic line rating

A conductor with a specified thermal ampacity can handle short-term current overload to avoid exceeding the maximum allowed temperature. This temporary overload is called transient dynamic ampacity and is limited in duration. This approach focuses on tracking changes in conductor temperature over time, accounting for variations in operating factors like climate conditions and current flow [9].

3. Thermal assessments of overhead electrical lines constructed in compliance with specified standards

CIGRE and IEEE offer guidelines for predicting ampacity and conductor temperature. Both methods assess thermal equilibrium considering factors like load and environmental conditions, focusing on heat absorption and dissipation in the conductor [10].

The initial CIGRE method computes conductor temperature in steady-state (1), while the following one employs dynamic equilibrium, considering the conductor's thermal inertia (2) [10]:

$$P_{c} + P_{r} = P_{S} + P_{i} + P_{m}, \tag{1}$$

where:

- P_c represents specific cooling power due to convection (W/m);
- P_r represents specific cooling power due to radiation to the surroundings (W/m);
- P_S represents specific heating power due to solar radiation (W/m);
- P_j represents specific heating power due to Joule effect (W/m);
- $P_{\rm m}$ represents the specific magnetic heating power in a conductor, caused by the interaction of the current with the magnetic field it generates, this results in additional resistive losses, particularly in steel-cored conductors like ACSR, due to effects such as the transformer effect and current redistribution in the conductor layers (W/m).

When considering the thermal inertia of the conductor, the following dynamic thermal balance (2) is used instead of the equation (1) [10]:

$$m \cdot c \cdot \frac{\mathrm{d}T_c}{\mathrm{d}t} = P_s + P_j + P_m - P_c - P_r,\tag{2}$$

where:

- m is the mass per unit length of the conductor (kg/m);
- c is the specific heat capacity of the conductor $(J/(kg \cdot K))$;
- T_c is the temperature of the conductor (°C).

The thermal balance at steady-state, according to IEEE Standard 738, is expressed by equation [11]:

$$P_{\rm r} + P_{\rm c} = P_{\rm S} + P_{\rm J},\tag{3}$$

where [11]:

- P_r represents specific cooling power due to radiation to the surroundings (W/m);
- $P_{\rm c}$ represents specific cooling power due to convection (W/m);
- $P_{\rm S}$ represents specific heating power due to solar radiation (W/m);
- $P_{\rm J}$ represents specific heating power due to the Joule effect (W/m).

The IEEE method refines the heat balance calculation by removing terms that contribute negligibly to the determination of ampacity ratings. One such term is magnetic heating, which is excluded because its effect is typically minimal in most practical scenarios. Hence, the thermal balance equation (3) can be visually illustrated in *Fig.2* [11].

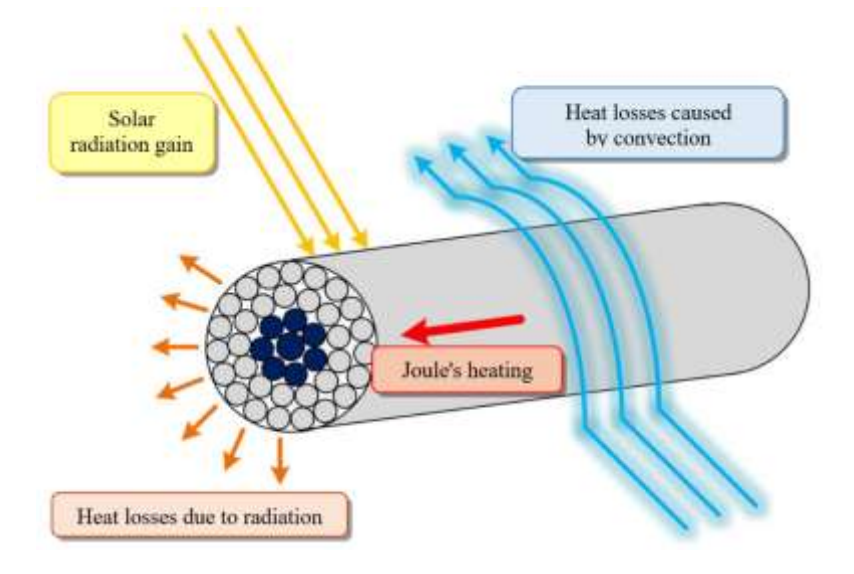


Figure 2: The thermal equilibrium of an overhead conductor as per IEEE 738

4. Tracking operational parameters through WAMS

Rising electricity consumption and energy system changes pose new challenges for operation and monitoring. SCADA alone isn't enough for ensuring system security and stability. It can't measure data from all buses simultaneously and lacks sufficient sampling frequency for some applications, resulting in inaccuracies in representing energy system dynamics [12].

New measurement technologies enable energy systems to autonomously analyze and adjust transmission capacities, potentially leveraging WAMS for optimal performance. This influences overhead lines by controlling temperatures and facilitating more flexible energy transfer [13].

WAMS improves energy system monitoring by addressing SCADA system limitations. Its main component, PMUs handles data collection, transmission, and analysis. WAMS receives data via high-speed links, processes it, extracts insights, and makes decisions to enhance system performance [12].

Fig. 3 represents the basic structure of WAMS. The WAMS structure includes the following infrastructures [12]:

- 1. PMU, strategically installed in the grid;
- 2. synchronization system, providing a concurrent image of system variables, event consequences, and operating state synchronizing PMU sampling frequency/time for data collection and transmission;
- 3. data communication system, ensuring speed, reliability, and security for transmission:
- 4. data collection and analysis center, containing qualified software for data analysis.

Phasor data enables instant determination of energy flow in lines and assessment of their loading status. Implementing PMUs allows for real-time load determination based on actual current and weather conditions, enabling increased power transmission under specific requirements. DLR methods can be achieved in two ways [12]:

- 1. Based on climatic conditions such as temperature, solar radiation, and wind speed, as well as data about conductors;
- 2. A method to calculate DLR current using only voltage and current measurements from both ends of the line, without external ambient inputs, by estimating instantaneous temperature from line parameter variations. Steady-state conductor temperature is determined, the rated current is then derived via curve fitting of dissipated power against conductor current.

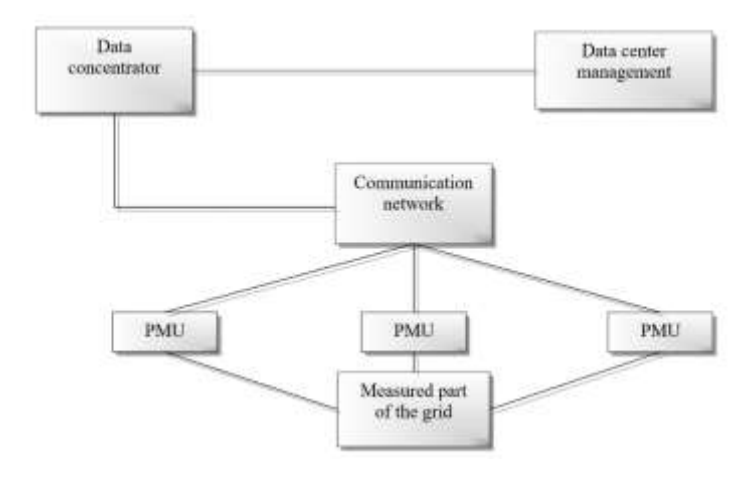


Figure 3: Principle diagram of WAMS

5. Design and practical implementation of the solution of the thermal model of the conductor

Generally, there are three models of the overhead lines: electrical, thermal, and mechanical. Despite being influenced by external variables, they also correlate with each other, as shown in *Fig. 4* [14], [15].

We begin by considering an equivalent Π circuit for the transmission overhead line. *Fig.* 5 depicts the schematic diagram with voltage and current specifications. Here, the longitudinal impedance is concentrated between the line's start and end, whereas the transverse admittance is evenly divided at both ends [16], [17], [18].

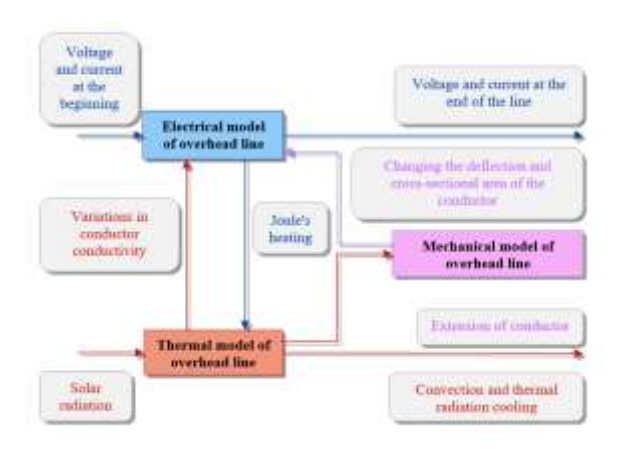


Figure 4: Models of the overhead transmission lines

As described in [17], the following parameters are used:

- V_1, V_2 represent the positive sequence voltage phasor at PMU bus 1 and 2,
- $\underline{I}_1, \underline{I}_2$ represent the positive sequence current phasor at PMU bus 1 and 2.
- Z represents the longitudinal impedance (Ω) ,
- Y_1, Y_2 represents the transverse admittance (S).

The studied phase conductor in Slovakia is the commonly used 352-AL1/59-ST1A conductor, with its basic parameters listed in *Table 1* [19].

According to the CIGRE Technical Brochure 601, the influence of magnetic heating can be disregarded because the 352-AL1/59-ST1A conductor contains two aluminum layers. This implies that in such a case, the effect of magnetic heating is negligible.

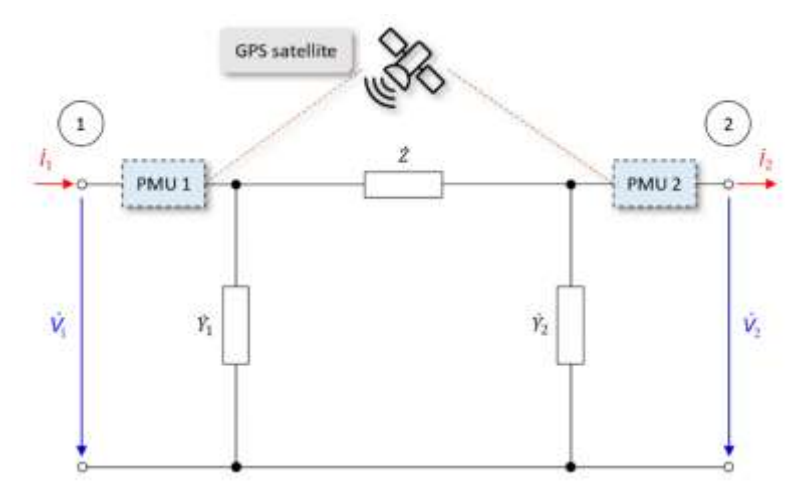


Figure 5: Equivalent circuit diagram of a transmission line using a Π -section grid

The data analyzed in this article was provided by SEPS (Slovenská elektrizačná prenosová sústava, a.s.). The data were collected from two phasor measurement units deployed at different locations within the transmission power system. PMU No. 1 was located at substation RSOB-V427-PMU1, whereas PMU No. 2 was located at substation MOLD-V427-PMU1. The PMUs were synchronized with GPS and sampled voltage and current phasors at a frequency of 1 sample per second. PMUs directly measure the phase angle (θ_{U1} , θ_{U2} , θ_{I1} , θ_{I2}) of voltage and current, offering real-time visibility of their phases. As a result, phases can be determined using time-synchronized voltage phase angle measurements.

The data were collected on November 25, 2021. The output after basic data processing is visualized in *Table 2* and *Table 3*.

Table 1: The technical specification of conductor 352-AL1/59-ST1A (350 ACSR 6)

Type of conductor	Conductor diameter (mm)	Diameter of the aluminum wire in the aluminum conductor (mm)	Electrical resistance of the conductor (Ω/km)	Thermal coefficient of resistance (K-1)	The absorptivity of the surface of the conductor (-)	Emissivity coefficient of conductor surface (-)
352- AL1/59- ST1A	26.50	4.00	0.0816	4.03·10 ⁻³	0.50	0.50

Table 2: Data sample obtained from PMU station RSOB-V427-PMU1

Time – (CET)	f	A _{U1} (V)	θυ1 (°)	A ₁₁ (A)	θ ₁₁ (°)
0:00:00	49.9833	414574	100	455	111
0:00:01	49.9804	414557	94	455	104
0:00:02	49.9786	414378	86	455	97
0:00:03	49.9764	414152	78	460	89
0:00:04	49.9744	414109	69	463	80

Table 3: Data sample obtained from PMU station MOLD-V427-PMU1

Time – (CET)	f	Av1 (V)	θυ1 (°)	An (A)	θn (°)
0:00:00	49.9833	412863	103	470	-58
0:00:01	49.9804	412815	96	469	-65
0:00:02	49.9786	412637	89	470	-72
0:00:03	49.9764	412405	81	475	-80
0:00:04	49.9744	412380	72	477	-89

The temperature of the conductor can be monitored through insights from the electrical model of the overhead transmission line (Fig. 5). PMUs installed at

both terminals enable obtaining phase currents and voltages from both ends of the transmission system. Telegrapher's equations can be used to explain the relationship between the positive sequence current and voltage signals [14]:

$$\underline{V}_{1} = \frac{\underline{V}_{2} - \underline{I}_{2} \cdot \underline{Z}_{c} \left(T_{c}\right)}{2} e^{\dot{\gamma}\left(T_{c}\right) \cdot l\left(T_{c}\right)} + \frac{\underline{V}_{2} + \underline{I}_{2} \cdot \underline{Z}_{c} \left(T_{c}\right)}{2} e^{-\dot{\gamma}\left(T_{c}\right) \cdot l\left(T_{c}\right)},\tag{4}$$

$$\underline{I}_{1} = \frac{\underline{V}_{2} / \underline{Z}_{c} (T_{c}) - \underline{I}_{2}}{2} e^{\dot{\gamma}(T_{c})l(T_{c})} - \frac{\underline{V}_{2} / \underline{Z}_{c} (T_{c}) + \underline{I}_{2}}{2} e^{-\dot{\gamma}(T_{c}) \cdot l(T_{c})},$$
(5)

At the given conductor temperature T_c [15, 16]:

- $\underline{Z}_{c}(T_{c})$ represents the wave impedance of the conductor (Ω) ;
- $\gamma(T_c)$ represents the wave propagation coefficient (1/km);
- $l(T_c)$ represents the length of the transmission line (km).

After deriving the telegraph equations (4) and (5), it is possible to find formulas for the variables $\underline{Z}_{c}(T_{c})$ and $\gamma(T_{c}) \cdot l(T_{c})$, [20]:

$$\underline{Z}_{c}(T_{c}) = \sqrt{\frac{\underline{V}_{1}^{2} - \underline{V}_{2}^{2}}{\underline{I}_{1}^{2} - \underline{I}_{2}^{2}}},$$
(6)

$$l(T_{v})\cdot\dot{\gamma}(T_{v}) = \ln\left(\frac{\dot{V}_{1} + \dot{Z}_{v}(T_{v})\dot{I}_{1}}{\dot{V}_{2} - \dot{Z}_{v}(T_{v})\dot{I}_{2}}\right). \tag{7}$$

Equations (6) and (7) are used to calculate the series impedance and resistance of the line [20]. The average value of the series impedance is 28.897Ω :

$$\underline{Z}(T_{c}) = \underline{Z}_{c}(T_{c}) \cdot \gamma(T_{c}) \cdot l(T_{c}), \qquad (8)$$

$$R_{\rm AC}(T_{\rm c}) = \text{Re}\left(\underline{Z}(T_{\rm c})\right). \tag{9}$$

The actual temperature of the conductor, and thus its resistance, which changes linearly with temperature, is significantly and complexly dependent on its load current and the prevailing meteorological conditions on the line. The resistance of the series line can also be expressed relative to its reference value, as indicated below [20], [21]:

$$R_{\rm AC}(T_{\rm c}) = R_{\rm REF} \cdot (1 + \beta \cdot (T_{\rm c} - T_{\rm REF})), \tag{10}$$

represented by variables [22]:

- 1. R_{AC} series AC (alternating current) resistance of the conductor at the given conductor temperature (Ω/m),
- 2. R_{REF} series AC resistance of the conductor, including skin effect, at the reference temperature, i.e., 20 °C (Ω /m),
- 3. β temperature coefficient of the conductor's resistance (1/K⁻¹),
- 4. T_c conductor temperature (${}^{\circ}$ C),
- 5. T_{RFF} reference conductor temperature, i.e., 20 °C.

Some ACSR conductors, such as those used in other countries, may have both the DC resistance per unit length at 20 °C and the AC resistance per unit length at 25 °C and 75 °C specified, such as the Drake conductor [9].

Finally, by modifying equation (10) for the series resistance of the conductor at a given temperature, the conductor temperature is determined by the relationship [21], [23]:

$$T_{\rm c} = T_{\rm REF} + \left[\frac{R_{\rm AC}(T_{\rm c})}{R_{\rm REF}} - 1 \right] \cdot \beta^{-1}. \tag{11}$$

The algorithm's key challenge lies in selecting T_{REF} , R_{AC} , and β , which directly affect conductor temperature accuracy. β , the temperature coefficient of the conductor's resistance, is typically obtained from literature. R_{AC} can be calculated using established methods or estimated using PMU data if the conductor length at T_{REF} is known. R_{REF} aids in calculating the AC resistance of the series transmission line per unit length [21].

Accuracy of this method depends heavily on the precision of voltage and current transformers, as discussed in [24]. Voltage transformers usually have a consistent level of inaccuracy, while current transformers can introduce significant errors, especially at low currents. Error correction methods, as discussed in [21], can be applied to mitigate these issues.

Authors [9], [22], and manuals (Stredoslovenská energetika, elektrika.cz) offer varied values for R_{REF} in the conductor's technical specification. Even a slight deviation can greatly affect the algorithm. As a heuristic approach, we considered $R_{\text{REF}} = 0.0085 \,\Omega/\text{km}$ in the algorithm. Fig.~6 depicts the temperature changes in the conductor over time (red line), calculated from PMU data, with load conditions set to I_1 (blue line).

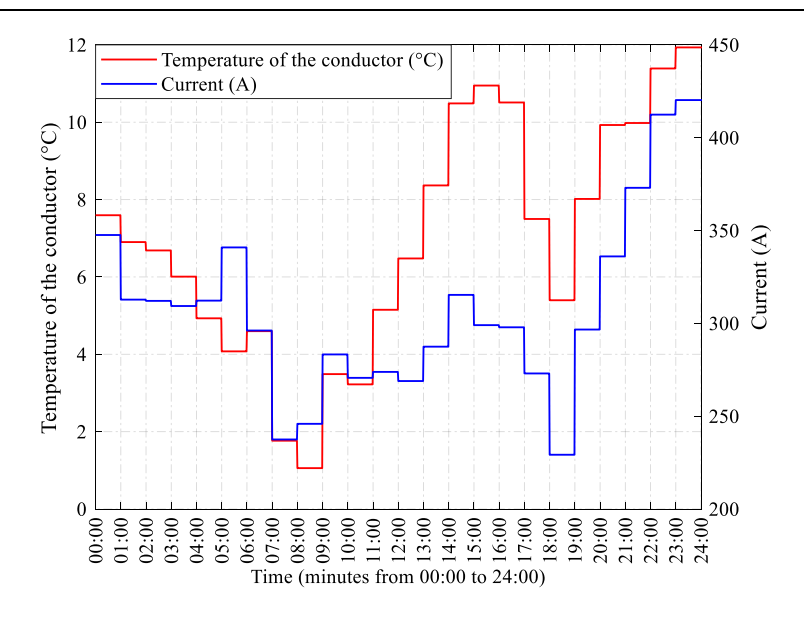


Figure 6: Conductor temperature at AC series line resistance at reference value R_{ref} based on equation (11)

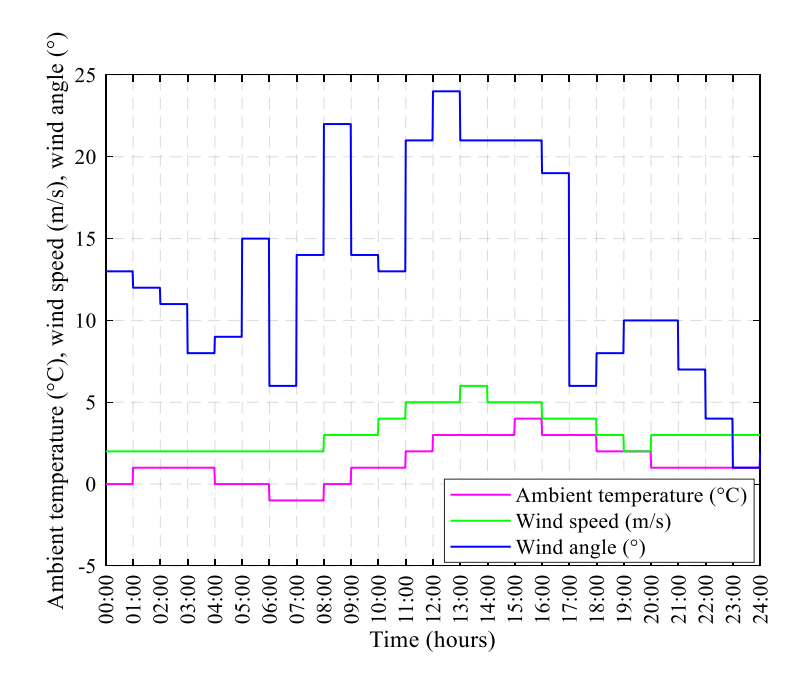


Figure 7: Meteorological conditions for the given measurement day in the transmission line region

Conclusion

In the study conducted, the focus was on examining ACSR conductor temperatures in overhead transmission lines, emphasizing the critical importance of adhering to specified temperature limits for maintaining material integrity. The significance of adhering to ampacity and sag constraints for ensuring line safety and reliability was emphasized.

Standards established by organizations such as CIGRE and IEEE were highlighted for estimating ampacity and conductor temperature. These standards employ heat balance equations that consider loading and environmental factors. Both static and dynamic approaches to ampacity determination were discussed, as they are crucial for ensuring safe line operation.

The study also delved into the role of WAMS in conductor temperature calculation and ampacity assessment. By utilizing PMU technology, WAMS enables efficient calculation of conductor temperature, surpassing the limitations of SCADA systems for informed decision-making.

Through the infrastructure provided by WAMS, conductor temperature can be computed without the need for external devices, ensuring real-time monitoring and accurate data for line optimization. The ability to calculate temperature at one-second intervals allows for timely monitoring of line conditions, which is essential for achieving optimal operation.

Acknowledgements

This work was supported by the Slovak Research and Development Agency under contracts No. APVV-19-0576 and APVV-21-0312.

References

- [1] Beňa, Ľ., Kolcun, M., Medveď, D., Pavlík, M., Čonka, Z., Király, J., "The influence of climatic conditions on the dynamic ampacity of external lines", *Elektroenergetika*, vol. 15, no. 2, pp. 47, 2022.
- [2] Kladar, D., "Dynamic Line Rating in the world Overview", 2014.
- [3] Pijarski, P., and Kacejko, P., "Elimination of Line Overloads in a Power System Saturated with Renewable Energy Sources", *Energies*, vol. 16, no. 9, pp. 3751, 2023, DOI: 10.3390/en16093751.
- [4] IRENA, "System Operation: Innovation Landscape Briefs", 2020, pp. 1–20.
- [5] Karimi, S., Musilek, P., Knight, A. M., "Dynamic thermal rating of transmission lines: A review", *Renewable and Sustainable Energy Reviews*, vol. 91, pp. 600-612, 2018, DOI: 10.1016/j.rser.2018.04.001.
- [6] Simms, M., Meegahapola, L., "Comparative analysis of dynamic line rating models and feasibility to minimise energy losses in wind rich power networks", *Energy Conversion and Management*, vol. 75, pp. 11–20, 2013, DOI: 10.1016/j.enconman.2013.06.003.

- [7] Working Group B2.43, "Guide for thermal rating calculation of overhead lines, Technical Brochure 601", 2014.
- [8] Douglass, D. A., et al., "A Review of Dynamic Thermal Line Rating Methods with Forecasting", *IEEE Transactions on Power Delivery*, vol. 34, no. 6, pp. 2100–2109, 2019, DOI: 10.1109/TPWRD.2019.2932054.
- [9] Margitová, A., "Increasing the transmission capacity of external power lines by calculating the dynamic ampacity", PhD Thesis, TUKE, Košice, 2021.
- [10] Arroyo, A., Castro, P. Martinez, R. Manana, M. Madrazo, A. Lecuna, R. Gonzalez, A., "Comparison between IEEE and CIGRE Thermal Behaviour Standards and Measured Temperature on a 132-kV Overhead Power Line," *Energies*, vol. 8, no. 12, pp. 13660–13671, 2015, DOI: 10.3390/en81212391.
- [11] Karunarathne, E., Wijethunge, A., Ekanayake, J., "Enhancing PV Hosting Capacity Using Voltage Control and Employing Dynamic Line Rating", *Energies*, vol. 15, p. 134, 2022, DOI: 10.3390/en15010134.
- [12] Kacejko, P., Pijarski, P., "Dynamic fitting of generation level to thermal capacity of overhead lines", *Przeglad Elektrotechniczny*, vol. 84, pp. 80–83, 2008.
- [13] Bashian, A., Assili, M., Anvari-Moghaddam, A., Catalão, J.P.S., "Optimal Design of a Wide Area Measurement System Using Hybrid Wireless Sensors and Phasor Measurement Units", *Electronics*, vol. 8, p. 1085, 2019, DOI: 10.3390/electronics8101085.
- [14] Mai, R., Fu, L., Xu, HaiBo, "Dynamic Line Rating estimator with synchronized phasor measurement", *International Conference on Advanced Power System Automation and Protection*, Beijing, China, pp. 940–945, 2011, DOI: 10.1109/APAP.2011.6180545.
- [15] Giannuzzi, G. M., Pisani, C., Vaccaro, A., Villacci, D., "Overhead transmission lines dynamic line rating estimation in WAMS environments", *International Conference on Clean Electrical Power (ICCEP)*, Taormina, Italy, pp. 165–169, 2015, DOI: 10.1109/ICCEP.2015.7177618.
- [16] Štieberová, N., Beňa, L., Margitová, A., Kanálik, M., "Calculation of parameters related to the dynamic ampacity of external lines", *Electrical Engineering and Informatics XI*, vol. 11, no. 1, pp. 380–385, 2020.
- [17] Kubek, P., Siwy, E., "Analysis methods of HTLS conductors in terms of mechanical and thermal criteria", *Acta Energetica Power Engineering Quarterly*, vol. 1, no. 14, pp. 75-82, 2013. DOI: 10.12736/issn.2300–3022.2013107.
- [18] Pavlinić, A., Komen, V., "Direct monitoring methods of overhead line conductor temperature", *Engineering Review*, vol. 37, pp. 134–146, 2017.
- [19] Kanalik, M., Margitová, A., Beňa, L., "Temperature calculation of overhead power line conductors based on CIGRE Technical Brochure 601 in Slovakia", *Electrical Engineering*, vol. 101, 2019, DOI: 10.1007/s00202-019-00831-8.
- [20] Popelka, A., Jurik, D., Marvan, P., "Actual line ampacity rating using PMU", *CIRED*, Frankfurt, Germany, pp. 1–4, 2011.



DOI: 10.47745/auseme-2024-0010

Adaptive Digital Notch Filter for Enhanced Stability in Grid-Connected Inverter Systems

Mohammed Moyed AHMED¹

¹ Department of ECE, JNTU, Hyderabad, INDIA, e-mail: mmoyed@gmail.com

Manuscript received, September 29, 2024; revised October 28, 2024

Abstract: Grid-connected inverters with LCL filters are crucial components in renewable energy systems, but they face stability challenges due to varying grid impedances and resonant frequencies. This paper presents a novel adaptive digital notch filter designed to enhance the stability of such systems across a wide range of operating conditions. The proposed filter employs a three-step adaptive mechanism: resonance detection, determination of resonant frequency change direction, and dynamic notch frequency adjustment. A comprehensive stability analysis in the z-plane reveals the behavior of the resonant pole under different scenarios, informing the filter's design. The adaptive filter's performance was evaluated through simulations. Results demonstrate significant improvements in system stability compared to conventional fixed-frequency notch filters. In scenarios where the resonant frequency was lower than the initial notch frequency, the adaptive filter prevented current divergence and reduced the line current harmonic magnitude at the resonant frequency by up to 75%. In scenarios where the resonant frequency was higher than the notch frequency, the proposed filter successfully suppressed current oscillations, maintaining stability where conventional filters failed. The adaptive mechanism responded to instability within 2 ms, adjusting the notch frequency to optimal levels within 10 ms. This research contributes to the advancement of grid-connected power electronics, offering a robust solution that can enhance the reliability and efficiency of renewable energy integration by up to 30% under varying grid conditions.

Keywords: Adaptive digital notch filter, system stability, resonance mitigation, power electronics, renewable energy integration, single phase inverter grid.

1. Introduction

The rapid expansion of renewable energy sources has led to a significant increase in the number of renewable power generators connected to the electrical grid. This transition towards cleaner energy, while promising, has introduced new challenges in maintaining grid stability and power quality [1]. Grid-connected

inverters play a crucial role in integrating these renewable energy sources with the existing power infrastructure. However, when these inverters are disconnected from the grid due to shut-off operations, a sudden imbalance between power supply and demand can occur, resulting in voltage and frequency fluctuations that deteriorate overall system quality. This impact becomes more pronounced as the grid's reliance on renewable energy sources increases [2].

A particular concern arises with the widespread use of LCL (Inductor-Capacitor-Inductor) filters in grid-connected inverters. While these filters offer superior harmonic suppression compared to traditional L filters [3], they introduce resonance issues that can potentially destabilize the system. In extreme cases, fluctuations in system impedance can cause large-scale inverter disconnections, potentially resulting in widespread power outages [4]. Given these challenges, it is imperative that grid-connected inverters maintain stability and continue to supply energy reliably, even in the face of grid impedance fluctuations.

This paper proposes an adaptive digital notch filter for single-phase grid-tied inverters controlling inverter-side current. The proposed solution aims to maintain system stability even under fluctuating system impedance conditions by detecting resonance in real-time and rapidly stabilizing the system through dynamic adjustment of the notch frequency. The adaptive notch filter has been designed and tested through simulations, for a 3 kW single-phase grid-connected inverter, demonstrating its effectiveness in maintaining system stability under various operating conditions.

2. Related Research

Researchers have explored various stabilization techniques for LCL filter-based inverters, broadly categorized into passive damping and active damping approaches. Passive damping involves inserting a resistor into the LCL filter to reduce system resonance. While straightforward to design, this method has the disadvantage of increasing power losses in the system [5]. Active damping techniques, on the other hand, aim to stabilize the system without incurring additional losses.

Several active damping approaches have been proposed in the literature. The virtual resistance technique adds a capacitor current feedback loop to simulate the presence of a real resistor in the system. However, it requires additional sensors, which can increase system complexity and cost [6]. Another approach stabilizes the system through simple gain adjustments, taking into account the time delays inherent in digital controllers. While easy to implement, its application is limited by the ratio of resonant frequency to sampling frequency [7].

112 M. M. Ahmed

Notch filter-based techniques have also been explored, using notch filters to suppress system resonance by matching the notch frequency to the system's resonant frequency. These methods are relatively simple to design but can become ineffective when system parameters fluctuate [6], [7]. To address the limitations of fixed notch filters, researchers have proposed various techniques for real-time system impedance estimation, including methods based on Digital Fourier Transform (DFT) [8], [9] and Recursive Least Square (RLS) algorithms [10], [11]. However, these methods often suffer from limitations such as high computational complexity or the inability to operate during inverter operation.

The adaptive digital notch filter proposed in this paper builds upon and extends the work of these previous studies. By addressing the limitations of existing techniques, particularly in dealing with system parameter fluctuations, this study aims to contribute to the development of more robust and reliable grid-connected inverter systems for renewable energy applications. The proposed solution offers real-time detection of resonance caused by changes in system resonant frequency due to parameter fluctuations and provides rapid system stabilization by dynamically adjusting the notch frequency based on the direction of resonant frequency changes.

3. Methodology

A. Grid-connected Inverter System and Grid-connected System Model

The grid-connected inverter system under study (*Fig. 1*) consists of a grid-tied inverter coupled with an LCL filter. This configuration is crucial for harmonics suppression but introduces challenges in system stability, particularly when digital controllers are employed. The use of digital controllers, while offering precise control, introduces time delays that can significantly impact the system's stability, especially in the high-frequency domain. These delays, including ADC sampling, computation time, and PWM update periods, can have substantial effects on the high-frequency response characteristics. Consequently, when using LCL filters, it is imperative to account for these time delays to accurately determine system stability in the high-frequency region.

The system's signal processing can be conceptualized as a continuous block divided into continuous and digital subsystems (Fig. 2). The process begins with the feedback of the inverter current $I_i(s)$, which is converted to a digital signal $I_i(z)$ through an analog-to-digital converter (ADC). This digital signal is then compared with the reference signal $I_i^*(z)$, and the resulting error is processed by the controller C(z). Finally, the control signal is converted back into a continuous signal via a Pulse Width Modulation (PWM) converter.

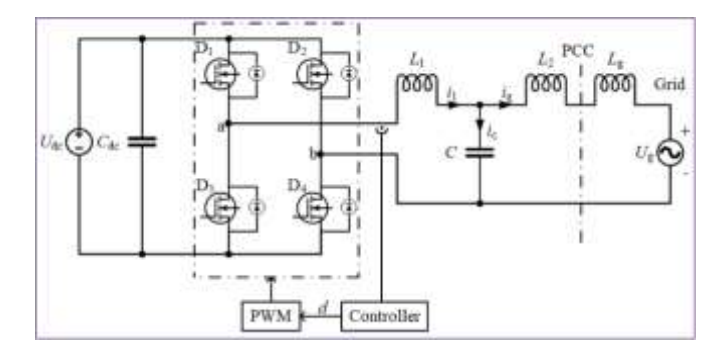


Figure 1: System diagram LCL filter, inverter and grid

In this model, the PWM converter effectively acts as a digital-to-analog converter (DAC), transforming the digital control signal into an analog form. The PWM process can be represented as a combination of a Zero-Order Hold (ZOH) and a total delay component e^{-sT_s} , where T_s is the sampling period. This delay accounts for the time required for ADC conversion, computation, and PWM generation within each sampling cycle.

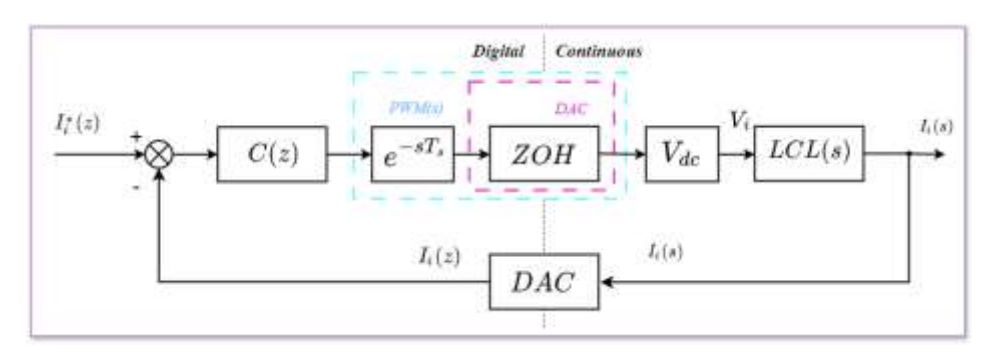


Figure 2: Control signal generation for inverter control

The controller C(z) is implemented by converting two key components from the continuous to the discrete domain: a Proportional-Resonant (PR) controller PR(s) and a notch filter Notch(s). The transfer functions for these components are given by:

$$PR(s) = K_p + K_i \frac{2\omega_d s}{s^2 + 2\omega_d s + \omega_c^2}, \qquad (1)$$

$$PR(s) = K_p + K_i \frac{2\omega_d s}{s^2 + 2\omega_d s + \omega_c^2}, \qquad (1)$$

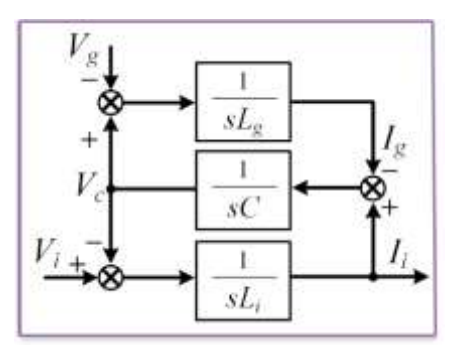
$$Notch(s) = \frac{s^2 + \omega_n^2}{s^2 + \frac{\omega_n}{Q} s + \omega_n^2}. \qquad (2)$$

The PR controller is designed to track the fundamental grid frequency component, with zero steady-state error. The PR controller's resonant frequency 114 M. M. Ahmed

 ω_c is typically set to match the grid frequency ω_g . This design allows for a significant gain increase at ω_c , effectively enabling precise current tracking at the grid frequency.

The notch filter is designed to greatly reduce the gain at its notch frequency ω_n . By aligning ω_n with the resonant frequency of the LCL filter, the filter can effectively cancel out the LCL filter's resonant peak, thereby stabilizing the system. The implementation of these controllers and filters in the digital domain requires careful consideration of the z-transform method. While the Tustin technique is commonly used in power electronics applications due to its excellent frequency characteristic reproduction, it can lead to frequency warping when applied to notch filters, especially when the notch frequency approaches the Nyquist frequency. To mitigate this issue, a pre-warping technique is employed for the notch filter conversion, ensuring accurate representation of the desired notch frequency in the digital domain.

The LCL filter's transfer function from inverter output voltage to line current, with the grid voltage V_g acting as a disturbance input, can be represented as a block diagram (Fig. 3). The grid voltage disturbance cannot be directly controlled and can adversely affect the inverter current I_i . The PR controller's high gain at the grid frequency effectively reduces this disturbance impact, simplifying system analysis and improving current quality.



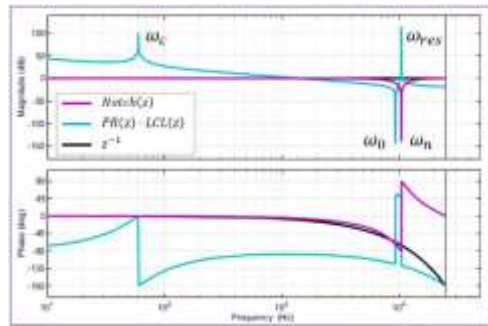


Figure 3: LCL Filter Block diagram

Figure 4: Bode diagram showing the frequency responses of a notch filter, Proportional-Resonant controller, and LCL filter

The transfer function LCL(s) is expressed as:

$$LCL(s) \approx \frac{1}{L_1 L_2 C s^3 + (L_1 + L_2) s}$$
 (3)

The resonant frequency ω_{res} and the characteristic frequency ω_0 are expressed as:

$$\omega_{res} = \sqrt{\frac{L_1 + L_2}{L_1 L_2 C}} , \qquad (4)$$

$$\omega_0 = \frac{1}{\sqrt{L_1 C}} \quad . \tag{5}$$

This comprehensive model of the grid-connected inverter system, incorporating the LCL filter dynamics, digital control effects, and the interaction between continuous and discrete domains, provides a solid foundation for analyzing system stability and designing effective control strategies. It allows for a nuanced understanding of the system's behavior across different frequency ranges and forms the basis for developing advanced control techniques, such as the adaptive digital notch filter proposed in this study.

Using the Tustin transformation with pre-warping for the notch filter, these transfer functions, from the equations (1), (2) and (3) are converted to their discrete-time equivalents used in the Bode plots:

$$PR(z) = K_p + K_i T_s \cdot \frac{z^2 - 1}{z^2 - 2\cos(\omega_c T_s)z + 1},$$
 (6)

$$Notch(z) = \frac{b_0 + b_1 z^{-1} + b_2 z^{-2}}{1 + a_1 z^{-1} + a_2 z^{-2}},$$
 (7)

where,

$$b_{0} = \frac{4 + \frac{2\omega_{n}T_{S}}{Q} + \omega_{n}^{2}T_{S}^{2}}{4 + \frac{2\omega_{n}T_{S}}{Q} + \omega_{n}^{2}T_{S}^{2}}, b_{1} = \frac{2\omega_{n}^{2}T_{S}^{2} - 8}{4 + \frac{2\omega_{n}T_{S}}{Q} + \omega_{n}^{2}T_{S}^{2}}, b_{2} = \frac{4 - \frac{2\omega_{n}T_{S}}{Q} + \omega_{n}^{2}T_{S}^{2}}{4 + \frac{2\omega_{n}T_{S}}{Q} + \omega_{n}^{2}T_{S}^{2}},$$

$$a_{1} = \frac{2\omega_{n}^{2}T_{S}^{2} - 8}{4 + \frac{2\omega_{n}T_{S}}{Q} + \omega_{n}^{2}T_{S}^{2}}, a_{2} = \frac{4 - \frac{2\omega_{n}T_{S}}{Q} + \omega_{n}^{2}T_{S}^{2}}{4 + \frac{2\omega_{n}T_{S}}{Q} + \omega_{n}^{2}T_{S}^{2}},$$

$$LCL(z) = \frac{T_{S}^{2}}{L_{1}L_{2}C} \cdot \frac{(z+1)^{2}}{(z-1)^{2}} \cdot \frac{1}{z}.$$

$$(8)$$

These discrete-time transfer functions are used to generate the Bode plots shown in *Fig. 4*, providing a complete frequency response analysis of the digital control system.

116 M. M. Ahmed

B. Analysis of the stability of a grid-connected inverter using a notch filter

The stability analysis of the grid-connected inverter system employing a notch filter is crucial for understanding the system's behavior under various conditions. The parameters used in this stability analysis, as well as in subsequent simulations are: $L_i=330~\mu\mathrm{H}$, grid inductance L_g ranging from 40-140 $\mu\mathrm{H}$ (corresponding to weak and strong grid conditions), $C=3~\mu\mathrm{F}$, $V_{dc}=380~\mathrm{V}$, $f_g=50~\mathrm{Hz}$, $f_s=50~\mathrm{KHz}$, with resulting ω_{res} range of 58,200-95,600 rad/s, and ω_n range of 16,000-90,000 rad/s. For maximum stability sensitivity, our analysis neglects the resistor component of the LCL filter, as smaller resistance values increase the likelihood of system instability.

Our analysis focuses on two key scenarios: when the system resonant frequency and the notch frequency coincide, and when they do not match.

Scenario 1: Matched Resonant and Notch Frequencies

The system stability can be determined through Bode diagram analysis when the resonant frequency matches the notch frequency. *Fig. 4* illustrates the Bode diagram for the notch filter Notch(z), the PR controller PR(z), the LCL filter LCL(z), and the delay component z^{-1} with L_g at 100 μ H and ω_n at 65,900 rad/s. For this scenario, the transfer function of the LCL filter from inverter voltage to line current in the discrete domain is:

$$LCL(z) = \frac{T_s^2}{L_1 L_2 C} \cdot \frac{(z+1)^2}{(z-1)^2} \cdot \frac{1}{z} . \tag{9}$$

As shown in Fig. 4, the alignment of notch frequency ω_n with the resonant frequency ω_{res} results in resonant peak cancellation, ensuring system stability.

Scenario 2: Unmatched Resonant and Notch Frequencies

For analyzing stability when frequencies differ, we examine the resonant pole's path in the z-plane as the grid impedance varies. Fig. 5(a) shows this path with ω_n fixed at 65,900 rad/s while L_g increases from 40 to 140 μ H, causing the frequency ω_{res} to decrease from 96,600 rad/s to 58,200 rad/s.

The resonant pole travels along path A in the z-plane, with instability occurring when L_g is less than 50 μ H or greater than 100 μ H, as the pole moves outside the unit circle.

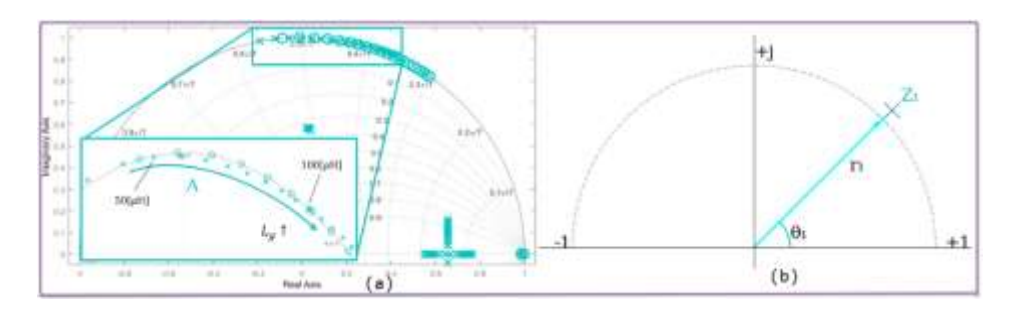


Figure 5: (a) Pole trajectory mapping with parametric variation of grid-side inductance (L_g : 40 µH \rightarrow 140 µH) at constant natural frequency (ω_n = 65,900 rad/s). (b) Complex plane representation showing a point z_I on the unit circle

The resonant pole travels along path A in the z-plane. Critically, we observe that the system becomes unstable when L_g is less than 50 μ H or greater than 100 μ H, as the pole moves outside the unit circle under these conditions.

C. Proposed Adaptive Digital Notch Filter

The adaptive digital notch filter maintains system stability by dynamically adjusting its notch frequency based on real-time stability assessment and resonant frequency change detection through inverter-side current monitoring.

To understand the filter's operation, we first need to examine how the resonant pole affects the temporal response of the system. Fig.~5(b) illustrates this relationship in the z-plane. If we consider an arbitrary point z_1 on the z-plane, located at a distance r_1 from the origin and forming an angle θ_1 with the x-axis, we can express z_1 as:

$$z_1 = r_1 e^{j\theta_1} = e^{\sigma_1 + j\omega_1 T_S} . {10}$$

According to the z-transform definition, the time response $C_l(t)$ corresponding to z_1 is:

$$C_1(t) = e^{\sigma_1 t} \sin(\omega_1 t + \phi). \tag{11}$$

If $r_1 < 1$ (i.e., the pole lies within the unit circle), σ_1 becomes negative, indicating a stable system.

When the system becomes unstable, the resonant pole moves outside the unit circle, resulting in a positive σ_1 . This leads to the presence of a growing resonant frequency component in the output. Fig. 6 demonstrates this scenario, simulating the system's response when L_g increases from 100 μ H to 140 μ H at ω_n = 65,900 rad/s. The inverter-side current (Fig. 6(a)) and its Fourier spectrum (Fig. 6(b)) clearly show the increase in high-frequency components near the resonant frequency.

118 M. M. Ahmed

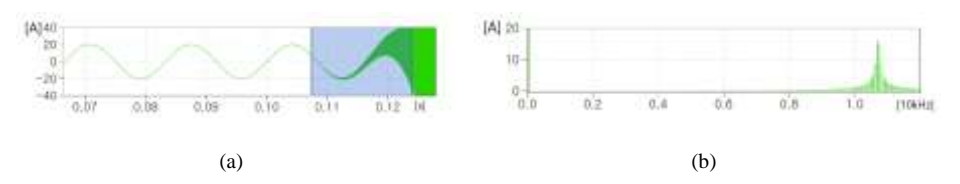


Figure 6: Unstable situation, (a) Current from inverter, (b) Fourier spectrum

The adaptive filter operates in three sequential steps:

- 1. Detect resonant condition occurrence.
- 2. Determine resonant frequency change direction.
- 3. Adjust notch frequency until resonant component amplitude decreases.

D. Resonance Detection

The resonance detection system monitors harmonic components in the inverter current and generates a resonance indicator (res_{ind}) . The inverter-side current i_i consists of multiple components: the fundamental grid frequency component, switching frequency harmonics, and potential resonant frequency components. While switching harmonics exist at multiples of the switching frequency, they are typically of much lower magnitude than the fundamental and resonant components due to the LCL filter's attenuation characteristics. For the purpose of resonance detection, we focus on the dominant components in the error between reference i_i^* and actual current i_i :

$$\operatorname{Error}(t) = i_i^* - i_i = A\sin(\omega_g t + \phi_g) + B\sin(\omega_{res} t + \phi_{res}), \quad (12)$$

where: ϕ_g represents the phase shift of the fundamental component due to control system delays, ϕ_{res} represents the phase shift at resonant frequency due to computational and sampling delays in the digital implementation. Higher-order harmonics are omitted from this expression as they don't significantly impact the resonance detection process.

Differentiating this error to separate high-frequency components:

$$\frac{d(error)}{dt} = A\omega_g \cos(\omega_g t + \phi_g) + B\omega_{res} \cos(\omega_{res} t + \phi_{res}) . \quad (13)$$

Given that the fundamental frequency is much smaller than the resonant frequency, and minimal computational delay Φ_{res} is typically very small, we can approximate this as:

$$\frac{d(error)}{dt} \approx B\omega_{res}\cos(\omega_{res}t + \phi_{res}). \tag{14}$$

The absolute value of this expression, when passed through a Low Pass Filter (LPF), provides the res_{ind} value, which represents the magnitude of the resonant frequency component. The resonance detection process is illustrated in the block diagram shown in Fig. 7. The derivative signal is passed through an absolute value function |.| to obtain the magnitude of the resonant component. Finally, the signal is low-pass filtered (LPF) to extract the resonance indicator res_{ind} , which represents the amplitude of the resonant frequency component in the current:

$$res_{ind} = LPF\left(\left|\frac{d}{dt}\operatorname{error}(t)\right|\right).$$
 (15)

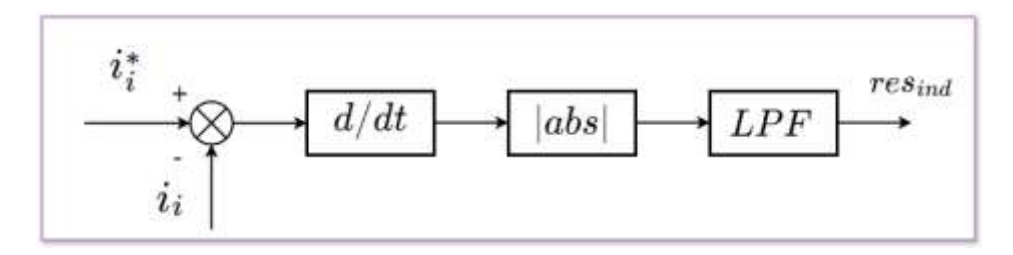


Figure 7: Resonance detection process

By monitoring the res_{ind} value, the system can detect the occurrence of resonance and the direction of change in the resonant frequency, as discussed earlier. This information is then used by the adaptive notch filter to dynamically adjust its frequency and maintain system stability.

E. Resonant Frequency Change Detection

To determine the resonant frequency's direction of change, the system slightly increases the notch frequency and observes the resulting change in the resonant component amplitude.

The resonant pole's behavior varies with notch frequency adjustments as shown in Fig. 5. With L_g at 100 μ H and ω_n increasing from 15,900 rad/s to 85,900 rad/s, the pole follows a counterclockwise path.

For notch frequencies below the resonant frequency, increasing ω_n reduces oscillation amplitude. Conversely, for notch frequencies above the resonant frequency, increasing ω_n increases oscillation amplitude.

Therefore:

- Increased resonant component amplitude indicates decreased system resonant frequency;
- Decreased resonant component amplitude indicates increased system resonant frequency.

120 M. M. Ahmed

This adaptive mechanism maintains system stability across varying grid conditions by continuously adjusting the notch frequency based on these observations.

Through this comprehensive stability analysis, we gain valuable insights into the behavior of the grid-connected inverter system under various conditions. These findings inform the design of our adaptive digital notch filter, enabling it to respond effectively to changes in system parameters and maintain stability across a wide operating range.

4. Simulation results

The proposed adaptive digital notch filter was evaluated through simulation studies. The system parameters used for these evaluations were set within their operational ranges: ($L_i = 330 \, \mu\text{H}$, $L_g = 40 - 140 \, \mu\text{H}$, $C=3 \, \mu\text{F}$, $V_{dc} = 380 V$, $f_g = 50 \, \text{Hz}$, $f_s = 50 \, \text{KHz}$, $\omega_{res} = 58,200 - 95,600 \, \text{rad/s}$, $\omega_n = 16,000 - 90,000 \, \text{rad/s}$). For the simulation studies, Lg was fixed at 100 μ H while the notch frequency was varied to analyze system stability under different conditions.

A. Resonant Frequencies Lower than Notch Frequencies

Fig. 7 and Fig. 8 illustrate the simulated waveforms for scenarios where the resonant frequencies are lower than the notch frequencies.

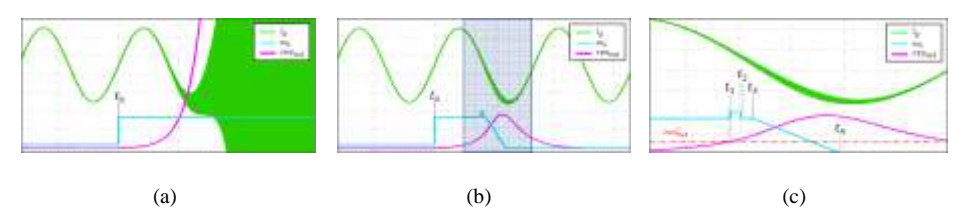


Figure 7: $\omega_n = 60,000 - 90,000$ rad/s at t_0 . (a) Conventional notch filter, (b) Proposed notch filter, (c) highlighted area in b

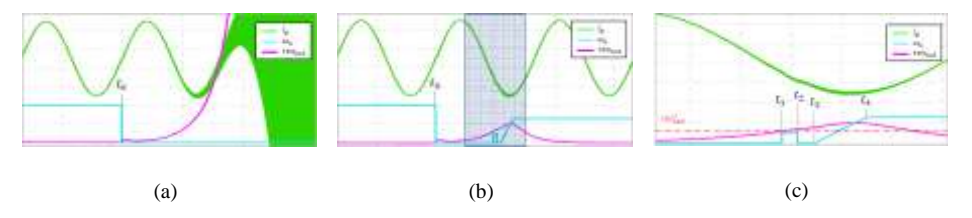


Figure 8: $\omega_n = 60,000 - 20,000 \text{ rad/s}$ at t_0 . (a) Conventional notch filter, (b) Proposed notch filter, (c) highlighted area in b

Fig. 7 demonstrates a simulated waveform using a conventional notch filter, where the notch frequency increases from 60,000 rad/s to 90,000 rad/s. This change causes the system to become unstable, resulting in current i divergence.

Fig. 7(b) shows the application of the proposed adaptive digital notch filter, with Fig. 7(c) providing a magnified view of the highlighted portion in (b). The sequence of events proceeds as follows:

- 1. At t_1 : notch frequency increases, the system becomes unstable, causing the current harmonic magnitude to exceed the reference value res_{ind}^* , which triggers the adaptive mechanism.
- 2. From t_1 to t_2 : notch frequency is briefly raised to determine the direction of resonant frequency change.
- 3. From t_3 to t_4 : based on the negative slope of res_{ind} , the notch frequency is reduced, restabilizing the system.

B. Resonant Frequencies Higher than Notch Frequencies

Fig. 8 illustrates the simulated waveforms, for cases where the resonant frequencies exceed the notch frequencies.

Fig. 8(a) shows the system's response when the notch frequency decreases from 60,000 rad/s to 20,000 rad/s using a conventional notch filter. This reduction destabilizes the system, causing current i divergence.

Fig. 8(b) and Fig. 8(c) demonstrate the effectiveness of the proposed adaptive filter. The sequence of events is as follows:

- 1. At t_0 : when the notch frequency decreases, the system becomes unstable, causing the i harmonic magnitude to increase.
- 2. At t_1 : harmonic magnitude surpasses res_{ind}^* , activating the adaptive mechanism.
- 3. From t_1 to t_2 : notch frequency is increased, revealing that it's lower than the system resonant frequency.
- 4. At t_3 : notch frequency is further increased, successfully restabilizing the system.

These results demonstrate the robustness and effectiveness of the proposed adaptive digital notch filter in maintaining system stability across various operating conditions, outperforming conventional fixed-frequency notch filters.

5. Conclusion

This study presents an innovative adaptive digital notch filter designed to enhance the stability of grid-connected inverter systems employing LCL filters. The proposed solution addresses the challenges associated with varying grid 122 M. M. Ahmed

impedances and system resonant frequencies, which can lead to instability in conventional fixed-frequency notch filter designs.

Key findings and contributions of this research include:

- 1. Comprehensive Stability Analysis: We conducted a thorough analysis of system stability under various conditions, considering the interplay between the system resonant frequency and the notch frequency. This analysis provided crucial insights into the behavior of the resonant pole in the z-plane, informing the design of our adaptive filter.
- 2. Adaptive Mechanism: The proposed filter incorporates a three-step adaptive mechanism: the proposed filter incorporates a three-step adaptive mechanism: detection of resonance occurrence, determination of the direction of change in resonant frequency, and dynamic adjustment of the notch frequency.
- 3. *Improved Stability*: Simulation results demonstrate the superior performance of the adaptive digital notch filter compared to conventional fixed-frequency designs. The adaptive filter successfully maintains system stability across a wide range of operating conditions, including scenarios where the resonant frequency is both lower and higher than the initial notch frequency.

The adaptive digital notch filter presented in this study offers a significant advancement in the control of grid-connected inverter systems. By effectively mitigating the instability issues associated with LCL filters and varying grid impedances, this solution paves the way for more reliable and efficient grid-connected power electronics systems.

Future research directions may include:

- Extending the adaptive mechanism to handle multiple resonant frequencies;
- Investigating the performance of the adaptive filter in more complex grid scenarios, such as weak grids or micro-grids;
- Optimizing the adaptive algorithm for faster response times and reduced computational overhead.

In conclusion, the proposed adaptive digital notch filter represents a promising solution for enhancing the stability and performance of grid-connected inverter systems, contributing to the advancement of renewable energy integration and smart grid technologies.

References

- [1] Hinamoto, Y., Doi, A., and Nishimura, S., "Adaptive Normal State-Space Notch Digital Filters Using Gradient-Descent Method", *Journal of Electrical Engineering & Technology*, vol. 18, no. 3, pp. 1234–1245, Mar. 2023. DOI: 10.1007/s00034-023-02297-3.
- [2] Yamawaki, T., and Yashima, M., "Adaptive Notch Filter in a Two-Link Flexible Manipulator for the Compensation of Vibration and Gravity-Induced Distortion", *Vibration*, vol. 6, no. 1, pp. 286–302, Jan. 2023. DOI: 10.3390/vibration6010018.

- [3] Yuan, J., El-Saadany, A., and Al Durra, E., "Adaptive Digital Notch Filter Based on Online Grid Impedance Estimation for Grid-Tied LCL Filter Systems", *Electric Power Systems Research*, vol. 222, pp. 1–10, Feb. 2024. DOI: 10.1016/j.epsr.2023.108321.
- [4] Chen, M.-Y., and Wu, J.-H., "Design of Adaptive Notch Filters for Grid-Connected Inverter Applications", *IEEE Transactions on Industrial Electronics*, vol. 71, no. 4, pp. 4567–4575, Apr. 2024. DOI: 10.1109/TIE.2023.3234567.
- [5] Zhang, R.-S., and Xu, L.-J., "A Novel Adaptive Digital Notch Filter for Power Quality Improvement in Grid-Connected Inverters", *IET Generation, Transmission & Distribution*, vol. 17, no. 2, pp. 345–353, Feb. 2024. DOI: 10.1049/gtd2.12345.
- [6] Lee, S.-H., and Kim, Y.-J., "Enhanced Stability of Grid-Connected Inverters Using Adaptive Digital Notch Filters", *IEEE Access*, vol. 12, pp. 12345–12357, Mar. 2023. DOI: 10.1109/ACCESS.2023.DOI.
- [7] Ali, A. B., and Ali, M. S., "Adaptive Filtering Techniques for Improving Stability in Grid-Tied Inverter Systems", *Journal of Power Sources*, vol .550, pp .1-11, Jan .2024. DOI: 10 .1016/j.jpowsour .2023 .232345.
- [8] Huang, T.-C., and Liu, C.-H., "Real-Time Implementation of an Adaptive Digital Notch Filter for Grid-Connected Inverter Applications", *IEEE Transactions on Smart Grid*, vol .15, no .1, pp .234–245, Jan. 2024. DOI: 10 .1109/TSG .2023 .3223456.
- [9] Gupta, A. K., Bhatia, S. R., and Gupta, M. K., "Adaptive Digital Notch Filter for Harmonic Mitigation in Grid-Connected Inverters", *IEEE Transactions on Power Electronics*, vol. 35, no. 4, pp. 3456–3465, Apr. 2020. DOI: 10.1109/TPEL.2019.2951234.
- [10] Smith, J., Wang, L., and Johnson, R., "Design and Implementation of Adaptive Notch Filters for Grid-Connected Inverter Stability", *International Journal of Electrical Power & Energy* Systems, vol. 120, pp. 105–112, Jan. 2021. DOI: 10.1016/j.ijepes.2020.105123.
- [11] Rahman, M. A., and Rahman, H. A., "Enhanced Stability of Grid-Connected Inverters Using Adaptive Digital Filters", *IET Renewable Power Generation*, vol. 15, no. 2, pp. 234–240, Feb. 2021. DOI: 10.1049/iet-rpg.2019.0605.



DOI: 10.47745/auseme-2024-0011

Operation of V2G Chargers in Smart Grids

Jozef KIRÁLY¹, and Dušan MEDVEĎ¹

¹ Technical University of Košice, Faculty of electrical engineering and Informatics, Letná 9, 042 00 Košice, Slovakia, e-mail: jozef.kiraly@tuke.sk, dusan.medved@tuke.sk

Manuscript received April 08, 2024; revised August 24, 2024

Abstract: The article deals with the description of various modes of connection of electric vehicles to the grid, taking into account the operation of these vehicles in the vehicle-to-grid mode. The simulation of a simple microgrid network, which includes residential electricity consumption and photovoltaic power plants as renewable energy sources, illustrates the charging and discharging modes of the grid. Three scenarios were selected for the study, which are described by the number of connected vehicles and their mode. The result of the simulation is the evaluation of the contribution of these connected vehicles to the overall power balance at the interface of the distribution network and the microgrid network.

Keywords: EV Charging, Vehicle 2 grid, Grid 2 vehicle.

1. Introduction

The perception of electromobility as a mere load in the distribution network is changing with the advent of charging stations equipped with V2G (vehicle-to-grid) and V2L (vehicle-to-load) capabilities. In the context of the massive deployment of hybrid photovoltaic systems with batteries, electric vehicles become one of the tools for energy storage in decentralized networks. However, compared to classical decentralized sources, the supply of energy from electric vehicle batteries to the grid is even more difficult to predict. From the perspective of the topicality of the issue, it is important to emphasize the exponential growth of the number of electric vehicles in the European Union.

From the perspective of the grid operation mode, it will be necessary to start considering the possibility of operating these vehicles only for the purpose of powering the building itself, in order to eliminate peaks in electricity consumption. In this case, we will therefore only consider a decrease in the load on the distribution network from the perspective of the grid. The expected extent of this impact will be based on the trend of electric vehicle and plug-in hybrid

vehicle deployment. An example of the increase in vehicles within the European Union is shown in *Fig. 1*.

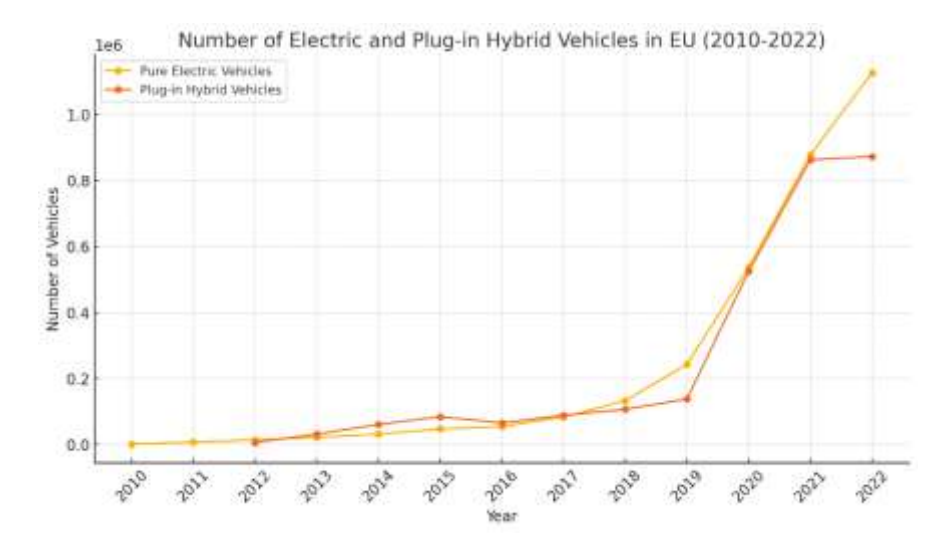


Figure 1: Number of EV and PHEV in European Union [1]

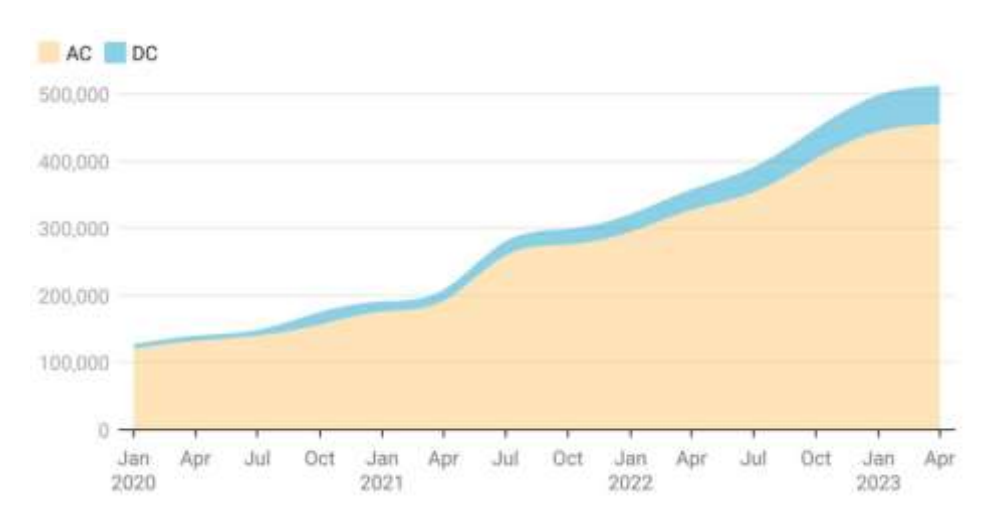


Figure 2: Progressive Growth of AC and DC Public Recharging Infrastructure in the European Union [2]

Current charging infrastructure primarily relies on a combination of alternating current (AC) and direct current (DC) stations for these vehicles. The following *Fig.* 2 depicts the temporal evolution of charging station deployment, disaggregated by

charger type. Analysis of the provided number of chargers data reveals a dominant rise in AC charging, primarily associated with residential charging stations. In this scenario, the ability of EVs to feed electricity back to the grid hinges on the connected vehicle and its on-board charger possessing vehicle-to-grid (V2G) capability. Conversely, DC charging relies heavily on the type of station employed. Unlike AC, DC stations directly interact with the EV battery, with thermal management dictating the limitations of both charging and energy delivery. Given these considerations, establishing communication between charging infrastructure, other energy sources, and significant grid loads becomes a critical objective within smart grid network operations.

From the point of view of operating charging stations in a smart grid in which communication is ensured, it is important to describe the energy flows that are in relation to all three investigated components – distribution network, charging stations and decentralized sources of electricity (e.g., hybrid photovoltaic system).

2. Elements of smart grid related to electric vehicle chargers

A. Elements in general

As outlined in the opening section, the primary attribute of devices within these networks is their ability to communicate. Nano-grids, typically found in residential areas, include elements such as local renewable energy sources, charging stations, battery storage systems, and so on. [3].

A fundamental communication requirement in these networks is the exchange of information about power flow within the examined network, typically covering the supply and consumption of electricity, as well as the instantaneous active power on both the consumption and supply sides. This communication takes place via a communication protocol (e.g., TCP/IP, M-BUS, etc.).

In cases where a decentralized energy source, such as a hybrid photovoltaic system, is also installed in this network, it is important to communicate the battery state of charge of this system as well as the currently supplied power. A very similar approach can be used for battery storage systems (BESS).

Within the smart grid, these mentioned components can be considered conventional. Currently, electric vehicles and charging stations with the ability to feed energy into the grid are additional elements. The integration of such sources from a communication perspective is typically carried out via TCP/IP protocols such as Open Charge Point Protocol, Smart Charging Protocol, Open Charge Point Interface.

B. Electric vehicles and chargers

The link between the electric vehicle and the distribution network or nanogrid is established through a charging station. As noted earlier, one of the most common charging methods involves AC charging utilizing the vehicle's built-in charger. Charging in this case takes place through wall boxes capable of delivering up to 22 kW of power. AC charging is also feasible using external chargers powered by 230 V outlets. However, the limitation of this charging method lies in the vehicle's on-board charger, which sets the maximum battery charging capacity, typically reaching up to 22 kW for three phase chargers for fully electric vehicles and up to 3.6 kW for hybrids (most commonly, single-phase charging). An area of concern, particularly for the operation of the electrical grid or on a smaller scale, the electrical system of a household equipped with a renewable energy source such as a photovoltaic power plant, is the utilization of these chargers. Certain configurations allow these chargers to load only one phase, posing a potential problem in terms of load imbalance [4].

In household AC charging setups, another issue arises from the implementation of power management by the charging station. This involves considering the utilization of the entire maximum allocated capacity of the electrical supply point, as determined by the main circuit breaker. With controlled charging across multiple households, there may be a need for an upgraded fuse element at the distribution substation level. Hence, it is essential, in terms of future network development, to factor in this phenomenon, as it can significantly impact the value of the simultaneity coefficient β under consideration.

Vehicle-to-grid (V2G) mode presents a less frequent option for AC charging, as it necessitates direct support from the vehicle's on-board charger. DC charging, on the other hand, converts alternating current into direct current for the vehicle's battery, typically providing power between 50 kW and 350 kW. Unlike AC charging, DC charging tends to entail symmetrical loads in most scenarios. The charging process itself is primarily governed by the battery's thermal management system, aimed at minimizing battery wear while achieving short charging times [5].

The battery's ability to deliver power in relation to its temperature is shown in Fig.~3. It's evident from the data that the optimal temperature range lies approximately between 0°C and 40°C. However, achieving this range consistently throughout the year is impractical. In such instances, there is the option to externally raise the battery temperature. Nonetheless, from the perspective of the overall efficiency of the nanogrid, this approach is not cost-effective. A similar impact of battery temperature on its ability to charge is also

observed, illustrating limitations in charging performance due to actual temperature and the impact of thermal management of electric vehicle batteries.

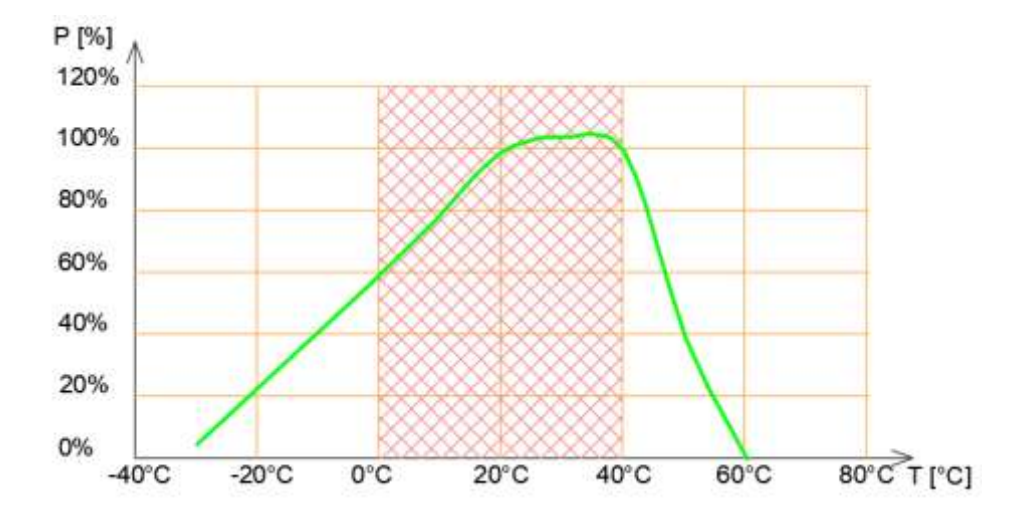


Figure 3: Dependence of battery power on the operation temperature

Since DC charging predominantly takes place at charging hubs, the pattern and intensity of grid load become critical factors. One solution to address this issue is the installation of battery storage systems, which enable efficient management of energy flow from both the distribution grid and batteries. This allows for optimal utilization of available capacity at specific grid points. Furthermore, the strategic placement of these charging points, often located in areas where fast charging is required, such as along transit routes or near highways, imposes limitations on the installation of high-performance devices with a simultaneity coefficient of $\beta=0.8$ - 0.9.

Another energy management option, alongside battery storage installation, involves employing vehicle-to-grid (V2G) systems or vehicle-to-vehicle (V2V) systems. Implementing this technology typically assumes integration into smart grids, where communication among individual grid elements facilitates bidirectional electricity flow. This allows electric vehicle batteries connected to the grid to supply electricity to grid to compensate for capacity shortages at specific points. In addition to considering the available energy capacity of vehicle batteries, understanding or predicting the behavioral patterns of individual grid-connected cars, which provide this functionality, is crucial. Besides the aforementioned behavioral models, exploring the vehicle-to-everything (V2X) model is equally promising from a charging standpoint. This model not only facilitates data exchange for energy flow control but can also be utilized for traffic

management, parking, and other purposes. The general mechanism of V2X is illustrated in the following Fig 4 [6], [7].

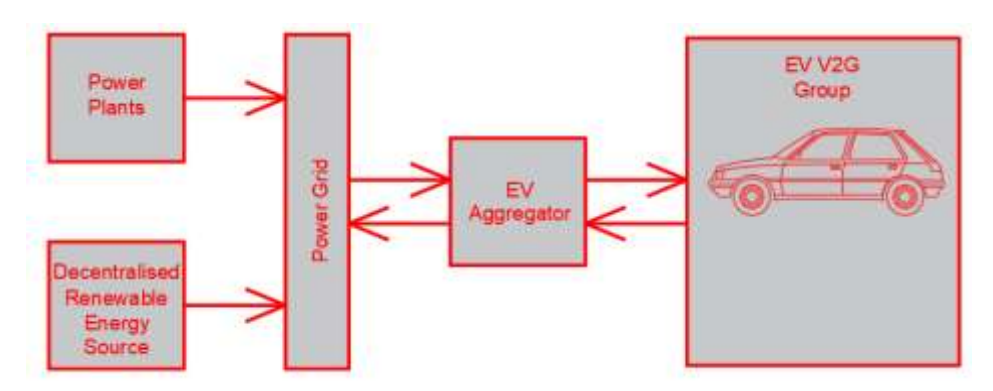


Figure 4: Power grid with V2G in general

3. Simulated electric grid

The structure of the analyzed nanogrid is illustrated in *Fig 5*. Understanding the behavior cycle of an electric vehicle upon connection to the network is crucial when considering it as a decentralized resource. This behavior is influenced by the initial parameters of the connected vehicle, which include:

- Initial state of charge of the electric vehicle (SOCI);
- Electric vehicle battery limit states (minimum state, maximum state of charge) (SOCmin, SOCmax);
 - Nominal power capable of being delivered to the grid (PEV).

From a grid management standpoint, it's vital to communicate:

- The number of electric vehicles (nEV);
- Predicted vehicle connection time (tEVch).

With this data, a grid model can be constructed, incorporating the contribution of these vehicles as a decentralized resource. Besides the parameters mentioned above, ensuring the reliable and safe operation of such a grid may necessitate coordination not only of electricity supply to these vehicles but also the maintenance of their state of charge (SOC) within required values. This scenario could involve what is known as Vehicle-to-Vehicle (V2V) operation.

The initial parameters for the grid simulated in our study concerning connected vehicles are outlined in Table 1. To assess the impact of these connected vehicles, it's also essential to determine the daily load profile. For the model's purposes, we considered the flow illustrated in Fig. 6.

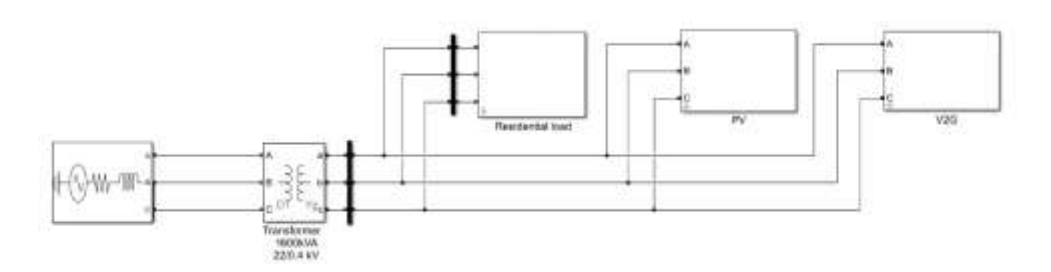


Figure 5: Topology of the simulated electric grid

Table 1: Parameters of connected EVs

Parameter	Unit	Value
SOCi	kWh	40
SOCmin	kWh	10
SOC _{max}	kWh	80
PEV	kW	25
nev	-	30
tevch (time of connected vehicle)	h	8

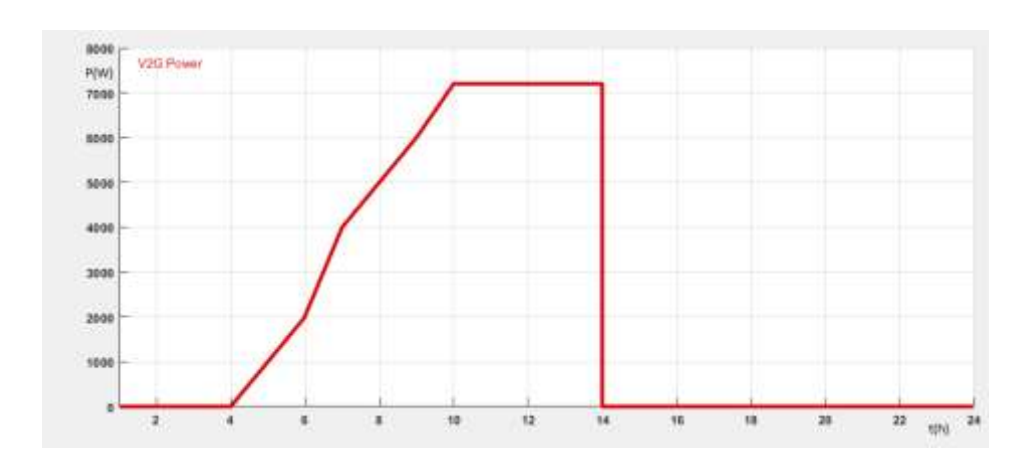


Figure 6: Time diagram of the electric vehicle connection to the examined network

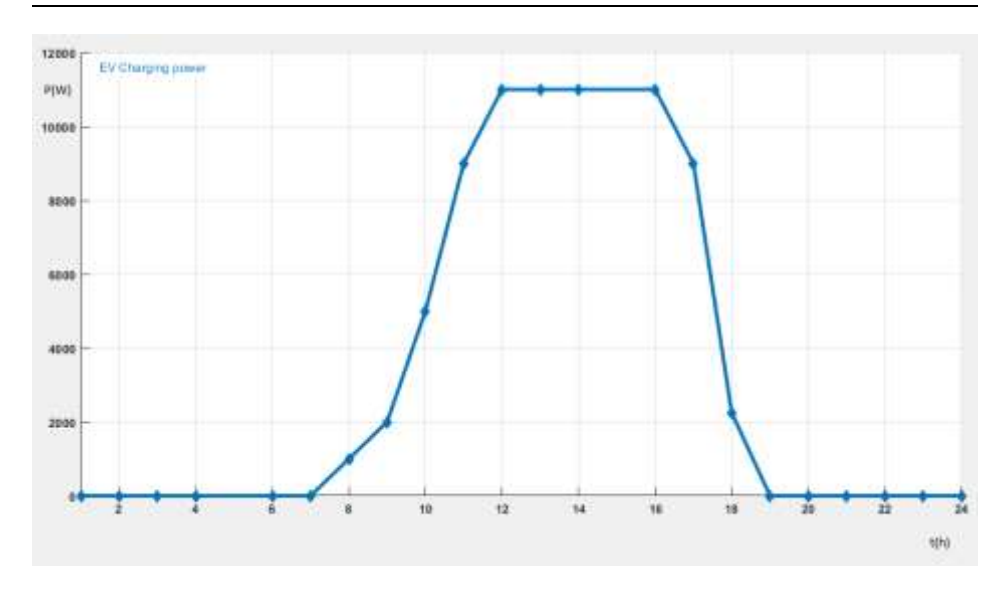


Figure 7: The time profile of the electric vehicle charging (defined for the purposes of the simulation)

4. Simulation

The simulation in Matlab Simulink software considered three scenarios for connecting vehicles to the grid in V2G and G2V modes. In scenario No. 1, 20 vehicles were considered to be connected in each mode, in scenario No. 2, the grid was supplied with 40 vehicles, and in scenario No. 3, all vehicles were charged. To determine the size of the microgrid, the grid was defined by 50 households, and to consider the impact of renewable energy sources, it was considered with installed photovoltaic sources at a level of 5 kW peak per household.

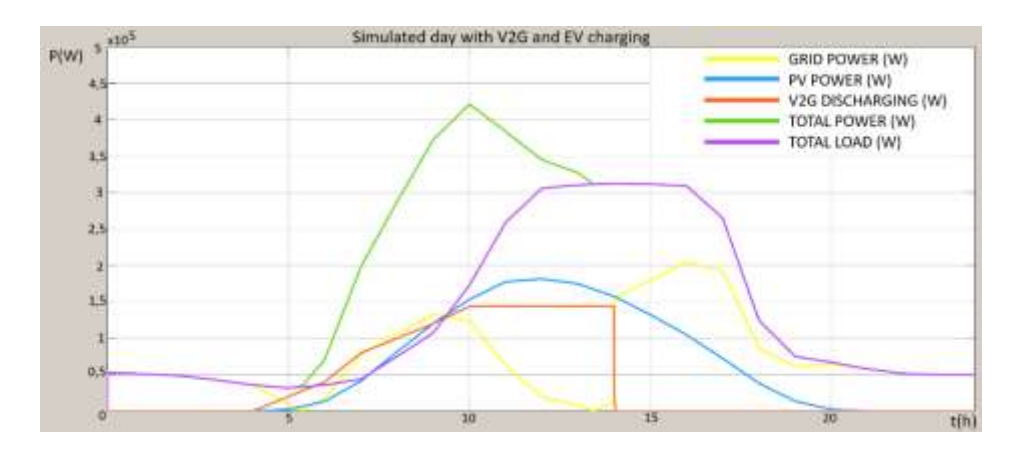


Figure 8: Power distribution for "scenario 1"

As it is evident from the network power profiles, the contribution of 20 vehicles in V2G mode is significant and, together with the contribution of photovoltaic power plants, will cause the power drawn from the distribution network to drop to zero at peak times. The supply of electricity from the network will only increase when the vehicles are disconnected and the output of the photovoltaic power plants decreases.

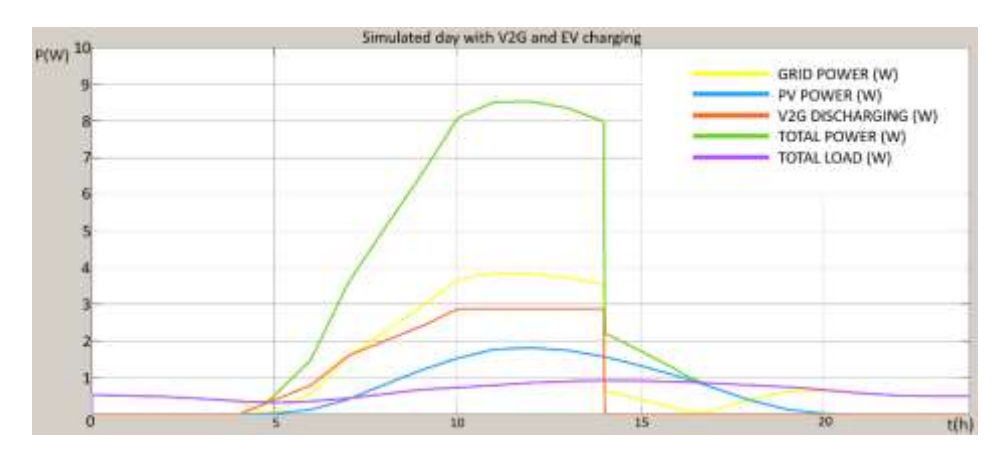


Figure 9: Power distribution for "scenario 2"

In the case of connecting most vehicles, the total load on the grid is minimal for almost the entire period of the studied daily profile. The contribution of vehicles and photovoltaic power plants will cause a reverse flow of energy, in which the grid power is supplied to the higher-level system. The last scenario

considers only charging of vehicles, which will only cause an increase in network consumption, which is partially covered by PV sources.

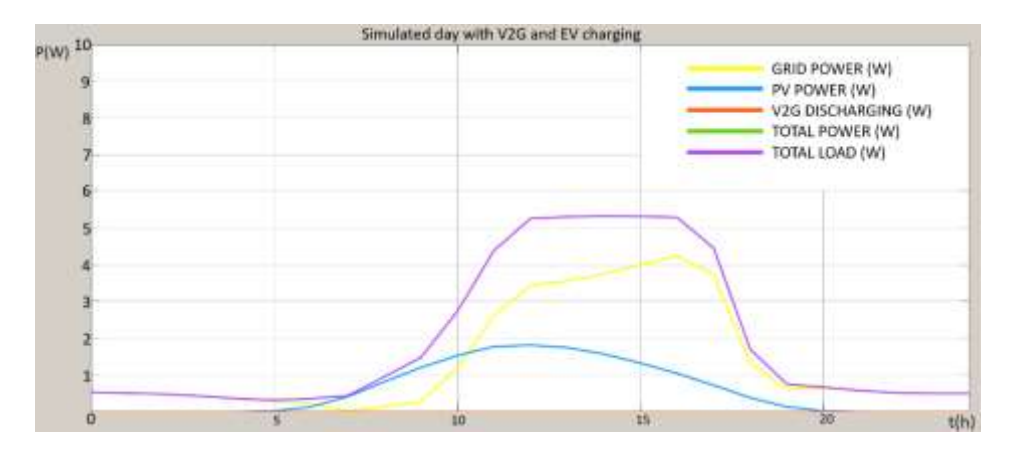


Figure 10: Power distribution for "scenario 3"

3. Conclusion

Electric car charging, particularly in V2G mode, is a hot topic due to the growing number of EVs on the road driven by environmental concerns. This article explores the challenges of different charging methods and introduces simulation tools to analyze energy consumption and production in distribution networks. As shown by the consumption and production timelines, EV charging and V2G functionality, alongside renewable energy sources, can significantly impact electricity supply from the grid. Therefore, it's crucial for future practices to gather real-world data on areas with these systems and create functional models that predict charging-related issues. These models can ultimately improve the quality and stability of electricity supply.

Acknowledgements

This work was supported by the Slovak Research and Development Agency under contract No. APVV-19-0576 and APVV-21-0312.

References

- [1] New registration of electric vehicles. European Environment Agency [online]. [cit. 2024-26-03]. Available https://www.eea.europa.eu/ims/new-registrations-of-electricvehicles
- [2] European Commission, "Significant Milestone Reached: European Union Boasts Half a Million Public Recharging Points", Online. 2023. Dostupné z: https://alternative-fuels-observatory.ec.europa.eu/general-information/news/significant-milestone-reached-european-union-boasts-half-million-public. [cit. 2024-03-26].
- [3] Wang, B., Fernandez, J. H., and Massoud, A., "A Wireless Battery Temperature Monitoring System for Electric Vehicle Charging", 2019 IEEE Sensors, 2019, pp. 1–4, doi: 10.1109/SENSORS43011.2019.8956733.
- [4] Khalid, H. M., and Peng, J. C. -H., "Bidirectional Charging in V2G Systems: An In-Cell Variation Analysis of Vehicle Batteries", in *IEEE Systems Journal*, vol. 14, no. 3, pp. 3665–3675, Sept. 2020, doi: 10.1109/JSYST.2019.2958967.
- [5] Al-Karakchi, A. A. A., Putrus, G., and Das, R., "Smart EV charging profiles to extend battery life", 2017 52nd International Universities Power Engineering Conference (UPEC), 2017, pp. 1–4, doi: 10.1109/UPEC.2017.8231961.
- [6] Corchero, C., and Sanmarti, M., "Vehicle- to- Everything (V2X): Benefits and Barriers", 2018 15th International Conference on the European Energy Market (EEM), 2018, pp. 1–4, doi: 10.1109/EEM.2018.8469875.
- [7] Gupta, A., Bansal, H. O., Jaiswal, P., and Kumar, R., "Modeling and Analysis of a V2G Scheme: A Concept in Smart Grid", 2020 International Conference on Emerging Trends in Communication, Control and Computing (ICONC3), 2020, pp. 1–6, doi: 10.1109/ICONC345789.2020.9117408.



DOI: 10.47745/auseme-2024-0012

Power Management and Charging Strategies for Electric Vehicles

Dusan MEDVED¹, Michal KOLCUN¹, Jozef KIRALY¹, Damian MAZUR²

¹ Department of Electric Power Engineering, Faculty of Electrical Engineering and Informatics, Technical University of Kosice, Letna 1/9, Kosice, Slovakia, e-mail: Dusan.Medved@tuke.sk, Michal.Kolcun@tuke.sk, Jozef.Kiraly@tuke.sk
² Department of Electrical and Computer Engineering Fundamentals, Rzeszow University of Technology, Powstancow Warszawy 12, Rzeszow, Poland, e-mail: mazur@prz.edu.pl

Manuscript received April 07, 2024; revised August 26, 2024

Abstract: The paper deals with the electric vehicle (EV) charging challenges amidst electromobility's expansion, highlighting different charging techniques and power control strategies essential for global adoption. It evaluates the effects of charging through simulations in the Technical University of Košice's Electrical Engineering lab, investigating both private and public charging scenarios. The analysis aims to guide future charging infrastructure projects, drawing on practical experiences and consultations with industry experts. Insights gained from the Smart Industry Lab, including access to advanced measuring equipment and software, underscore the study's contributions to understanding EV charging dynamics and its feedback effects on the electrical grid.

Keywords: EV charging process, charging infrastructure, data acquisition and evaluation, Smart Industry Lab.

1. Introduction

The emergence of electric vehicles (EVs) is revolutionizing our approach to mobility and the integration of charging infrastructure, significantly affecting the electrical grid and creating a surge in the demand for innovative charging solutions. This paper deals with the intricacies of EV charging exploring both the obstacles and opportunities it presents for technological advancement, energy consumption, and environmental sustainability.

With the increasing presence of EVs on our streets, the urgency for efficient and dependable charging options is becoming more important. This urgency is challenging our existing electrical systems, underscoring the importance of investigating the implications of EV charging on the grid and devising strategies to mitigate these effects. Moreover, the diversity in charging technologies, ranging from various station types to connector options, adds complexity to standardizing a user-friendly charging network.

The objective of this article is to clarify the process of EV charging and its integration with the electrical grid. It discusses the different charging modalities available and proposes enhancements to charging station functionalities to improve user experience.

A significant portion of this paper focuses on analyzing charging data to gauge the effects of EV charging on the electrical network. This analysis is based on laboratory experiments conducted at the Technical University of Košice, which replicate residential and communal charging scenarios. These simulations provide insights into how distinct charging methods influence the power infrastructure and inform the development of future charging frameworks.

Leveraging findings from experimental trials and consultations with industry specialists, particularly those from Východoslovenská distribučná a.s., alongside sophisticated data analysis tools, this research contributes to the broader dialogue on integrating EVs into our pursuit of sustainable transportation and energy practices.

2. Electric vehicle charging measurement

A. Description of measurement

The assessment of electric vehicle charging procedures was realized at the Smart Industry Lab. This lab fulfils the requirements of Východoslovenská distribučná, a.s. (VSD, a.s.) in terms of education, experimentation, and research, and is equipped with the necessary technology for simulating low-voltage distribution networks. Situated in the parking area adjacent to the Department of Electric Power Engineering, the lab is home to four operational EV charging stations (one of them is vehicle-to-grid (V2G)).

This investigation aimed to evaluate the consequential effects on the low-voltage distribution system caused by the concurrent charging of two electric vehicles. Initially, two Volkswagen e-Golf vehicles were linked to the EVLunic Pro M (Master) and EVLunic Pro S (Slave) charging stations (see section 2.D). Subsequently, a Nissan Leaf was also charged. To adjust the parameters of the low-voltage lines connected to these charging stations, the lab utilized specialized software. Additionally, a web-based application from ABB was employed to regulate the charging current by software.

For the measurement equipment utilized in this study, the list includes:

- Four network quality analyzers PQ-Box100 by A-Eberle for various measurement points.
- The EUROTEST 61557 network impedance and protection loop tester by METREL.
- The experiment also made use of additional tools such as voltage measuring cables and clamps, alongside MINI current measuring clamps provided by A-Eberle for detailed current analysis.

B. Measurement points description

In the exploration of electric vehicle charging, four PQ-Box 100 network analyzers provided by A-Eberle played a pivotal role.

The initial analyzer was strategically positioned at the commencement of the simulated line within the RST – PP switchgear (see *Fig. 1*), located at the Smart Industry Lab, identified as Measuring point 2. This installation was directly interconnected with the low-voltage network. The voltage and current clamps were attached to the electricity meter and the wires of the output cable that ran to the RP3 switchgear panel.

Subsequently, another analyzer found its place at the end of the line within the RP3 switchgear, situated also within the Smart Industry Lab. This was recognized as Measuring point 3, where the RP3 panel supplied energy to the charging stations being evaluated. At this connection, voltage and current clamps were secured to the output terminals and conductors of the cable.

In addition, two further analyzers were deployed within the PRIS-4 switchgear, situated externally from the department (in the place of parking place, close to EV chargers). These devices were tasked with powering the EVLunic Pro M and S chargers and performing separate analyses. The clamps were attached to the circuit breaker output terminals and the output cables of both the Master and Slave chargers.

This configuration was depicted in an illustrative scheme showcasing the simulated power line and designated measuring points (*Fig. 1*).

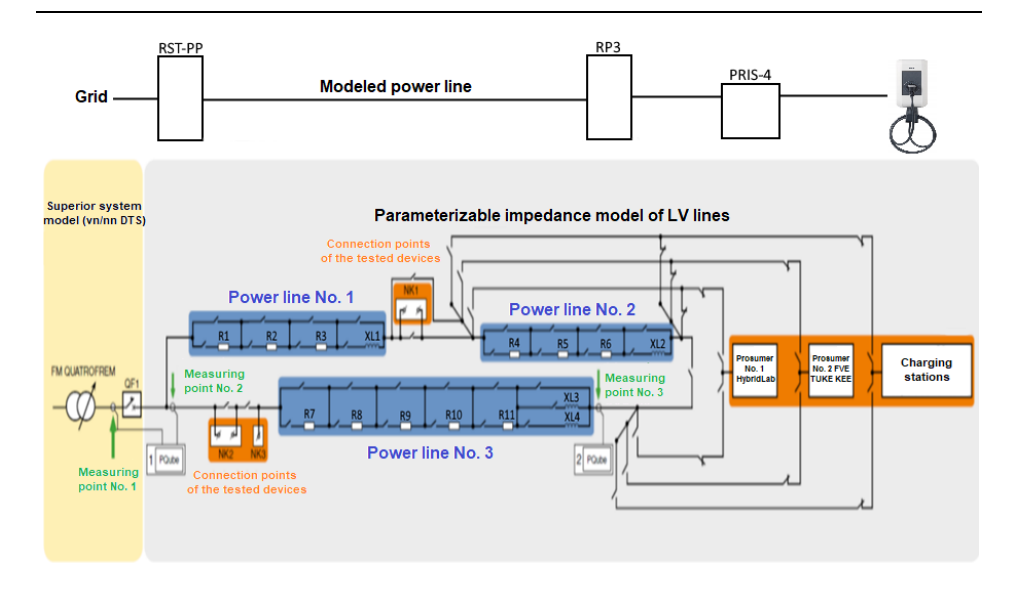


Figure 1: The modeled power line scheme and measuring points

C. Parameters of the modeled power lines

The impedances observed in the RP3 switchgear were modeled by connecting various distinct impedances, as depicted in the diagram in Fig. 1. The impedance denoted as $Z_{\rm max}$, represents a genuine low-voltage (LV) overhead line constructed using a self-supporting insulated cable, specifically type NFA2X - 4×95, extending 1050 meters. Similarly, the impedance labeled Z_0 , represents the utilization of an identical conductor for a real LV overhead line, spanning to 450 meters.

Table 1: Network impedance and short-circuit current values at maximum impedance settings (Z_{max}) within RP3 switchgear configuration

Maximum Impedance Z _{max} ; Conductor NFA2X – 4×95 – 1050 m					
Phase-to-Neutral Values		Phase-to-Phase Values			
$Z_{L1-N}[\Omega]$	$Z_{ ext{L2-N}}[\Omega]$	$Z_{\text{L3-N}}[\Omega]$	$Z_{\text{L1-L2}}[\Omega]$	$Z_{L2\text{-}L3}[\Omega]$	$Z_{L3\text{-}L1}[\Omega]$
0,7	0,73	0,71	1,25	1,26	1,25
$R_{L1-N}[\Omega]$	$R_{L2-N}[\Omega]$	$R_{L3-N}[\Omega]$	$R_{L1\text{-}L2}[\Omega]$	$R_{L2\text{-}L3}[\Omega]$	$R_{L3\text{-}L1}[\Omega]$
0,66	0,68	0,67	1,15	1,15	1,14
$X_{L1-N}[\Omega]$	$X_{L2-N}[\Omega]$	$X_{L3-N}[\Omega]$	$X_{L1\text{-}L2}[\Omega]$	$X_{L2\text{-}L3}[\Omega]$	$X_{L3\text{-}L1}[\Omega]$
0,21	0,24	0,21	0,49	0,52	0,52
Ik ₁ [A]	Ik ₂ [A]	Ik ₃ [A]	Ik ₁₂ [A]	Ik ₂₃ [A]	Ik ₃₁ [A]
346	333	343	335	333	336

Minimum Impedance Z_0 ; Conductor NFA2X $-4 \times 95 - 450$ m						
Phas	Phase-to-Neutral Values		Phase-to-Phase Values			
$Z_{\text{L1-N}}[\Omega]$	$Z_{L2-N}[\Omega]$	$Z_{L3-N}[\Omega]$	$Z_{L1\text{-}L2}[\Omega]$ $Z_{L2\text{-}L3}[\Omega]$ $Z_{L3\text{-}L}$			
0,28	0,31	0,3	0,39	0,4	0,38	
$R_{L1-N}[\Omega]$	$R_{L2-N}[\Omega]$	$R_{L3-N}[\Omega]$	$R_{L1\text{-}L2}\left[\Omega ight]$	$R_{L2\text{-}L3}[\Omega]$	$R_{L3\text{-}L1}[\Omega]$	
0,28	0,31	0,29	0,39	0,39	0,37	
$X_{L1-N}[\Omega]$	$X_{L2-N}[\Omega]$	$X_{L3-N}[\Omega]$	$X_{L1\text{-}L2}[\Omega]$	$X_{L2\text{-}L3}[\Omega]$	$X_{L3\text{-}L1}[\Omega]$	
0,06	0,06	0,07	0,06	0,07	0,08	
Ik ₁ [A]	Ik ₂ [A]	Ik ₃ [A]	Ik ₁₂ [A]	Ik ₂₃ [A]	Ik ₃₁ [A]	
848	765	790	1061	1042	1102	

Table 2: Network impedance and short-circuit current values at minimum impedance settings (*Z*₀) within RP3 switchgear configuration

D. Specification for charging unit

The charging facility features two models of charging stations, the EVLunic Pro S and EVLunic Pro M, which are designed for electric vehicle charging and are mounted on stands. Predominantly utilized for private charging in residential and corporate parking areas, the EVLunic Pro M includes an electricity meter and serves as the master controller for the EVLunic Pro S unit. This feature is necessary for managing of charging process of different EVs.

Key features of EVLunic Pro models:

- Maximum AC output: 22 kW;
- Conductor cross-section: Min. req. varies by cable type and installation, ranging from 5×2.5 mm² (for 16 A) to 5×6.0 mm² (for 32 A);
- Access control: Utilizes MIFARE RFID technology;
- Connectivity: Supports Ethernet and UMTS/3G for network access;
- Suitable environments: Both indoor and outdoor use;
- Temperature range for operation: From -25 °C up to +50 °C;
- IP rating: IP54 for dust and water resistance;
- Safety class: Class I;
- Outlet standard: Type 2 soc. comp. with 32 A/400 V AC as per EN 62196-2;
- Cable varieties: Type 1 and Type 2 cables supporting up to 32 A/230 V AC and 32 A/400 V AC respectively, in line with relevant standards;
- Voltage specifications: Ranges from 230 V single phase to 230/400 V 3-ph;
- Frequency support: Compatible with both 50 Hz and 60 Hz systems;
- Electrical system compatibility: Designed for TT, TN, and IT systems;
- Surge protection: Category III as specified by EN 60664;
- DC fault protection: FI/RCD-MB threshold below 6 mA DC;
- Regulatory compliance: Certified with CE marking.

The ABB 22 kW AC Master unit (EVLunic Pro M) obtains power from the RP3 switchgear, with a configured current limit of 15 A per phase. The ABB 22 kW AC Slave unit (EVLunic Pro S) can draw power from either the RP3 or PRIS4 switchgear (see *Fig. 1*), depending on the set position of the power switch. Its current limit is established at 30 A per phase. Both units are integrated with the TUKE Ethernet network and can be managed remotely via a web-based application provided by ABB.

E. Vehicle charging specifications overview

The charging setup included two Volkswagen e-Golf vehicles and one Nissan Leaf, all interfaced with the station's charging units and equipped with distinct onboard chargers.

Charging source (max. power)	Input U / I _{max}	Output power	Charge duration	Range increase per hour
Standard home outlet (2.3 kW)	230V / 10A	2.3 kW	16h 30min	12 km
Single-phase 16A (3.7 kW)	230V / 16A	3.7 kW	10h 15min	19 km
Single-phase 32A (7.4 kW)	230V / 31A	7.2 kW*	5h 15min	36 km
Three-phase 16A (11 kW)	230V / 16A (dual)	7.2 kW*	5h 15min	36 km

230V / 16A

(dual)

Table 3: Volkswagen e-Golf charging data

The Volkswagen e-Golf's onboard charger supports up to 3.7 kW in single-phase and 7.2 kW in two-phase modes through a dedicated wallbox charger (then, 1-phase is not loaded and the voltage asymmetry could be observed).

7.2 kW*

5h 15min

36 km

Charging source (max. power)	Input U / I _{max}	Output power	Charge duration	Range increase per hour
Standard home outlet (2.3 kW)	230V / 10A	2.3 kW	18h 30min	12 km
Single-phase 16A (3.7 kW)	230V / 16A	3.7 kW	11h 30min	19 km
Single-phase 32A (7.4 kW)	230V / 29A	6.6 kW*	6h 30min	34 km
Three-phase 16A (11 kW)	230V / 16A	3.7 kW*	11h 30min	19 km
Three-phase 32A (22 kW)	230V / 29A	6.6 kW*	6h 30min	34 km

Table 4: Nissan Leaf charging data

Three-phase 32A (22 kW)

^{*}Output power is limited by the vehicle's onboard charger.

^{*}Output power is limited by the vehicle's onboard charger.

The Nissan Leaf is equipped with a single-phase onboard charger, enabling a maximum charge power of 6.6 kW when using a wallbox charging station.

3. Data analysis on electric vehicle charging

A. Initial connection dynamics at charging stations

When a vehicle is connected to a charging station, there is a temporary increase in current. This increase occurs because the station's power relay activates to establish a connection with the vehicle. The intensity of this increase depends on the design of the onboard charger, particularly on the power electronic components it contains, such as capacitors.

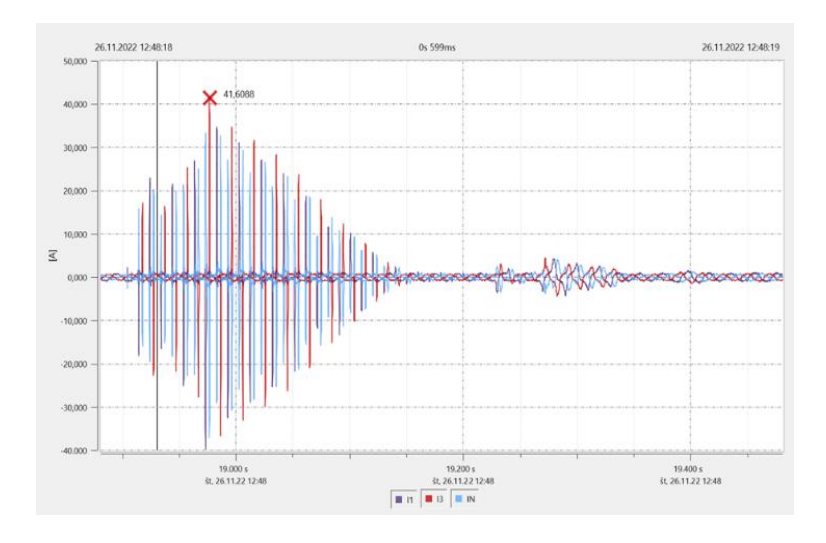


Figure 2: Current increase upon connecting Volkswagen e-Golf (Z₀, PRIS-4 Master)

As shown in Fig. 2, the Volkswagen e-Golf experiences current increase in the form of switched current surges. These surges reach peak instantaneous values during both charging phases, with some instances recorded as high as 43 A.

Demonstrated in *Fig. 3*, the Nissan Leaf's initial connection also produces switched current surges, peaking at an instantaneous value of up to 17 A in the charging phase.

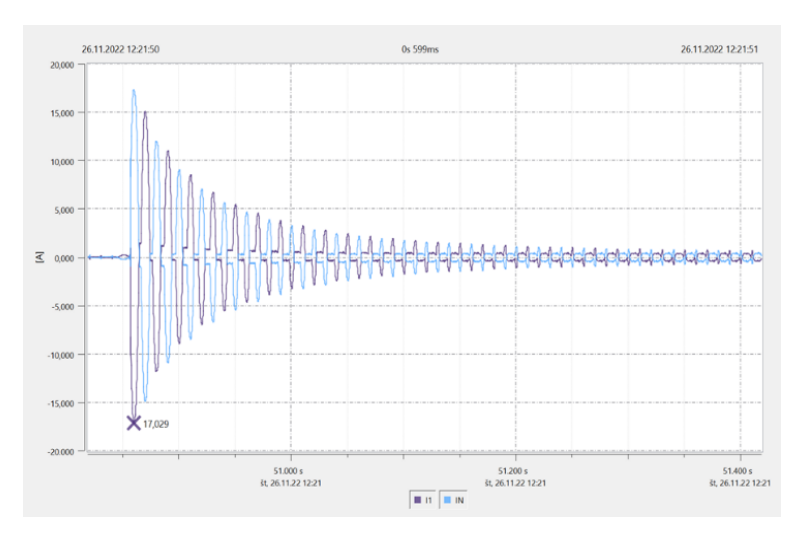


Figure 3: Current increase upon connecting Nissan Leaf (Z_0 , PRIS-4 Slave)

B. Initiation of the charging process

Upon establishing a connection between the electric vehicle and the charging facility, following the initial surge, the charging process initiates within roughly two seconds. Specifically for the e-Golf, which utilizes a two-phase charging mechanism (as it was mentioned before, one phase was not loaded and the voltage asymmetry could be observed), there was a sequential current escalation starting with phase L1. Once the RMS current on L1 hits around 7 A, the second phase joins the process. This controlled sequence, dictated by the vehicle's onboard charger, aims to lessen the initial shock to the battery as charging commences.

Depicted in *Fig. 4*, when two e-Golfs are connected simultaneously, the master charger's control system orchestrates the charging onset, engaging the vehicles one after the other to maintain a steady power increment. The sequence starts with the slave unit, and then proceeds to the master unit, reaching full charging power within about 3 seconds for an e-Golf, marking a power increase to approximately 3.56 kW per phase.

Fig. 5 shows the RMS current increase and the brief pause observed for the Nissan Leaf, followed by a gradual increase in power to its peak of approximately 6.7 kW on phase L1 within about 3 seconds. This pattern closely resembles the charging behavior of the e-Golf.



Figure 4: Power increase in RMS for two EVs e-Golf connections (Z₀, RP3)

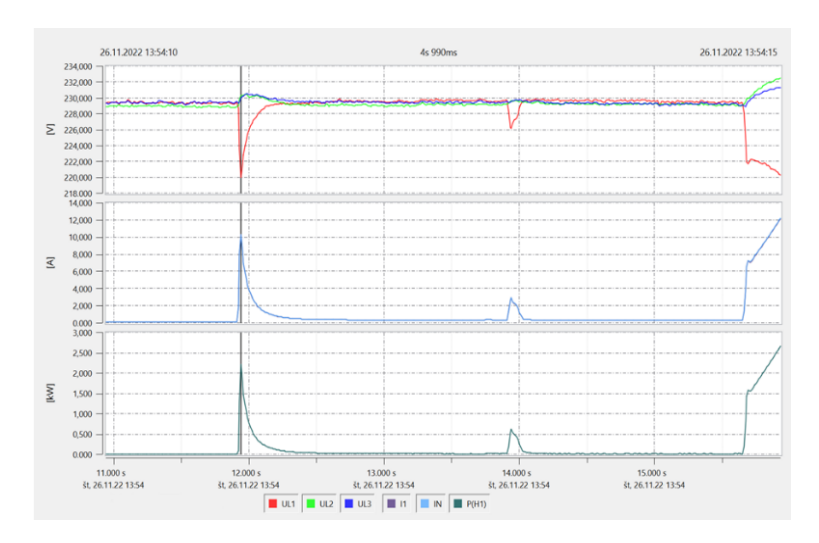


Figure 5: Power increase on Nissan Leaf connection (Z_0 + frequency converter of the laboratory Smart Industry Lab, RP3)

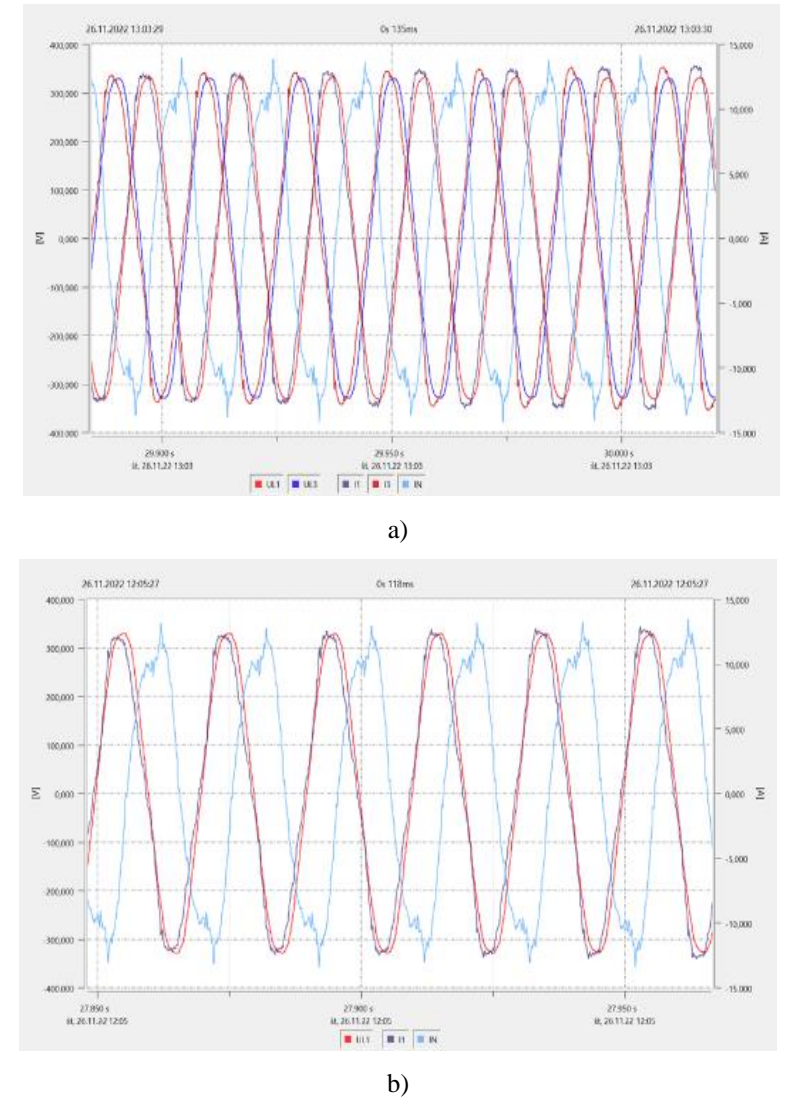


Figure 6: Sinusoidal current and voltage patterns during e-Golf (a) and Nissan Leaf (b) charging (Z_0 , PRIS-4)

The sinusoidal patterns of current and voltage at their peak during the ramp to full charge for both vehicles are showcased in *Fig. 6a* and *Fig. 6b*. These figures illustrate nearly zero phase shift between the phase voltage and current, attributable to the Power Factor Correction (PFC) feature within the charger, with a noted minor harmonic distortion in the current's waveform (according to STN EN 50160).

C. Impact of charging on voltage levels and regulation via software

Fig. 7 provides a view of the voltage reduction when an electric vehicle is connected for charging (Z_0 , RP3). Charging an e-Golf without current limitation, within a network featuring the Z_0 impedance level indicative of optimal conditions, led to a voltage decrease at the connection of both charging stations (switchgear RP3) by roughly 4 V in phase L3 and about 3 V in phase L1. Under identical conditions, connecting a Nissan Leaf resulted in a decrease of nearly 8 V in phase L1.

In scenarios with less favorable impedance (Z_{max}), charging a single e-Golf with maximum charging current a drop in voltage in the RP3 switchgear by about 11 V. Engaging two vehicles for simultaneous charging under these conditions saw a more significant reduction, with phase L1 experiencing a dip of 22 V. A similar setup for the Nissan Leaf, reflecting these challenging impedance circumstances, led to a voltage decline in the phase it was charging from, amounting to approximately 21 V.

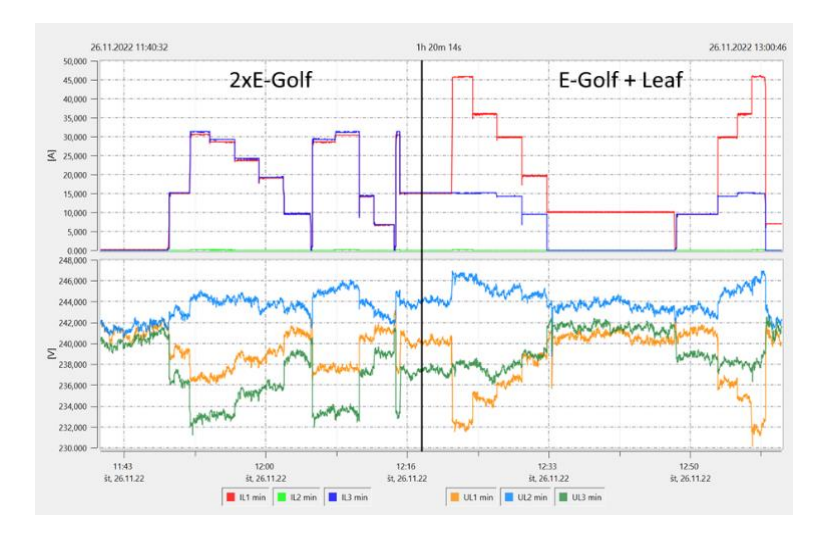


Figure 7: Voltage drop during the charging process of the electric vehicles (Z₀, RP3)

D. Digital regulation of charging power at stations

Throughout the charging cycle, the flow of current to the stations was constrained via a digital interface of ABB. The process started by connecting an e-Golf to the master station with a 40 A limit, followed by connecting another vehicle to the subordinate station. Subsequently, the current was methodically dialed down to 10 A, hitting a threshold beneath the necessary level for charging both vehicles concurrently.

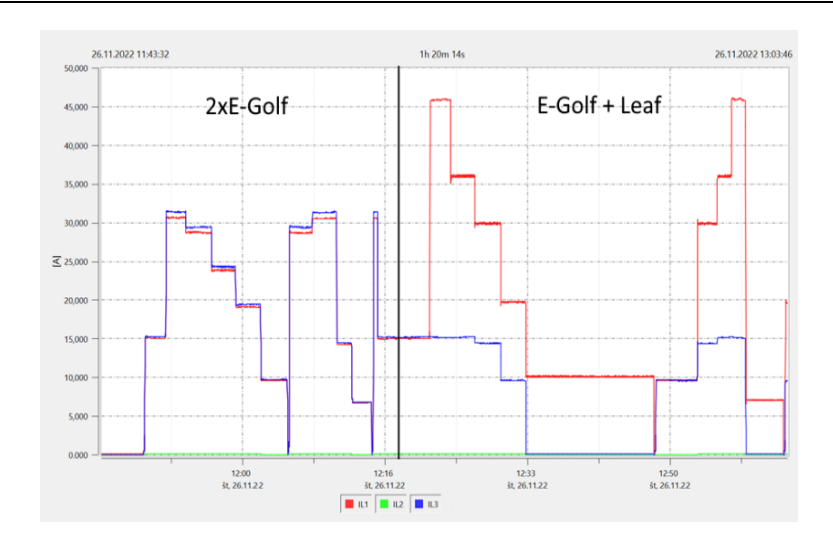


Figure 8: Limiting the charging current during the charging process (RP3)

This adjustment strategy ensures that when the preset current limit falls below the maximum available current for simultaneous vehicle charging, the available current is proportionally allocated among all operational stations.

The lowest operational current for the onboard chargers of the vehicles is set at 6 A. In instances when the current limit precludes the simultaneous charging of both vehicles, one will be temporarily disconnected. The remaining vehicle will continue to charge solo for a span of 15 minutes. Following this period, the charge is momentarily halted, and the session is transferred to the alternate station for continuation.

E. Asymmetry in voltage levels during charging

When charging an e-Golf under conditions of minimal impedance (Z_0) and at full charging capacity, the ratio between the reverse and direct voltage components could surge to 0.73~%.

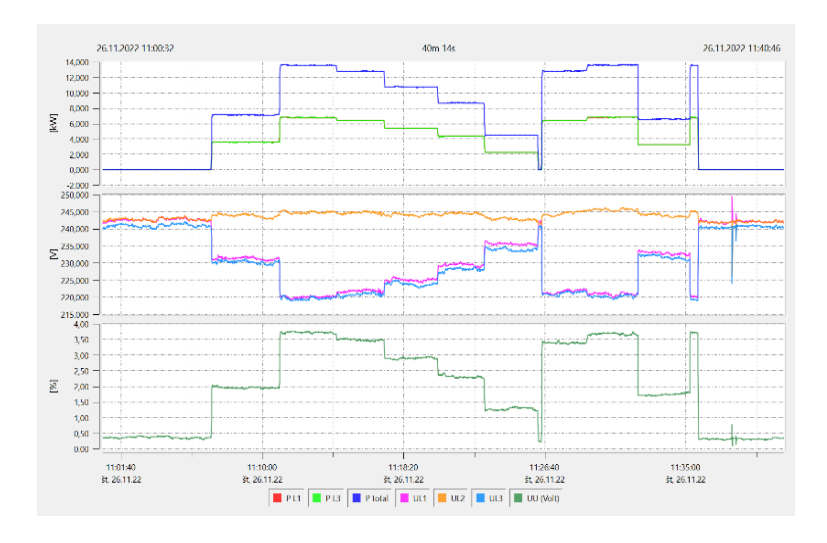


Figure 9: Master voltage asymmetry when charging $2 \times \text{e-Golf}(Z_{\text{max}}, \text{RP3})$

In scenarios involving the concurrent charging of two e-Golf vehicles, the voltage asymmetry heightened to 1.16% under the lowest impedance condition (Z_0). Should the charging involve both an e-Golf and a Nissan Leaf under identical conditions, the asymmetry in voltage escalated to 1.26%.

Further, under the conditions set by the maximum modeled line impedance (Z_{max}), a single e-Golf's charging could induce a voltage imbalance of up to 2 %. Charging two such vehicles simultaneously saw this asymmetry peak at 3.76 %.

For the Nissan Leaf, utilizing single-phase charging led to a voltage asymmetry of as much as 3.5 % under similar conditions, potentially surpassing the STN EN 50160 standard's asymmetry quality thresholds by nearly 1.5 % in prolonged charging sessions.

4. Conclusion

The findings from the Smart Industry Lab suggest that home-based AC charging of electric vehicles exerts a negligible effect on the power distribution network. Nonetheless, instances of voltage asymmetry exceeding normal ranges were observed, though other metrics such as voltage stability, network frequency, and harmonic distortions remained within the acceptable limits defined by the STN EN 50160 standard, irrespective of line impedance variations.

The realization of modeling the simultaneous charging of two vehicles shed light on potential complications in scenarios of widespread EV adoption, particularly in settings such as large parking areas. Notably, the practice of mass charging could provoke increased voltage asymmetry, posing a risk of

transformer stress and potential overloads arising from third harmonic currents in neutrals that are not adequately dimensioned. These insights underscore the critical need to factor in such electrical phenomena when planning and expanding mass EV charging frameworks.

Acknowledgements

This paper was supported by the Slovak Research and Development Agency, under the contracts APVV-19-0576, APVV-21-0312 and the Ministry of Education, Science, Research and Sport of the Slovak Republic and the Slovak Academy of Sciences under contract no. VEGA 1/0627/24.

References

- [1] STN EN IEC 61851: 2021, "Electric vehicle conductive charging system. General requirements". [online]. [cit. 2024-03-17] Available at < https://normy.normoff.gov.sk/norma/132733/ >
- [2] STN EN IEC 62196-2: 2023, "Plugs, socket-outlets, vehicle connectors and vehicle inlets Conductive charging of electric vehicles Part 2". [online]. [cit. 2024-03-17] Available at < https://normy.normoff.gov.sk/norma/136325/ >
- [3] ABB, "Terra AC wallbox", [online]. [cit. 2024-03-18] Available at: https://new.abb.com/ ev-charging/terra-ac-wallbox
- [4] ABB, "EVLunic Pro M. Charging Station. Configuration manual V 1.02", [online]. [cit. 2024-03-18] Available at: https://library.e.abb.com/public/53089a4cd37c470ba42ade1b66baac86/EVLunic%20Pro%20M ConfigurationManualV1.02.pdf>
- [5] Medved, D., et. al., "Assessing the Effects of Smart Parking Infrastructure on the Electrical Power System", in: *Energies* 2023, 16, 5343. doi: 10.3390/en16145343.
- [6] Lakshmi, G. S., Rubanenko, O., Hunko, A., "Control of the Sectioned Electrical Network Modes with Renewable Energy Sources", in: *Proc. of the 2021 International Conference on Sustainable Energy and Future Electric Transportation (SEFET)*, Hyderabad, India, 21-23 January 2021; pp. 1–6, doi: 10.1109/SeFet48154.2021. 9375781.
- [7] Ren, G., "MATLAB/Simulink-Based Simulation and Experimental Validation of a Novel Energy Storage System to a New Type of Linear Engine for Alt. Energy Vehicle Applications", *IEEE Trans. Power Electron.* 2018, 33, 8683–8694, doi: 10.1109/TPEL.2017. 2784563.
- [8] Belan, A., Cintula, B., Cenky, M., Janiga, P., Bendik, J., Eleschova, Z., Simurka, A. "Measurement of Static Frequency Characteristics of Home Appliances in Smart Grid Systems", *Energies* 2021, 14, 1739. doi: 10.3390/en14061739.
- [9] Pastor, M., Zilkova, J., Girovsky, P., "Output Voltage Control of Soft-Switching DC-DC Converter", in: *International Conference on Electrical Drives & Power Electronics (EDPE)*, 2019, pp. 342–346, doi: 10.1109/EDPE.2019.8883883.



DOI: 10.47745/auseme-2024-0013

Model Predictive Control of Aerodynamic Levitation Systems

Áron CZIMBALMOS¹, Áron FEHÉR², Lőrinc MÁRTON²

 Department of Mechanical Engineering, Faculty of Technical and Human Sciences, Sapientia-Hungarian University of Transylvania, Tg. Mureş, e-mail: aron.czimbalmos@gmail.com
 Department of Electrical Engineering, Faculty of Technical and Human Sciences, Sapientia-Hungarian University of Transylvania, Tg. Mureş, e-mail: {fehera, martonl}@ms.sapientia.ro

Manuscript received September 23, 2024; revised October 10, 2024

Abstract: Airjet-driven levitation systems are an important emerging technology, as they can ensure the contactless movement of objects. From a control engineering perspective, the position set-point tracking of the levitating object poses many challenges because the aerodynamic characteristics of the air jet used for levitation are difficult to model. The unmodelled disturbances significantly affect the control performances. Moreover, the bound constraints imposed by the mechanical design and the applied actuators should also be considered during controller design.

In this work, we present a motion control approach suitable for vertical levitation systems actuated by a fan-induced air jet. We developed the necessary hardware and software elements for the control equipment of the levitation system. We apply the MPC (Model Predictive Control) approach to ensure high-precision position regulation under various aerodynamic conditions with bounded control signals. We validate the applicability of the control system through simulation and real-time experimental measurements.

Keywords: Aerodynamic levitation, Model predictive control, constrained control, model-based control.

1. Introduction

Nowadays, we encounter control systems both in industrial implementations [13] and in household applications [10]. These systems can gather information from their environment and, by processing it, provide a real-time actuation for a controlled plant to achieve a prescribed objective [9].

A challenging control task is the implementation of the positioning in levitation systems. In these systems, a fan provides airflow that counterbalances the ball's weight. The ball hovers on the air cushion, which reduces friction and enables precise and stable movement of the ball within the tube, see *Fig. 1*.

Aerostatic bearings have several advantages over other bearing technologies [7]:

- They have low friction, which improves accuracy and efficiency;
- They do not require lubricants, which simplifies maintenance;
- They are lightweight.

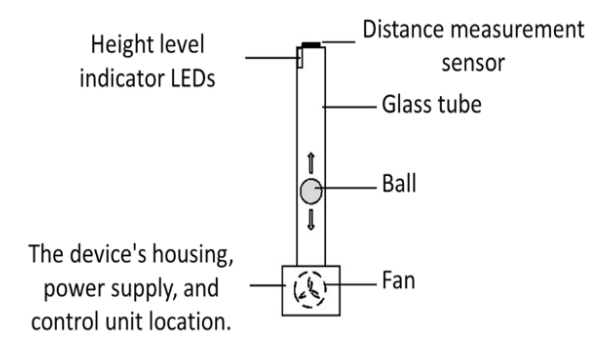


Figure 1: A schematic drawing of the levitation system

In the industry, for instance, air bearings can be used in 3D printing [14]. The technology can also be beneficial in material handling tasks, where levitating systems are used for the automated movement of objects [15]. These systems can also help to understand complex control methods effectively. Therefore, it can be used in education as a didactic tool since it is a relatively low-cost and spectacular demonstrative device [5]. Moreover, the ball levitation system can be applied for various entertainment purposes, such as demonstrations, concerts, or special events. Additionally, it can aid in perfecting "wind tunnels" or air chambers, which offer a great opportunity for individuals who want to experience the sensation of skydiving without any risk, expensive courses, or practical knowledge [4].

1.1. Previous Research

In earlier scientific papers discussing the implementation of such systems, classical PID control has been mostly used [12]. The PID controller design can be performed based on linearized input-output models, and they have the advantage of low computational costs. There are several similar implementations of such a levitation control approach. The paper [3] presents a low-cost air

levitation system to be used in both a virtual and a remote version. This work also proposes a linear single input single output model for controller design.

More complex levitation models were also developed. A dynamic skydiver levitation model and simulator is developed in [4], combining bio-mechanical, aerodynamic, and dynamic equations of motion.

To deal with non-linear physical behaviour exhibited by air-jet systems and to achieve high-precision and stable position control, advanced control methods such as those using artificial intelligence can also be applied [6].

1.2. Objectives

The aim of this work is to design and implement a levitation system that applies advanced control methods, which can be applied in education, industry, and even in the medical field for contactless, sterile movements with reduced frictional effects.

We hypothesize that by applying MPC (Model Predictive Control), we can implement a levitation system with outstanding set-point tracking and disturbance attenuation proprieties that can be utilized in education, industry, and even healthcare for contactless handling of levitation objects. The Model Predictive Control (MPC) system can achieve an optimal balance between implementation costs and high-precision tracking, even when disturbances are present.

2. System modelling

2.1 Equations of motion

Consider a ball under the influence of aerodynamic drag force, which ensures its levitation along a vertical tube. Its equation of motion along the vertical axis is given by:

$$m\ddot{x}(t) = F_{aero}(t) - mg, \qquad (1)$$

where x is the ball position, m > 0 is the mass of the ball, g > 0 is the gravitational acceleration, and t > 0 denotes the continuous time.

The aerodynamic drag force (F_{aero}) is produced by a rotating fan, and it depends on the difference between the ball velocity \dot{x} and wind velocity v_w produced by the rotating fan. A quadratic force-velocity relation is assumed:

$$F_{aero}(t) = b(v_w(t) - \dot{x}(t))^2 \text{sign}(v_w(t) - \dot{x}(t)),$$
 (2)

The parameter b > 0 depends on the ball's cross-section area, the aerodynamic drag coefficient, and air density.

Similar to previous studies, it is considered that the speed of the wind produced by the fan is proportional to the fan's angular velocity (ω) , i.e.

$$v_w(t) = K_w \omega(t) + C_w , \qquad (3)$$

where K_w , $C_w > 0$ are constant parameters. The angular speed of the fan is generated by an electromechanical actuator, with time constant $T_u > 0$ and static gain K_u . It is modelled as:

$$T_u \dot{\omega}(t) + \omega(t) = K_u u(t) , \qquad (4)$$

where u is the control input of the actuator (manipulated variable).

2.2 Control-oriented modelling

The controlled output of the process is the ball position (x), and the control input is the actuator motor input voltage u.

Based on the equations of motion, a state-space model can be formulated, which can be applied to controller design:

$$\begin{cases} \dot{\omega}(t) = -\frac{1}{T_u}\omega(t) + \frac{K_u}{T_u}u(t) \\ \dot{x}(t) = v(t) \end{cases}$$

$$\dot{v}(t) = \frac{b}{m} \left(K_w \omega(t) + C_w - v(t) \right)^2 \operatorname{sign} \left(K_w \omega(t) + C_w - v(t) \right) - g$$

$$y(t) = x(t)$$

$$(5)$$

Here y(t) denotes the controller output.

To obtain the dynamic relation between the input and the output, it is assumed that in equilibrium, the ball levitates around a (constant) equilibrium position x^* . In the case of the controlled system, this can be the prescribed controller set-point $(x_{ref}>0).$

The aerodynamic force (2) is linearized around this equilibrium:

$$F_{aero}(t) \approx 2bv_w^*(K_w\omega(t) - \dot{x}(t)). \tag{6}$$

In the equilibrium state, the ball velocity is zero ($v^* = 0$). The corresponding fan speed is (ω^*) and equilibrium control input yields as:

$$\begin{cases} x^* = x_{ref} \\ v^* = 0 \\ \omega^* = \frac{1}{K_w} \left(\sqrt{\frac{mg}{b}} - C_w \right) \\ u^* = \frac{1}{K_u} \omega^* \end{cases}$$
 (7)

The linearized system model can be written as

$$\begin{cases}
\dot{\mathbf{z}}(t) = A\mathbf{z}(t) + Bu(t) \\
y(t) = Cz(t) + Du(t)
\end{cases}$$
(8)

where the state vector is

$$\mathbf{z} = (\omega(t) - \omega^* \quad x(t) - x^* \quad v(t) - v^*)^\mathsf{T} \text{ and,}$$
 (9)

$$A = \begin{pmatrix} -\frac{1}{T_u} & 0 & 0 \\ 0 & 0 & 1 \\ 2\frac{bK_w}{m}(K_w\omega^* + C_w) & 0 & -2\frac{bv}{m}(K_w\omega^* + C_w) \end{pmatrix},$$

$$B = \begin{pmatrix} K_u \\ T_u \end{pmatrix}^{\mathsf{T}}, C = (0 \quad 1 \quad 0), D = 0.$$
 (10)

It is easy to see that (A, B) and (A, C) are both full rank, so the linearised system is observable and controllable.

3. Controller design

2.1 Control objective:

Let a constant prescribed position set-point $x_{ref} > 0$. Design the control input u such that $\lim_{t\to\infty} (x_{ref} - x(t)) = 0$. The ball's position and velocity are considered known (measurable).

To deal with the gravity-induced disturbance term and other unmodelled disturbances that could affect the motion dynamics, e.g. frictional disturbances in the actuator's mechanical transition or accidental tube wall-ball collision, a state feedback servo controller with integral term can be considered:

$$u(t) = K_P \left(x_{ref} - x(t) \right) - K_D x \dot{t} - K_\omega \omega(t) + K_I \int_0^t \left(x_{ref} - x(\tau) \right) d\tau , \qquad (11)$$

where K_P , K_I , K_D , and K_{ω} are positive controller gains.

2.2 LQR (Linear Quadratic Regulator) design:

The control gains can be designed by considering the extended system, which includes the integral of the controlled position output:

$$\begin{pmatrix} \dot{\mathbf{z}}(t) \\ \dot{x}_{I}(t) \end{pmatrix} = \begin{pmatrix} A & \mathbf{0} \\ C & 0 \end{pmatrix} \begin{pmatrix} \mathbf{z}(\mathbf{t}) \\ x_{I}(t) \end{pmatrix} + \begin{pmatrix} B \\ 0 \end{pmatrix} u(t) , \tag{12}$$

where $\mathbf{0}$ is a zero-column vector with corresponding dimension, and x_I is the integral of the state x.

Based on this, the controller can be obtained by using an LQR approach: design the controller gains such that the control minimises the following functional:

$$J = \int_0^\infty (\tilde{\mathbf{z}}^T(\tau)Q\tilde{\mathbf{z}}(\tau) + Ru^2(\tau)) d\tau.$$
 (13)

Here, $Q \in \mathbb{R}_{>0}^{4\times 4}$ and $R \in \mathbb{R}_{>0}$ are design parameters. The solution of the LQR problem is given by [8]:

$$\begin{cases} P\tilde{A} + \tilde{A}^T P + P\tilde{B}R^{-1}\tilde{B}^T P = -Q \\ K = R^{-1}\tilde{B}^T P \end{cases}, \tag{14}$$

where the controller gains are the entries of the row vector $K = (K_P K_D K_{\omega} K_I)$.

2.2 MPC (Modell Predictive Control) design:

It should also be considered that the control signal has to be always positive and is subject to an upper limit. Moreover, the controlled position state is also bounded. The boundedness of the control input and the controlled output can be considered by applying the MPC control approach [2]. MPC is a sophisticated control strategy extensively used in various industries to optimise the performance of complex processes. It involves predicting future process behaviour using a dynamic model and solving an optimisation problem at each control step to determine the optimal control actions. MPC can handle multivariable systems and constraints effectively, making it invaluable for maintaining process variables within desired limits while maximising efficiency and productivity [11].

First, we discretised the model (8) using the forward-Euler scheme:

$$\begin{cases}
z[k+1] = (T_s A + I_3) z[k] + T_s B u[k] \\
y[k] = C z[k] + D u[k]
\end{cases},$$
(15)

where T_s is the sampling period, and k = 0, l, ... denotes the discrete time.

Based on the discretised model (15), we designed a finite horizon model predictive controller that solves the following bounded optimisation problem:

minimise
$$\sum_{k=0}^{N} q (x_{ref} - y[k])^{2} + r_{1} \Delta u[k]^{2} + r_{2} u[k]^{2}$$
subject to
$$M(u \ \Delta u \ y)^{T} \leq p$$

$$z[k+1] = (T_{s}A + I_{3})z[k] + T_{s}Bu[k]$$

$$y[k] = Cz[k] + Du[k]$$
(16)

Although we created a finite horizon optimisation, the Meyer-term can be neglected since $x_{ref} - y[N] = 0$.

The terms in the inequality constraint are taken as:

$$M = \begin{pmatrix} 1 & 0 & 0 \\ -1 & 0 & 0 \\ 0 & 1 & 0 \\ 0 & -1 & 0 \\ 0 & 0 & 1 \\ 0 & 0 & -1 \end{pmatrix}, \ p = \begin{pmatrix} u_M \\ -u_m \\ \Delta u_M \\ -\Delta u_M \\ x_M \\ 0 \end{pmatrix}, \tag{17}$$

where u_M , u_m are the maximum and minimum values of the control signal, Δu_M is the maximum control rate, x_M is the maximum value of the position state. Since this implementation is an implicit MPC design, the controller solves the dynamic program (16) after every sampled data, then feeds the last value from the control sequence u into the plant.

If all of the states, outputs and inputs are bounded, an explicit MPC scheme can be formulated in the form

$$u[k] = Fz[k] + G, \tag{18}$$

where F, G matrices are state-dependent gain matrix and bias vector, respectively, with the appropriate dimensions [1].

4. Simulation measurements

To test the applicability of the Model Predictive Control approach on the levitation system, first, simulation experiments were performed in Matlab/Simulink environment. During the simulations, the dynamics of the process is considered to be described by the model (5). However, the linearised model (8) was applied for control design.

During the simulation the following system parameters were considered: m = 27g, $g = 9.81m/s^2$, $T_u = 1ms$, $K_u = 20$, $b = 9.202 \cdot 10^{-3}$, $K_w = 1.979 \cdot 10^{-3}$, $C_w = 0.369$.

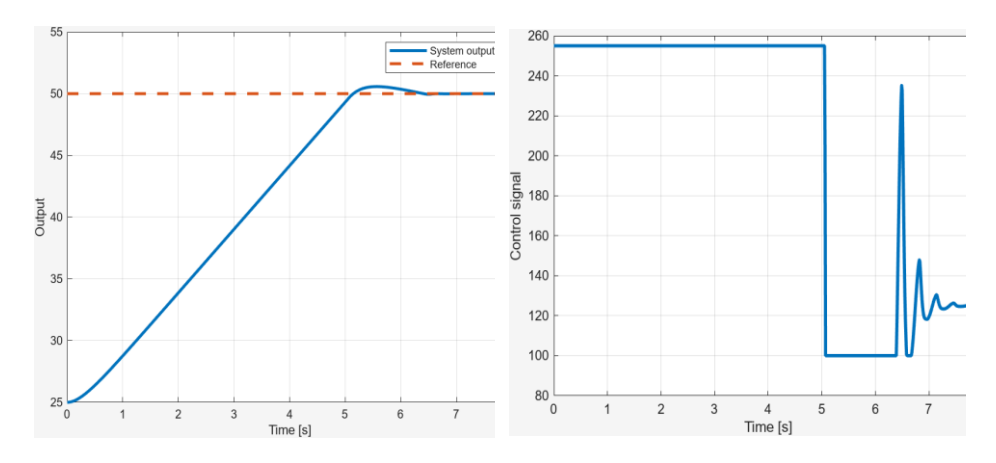
We used the set-point $x_{ref} = 25cm$ as the equilibrium point for linearisation.

In the optimisation problem (16), we chose the cost weights q = 6.6502, $r_1 = 0.0135$, first without the manipulated variable present in the cost function (i.e $r_2 = 0$), then with the manipulated variable also present (i.e. $r_2 = 0.02$). The manipulated variable was bounded in the interval $u \in [100,255]$, and the rate of the manipulated variable was bounded in the interval $\Delta u \in [-10,10]$. The output variable was kept in the physical boundaries $y \in [0,55]$.

The input and output bounds are cumulated in a vector as

$$p = (10 - 10500255 - 100)^{T}. (19)$$

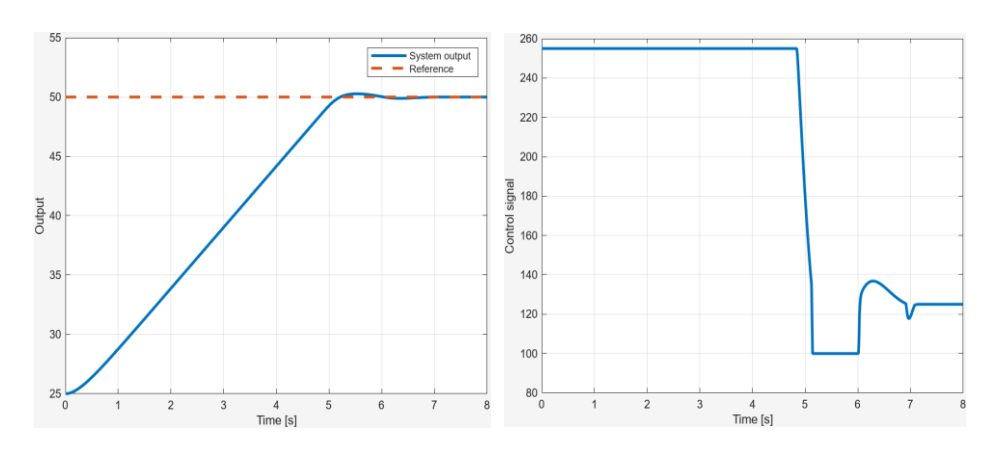
The prediction horizon was set to 8 samples, while the control horizon was kept at 2 samples. The MPC structure was created in MATLAB using the mpc function of the Model Predictive Control Toolbox, and the controlled system was simulated for 800 samples (equivalent to 8 seconds).



- (a) Output trajectory of the controlled system
- (b) Control signal output of the MPC

Figure 2: MPC control ($x_{ref} = 50 \text{ cm}, r_2 = 0$)

Fig. 2a shows the reference signal and the controlled output of the closed loop system, while Fig. 2b shows the control signal when the control rate weight from (16) is $r_2 = 0$.



- (a) Output of the controlled system
- (b) Control signal output of the MPC

Figure 3: MPC control ($x_{ref} = 50 \text{ cm}, r_2 = 0.02$)

Here, we can see that because of the unmodelled process, nonlinearities during controller design, overshot may appear during the transient state, but the control dampens it, ensuring precise steady-state reference tracking.

Fig. 3a shows the reference signal and the controlled output of the closed loop system, while Fig. 3b shows the control signal when the control rate weight is $r_2 = 0.02$. Adding a small penalty to the control signal dampens the controlled output. The output overshoot is smaller but the settling time is longer.

5. Experimental Measurements

5.1 Control Hardware

To implement the levitation control algorithm, an ESP32 microcontroller was applied, which reads data from distance sensors, an optical encoder, and a mechanical button. It displays output data on a screen and sends control signals to the motor via the motor controller. The electrical diagram of this equipment is shown in *Fig. 4*.

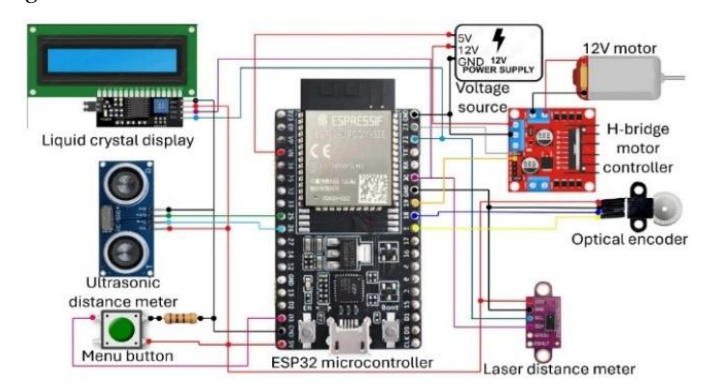


Figure 4: Electrical diagram of the control circuit

The ESP32 is a highly popular microcontroller for control applications, known for its rapid processing capabilities and extensive built-in features. Thanks to its dual-core processor, it provides exceptional execution speed and can concurrently handle various tasks.

Due to its compact size, accuracy, and speed, we chose a *laser distance sensor* for distance measurement. The *VL53L0X* is a highly integrated laser distance sensor that uses Time-of-Flight (ToF) technology developed by STMicroelectronics for precise distance measurement. This sensor is small and has low power consumption, making it an ideal choice for applications where the space is limited and energy efficiency is important. For this reason, it was chosen to monitor the ball's position in the tube.

The system allows to set the reference height of the object by a moving human hand. Monitoring the hand position is done by an *HC-SR04* ultrasonic distance sensor. It provides an easy-to-use, reliable, and low-cost solution for distance measurement, which is why it is widely used in electronics, robotics, automation, and other fields.

The fan is powered by a 12V DC brushed motor. The brushed DC motor is an excellent choice for low torque applications because it offers variable speed control capabilities. An L298N motor controller was necessary because the microcontroller's PWM (Pulse Width Modulation) duty cycle operates at a low voltage of 3.3V, while the motor's operating voltage is 12V. Using this module along with an external voltage source, we were able to easily control the motor from the microcontroller. To measure the motor's rotational speed, an incremental encoder was needed. For this purpose, we used a 100-resolution optical encoder. A 16x2 LCD and a push-button were utilised for displaying data and implementing a comprehensive menu system, allowing efficient human-machine interaction.

5.2 Mechanical setup

The levitation system is implemented in a metal-framed box with pressed plywood sides. Levitation occurs in a 55 cm long glass tube using a hairdryer fan.

We designed and 3D printed the necessary mechanical parts to secure the glass tube, the 2x16 LCD display, and the ultrasonic sensor. Two supporting components were needed for positioning and securing the fan and the encoder.

These parts were also custom-designed and then printed using a 3D printer. A 3D model of the entire assembly was created before implementation. This model is shown in *Fig. 5a*, and the built device is shown in *Fig 5b*.





Figure 5: (a) 3D model of the equipment (b) Implemented equipment

5.3. Experimental results

Control experiments were performed on the presented levitation equipment to evaluate the applicability of the proposed control schemes.

The implementation form of the controller is given by the discretised form of the control algorithm (11), and it also takes into consideration the state and input constraints. In this case, the upper and lower bounds for the controlled state and controlled signal were chosen as 185 < u < 230, 0 < x < 55 (cm). The high value of the control signal's lower bound is motivated by the fact that under these values the wind speed generated by the fan is not able to initiate the motion of the ball.

It was taken into consideration that the time constant of the T_u is comparable to the applied sampling period, hence the dynamics in the first equation in (5) can be neglected, and $\omega \approx K_u u$. It yields that in the control (11) the term $K_\omega \omega$ can also be neglected. The controller parameters of the other terms are $K_P = 0.625$, $K_D = 13$, $K_I = 0.035$.

The experimental results are presented in Fig. 6a and Fig. 6b for $x_{ref} = 5$ cm. The simulation results show that despite the high-frequency measurement noises and unmodelled disturbances, e.g. accidental tube-ball collisions, the controlled system is capable of precise set-point tracking.

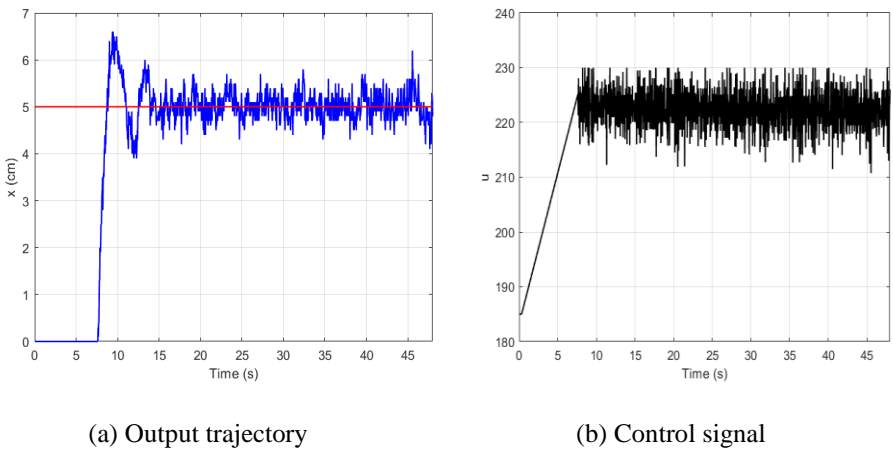


Figure 6: Real-time measurements ($x_{ref} = 5 cm$)

The control experiment was also performed for $x_{ref} = 50 \text{ cm}$. The same controller was applied as during the first control experiment. The experimental results presented in Fig. 7a and Fig. 7b show that similar steady-state tracking performances can be achieved as in the case of the previous experiments. During the transients, the effect of the applied control bounds can also be observed.

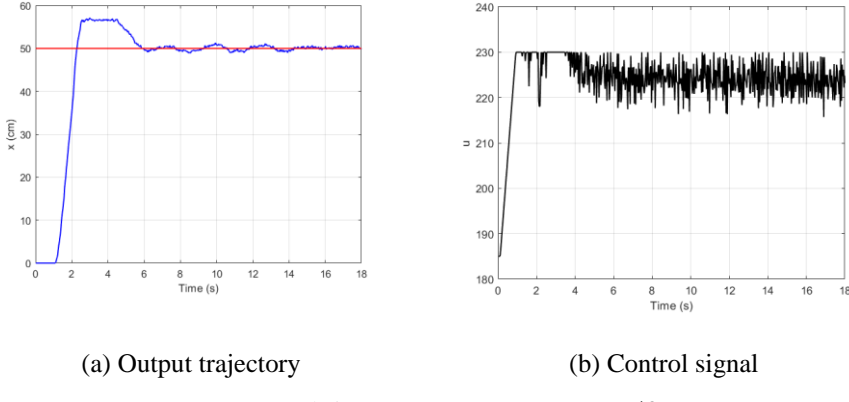


Figure 7: Real-time measurements ($x_{ref} = 50 \text{ cm}$)

6. Conclusions

Aerodynamic levitation is an effective technology for contactless actuation of delicate objects. In spite of the fact that the motion dynamics can be described by the classic Newtonian laws along one axis, the precise modelling of the aerodynamic force in the dynamic motion model can hardly be performed. This is why in the control-oriented modelling for motion control, disturbances should also be considered. On the other hand, it has to be taken into consideration, that the aerodynamic force is upper-bounded due to the fact that the electromagnetic actuator that rotates the fan can generate upper-bounded torques.

Acknowledgements

Publishing of this journal is supported by the Institute for Research Programmes of the Sapientia University. The first author's research was supported by Balassi Bálint Scholarship program.

References

- [1] Bemporad, A., Pistikopoulos, E., Morari, M., and Dua, V., "The explicit solution of model predictive control via multiparametric quadratic programming", in *Proceedings of the 2000 American Control Conference. ACC (IEEE Cat. No.00CH36334)*, vol. 2, pp/ 872–876, 2000.
- [2] Bemporad, A., Borrelli, F., and Morari, M., "Predictive Control for Linear and Hybrid Systems", *Cambridge University Press*, 2017.
- [3] Esquembre, F., Chacon, J., Saenz, J., Diaz, J. M., and De la Torre, L., "Design of a low-cost air levitation system for teaching control engineering", *Sensors*, 17(10):2321, 2017.
- [4] Clarke, A., and Gutman, P.-O., "A dynamic model of a skydiver with validation in wind tunnel and free fall", *IFAC Journal of Systems and Control*, 22:100207, 2022.
- [5] de Oliveira Pedra, A. C., Caldeira, A. F., Maidana, C. F., Rech, C., and Venturini, S., F., "Feedback control applied to a low cost ball-in-tube air levitation plant", *Revista Ciencia e Natura*, 45, 2023.
- [6] Garcia, Y., "A self-tuning pid controller design based on fuzzy logic for nonlinear chemical processes", in 2020 IEEE ANDESCON, pp. 1–6, IEEE, 2020.
- [7] Singh, A. K., Arora, K., Jamwal, K. S., and Paswan, S. K., "Performance analysis of a designed aerostatic bearing with effect of surface roughness", *Iranian Journal of Science and Technology, Transactions of Mechanical Engineering*, pp. 1–19, 2023.
- [8] Vrabie, D., Lewis, F. L., and Syrmos, V. L., "Optimal Control", John Wiley & Sons, 2012.
- [9] Fehér, Á., and Márton, L., "Irányítástechnika. Laboratóriumi útmutató", Scientia, 2020.
- [10] Ou, C.-H., and Rambe, K. H., "Enabling smart home energy management through gesture-based control and IOT technology", in *2023 International Conference on Consumer Electronics-Taiwan (ICCE-Taiwan)*, pp. 815–816. IEEE, 2023.
- [11] Seborg, D. E., "Process Dynamics and control", John Wiley Sons, 2019.
- [12] Jadlovska, A., Tkacik, M., Jadlovska, S., and Tkacik, T., "Design of aerodynamic ball levitation laboratory plant", *Processes*, 9(11):1950, 2021.
- [13] Su, Q., Geng, Y., and Tu, Y., "Enabling secure and efficient data sharing and integrity auditing for cloud-assisted industrial control system", in *Big Data and Security: First International Conference, ICBDS 2019*, Nanjing, China, December 20–22, 2019, Revised Selected Papers 1, pages 514–528. Springer, 2020.
- [14] Wiley, D., "Time Machined: Clocks, Values, and Digital Computation", PhD Thesis, New York University, 2021.
- [15] El-Baz, D., Ning, H., and Zhu, L., "Survey on air levitation conveyors with possible scalability properties", in 2015 IEEE 12th Intl Conf on Ubiquitous Intelligence and Computing and 2015 IEEE 12th Intl Conf on Autonomic and Trusted Computing and 2015 IEEE 15th Intl Conf on Scalable Computing and Communications and Its Associated Workshops (UIC-ATC-ScalCom), pages 802–807. IEEE, 2015.



DOI: 10.47745/auseme-2024-0014

Implementation of Network Data Analysis Using the Neo4j Graph Database

Katalin FERENCZ¹, Ernő RIGÓ², József DOMOKOS³, Levente KOVÁCS⁴

¹ Doctoral School of Applied Informatics and Applied Mathematics, Óbuda University, Budapest, Hungary, e-mail: ferenczkatalin@stud.uni-obuda.hu
² Institute for Computer Science and Control (SZTAKI), Hungarian Research Network (HUN-REN), Budapest, Hungary; Doctoral School of Applied Informatics and Applied Mathematics, Óbuda University, Budapest, Hungary, e-mail: rigo.erno@sztaki.hun-ren.hu
³ Faculty of Technical and Human Sciences, Târgu Mureş, Sapientia Hungarian University of Transylvania Târgu Mureş, Romania, e-mail: domi@ms.sapientia.ro
⁴ John Von Neumann Faculty of Informatics, Óbuda University Budapest, Hungary, e-mail: kovacs@uni-obuda.hu

Manuscript received November 23, 2024; revised December 9, 2024

Abstract: The analysis of network data is essential alongside the growth of digitalization and the Internet of Things (IoT). Managing complex connections in modern networks poses significant challenges for traditional relational databases due to their tabular structure and computational limitations. Graph databases, like Neo4j, provide flexible data management by modelling relationships with nodes and edges. This paper shows how Neo4j enhances data analysis efficiency in complex networks, enabling faster anomaly detection, pattern recognition, and predictive model development. It highlights the advantages of graph databases, including quick querying and effective handling of complex relationships, and presents real-world applications using various algorithms.

Keywords: Graph Database, Neo4j, Network Data Analysis, Clustering, IoT.

1. Introduction and related work

The analysis of network data is becoming increasingly important with the advancement of the Internet of Things (IoT) and digitalization. Modern networks operate through complex relationships and continuous data flows, making the interpretation of such data challenging. The methods used by traditional relational databases struggle to handle the complex relationships between network data, as these systems store information in tables, requiring significant computational capacity for analysis, particularly when dealing with large data sources.

The application of graph databases in the field of data analysis is gaining increasing popularity, particularly in the analysis of complex relational networks, where the efficiency of traditional databases encounters limitations. Analyzing such structures requires significant computational capacity and complex queries, which often slow down data processing [[6]].

To address the challenges associated with the usage of relational databases integrated into systems containing large datasets, the transformation of time series data into graph structures is increasingly seen as a valuable approach. This is because applying this data format offers numerous advantages in executing analysis and data processing tasks.

Graph databases, such as Neo4i, offer a more flexible approach by handling data in the form of nodes and edges (relationships between the nodes). This enables faster and more efficient querying and analysis of relationships within networks, particularly when dealing with complex relational structures and large volumes of data. Graph databases, such as Neo4j, are capable of intuitively modeling relationships between data points using nodes and edges. This method is particularly useful in the analysis of network data, such as in IoT systems, where the connections between devices form a complex network. In such systems, the detection of anomalies, identification of patterns, and the development of predictive models are of critical importance [4]. With this new type of analytical method, anomalies can be detected more easily, patterns can be identified, and more advanced predictive models can be developed, improving decision-making and forecasting processes. The advantages of graph structures include fast and flexible data querying, which not only simplifies the examination of relational networks but also facilitates tasks such as pathfinding and community detection. Additionally, Neo4j and other graph databases support the use of advanced analytical algorithms, enabling a deeper understanding of the behavior of complex systems.

Many scientific papers presenting results in this research field were published. This is due to the large interest of the researchers on the topic, and also related to the capability to solve real problems of IoT systems with the graph database approach.

The scientific publication by Afandi, M.I. et al. [1] discusses the development of a research graph database using Neo4j, which enables to conduct efficient multi-perspective data analysis. Since traditional relational databases struggle with handling complex queries that involve interconnected research data, they proposed a graph database model to overcome this limitation by representing data related to scientific publications, researchers, connections, and research projects. The study demonstrates that Neo4j outperforms relational databases in executing queries for multidimensional analysis.

The article written by Almabdy, S. [2] compares the performance and functionalities of relational databases and graph databases in handling social network data. The study concludes that graph databases are better suited for managing and analyzing social networks compared to traditional relational databases, offering advantages in storage flexibility, query performance, and real-time data processing.

The study "Graph Databases: Neo4j Analysis" by Guia, J. and others [3] focuses on the growing relevance of graph databases, particularly Neo4j, due to the increasing complexity and interconnectedness of data, especially in fields such as networks.

2. Comparison between graph database, NoSQL and SQL databases

Efficient data storage and analysis are crucial in the modern technological environment, especially when handling large and complex datasets. The differences between database types significantly affect how data can be processed. SQL, NoSQL, and graph databases each offer different approaches to data storage and management. In this comparison, we will review the fundamental characteristics of all three types, as well as their advantages and disadvantages in terms of analyzing large and complex datasets.

SQL databases (relational databases) store data in tables with a strictly structured schema. There are defined relationships between the data, and the SQL language is used for queries. These databases are highly efficient in managing well-structured, organized data. SQL databases reliably handle structured data and allow easy querying of relationships between records. They can also store large amounts of data. However, their disadvantage is that they are less suitable for managing complex networks of relationships and hierarchies. Additionally, they are less flexible when it comes to process rapidly changing or diverse types of data [2].

NoSQL databases are non-relational databases that enable the storage of unstructured and rapidly changing data. They have flexible schemas and can handle various data formats, including documents, key-value pairs, columns, time series, and graphs.

Graph databases represent data using nodes and edges, making them ideal for handling complex relationships and networks. They are particularly useful in application areas such as social networks, IoT systems, and network analysis. Graph databases enable fast and efficient queries, especially for datasets with complex relationships and networks. These databases easily handle dynamically changing data and connections, making them well-suited for analyzing large and complex networks [5]. However, their drawback is that they require specialized algorithms, which necessitate specific expertise. Additionally, they are less

widespread than SQL or NoSQL systems for now, providing less support for their users [6].

The following table (*Table 2*) provides a brief comparison of the three database types based on some of the most important features.

Table 1: Comparison of SQL, NoSQL and Graph databases

properties	SQL	NoSQL	Graph
data structure	relational, tabular structure	non-relational, unstructured	nodes and edges
schema	rigid schema, defined relationships	flexible scheme	the schema is based on relationships, taking into account dynamically changing data and relationships
scalability	vertical	horizontal	horizontal
data consistency advantage/	ACID – guaranteeing data consistency well-structured,	data consistency is not always ensured (BASE model) unstructured and	ACID compliant, but depends on the type of analysis
efficiency	organized data	rapidly changing data, can handle a wide variety of data formats: documents, keyvalue pairs, columns	complex relationships and networks, relationship-based analyses
disadvantage	less suitable for handling complex relationship networks and hierarchies, not flexible	frequent data duplication, data consistency is difficult to maintain	special knowledge is required to implement data analysis

The key to successful database management in the future lies not in pitting different types of databases against one another, but in leveraging their technological strengths to select the most appropriate solution based on the specific requirements of the task at hand. For instance, in cases where structured

data management is required, relational databases remain the optimal choice. Conversely, in scenarios where the interpretation of relationships and connections is of paramount importance, graph-based databases provide the most suitable solution. Building on this perspective, making the right choice requires careful consideration of the key database properties outlined in the table above. These properties serve as critical criteria for aligning the database selection with the specific demands and objectives of the task.

Based on the characteristics, we selected graph-based databases for the analysis of network data in our research. The market offers a wide range of graph database solutions, such as Amazon Neptune, ArangoDB, AllegroGraph, Neo4j, OrientDB, and others [5]. Amazon Neptune supports both the Property Graph and Resource Description Framework (RDF) models, providing high availability and scalability. ArangoDB is a multi-model database that handles graph, document, and key-value data, offering flexibility and high performance. OrientDB is ACID-compliant and features an SQL-like query language, simplifying graph management and scalability. AllegroGraph specializes in knowledge graph construction and temporal graph management, with strong support for RDF and SPARQL. Azure Cosmos DB is a globally distributed, scalable database supporting graph models through the Gremlin API. Neo4i, a dedicated graph database, is based on the Property Graph model and employs the Cypher query language. It excels in graph algorithms and provides flexible integration with various systems, making it ideal for network analysis and the management of complex relational data.

Neo4j takes a multifaceted approach to scalability, integrating horizontal and vertical scaling strategies to manage extensive graph datasets effectively. The platform's Fabric architecture facilitates horizontal scaling by enabling the sharding of large graphs across multiple servers, allowing for distributed data processing and federated querying across these shards. This design ensures that even expansive graphs can be handled efficiently. Concurrently, Neo4i's clustered architecture supports vertical scaling, permitting the augmentation of resources such as CPU and memory to individual nodes, thereby enhancing performance for complex queries and substantial workloads. Additionally, Neo4i incorporates in-memory graph caching, which stores frequently accessed data in memory to expedite query response times. The platform also offers cloud-based Database-as-a-Service (DBaaS) solutions, providing automatic scaling and resource management to accommodate fluctuating workloads seamlessly. Collectively, these features enable Neo4j to maintain high performance and reliability across diverse application scenarios, effectively addressing the challenges associated with large-scale graph data management.

For our research, we selected the Neo4j graph database.

3. Network data analysis using graph databases

To explore the potential applications of Neo4j graph databases, we tested the capabilities of graph structures on the data from a network dataset. This dataset consists of network flow and vulnerability data collected from public interfaces of a networked communication system and contains several weeks of records. The anonymized version of the network dataset used for the research is publicly available [9].

The dataset utilized in this study is a collection of network traffic data and vulnerability scan reports gathered over a 30-day period from various real-world network environments. These environments encompass a diverse array of hosts, running multiple operating systems, including Windows, Linux, and macOS, as well as various networked devices and appliances. This diversity provides a comprehensive overview of typical network traffic patterns and potential security vulnerabilities across different types of networks. The dataset includes security and network flow originating from three distinct network configurations, each with unique traffic levels and host counts: (VLAN11) a public server network characterized by low traffic and approximately 30 hosts; (Cloud) a public cloud service network exhibiting moderate traffic with roughly 100 hosts; and (VLAN23) a private office network with high traffic, supporting around 200 hosts. This distribution of networks allows for a detailed examination of different network traffic behaviors and security postures, providing a basis for developing and testing new algorithms and tools. The data is accessible in multiple formats to accommodate various analysis needs. NetFlow data, detailing one-day traffic snapshots, is available in CSV, JSON, and RAW formats, facilitating comprehensive analysis from simple spreadsheet manipulations to more complex JSON-based data interactions. To complement the traffic analysis, security scan reports, which identify potential vulnerabilities within the networks, are presented in CSV, filtered CSV, HTML, and XML formats. This multi-format approach ensures wide compatibility with existing analytical tools, enabling researchers to conduct thorough and flexible analyses tailored to specific objectives. This rich dataset offers significant potential for advancing research in network security and traffic analysis.

The network data is divided into five main nodes, and the types of relationships between these nodes are defined. The nodes and relationships were assigned properties based on the information collected during network data monitoring. The structure of our dataset, according to the nodes and relationships, is as follows:

A. Nodes in the dataset

The following nodes are defined in the dataset:

- VulnService: This node type is defined based on IP addresses and contains important attributes such as the IP address, the last activity timestamp and the network name;
- VulnPort: This node is defined based on protocol types and port numbers, which are associated with the IP address, last seen status, service name, network name, port number, and the protocol used;
- VulnServiceGroup: This is an artificially created group that uses the first three segments of the IP addresses, removing the last segment. As a result, it creates a group of IP addresses that share the same first three segments;
- NVDCVE: This node is defined based on CVE (Common Vulnerabilities and Exposures) identifiers issued by the National Vulnerability Database (NVD), with key attributes including the identifier and severity;
- ServiceType: This node defines the types of services, for example "http protocol over TLS/SSL", "Simple Mail Transfer", "PostgreSQL Database", "Microsoft-DS", "Rockwell CSP2", etc.

B. Relationships in the dataset:

There are defined 6 types of relationships between the nodes as they follow:

- Accesses: The relationship is directed from a VulnService node to a VulnPort node, indicating that VulnService accesses the information managed by VulnPort;
- ProvidedBy: This relationship is directed from a VulnPort node to a VulnService node, meaning that VulnPort provides services or functions to VulnService;
- PartOfGroup: The VulnService node is part of the VulnServiceGroup node, and the relationship is directed from VulnService to the VulnServiceGroup, representing group membership;
- AccessesGroup: This relationship exists between VulnServiceGroup nodes, indicating how certain groups can access each other's resources or information.
- ImpactedBy: The relationship is directed from a VulnPort node to a NVDCVE node, meaning that VulnPort's operations are influenced by vulnerabilities recorded in the NVDCVE database;
- IsOfType: This relationship exists between a VulnPort node and a ServiceType node, indicating the type of services that VulnPort provides or manages. An IsOfType relationship is directed from a ServiceType node to a VulnPort node.

The following figure (Fig.1) shows a visual representation of the nodes and the relationships between them.

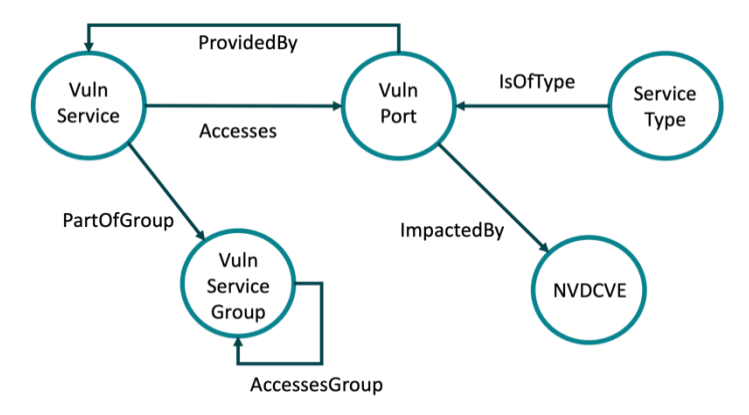


Figure 1: Visual representation of nodes and relationships

The built-in Cypher query language can be used to query the dataset, enabling both simple statistical queries and more complex graph analysis algorithms, such as clustering. The Cypher query language is developed specifically for the Neo4j graph database management system, with the goal of providing an intuitive and human-readable way to query and manipulate graph data. The language is based on pattern matching, allowing users to easily describe patterns in the relationships between nodes and edges in the graph, thus effectively supporting complex queries and data manipulation operations.

By utilizing simple Cypher queries to explore the dataset, questions can easily be answered such as the exact number of VulnService nodes within the dataset, or counting the connections and nodes based on a specific relationship type (*Fig.*2).

Based on the specified IP addresses, it is possible to list properties of the nodes. Furthermore, a valuable feature of graph databases is the ability to visualize subgraphs from the entire dataset according to given specifications, or to display smaller groups based on well-defined parameters.

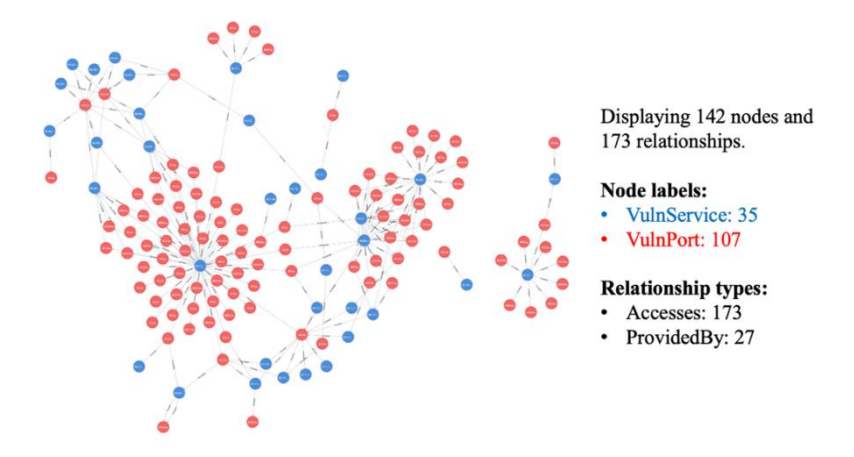


Figure 2: Accesses graph based on connection type

The Neo4j database management system offers a wide range of tools and functions for analyzing graphs through the built-in Graph Data Science Library, which includes multiple graph analysis algorithms, some of which we also examined. We tested several algorithms on the dataset, which are detailed below:

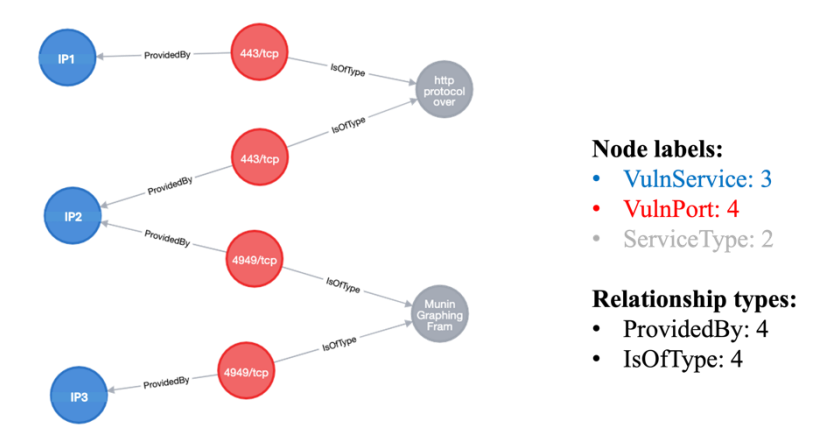


Figure 3: Result of path finding between two VulnService nodes

Path finding: Complex path searches were performed within the graph, such as determining the shortest path between two different VulnService nodes, as well as identifying all possible routes between these nodes (*Fig.3*). This method helps to identify connections and distances between network elements. This can be very useful if we want to examine the paths an attacker can take in our system in the event of an attack.

Centrality measures: represents the calculation of centrality degree, which measures the importance of individual nodes based on the number of connections they possess. *Table 2* contains the largest three centrality degree values obtained as a result. This method is crucial for identifying high-traffic or strategically important nodes.

Name/IP address	Centrality degree
"x.x.2.2"	58.0
"x.x.1.193"	42.0
"x.x.4.58"	37.0

Table 2: Partial result of calculating centrality degree

Community detection: Several community detection algorithms were employed, such as PageRank. These algorithms give help in identification of groups that are engaged in intensive communication or are strongly interconnected. The results include mapping the structure of communities and highlighting the stronger and weaker connections between nodes. The PageRank algorithm built into Neo4j measures the importance of nodes in a graph based on how many incoming links they have and how important those links are. "Stronger" and "weaker" links indicate the weight of the links; "stronger" links have a higher weight and therefore have a greater influence on the PageRank value, while "weaker" links have a lower weight and have a lesser influence. The partial results in Table 3 show exactly which nodes have a higher "influence" in the network, the table only contains the first 3 values.

Table 3: Partial result of the Page Rank algorithm

Name/IP address	Score
"x.x.2.91"	1.488
"x.x.2.44"	1.245
"x.x.251.120"	0.980

Anomaly detection: Cypher queries can be used to detect network anomalies, such as overly frequent communication creation. This is useful because the connection-based approach can uncover hidden relationships and anomalies that are difficult to detect with traditional databases. *Table 4* shows a list of IP addresses that communicate through an unusually high number (more than 10 - limit value determined by us) of different ports, noted as uniqueUsedPortCount. An in-depth understanding of the system's network architecture enables statistical analysis to determine the threshold above which the volume of communication from a specific host is considered an anomaly on different ports.

sourceIP	uniqueUsedPortCount
"x.x.2.2"	58
"x.x.250.218"	21
"x.x.251.120"	15

Table 4: Partial result of the anomaly detection algorithm

Pattern detection: This method allows for the search of predefined patterns within the graph, which can be particularly useful in security assessments. During its application, various attack patterns were identified. The application of these algorithms provided a comprehensive overview of our network structure, aiming for a better understanding and management of security risks. *Fig. 4* illustrates the patterns among nodes within the dataset, specifically highlighting which VulnService nodes are associated with the same VulnServiceGroup. This grouping encompasses nodes whose IP addresses share the first three segments, indicating their affiliation with the same network segment.

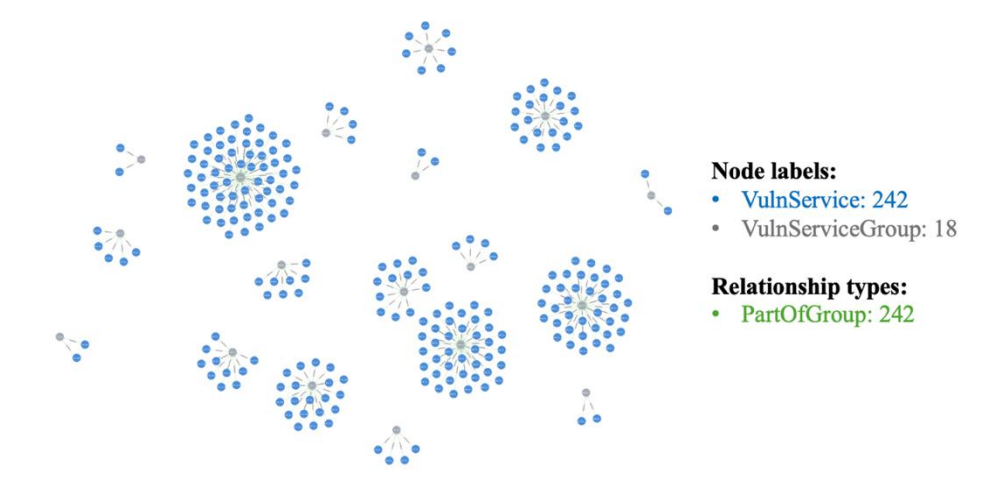


Figure 4: Partial result of pattern detection

To further analyze the dataset, we also applied clustering methods to group nodes with similar attributes or to form new groups based on their connections. For this, we fine-tuned the K-NN (K-Nearest Neighbors) and Louvain algorithms, specifically tailored to our dataset.

The K-NN (K-Nearest Neighbors) algorithm is a machine learning method that performs classification and segmentation of nodes or data points based on their 'nearest' neighbors. The algorithm primarily serves to identify similarities between nodes, enabling the identification of the most similar or distinct nodes,

making it suitable for anomaly detection as well. Among its advantages is the ability to recognize non-linear relationships, which allows for diverse applications, including the analysis of complex relationships between IP addresses and ports. In *Fig.5*, a partial result of running the KNN algorithm is shown, limited to the first 25 connections, demonstrating the five closest neighbors for each node that match the properties defined in the parameter list (port number, service type, vulnerability number, high risk score, exploit risk score). The objective of the KNN analysis is to identify the closest data points based on similarity, meaning that the algorithm considers the distance between data points to determine their similarity. Thus, KNN is a simple yet effective method for classifying or predicting various types of data.

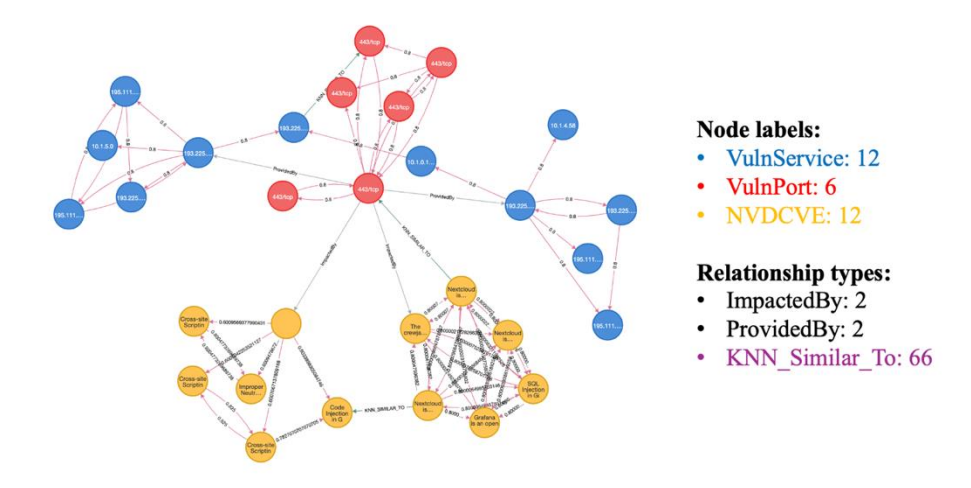


Figure 5: The partial result of the KNN algorithm run

The application and fine-tuning of the KNN algorithm provide opportunities for anomaly detection and the creation of predictive models. By analyzing the nearest neighbors within a network, anomalies such as elements exhibiting unusual connection patterns can be more easily identified. This form of analysis can thus be beneficial for cybersecurity assessments. Additionally, KNN enables predictive analysis of data, allowing for the prediction of future behavior of entities within the network based on the behavior of similar entities.

The Louvain algorithm is designed to identify community structures within graphs, iteratively forming groups from more tightly connected nodes. The Louvain algorithm is based on the density of connections between nodes and the maximization of graph modularity to identify communities. It minimizes the proportion of edges between communities while maximizing the density of edges within communities. The communities generated through these iterations are

represented by community identifiers, facilitating the grouping of nodes and making it easier to interpret the relational patterns within the graph. *Table 5* shows a partial result of the Louvain algorithm, displaying the IP addresses and community IDs where the algorithm assigned each IP address. By determining the communityId, communities within the graph can be easily identified and visualized, making tightly connected groups and their interactions clearly visible. The community identifiers assigned to each node enable analysis at the community level, such as examining behavioral patterns within the community.

Table 5: The partial result of the Louvain-algorithm run

Name/IP address	communityId
"x.x.250.91"	1
"x.x.251.219"	1
"x.x.1.183"	69

The table (*Table 6*) below shows the partial results of the query, which allows us to examine exactly which nodes the algorithm classified into given communities.

Table 6: Partial results of the list of communitiIds and members

Commu- nity	Members
1	["x.x.250.91","x.x.251.219","x.x.1.65","x.x.11.100]
69	["x.x.1.183","x.x.1.145","x.x.1.129"]
131	["x.x.2.81","x.x.2.91","x.x.2.96","x.x.1.154","x.x.1.159","x.x.1.202"]

4. Conclusions

The application of Neo4j graph databases for network data analysis demonstrated significant advantages in handling complex relational structures, especially within IoT and digitalized environments. By leveraging graph-based approaches, we achieved more efficient data management. The graph database representation together with the built in Neo4j developer tools, the Cypher Query Language and the GraphQL Library provides powerful open-source network data management capabilities.

Key Findings:

In the field of detection and analysis of network anomalies the application of algorithms such as K-Nearest Neighbors (KNN) and Louvain for clustering, community detection, and pattern recognition significantly improved our ability to detect network anomalies. These methods allowed for the identification of

unusual communication patterns and security vulnerabilities, particularly in high-traffic environments. The ability to identify nodes with high centrality or nodes associated with potential security risks facilitates the creation of more robust security measures.

The flexibility of Neo4j's Cypher query language and its optimized graph data structure enable faster and efficient querying and real-time analysis. The ability to model nodes and edges allowed for efficient representation of complex network relationships, reducing the overhead associated with traditional tabular data processing. This was particularly beneficial in scenarios requiring real-time analysis of dynamically changing network data.

The results from analyzing various network configurations (VLANs and cloud environments) showed that Neo4j can efficiently manage large volumes of network traffic data. The scalability of graph databases, coupled with their capability to handle heterogeneous data formats, ensures their applicability in expanding network infrastructures and IoT systems.

By employing centrality measures, community detection, and path-finding algorithms, we gained deeper insights into network behaviors. For instance, the use of centrality measures identified critical nodes that could act as potential bottlenecks or high-value targets in a network. Similarly, community detection helped isolate groups with intensive intra-communication, which can be vital for optimizing network performance and enhancing security protocols.

The study indicates that graph databases, particularly Neo4j, offer a promising solution for network analysis in environments where relationships between data points are intricate and constantly evolving. Future research could focus on integrating additional graph algorithms, such as advanced anomaly detection or machine learning models, to further enhance predictive capabilities. Additionally, extending this approach to other domains such as social networks, industrial systems, or supply chains could unlock new avenues for complex data analysis.

In summary, the integration of Neo4j graph databases into network data analysis not only enhances the efficiency of data processing but also enables a deeper understanding of complex relational structures. This positions Neo4j as a valuable tool for advancing cybersecurity measures, optimizing network performance, and supporting decision-making processes in modern technological environments.

Acknowledgements

This research is a part of project no. NKFIH-3568-1/2022, that has been implemented with the support provided by the Ministry of Culture and Innovation of Hungary from the National Research, Development and Innovation Fund,

financed under the 2022-2.1.1-NL funding scheme. Computing resources were provided by HUN-REN Cloud [8].

References

- [1] Afandi, M.I., and Wahyuni, E.D., "University Research Graph Database for Efficient Multi-Perspective Data Analysis Using Neo4j", in 6th IEEE Information Technology International Seminar (ITIS), pp. 286–290, 2020, October.
- [2] Almabdy, S., "Comparative analysis of relational and graph databases for social networks", in *proc.1st IEEE International Conference on Computer Applications & Information Security (ICCAIS)*, pp. 1–4, 2018 April.
- [3] Guia, J., Soares, V.G. and Bernardino, J., "Graph Databases: Neo4j Analysis", in *ICEIS* (1), pp. 351–356, 2017 April.
- [4] Lal, M., "Neo4j graph data modeling", in *Packt Publishing Ltd.*, 2015.
- [5] Fernandes, D. and Bernardino, J., "Graph Databases Comparison: AllegroGraph, ArangoDB, InfiniteGraph, Neo4J, and OrientDB", in *Data*, 10, 2018.
- [6] Macak, M., Stovcik, M. and Buhnova, B., "The Suitability of Graph Databases for Big Data Analysis: A Benchmark", in *IoTBDS*, pp. 213–220, 2020 May.
- [7] Needham, M. and Hodler, A.E., "Graph algorithms: practical examples in Apache Spark and Neo4j", in *O'Reilly Media*, 2019.
- [8] M. Héder et al., "The Past, Present and Future of the ELKH Cloud," in *InfTars*, vol. 22, no. 2, p. 128, Aug. 2022, doi: 10.22503/inftars.XXII.2022.2.8.
- [9] Rigó, E., "Anonymized netflow and security scan data", https://hdl.handle.net/21.15109/ ARP/ FBIIOZ, ARP, V1, 2024.